Three-dimensional dosimetry around small distributed high-Z materials

A THESIS
SUBMITTED TO THE FACULTY OF THE GRADUATE SCHOOL
OF THE UNIVERSITY OF MINNESOTA
BY

Leighton Warmington

IN PARTIAL FULFILLMENT OF THE REQUIREMENTS
FOR THE DEGREE OF
Doctor of Philosophy

Advisor: Yoichi Watanabe, PhD
Co-advisor: Bruce J Gerbi, PhD

May, 2016

Acknowledgements

I would like to thank my advisor, Professor Watanabe, for his guidance, support and friendship through out the course of my program. I truly appreciate the level of access that I had to him and allowing me to volunteer with him to gain clinical experience. I would like to thank my co-advisor, Professor Bruce Gerbi. Thank you for your useful discussions especially when trying to solve the contamination problem with the polymer gels. I want to extend my thanks to your wife, Dr. Diana Gerbi. Thank you for your suggestions in dealing with this issue and the provision of materials. I want to thank Dr. N Gopishankar and Dr. Senthil Kumar for useful discussions on polymer gel dosimetry and insights into the manufacturing process. I want to thank Dr. Faiz Khan for his useful discussions and perspective on interface dosimetry. I also want to thank Dr. Frédéric Tessier at the National Research Council Canada. Thanks for answering my questions on the EGSnrc tool kit when specific documentation or a user community were not available.

I want to give a special thanks to Dr. Pat Higgins and the Department of Radiation Oncology for financial support at various critical points of the journey. I also want to thank the other members of my committee, Prof. Bruce Hammer, Prof. Russell Ritenour and Prof. John Broadhurst. Thanks for serving on both my preliminary and final oral committees, and taking the time to review my dissertation.

Finally, I would like to thank my parents, brother and friends for their support and encouragement. Thank you for believing in me when I wanted to leave. Without you

this journey would not have been possible.

Dedication

To my Heavenly Father and Family.

Abstract

Patients are increasingly undergoing radiotherapy procedures, in which small metals are implanted in the body for target localization for IGRT or targeted therapies. Previous, interface dosimetry studies focused high-Z materials irradiated by low energy beams where the dose enhancement is large. In the majority of the cases, they used one or two dimensional detectors. Therapeutic beams, however, are mostly 6 MV and higher with significantly less dose enhancement. Over the last decade, significant improvements in polymer gel dosimetry have been made allowing for improved 3D dose measurements. The purpose of this study was to better understand the dose around distributed high-Z materials irradiated by high energy photon beams and investigate the feasibility of 3D dose measurements.

A Monte Carlo code was used to determine the effect of various foil configurations. The dosimetric effect of foil thickness, separation, energy and other factors were investigated. Software tools were also developed to process the data. These results were used to help identify suitable experimental setups. The dose around two foils was compared to the dose resulting from adding the dose of two single foils. The dose around a single foil was also compared to the dose around a fiduciary marker. Later on, we looked at how distributing the thickness of the high-Z foil over a wider area affected dose and how that compared to a to the dose around a single foil. Finally, we looked at the effect of pair production and how it affected the distribution of dose in select configurations.

Several polymer gel dosimeter (PGD) were evaluated and two were selected for further study. Various formulations were investigated and procedures developed to meet the needs of the project. Materials compatibility studies were performed to ensure that there were no reactions between the PGD and inserted materials within the time frame of the studies. PGDs were manufactured and thin lead foils with the configuration determined earlier were inserted into the polymer gel. The PGDs was irradiated with 18

MV photons and the dose was quantified using MRI with a multiple spin echo technique for the measurement of the spin-spin relaxation rate (R_2). The measured dose data were compared to theoretical data obtained from Monte Carlo experiments.

The dose profiles around the foils from the PGD were in agreement with dose values from simulation. This project demonstrated that it is feasible to use polymer gel dosimetry to measure the fine dosimetric structures around a small metallic object. We also determined that material, foil thickness, separation and photon energy had the largest effect on the dose in-between a two foil configuration. When the foils were close, we found that the dose around the two foils was larger but not significantly different from the combined dose of two single foils with the same separation. We also found that the dose upstream and downstream of a distributed foil is less that the upstream and downstream dose around a single foil of equivalent thickness.

Contents

List of Tables

List of Figures

List of Abbreviations

ABS	Acrylonitrile Butadiene Styrene
BANANA	Bis, Acrylmide, Nitrous oxide and Agarose
BANG	Bis, Acrylamide, Nitrogen and Gelatine
Bis	N-N'-methyIene-b Is-acrylamide
GNP	Gold Nanoparticle
HU	Hounsfield Unit
HDPE	High Density Polyethylene
MAA	Methacrylic Acid
MAGAT	Methacrylic Acid, Gelatin, THPC
MAGIC	Methacrylic Acid, Gelatin, Ascorbic acid Initiated by Copper Sulphate
nMAG	Methacrylic Acid, Gelatin, THPS
NMR	Nuclear Magnetic Resonance
nPAG	PolyAcrylamide Gelatin gel
OD	Optical Density
PAGAT	PolyAcrylamide, Gelatin, N,N'-Methylenebisacrylamide, THPC
PDD, %DD	Percent Depth Dose
PGD	Polymer Gel Dosimeter
R1	Longitudinal (spin latice) relaxation rate
R2	Transverse (spin–spin) relaxation rate (1/T2)
SSD	Source-Surface Distance
TE	Echo Time
THPC	Tetrakis (Hydroxymethyl) Phosphonium Chloride
THPS	Bis[tetrakis(hydroxymethyl)phosphonium] sulfate
THP	THPC or THPS
TLD	Thermoluminescent Dosimeter

Chapter 1

Introduction

1.1 Description of the Problem

The magnitude of absorbed dose delivered to patients is the most important physical parameter for radiation therapy. It is well known that the higher the dose to tumors, the better the effect of the treatment. However, the maximum dose safely given to a patient is limited by the dose to the area outside the tumor where healthy tissue is present. The tumor volume often presents a complex shape in three-dimensional (3D) space. Hence, very sophisticated radiation delivery techniques have been developed to maximize the dose delivered to the tumor while minimizing the dose to normal tissue. These include intensity modulated radiation therapy (IMRT), volumetric modulated arc therapy (VMAT), proton therapy (PR), image-guided radiation therapy (IGRT), stereotactic radiosurgery (SRS), stereotactic body radiosurgery (SBRT), and high dose-rate brachytherapy (HDR)[2].

In photon-based radiotherapy, the photon energy is indirectly deposited in tissue by secondary electrons generated by the interaction of photons with atoms composing the tissue. For materials heavier than tissue (or tissue-like material), this can result in significant local dose increases in the vicinity of the material. Extremely high dose in

both backward and forward directions of a thin high atomic number (Z) metal such as lead and gold was theoretically predicted and experimentally demonstrated [3, 4, 5, 6, 7, 8, 9].

Traditionally, dose measurements were done in a simple geometrical setting such as in the vicinity of thin foils using small detectors such as micro-TLDs or thin plane type detectors such as radiographic films and plane-parallel ionization chamber. In particular, the latter was an ideal detector to obtain dose distribution along the beam axis orthogonal to the foil plane with high precision and accuracy [4, 6]. When the geometrical shape of the object is not a plane, a planar detector is not suitable and a small volume detector is needed. Micro-TLD chips are acceptable to some extent, but obtaining the 3D dose distribution with the TLDs is time-consuming and, after all, the measurable spatial resolution is still limited.

Polymer gel dosimeters (PGD) were developed as true 3D dosimeters [10] and they have been used for measurements of 3D dose distribution around small radioactive sources by many researchers successfully[11, 12, 13, 14, 15, 16, 17]. Meanwhile, there were only a few experiments, in which one attempted to measure the 3D dose distribution near a high-density material when the subject is irradiated with photon beam externally. Watanabe et al measured the dose distributions near bone-like high-density material embedded in a BANG PGD phantom, which was irradiated with a photon beam [18, 19]. Recently, two other groups published brief reports on the dose measurement results for titanium plates and prosthetic objects implanted in PGD [20, 21].

More recently, researchers have sought to take advantage of the increased dose from high-Z materials to treat tumors. Gold, in particular, is important because its desirable chemical characteristics make it an attractive material for therapeutic applications. It is inert and generally biocompatible making it ideal for use in the body. Gold nanoparticles (GNPs) permeate leaky angiogenic endothelium due to enhanced permeability and retention [22]. This combined with PEGylation can cause gold nanoparticles to stay in

the blood longer than smaller molecules. These factors along with many others have led to an explosion of research in gold nanoparticles over the last 15 years. The three areas of interest in radiation therapy are the use of nanoparticles for drug delivery, thermal therapy, and enhanced radiation dosimetry.

Effective drug delivery to the intended site is an important problem in treatments. Filtration by the liver and kidney can reduce the effectiveness of treatment and increase the cost. To improve targeting and outcome, GNPs can be used as a delivery mechanism by grafting ligands for drugs. An example of this is the work by Patra et al, who used GNPs for the treatment of pancreatic cancer resulting in an improved outcome[23]. They used cetuximab and gemcitabine as the targeting agent and the anticancer drug, respectively. GNPs also have been used in thermal therapy applications. It is well known that hyperthermia induces apoptotic cell death and it is often used in combination of other treatments such as radiotherapy [24, 25]. Though traditional hyperthermia approaches have been limited by a lack of tumor specificity and temperature limitation, advances in nanoparticle research have made localized heating possible. Nanoparticles in thermal applications are often in the form of gold coated rods or shells to better absorb near infra-red light which in turn radiates heat. One limitation that still exists is that the laser will only penetrate a few centimeters of soft tissue. MR-based hyperthermia, however, might be able to treat those tumors at deeper locations [26]. Since photon interactions with gold atoms are much stronger than the interaction with tissue atoms, the photon energy deposition can be effectively localized inside the tumor volume. This idea was experimentally tested and confirmed to be viable [27]. This technique, however, is the most effective when the photon energy is in the keV range because of the increased electron production due to the photoelectric effect. Low energy photons cannot penetrate deep into the tissue; hence the technique is only effective for the treatment of tumors located at a shallow depth.

So far, all indications are that these techniques work best when combined with radiation therapy or other therapies. The increased interest in alternative therapies

using gold nanoparticles for thermal ablation and drug delivery means that we have to understand how the high-Z materials used for these applications affect the absorbed dose. The increase in patients receiving implants for health reasons will also become a significant treatment-related issue in coming years. Therefore, the magnitude of the change in the local dose near metallic materials should be carefully considered and more accurately known for appropriate handling of such patient populations. Both theoretical studies, mainly by Monte Carlo simulations, and experimental measurements should be performed to gain more detailed knowledge and more accurate data on the dose distribution.

The most accurate computational method to evaluate how 3D dose distribution varies in the vicinity of high-Z materials is Monte Carlo simulation. Significant improvements have been made in Monte Carlo codes in recent years, in particular, more accurate transition zone algorithms[28, 29]. One area that still needs more work, however, is simulation in a medium containing nanoparticles. Simulations have also been attempted but there has also been some debate on the validity of their approach. Dose depends on many factors including particle size, shape, concentration and distance from DNA. Often compromises have to be made in the particle shape, beam size, among others which are often unrealistic and lead to significant errors in dose and incorrect conclusions [30, 31]. One simplification for instance is to use a pencil beam with a single particle. This is nowhere near sufficient to describe how dose is affected by distributed high-Z materials. There also needs to be a way to correlate damage at the DNA level to dose at the macroscopic level.

On the measurement side, experiments have produced conflicting results regarding the feasibility of nanoparticle dose enhancement. Some attempts to quantify the dose enhancement effects in PGD with gold nanoparticles have been made, but none were done at high energies [32, 33]. Regardless, a PGD with embedded nanoparticles has a very scattered particle distribution. This would make it more difficult to isolate and determine the effect of various parameters on dose. Perhaps one of the biggest issues

with working with nanoparticles is the lack of control in the positioning of the particles. How do they know exactly where the nanoparticles are or how they are distributed? It is very likely that the nanoparticles are unevenly distributed or accumulated near cellular targets [34].

1.2 Proposal

At photon energies used for radiation therapy, we cannot take significant advantage of photoelectric-based dose enhancement. If much higher energies, i.e., 10 MV or higher, are used, we can take advantage of pair production. This approach has the advantage of allowing the treatment of deeper tumors without having to worry about high surface doses from low energies. The probability of pair production is proportional to Z^2 and it increases with energy when photons have energy much higher than 1.022 MeV. Alkatib et al demonstrated that there was as much as 44% dose increase when 18 MV photon beams were used in a water-like medium containing gold plates [35].

While researchers struggle with problems in delivering nanoparticles to target areas and obtaining the proper distribution in the organ, a subset of patients may have an alternative approach. Patients with large solid tumors often have surgery first to reduce the size of the tumor. Reducing the tumor significantly improves the chance of success of radiotherapy and chemotherapy. Sometimes, however, large portions of the tumor can't be removed because of its proximity to other critical structures or because removal would result in a significant loss of function. In these cases, placing gold materials directly into the tumor and giving high energy photons might be a method of providing significant dose to the tumor. By using small distributed high-Z materials in the order of 0.1mm-1mm, we have more control over placement of the material. Logistically, this could work well since the patients are already going through surgery. The material could remain in the person permanently and could also use as an aid in tracking. This approach would require multiple high-Z materials with appropriate distribution and shape to optimize

the treatment. Before we can begin to apply these techniques, we need to gain a much deeper understanding of how dose is distributed between high-Z materials.

I propose that extended simulations be carried out to better understand how dose is distributed around the high-Z materials. I'm interested in two setups. One is a two foil system similar to the one used by Alkhatib [35] and the other is using fiducial markers. For the foils, I will investigate the effect of foil separation, foil thickness, foil size, field size, depth, energy and material on the dose around and in-between the foils. For the marker, I will simulate the dose around it when oriented vertically and horizontally. From these results, we will select a couple of sample configurations, then look at the feasibility of measuring dose around the foils when those are inserted in a PGD and irradiated by high energy photons. We will investigate various polymer gel formulations and customize one for the needs of the project. The dose from the PGD will be compared to the Monte Carlo simulation.

Along the way, we will answer some other questions. We know how pair production affects dose, but we know less about how it affects the dose distribution. The effect of pair production will be determined for the configurations above. We will also look at the effect on dose of a single foil and a distributed foil of equivalent thickness.

A future goal of this project is to develop a framework for estimating the dose in the vicinity of many (or more than two) small distributed high-Z materials that are placed in the body. Even further down the road, we may be able to estimate dose in the vicinity of nanoparticles. Assuming that the parameter dependencies scale down in a predictable way, one could estimate the dose based on concentration, particle size, energy rather than by simulating each case. This would result in significant time savings especially if the base dose roughly uniform in that area.

1.2.1 Goals of the project

The specific aims of the project were:

- To develop the computational tools for the large scale analysis of the data from Monte Carlo simulation and polymer gel dosimetry for the Windows operation systems.
- To investigate the dependency of various parameters on dose in the vicinity of a two foil system.
- To investigate the effect of distributed high-Z material on the overall dose.
- To determine the effect of pair production on distributed dose.
- To optimize the composition, manufacturing procedures and scanning parameters of a polymer gel dosimeter, which meets the needs of the project.
- To investigate the feasibility of using polymer gel dosimetry for measuring the dose in the vicinity of high Z materials.

Chapter 2

Background and Literature Review

2.1 Particle Interactions

2.1.1 Photon Interactions

If a photon interacts with an atom, it is either absorbed or scattered. The attenuation of photon intensity depends on the number of photons and the thickness of the material. This is governed by

$$dI = -\mu I dx \tag{2.1}$$

where μ is the linear attenuation coefficient. This can also be represented as

$$I(x) = I_0 e^{-\mu x} \tag{2.2}$$

where x is depth in the material and I_0 is the initial intensity. The linear attenuation coefficient is a property of the material and depends on the photon energy. It is related

to the cross-section, σ_{tot} by:

$$\mu = \frac{\sigma_{tot}\rho N_A}{A}. \tag{2.3}$$

Several types of interactions are possible in radiation therapy. The most important ones, however, are Raleigh scattering (σ_{ral}), Photoelectric effect (σ_{phot}), Compton scattering (σ_{comp}) and Pair production (σ_{pair}). Each contributes to the overall interaction such that:

$$\sigma_{tot} = \sigma_{ral} + \sigma_{phot} + \sigma_{comp} + \sigma_{pair}. \tag{2.4}$$

It is often advantageous to make μ independent of the material density. This is defined to be the mass attenuation coefficient:

$$\mu_{mass} = \frac{\mu}{\rho} = \frac{\sigma_{tot}N_A}{A}. \tag{2.5}$$

Fig. 2.1 shows how the mass attenuation coefficient varies with energy for gold.

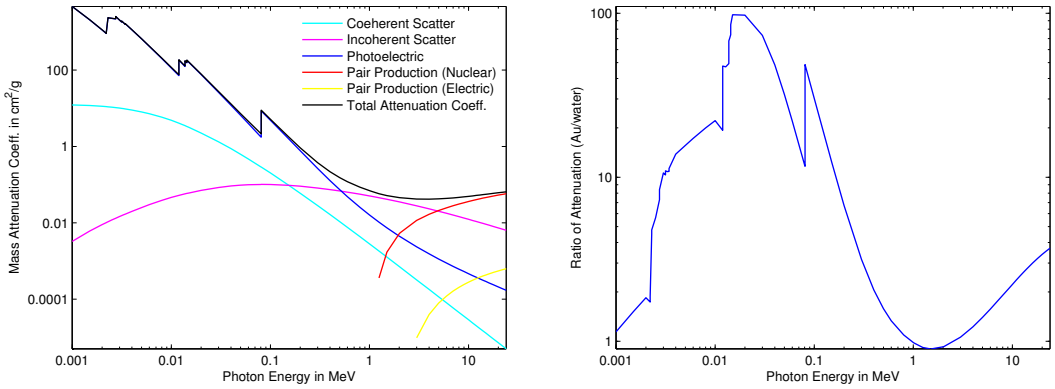

Figure 2.1 – Mass attenuation coefficients vs energy for gold. (a) Shows the mass attenuation coefficient of coherent (Raleigh), incoherent (Compton), photoelectric effect and pair production (nuclear and electric) and total mass attenuation coefficient. (b) Shows the relative attenuation for gold to water. The data was generated from interaction cross section information in the XCOM 1.5 software [36].

2.1.1.1 Rayleigh (Coherent) Scattering

In Raleigh scattering, the photon interacts with the electrons of the atom as a group. The electric field from the photon sets the electrons in oscillation at the same frequency of the photon, then it re-radiates the photon at the same frequency but in slightly different direction. There is no loss of energy in the process, and the deflection angle decreases with increasing energy. In high-Z materials, this process can occur with energies up to 150 – 200 keV, but in tissue equivalent material it only occurs at low energies [37]. Raleigh scattering is not very significant in radiation therapy and has the least contribution to the total cross section.

2.1.1.2 Photoelectric Effect

Photoelectric effect occurs when a photon is absorbed by an atom and an orbital electron is emitted. The electron has kinetic energy, E_k , which is the incident photon energy minus the binding energy, E_B.

$$E_k = h\nu - E_B \tag{2.6}$$

This can only occur when the incoming photon energy is greater than the binding energy of the electron. When the electron is ejected, a vacancy is created in the inner shell that is immediately filled by another electron from a higher energy electron orbital. A characteristic x-ray is released, having the energy of the difference in binding energies of the two electron orbitals. This results in an electron cascade and a release of a series of characteristic x-rays. The probability is highest just above the binding energy of each shell and is approximately proportional to Z^3/E^3.

2.1.1.3 Compton (Incoherent) Scattering

In Compton scattering, the photon interacts with a loosely bound electron, an electron is ejected and the photon is scattered with reduced energy. This usually occurs with the outer shell electrons and with photon energies much greater than the electron binding

energy. In this case, the binding energy is considered negligible.

Equation 2.7 shows the Compton wavelength shift relationship, where λ is the wavelength of the incident photon, λ' is the wavelength of the scattered photon and θ is the photon scattering angle.

$$\Delta\lambda = \lambda' - \lambda = \frac{h}{m_0 c}(1 - cos\theta) \tag{2.7}$$

The kinetic energy of the recoil electron depends on the photon energy and the photon scatter angle and is given by,

$$E_k = h\nu - h\nu' = h\nu\frac{\alpha(1 - cos\theta)}{1 + \alpha(1 - cos\theta)} \tag{2.8}$$

where $\alpha = \frac{h\nu}{m_0 c}$. The electron kinetic energy is zero when the photon scattering angle is zero (forward scattering) corresponding to the electron recoil angle of $\pi/2$. The electron kinetic energy is largest when the photon scattering angle is π (backscattered) corresponding to the electron recoil angle equal zero.

This is the dominant process in radiation therapy and it has an effective energy range of a couple hundred keV to 30 MeV. Since the photon interacts with loose electrons, the Compton interaction is independent of atomic number. The mass attenuation coefficient only depends on the electrons per gram.

2.1.1.4 Pair Production and Triplet Production

In pair production, a photon can interact with the electric field of a nucleus, where the photon is absorbed and a positron-electron pair is created. A photon energy in excess of 1.022 MeV is required for this process and can be represented by the equation:

$$h\upsilon = 2m_0 c^2 + K_{e+} + K_{e-}. \tag{2.9}$$

The threshold energy is necessary to account for the combined rest mass energy of the positive and negative electron, $2m_0c^2$ and any remaining energy is distributed as kinetic energy to the electron and positron. On average, the kinetic energy is shared equally between the particles, but this is not always the case. This interaction is proportional to Z^2 and increases logarithmically with energy above the threshold [2]. The particles lose energy by ionization, excitation, and bremsstrahlung and as they slow-down they are eventually absorbed. The positron combines with an electron and produces two annihilation photons having 511 keV energy and traveling in roughly opposite directions. Sometimes an electron from the electron cloud of an atom interacts with the incoming photon and ejects that electron in addition to the electron-positron pair. This process is called triplet production and is proportional to Z. This process is also subject to a minimum photon energy and is governed by:

$$h\upsilon_{min} = 2m_0c^2\left(1 + \frac{2m_0c^2}{2Mc^2}\right). \tag{2.10}$$

In triplet production, $M = m_0$, resulting in minimum photon energy of $4m_0c^2$; where as in pair production $M = M_{nucleous}$ so the equation breakdowns resulting in a minimum photon energy of $2m_0c^2$.

2.1.1.5 Photodisintegration

Photodisintegration can occur when the very high energy photons interact with or get absorbed by the nucleus. In this process, one or more nucleons are emitted resulting in a change in the element. Photodisintegration has a threshold energy defined to be the difference between the rest energy of the target nucleus and residual nucleus plus the emitted nucleons [2]. This plays only a minor role in attenuation in photons above 10 MeV, contributing a few percent.

2.1.2 Charged Particle Interactions

As an electron moves through a material, interactions occur as the electric field of the particle interacts with the electric field of the orbital electrons and the nucleus. Light charged particles interact with an atom by a few mechanisms. Fig. 2.2 describes the different interactions. They interact by inelastic collisions (ionization, excitation) with the orbital electron ($b \gg a$), elastic collisions with an orbital electron ($b \sim a$), inelastic collisions with the nuclei (bremsstrahlung) ($b \ll a$) and elastic collisions with the nuclei ($b \ll Rnucl$). Here, the impact parameter b is defined to be the shortest distance between charged particle and the atom and the parameter a is the average radius of the electron cloud.

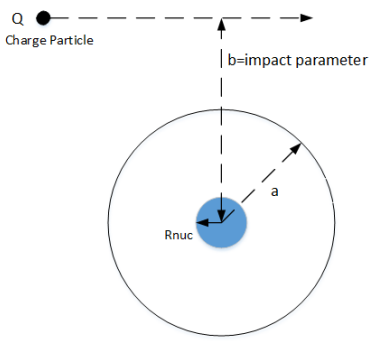

Figure 2.2 – The interaction of an electron with an atom with atomic radius a and impact parameter b

Ionization dominates for low-Z materials and bremsstrahlung dominates in high-Z materials. These result in continuous energy loss which deposit dose in the material.

2.1.2.1 Inelastic(Soft) Collisions ($b \gg a$)

If an electron passes some distance from the atom but does not collide with an orbital electron, then it will interact with many electrons at once through the particle's Coulomb field. This is called a soft collision and leads to continuous electron energy loss by excitations and sometimes the electron ionizes a valence electron. Only a very small

amount of energy is transferred to the atom by this process. This situation is most common and about half the kinetic energy is lost in the matter through this mechanism.

2.1.2.2 Hard (knock on) Collisions ($b \sim a$)

When the impact parameter is close to the orbital electrons, then it becomes more likely that a hard collision will take place. In this process, the particle interacts primarily with an outer shell electron leading to ionization. Often if the energy is large enough, the secondary electrons can also lead to additional ionizations and excitation and is referred to as a δ ray. Energy is continually lost until the electrons reach thermal energy and are absorbed. The probability of this interaction is slightly less than a soft collision, but in both cases, the amount of energy loss from the particle is about the same [38].

2.1.2.3 Inelastic Radiative losses (Bremsstrahlung) ($b \ll a$)

When electrons get accelerated and get very close to the nucleus, they interact primarily by Coulomb forces. In about 2-3% of the cases, the electron slows, changes its direction and a photon is released. For low energies, the photon tends to be emitted between 60-90 degrees, while for higher energies the photon tends to go in the forward direction [39]. The bremsstrahlung x-ray can have any energy up to the value of the full kinetic energy of the electron resulting in a continuous spectrum. The probability of this process increases with the square of the atomic number and inversely with the square of the mass of the absorber, Z^2/m^2. In general, bremsstrahlung is insignificant in low atomic number materials for energies below 10MeV. The bremsstrahlung photons are penetrating enough to leave materials several cm thick and do not deposit much dose in the material [38].

2.1.2.4 Elastic Scattering

In the rest of the cases, the electrons scatter elastically and do not emit a photon or excite the nucleus. It results in an insignificant change in energy, but a significant

change in direction. This is not a mechanism for dose deposition and the energy change is to conserve momentum [38].

2.1.2.5 Stopping Power

The rate of energy loss for distance traversed is defined as the stopping power, S. The stopping power depends on the density. The total mass stopping power removes the density dependence and is defined as:

$$\frac{S}{\rho} = \left(\frac{dE}{\rho dx}\right)_{col} + \left(\frac{dE}{\rho dx}\right)_{rad} \tag{2.11}$$

and has units $MeV.cm^2/g$. It is subdivided into the collision stopping power which is a combination of hard and soft collisions and the radiative stopping power which comes from radiative processes. The mass stopping power is greater for low Z material than high-Z materials [2].

2.1.2.6 Range

Charged particles undergo many interactions changing their direction before being absorbed. The horizontal distance traveled is called the range. The range can be calculated by using the reciprocal of the mass stopping power. It assumes that the energy loss at every interaction is equal to the total mass stopping power. This approximation is called the continuous slowing down approximation (CSDA). The CSDA range is given by equation 2.12.

$$R_{CSDA} = \int_0^{E_k} \left(\frac{dE}{\rho dx}\right)^{-1} dE \tag{2.12}$$

Fig. 2.3 shows a plot of the CSDA range of an electron for gold and water.

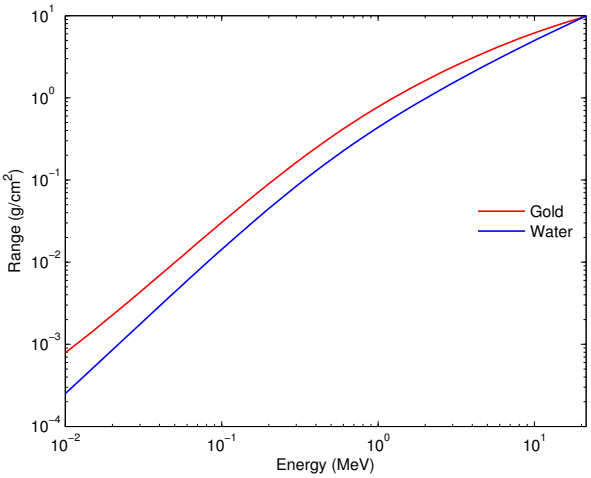

Figure 2.3 – The CSDA range for Gold and Water

2.2 Dose Calculations

2.2.1 What is Monte Carlo

Monte Carlo simulation is a statistical technique for performing numerical integrations. The modern version of Monte Carlo was first proposed at the end of World War II by scientists at Los Alamos. They were working on nuclear weapons and the completion of the ENIAC computer provided a significant opportunity. John Von Neuman approached Stanley Ulam and asked him to come up with a simple simulation of a thermonuclear reaction. His results were enough for guarded optimism about the feasibility of thermonuclear weapons and opened the door to pursue applications in statistical methods [40]. The attempt to apply these methods to radiation transport led to the Monte Carlo Method. The advance of digital computers led to an explosion of the technique and today it is used in areas ranging from finance, social sciences, genetics, physical sciences, circuit design and radiation transport. Monte Carlo is often used to answer questions that would be impossible to answer analytically or be too time-consuming. It is not suited, however, for nonlinear problems. Nonlinear problems would have to be linearized first since the expectation is linear [41].

Radiation Transport

There are various analytical approaches for solving radiation transport problems [42]. However, due to the complex nature of electrons and photon, most require many simplifying assumptions. One advantage of statistical approaches over analytical approaches is that intermediate processes can be observed. Statistical approaches can tell a particular interaction occurred for a particle while most analytical approaches cannot. Analytical approaches, in general, are not able to provide accurate solutions to problems. Radiation Transport is a stochastic process and is ideally suited for Monte Carlo. In fact, it is considered to be the gold standard in radiation therapy [43].

For Monte Carlo simulation, a random number generator can be used to determine the step size and the direction of a particle. Probability distributions are used to determine the likelihood of various interactions. A certain amount of energy is lost in the process and this repeats until the particle leaves the phantom or is absorbed. If enough particles pass through the phantom, then realistic information about the amount of dose deposited can be obtained.

2.2.2 Analog and Non Analog Simulations

Various Monte Carlo code systems exist to simulate radiation transport in Medical Physics. Some have arisen to solve problems in specific applications while others use different strategies to improve simulation efficiency. Most code systems fall into one of two categories, analog or non-analog simulations.

Analog

In analog or event by event simulations, every electron interaction is simulated until all the energy is lost. An average fast electron undergoes between $10^5 - 10^6$ interactions before being absorbed locally. This can make simulation impractical and is modeled only if necessary. With the advent of faster computers, there has been increased interest in

event by event simulation in certain applications such as microdosimetry. Two Monte Carlo codes which use event by event simulation are the NOREC code by Oak Ridge National Lab [44] and the microbeam radiation therapy (MRT) toolkit from GEANT4 [45]. The most common applications for these codes are the modeling of radiation damage to DNA and the evaluation of dose to nanoparticles [46]. Newer general-purpose algorithms implement the event by event approach at various points in the simulation when it is important. One example of this is near boundaries where the path traversed might result in significantly different outcomes [47]. Fig. 2.4 shows an example of this. Other instances are when the scoring grid is different from the geometry grid and during the transport of neutral particles.

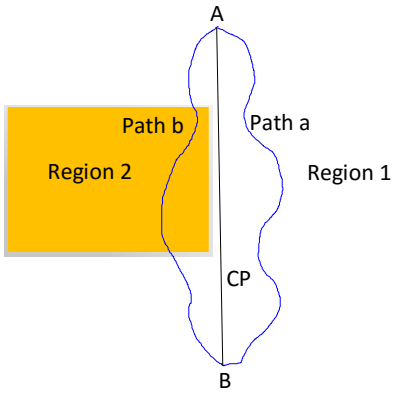

Figure 2.4 – Path a and b represent two paths of moving from location A to B. Though the calculated path (CP) is the same, analog simulation is required on portions of path b to ensure accurate modeling.

Non Analog

Non-analog algorithms do not simulate all interactions. In 1963, Berger introduced the Condensed History Technique for charged particle transport in his seminal work [48]. It was based on the observation that a significant amount of interactions led to very small changes in energy and direction. He proposed condensing a large number of transport and collisions into one electron step. The corresponding change in energy and direction from the single step is the same as the analog steps. The probability density function

is used to determine the energy, direction and position changes and it is obtained from multiple scattering theory. The approach is valid as long as the energy loss between collisions is small compared to the particle energy. It starts to break down at very low energies when this is no longer valid.

Condensed history approaches can be divided into two classes. A class I algorithm is one where all collisions are grouped together for each condensed history step. It uses a predetermined set of path-length or average loss fractions. A class II algorithm is based on a mixed procedure in which collisions are divided into hard and soft collisions. Soft collisions have small energy loss subject to grouping as the Class I approach. Hard collisions with energy loss above a particular threshold are simulated as an analog approach. Table 2.1 shows the classification of some popular Monte Carlo codes.

Table 2.1 – Various Monte Carlo codes condensed history classification.

Class	Code
I	ETRAN, ITS, MCNP
II	EGS4, EGSnrc, PENELOPE, Geant4, VMC++

All general purpose MC code systems and treatment planning codes implement condensed history techniques. Even though the rate of convergence is different, all implementations converge to the correct result in the limit of small steps [49]. This means that the multiple elastic scattering is correctly simulated. Condensed History introduces an artificial step size which can significantly influence the speed and accuracy of the simulation [50]. The goal of each code is to make the step size as independent of the result as possible for as many applications as possible. Much progress has been made in this regard in recent years.

2.2.3 Radiation Transport Monte Carlo Codes

The EGSnrc (Electron Gamma Shower) code system [51, 29] is the most widely used general purpose Monte Carlo package in medical physics. It is the successor to EGS4

and has specialized codes for modeling various experiments. Due to its wide usage and many benchmarks, many of the errors associated with a large complicated project have been addressed. It is currently the only Monte Carlo package capable of modeling a gas filled ion chamber accurately. Another popular package is the MCNP (Monte Carlo N-Particle) code system [52]. It is maintained at Los Alamos National Laboratory and incorporates the ETRAN code that was originally developed by Berger. MCNP does not require programming and has a powerful geometry package. The current version, Version 6, is a merger of MCNP5 and MCNPX. The PENELOPE (PENetration and Energy LOss of Positrons and Electrons) code system simulates the transport of electrons, positrons and photons with energies from 100eV to 1 GeV [53]. There has been a significant effort to model electron transport accurately and it has incorporated principles from EGSnrc. Various benchmarks have shown good agreement between other codes and experiments [54]. The PRIMO software combines a graphical user interface with a computation engine based on the PENELOPE code [55]. A couple of interesting features is the ability to distribute the job across all processors on the machine and support for DICOM and DICOM-RT. GEANT (GEometry ANd Tracking) has become increasingly popular in medical physics in recent years [56, 57]. It is a series of toolkits developed at CERN and is used in other areas such as space physics and high energy physics. Benchmarks against other codes showed good agreement with photon transport but less agreement with electron transport [58, 59]. The problem was rooted in step size artifacts and proper parameter selection later produced accurate results. This, however, resulted in a significant slowdown of the code. The latest version 4.10 presumably addresses some of these issues. For simple geometries, the MCNP and EGS code systems have about the same efficiency without variance reduction [60]. The other codes, however, tend to be significantly slower. MCNP slows down considerably for complex geometries. EGSnrc is around 3-5 times faster than PENELOPE ignoring variance reduction and is around 5-10 times faster than GEANT4. In general, these

codes are considered too slow for routine treatment planning. The use of parallel computing is possible, but there are other Monte Carlo codes that are highly optimized for this process. Some of these include Macro Monte Code (MMC), PEREGRINE, MCDOSE/MCSIM, Voxel-MC (VMC++) and DPM.

2.2.4 The EGSnrc Monte Carlo System

The EGSnrc code system [29] version 4.2.4 was used for this project. The primary reasons were the excellent electron transport capabilities and proven accuracy in interface dosimetry. EGSnrc allows the transport of electrons, positron or photons. Any element, compound, or mixture can be created with the material preparation software PEGS4 using cross section tables for elements 1 through 100. The dynamic range of charged particle kinetic energies covers the entire range of clinical treatment energies all the way down to a few tens of keV. The DOSXYZnrc user code [61] is a general purpose code for calculating dose distributions in a rectilinear voxel phantom. It has a wide variety of source configurations, it includes the ability to create a phantom from CT data in DICOM format using the program ctcreate, and it can use phase space source data. The voxel sizes are completely variable in all dimensions and can have any material or density. It also includes the user code BEAMnrc which was developed to simulate the linac head. This is not optimized for speed, however. Some of the physics processes taken into account by the EGSnrc Code System include bremsstrahlung production, Positron annihilation in flight and at rest, Pair production, Compton scattering, Coherent (Rayleigh) scattering and Photoelectric effect. It also has an improved boundary crossing algorithm and incorporates spin effects. Furthermore, the latest version has a more accurate simulation of atomic relaxation. A lot of time and effort have gone into modeling different physics and making them as accurate as possible. The details can be found in the documentation [29] and many publications.

2.2.4.1 Photon Transport and Electron Transport

The purpose of this section is to briefly review the transport processes involved with simulating electrons and photons. The photon and electron transport in EGSnrc is similar for the most part except the transport to the interaction site. Here are some of the considerations.

- Photons -
  - Travel in a straight line between discrete interactions
- Electrons -
  - Do not travel on straight lines between discrete interactions
  - Lose energy continuously.
  - Changes in step size near boundaries

Next we describe the logic in photon and electron transport. Scoring of the geometry is a separate process and is not included. First, the concept of the STACK is introduced and defined as an array that retains the necessary phase space parameters generated during simulation for later use [42, 62]. The STACK is necessary because each photon interaction can generate additional particles and the phase space must be stored to process each particle. This is possible since the probability of a photon interaction is independent of its history. The second term we introduce is 'sample.' This means that we can use pseudo-random numbers to sample the appropriate probability distribution and determine the parameters of the interaction while taking into account the knowledge of transport process.

Photons A simplified flow chart of the photon transport algorithm is shown in Fig. 2.5. It assumes a single region and ignores electron creation. The process begins by obtaining the initial photon's information from the STACK. Next, the photon energy is

compared to the cutoff energy. If it is below the cutoff, then, the photon is immediately absorbed. If the stack is empty, then a new particle history is started. If the photon energy is above the cutoff, then the distance to the next interaction is determined by sampling. It travels to the new location. If it has left the geometry, it is terminated. If not, the probability distribution is used to determine what interaction takes place. Any particles produced by this interaction have a specific energy, direction and other properties chosen from appropriate distributions. The particles are then placed on the STACK. The process is then restarted and continues until the STACK is empty and all particles used up.

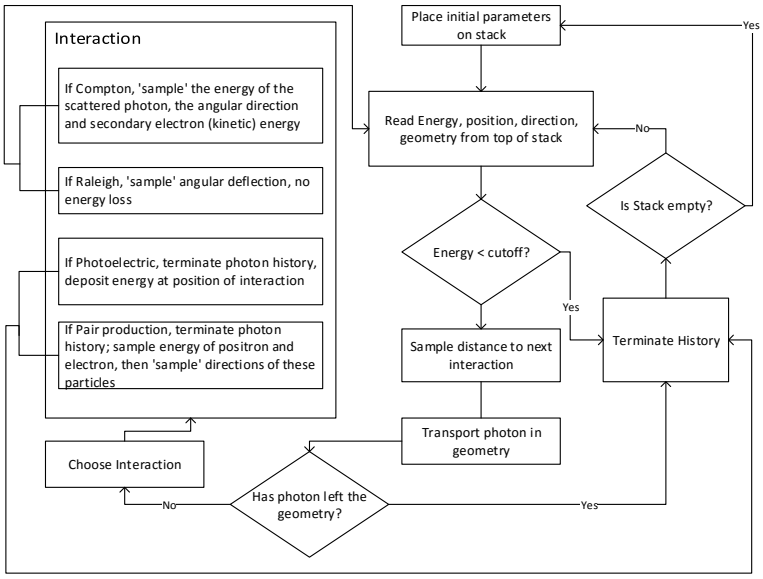

Figure 2.5 – Simplified Flow Chart for Photon Transport. Modified from Bielajew[1]

Electrons A simplified flow chart of the electron transport algorithm is shown in Fig. 2.6. It begins by selecting an electron from the particle stack and comparing the energy to the cutoff energy. If the electron energy is lower than the cutoff energy, then it is discarded and the scoring routing is informed that the particle is being removed from the stack. If there is no electron on the stack, then the control is given to the photon transport routine. Otherwise, the electron on the stack is transported. If the

electron energy is above the cutoff energy, then the distance to the next "catastrophic" interaction is determined by sampling. Next, the multiple scattering step size is selected and the electron is transported while taking the geometry into consideration. The deflection angle is then sampled and the particle direction is changed. Following this, the continuous energy loss is applied. If the electron has left the geometry, the history is terminated. If not, the electron energy is compared to the cutoff energy. If it is below the cutoff, then the history is terminated, if not, then it is checked to see if it reached the point of interaction. If it has not reached the point of interaction, then a new multiple scatter step size is selected. This loop occurs many times since there are multiple scattering in between catastrophic interactions. If it reaches the interaction site, the type of interaction is sampled from the total interaction cross section. The energy and direction of any secondary particles are also sampled from appropriate differential cross-section data and the results placed on the STACK. The energy and direction of the original particle are adjusted. The process repeats until the stack is empty or all energies have fallen below the cutoff energy.

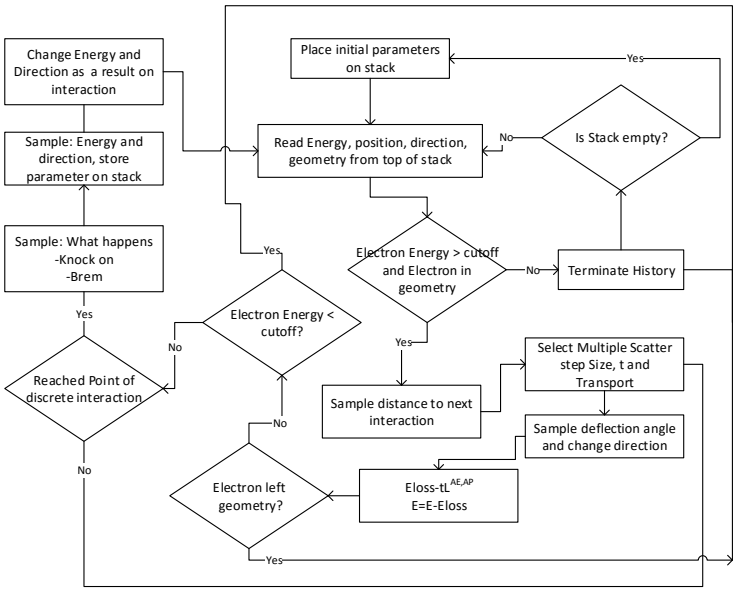

Figure 2.6 – Simplified Flow Chart for Electron Transport. Modified from Bielajew [1]

Positrons are transported with the same routine as electrons. The difference is that the annihilation cross-section is included in addition to the bremsstrahlung and inelastic collisions with atomic electrons.

Boundary Crossing For heterogeneous material, the crossing of material boundaries has to be considered. EGSnrc incorporates the EXACT boundary crossing algorithm to address this [63]. It works by going into single scattering mode whenever the participle gets within t_{min} of the boundary. The t_{min} distance is selected to be around 3 elastic mean free paths to the boundary. This is based on the observation that the transport algorithm actually becomes more efficient using single scattering after this point [29].

2.2.4.2 Variance Reduction and Efficiency Enhancement

The efficiency of a Monte Carlo simulation is defined by equation 2.12, where T is the total time for the simulation and s is the uncertainty of the area of interest.

$$\varepsilon = \frac{1}{Ts^2} \tag{2.13}$$

The efficiency can be increased by reducing the simulation time without changing the uncertainty, decreasing the uncertainty without decreasing the time or changing the number of histories. There are two main classification methods for improving the simulation efficiency.

Approximate Efficiency Improvement Techniques (AEIT) involve making approximations by not modeling the physics under conditions that are deemed to not have a significant influence on the final result. Depending on the situation, the results obtained with these methods can be a couple percent off, but produce a several fold reduction in time. The condense history method, howfarless, energy cutoffs and range reduction are examples of efficiency enhancement techniques.

Variance reduction techniques (VRT), however, do not make approximations and reduces the statistics without modifying the underlying physics. These techniques should give the same outcome compared with not using VRT. Several of these techniques were used in this project. Photon splitting and parallel computing would be considered examples of this.

Photon splitting When photon splitting is employed, then all photons are split into nsplit photons with a weighting of w_0/nsplit where w_0 is the initial weight. The interaction sites of the photon are distributed uniformly along the path of the original photon. The scattered photons are terminated with survival probability of 1/nsplit and charged particles are kept with weighting w_0/nsplit [64]. Photon splitting is the only VRT available in DOSXYZnrc.

Howfarless This algorithm can be applied to homogeneous phantoms and increases efficiency by allowing larger steps as it moves through the material. It only considers the outer boundaries of the phantom since there are no need to stop at a material interface. Details of this can be found in Walters and Kawrakow's paper [65].

ECUT The global electron cutoff energy is defined to be the energy at which the history of an electron is terminated. It is defined in keV and includes the rest mass of the electron. If the electron needs a certain amount of energy to escape a region and its current energy is less than the escape energy, then the history can be terminated and the remaining energy is deposited in the current region. For this reason, it is imperative that proper selection of cutoff energy is selected. In general, the cutoff energy should be chosen so that the CSDA range in the material at that energy is less than 1/3 of the smallest voxel in the area of interest. This ensures that the energy is deposited in the correct region. In general, low energy electrons do not contribute significantly to the phantom dose in radiation therapy applications, but low energy electrons are expected to play an important role in this project [61].

PCUT The global photon cutoff is defined as the energy at which the history of a photon is terminated. It is similar to ECUT, but it is less consequential since little time saving is achieved by using a slightly higher cutoff energy.

Range Reduction Range reduction is an option to terminate charged particles immediately if they can't get out of the current region while having energy greater than Ecut and its energy is less than Esave. Esave Global is the defined as maximum energy for which range rejection is applied and is used to prevent the termination of high energy electrons which might result in the generation of bremsstrahlung. Region rejection discards electrons in regions far away from your region of interest in a more liberal manner.

2.2.4.3 Dose scoring

In order to determine the dose delivered we need to score it. Scoring is defined as the process by which we monitor certain aspects of the simulation and keep track of parameters of interest. There are several ways to score a physical quantity. EGSnrc/DOSXYZnrc uses a cartesian volume and scores energy deposition in the relevant voxel. Generally, the scoring region is the same as the geometric region, though in certain complex geometries, it may be necessary to use different regions. In these cases, small electron step sizes are necessary to reduce errors [42].

2.2.5 Statistics

Monte Carlo techniques depend on many histories to gain the necessary statistics. EGSnrc determines the dose statistics by grouping scored quantities by the history by history method and calculating the uncertainty. If N histories are obtained and the X_i is the dose in a voxel from the i-th history, then the average dose from all histories is given by:

$$\bar{X} = \frac{1}{N} \sum_{i=1}^{N} X_i \tag{2.14}$$

The estimate of the variance associated with the X_i is given by equation 2.15 and the estimated variance of $\bar{X}$ is given by the standard deviation of the mean[62], equation 2.16.

$$s_X^2 = \frac{1}{(N-1)} \sum_{i=1}^{N} (X_i - \bar{X})^2 \tag{2.15}$$

$$s_{\bar{X}} = \sqrt{\frac{s_X^2}{N}} = \sqrt{\frac{1}{N(N-1)} \sum_{i=1}^{N} (X_i^2 - \bar{X}^2)} \tag{2.16}$$

There are several ways to improve the statistics of a Monte Carlo simulation. Accurate statistics leads to accurate estimates of the efficiency and accurate estimates of the number of histories required to gain the desired accuracy. For N independent histories, the statistical uncertainty is proportional to $1/\sqrt{N}$ and the number of interactions is proportional to N. Hence, the statistics can be improved by increasing the amount of interactions.

Generally, low dose regions or regions outside the areas of interest will have high uncertainties. For this project, we are concerned mostly with the region within 50% of Dmax. More specifically, enough histories were done such that the average of the fractional uncertainty of dose values within 50% of Dmax was less than 1% [66]. Equation 2.17 describes the requirement, where D_i is the dose estimate to the i-th voxel, s_{D_i} is its uncertainty and K_D is the number of voxels within 50% Dmax.

$$\bar{F}_{D>0.5D_{max}} = \sqrt{\frac{1}{K_{D>0.5D_{max}}} \sum_{D>0.5D_{max}} \left(\frac{\overline{s_{D_i}}}{D_i} \right)^2} \tag{2.17}$$

2.3 Radiation Detectors

There is a wide variety of detectors available for dose measurements today. Each has its advantages, disadvantages, and suitability for different applications. Dependencies such as temperature, energy and orientation as well as other characteristics such as the sensitivity have to be considered when choosing a detector for an application. Detectors such as TLDs, diodes, ion chambers are point detectors, while a film is a 2D detector. Many great references are available on how these work [2, 37]. The focus of this section will be on 3D detectors.

2.3.1 3-D Detectors

There are a few detectors that allow 3D dose measurements. The Delta 4 phantom from ScandiDos consists of 2D detector array units assembled in a cross. It has 1069 diodes placed 5mm apart at the center and 10mm apart at the periphery. Overall it has 20x20cm detection area and sensitivity of 5nC/Gy. ArcCHECK is another such tool. This has the detectors distributed in the form of a cylinder. The center 10cm area has 221 detectors and 1386 detectors overall. It has 1cm detector spacing and sensitivity of 32nC/Gy. These detectors do not allow the insertion of materials and rely on interpolation. One detector that has been gaining a lot of interest recently is the PRESAGE ® Dosimeter [67]. This is a radiochromic dosimeter, made of polyurethane, a leouco dye and a halocarbon as a radical source. When radiation or UV energy comes in contact with the dosimeter, the free radicals oxidize leucomalachite green into malachite green in the areas of exposure. The intensity of the color change is proportional to the dose delivered. The dose can be seen and determined by optical tomographic techniques.

2.3.2 Gel Dosimeters

Gel dosimeters are radio-sensitive chemicals where reactions can be initiated by radiation. The gel normally responds by changing color or changing density proportional to

the dose delivered. These gels can be poured into any anthropomorphic phantom and captures dose in 3D. The radiation sensitive gel for dosimetry was first suggested by Stein and Day[68] after observing color changes in gels containing dyes. In 1984, Gore showed that a ferrous sulphate chemical (Fricke) dosimeter could be probed by nuclear magnetic relaxometry [69]. It was later discovered that there was an ion diffusion problem leading to spatial stability issues with irradiated gels [70]. Various attempts have been made to solve the problem, but in general, they have not been successful. The most common approach is to use some kind of chelating agent such as xylenol orange to reduce diffusion, but this has the undesired effect of reducing the R1 and R2 sensitivity [71].

2.3.2.1 Polymer Gel

Polymer gel dosimeters were first proposed in radiation dosimetry by Alexander et al in 1954 where he discussed the effects of radiation on polymethylmethacrylate [72]. This led to the investigation of radiation induced polymerization in liquids by Hoecker in 1954 and later the use of polyacrylamide in making a gamma dosimeter by Boni [73].

In 1992, Kenan found that irradiated aqueous solution of N,N'-methylene-bis-acrylamide (Bis) and agarose had increased relaxation rate with NMR longitudinal relaxation [74]. At the same meeting, Maryanski proposed the BANANA gel which used acrylamide and N,N'-methylene-bis-acrylamide as monomers and an aqueous agarose matrix [75]. This gel did not exhibit the ion diffusion problems seen with the Fricke dosimeters. It was later modified to use gelatin instead of agarose and then patented [76]. The BANG® and subsequent versions became available commercially through MGS Research Inc. During this time various experiments have been performed to characterize polymer gels, to investigate clinical applications and to develop improved formulations. One significant limit of polymer gels is its susceptibility to oxygen. Oxygen inhibits the reaction because it scavenges the free radical initiators generated from the radiolysis of water thus limiting polymerization. This restricted the manufacturing to inside

a glove box or to bubbling nitrogen through the water. The difficulty in manufacturing was one of many reasons that restricted the use of polymer gels to research. In 2001, a significant breakthrough was reported by Fong et al [77]. Their polymer gel, dubbed MAGIC, incorporated the oxygen scavenger ascorbic acid and used copper sulphate as a catalyst. The scavenger binds oxygen into a metallo-organic complex allowing the gel to be manufactured in normal room environments. All polymer gels now use antioxidants and are classified as normoxic polymer gels. Previous gels have come to be known as anoxic or hypoxic gels. Since then, other antioxidants have been identified, which include tetrakis (hydromethly) phosphonium chloride (THPC) and Bis[tetrakis(hydroxymethyl)phosphonium] sulfate (THPS). Research has since focused on identifying better components and the right composition for various applications. Today there are two major classes of polymer gel: methacrylic acid based (or MAG) and acrylamide based (or PAG). The choice in monomers can have significant changes in properties and is often guided by the applications. Sometimes standard formulations are not sufficient and custom formulations are required for the task. In general, a good polymer gel has the following characteristics:

- Tissue equivalence: The dose response should be as close as possible to that of soft tissue.
- Spatial and Temporal Integrity: The dose distribution should be constant for a period long enough to gather the required information.
- Temperature Independence: The temperature at which irradiation, scanning and storage occurs often vary by more than 2 degrees.
- Dose Rate Independence: The dose rate should not affect the dose response of the gel.
- Energy Independence: The beam energy should not affect the dose response of the gel.

2.3.3 Dose Quantification

The dose delivered to the polymer gel can be correlated with the amount of cross-linking and polymerization that the gel experiences. This often results in density changes which can be quantified by a calibration curve. There are four primary means of dose quantification: MRI, X-ray CT, Optical CT, and ultrasound.

MR MRI is currently the most common form of dose quantification and is considered the gold standard. The polymer gel consists of monomers, cross-linkers, various modifying materials and water which is the primary source of protons. The mixing of the gel components gives rise to three major pools of protons in the gel. They are 1) bulk water and unreacted monomer, 2) the protons associated with the polymer and water connected to it and 3) the gelatin and water associated with it [10]. The relaxation rate from the water and unreacted monomer are very similar, but the relaxation rate of water attached to the bigger molecules is much larger due to more slow and restricted motion. It is concluded that polymerization is correlated with relaxation rate. There are two approaches to measuring the spin-spin relaxation rate, R_2. The first is the two-point method using a conventional single spin echo sequence. In this approach, two images are acquired with different echo times and the R_2 value can be obtained using equation 2.18.

$$R_2(i,j) = \frac{1}{TE_2 - TE_1} \ln \left[\frac{S_1(i,j)}{S_2(i,j)} \right] \tag{2.18}$$

In this equation, TE_1 is the echo time for the first image and the S_1 is the signal intensity of the pixel at index (i,j). The second approach is a multiple spin echo method based on work by Carr and Meiboom [78, 79]. More specifically, the Carr Purcell Meiboom Gill (CPMG) sequence and variations use a 90° RF pulse followed by echo train of equally spaced spin echoes separated by a 180° refocusing pulse. R_2 can be found by obtaining the best fit. This method results in a superior signal-to-noise ratio relative to the single

echo method but is subject to errors in T_2 because of imperfect 180° pulses. Artifacts can be reduced by using multiple single echo scans with varied echo times but this is significantly more time consuming.

X-ray CT The use of x-rays to evaluate polymer gel dosimeters has been investigated and shown to be feasible. Photons initiate a small amount of polymerization which leads to a change in density and thus a change in linear attenuation coefficients [80]. CT images are governed by the relationship,

$$N_{CT} = 1000.\frac{\mu - \mu_w}{\mu_w} \tag{2.19}$$

where μ and μ_w are the linear attenuation of the sample and water respectively. CT has several advantages compared to MRI. It is more readily available in the clinic, it has faster scan times and much higher signal to noise ratio. It has the disadvantage, however, of having a limited dynamic range and cannot be used with high Z materials. There is no addition of mass and so density changes correspond to a change in volume or a redistribution of mass. This might result in a potential loss in spatial integrity, but qualitative calculations have shown that density changes of up to 4 times are fine before spatial resolutions exceed 2mm [10].

Optical CT The work load of most clinics make it very difficult to get extended time on imaging modalities such as MRI and CT. The long scanning time for MR, in particular, necessitates that scanning be done after hours or is limited to institutions with a dedicated research scanner. This has driven the need for alternative methods of dose quantification. In 1996, Gore introduced an Optical CT approach for scanning polymer gels [81]. These scanners use a laser and so have the limitation of only scanning transparent gels. All optical scanners work in a similar manner, with newer variations giving much faster scan times. Different groups have attempted to make their own

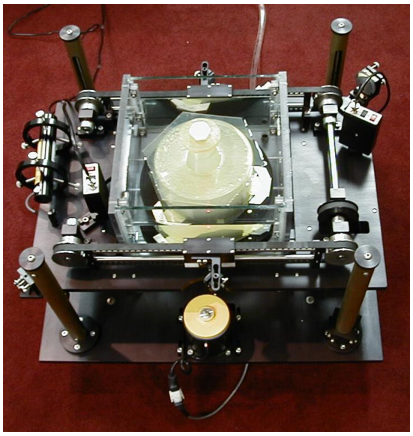

Figure 2.7 – OCTOPUS Optical CT scanner with polymer gel

customized scanners, but the most popular is a commercial version sold by MGS research (Madison, Connecticut) called OCTOPUS. The latest version can achieve scan times of 5 minute per slice [82]. Fig. 2.7 shows an image of the OCTOPUS scanner.

Various gels have been developed for this purpose and they are often based on PAG type gels because of its clarity. The polymer gel is often placed in a tank with a matching solution to reduce reflection and refraction.

Ultrasound Another relatively new method of gel quantification is Ultrasound. Mather et al found that ultrasonic transmission, reflection and speed change with radiation induced polymerization [83]. These changes are due to changes in elastic modulus and density, though the primary factor depends on the type of gel. Various tomographic prototypes have been produced and it basically requires a rotary stage, translation stage, a transducer, a microphone and a water tank. The water tank prevents attenuation in air, but the acoustic impedance mismatch between water and the gel phantom produces artifacts in the transmission image. The primary advantage of this technique is cost, but the disadvantage is lower image quality compared to the other techniques. Better matching fluid and equipment will help to improve the quality. A lot of work still needs to take place in this area and wide spread use remains to be seen.

2.3.4 Measurement Uncertainty

There are many potential sources of error in polymer gel dosimetry. These arise from manufacturing, irradiation, storage, scanning, processing, and calibration of the gel. The errors can result in spatial or dosimetric uncertainty. Many of these can be reduced by following good manufacturing practices. Below we described some of the uncertainty related to this project. The uncertainties involved were all assumed to be normally distributed and uncorrelated.

2.3.4.1 Sources of Error

Differences in container size The calibration gel and phantom are made from the same batch but often a deviation in dose response is observed. De Deene et al showed that the temperature history after manufacturing has a significant influence on the gel [84]. Specifically, the difference in size between the calibration vial and phantom lead to different cooling rates which lead to differences in response.

Temperature effects The temperature during fabrication, irradiation, and scanning all play a role in uncertainty. During fabrication, the gelatin is the primary component that is susceptible to temperature history [85]. During irradiation, temperature differences in the gel can result in differences in the chemical reaction kinetics and monomer diffusion coefficients in the gel. For MR scanning, the R2 value is temperature dependent. Before irradiation and scanning, sufficient time must be allowed for proper equilibration of the calibration vials and phantom with room temperature.

Transient chemical reactions During irradiation, polymerization is initiated but the reactions do not stop after the beam is turned off. It keeps going until it runs out of monomers or is terminated. This can last up to 12 hours or so depending on the type of gel. Scanning the calibration vial together with the phantom will reduce this error.

Spatial integrity Spatial integrity can be lost for several reasons. Perhaps the most common is due to diffusion of molecules such as ferrous ions in the Fricke dosimeter. The diffusion of unreacted monomers can influence dose if it moves to the irradiated region and reacts with polymer radicals [86]. The loss of spatial integrity can also occur when the gel loses its solidity due to an increase in temperature by such as RF heating in long MR scans.

Dose rate and fractions Some gels have dose rate dependence which is undesirable in a dosimeter. This is more pronounced at higher total dose and is more common in methacrylic acid based gels compared to acrylamide type gels [87, 88]. This simply means that you should avoid breaking the dose into multiple fractions and use the same dose rate for both calibration vials and phantom. Using the same dose rate is already standard.

Wall effects A major issue with PGD is the effect of oxygen. Oxygen might diffuse through some materials and prevent polymerization. One solution is to use Barex® or glass but care must be taken as some glass materials contain heavy metals such as lead. This could lead to more attenuation and results in beam hardening. Even when oxygen diffusion does not occur through the material, oxygen on the container wall might still be an issue.

Imaging artifacts Imaging artifacts originate with the scanner or the phantom. Artifacts originating from the scanner are more common and arise because of eddy currents, B1 field inhomogeneity, sequence imperfections and standing waves. Common artifacts from the phantom arise because of temperature drifts, molecular self-diffusion, susceptibility differences or chemical shift. In this project, the presence of high-Z metal is of interest. Deviations in the magnetic field will result in a deviation in dose. Various strategies can be used to compensate these artifacts [89].

Position error Positioning errors in either the calibration vials or the phantom will result in dose deviations. Dose errors in the calibration vials are more significant because it results in errors in the calibration curve. Depending on what the gel will be compared to, errors in the phantom position might not be an issue. In this case, small shifts in position can be addressed by simulating the modified configuration.

2.3.4.2 Error Analysis

In addition to the above uncertainties, there is uncertainty in the calibration process and noise in the R_2 image. When the calibration curve is in a quadratic form with $D = aR^2 + bR + c$, the calibration error is given by

$$Error_{Calibration} = \left(\frac{\partial D}{\partial R}\right)^2 \sigma_R^2 + \left(\frac{\partial D}{\partial a}\right)^2 \sigma_a^2 + \left(\frac{\partial D}{\partial b}\right)^2 \sigma_b^2 + \left(\frac{\partial D}{\partial c}\right)^2 \sigma_c^2 + CoVar \quad (2.20)$$

where the covariance term is

$$CoVar = 2\left(\frac{\partial D}{\partial a}\right)\left(\frac{\partial D}{\partial b}\right)\sigma_{ab} + 2\left(\frac{\partial D}{\partial a}\right)\left(\frac{\partial D}{\partial c}\right)\sigma_{ac} + 2\left(\frac{\partial D}{\partial b}\right)\left(\frac{\partial D}{\partial c}\right)\sigma_{bc}. \quad (2.21)$$

The error from the noise of the image is given by

$$Error_{image} = \frac{\sigma_{background}}{\sqrt{Number\ of\ Pounts}} \quad (2.22)$$

The resulting uncertainty is the sum of the error components in quadrature [90].

2.3.4.3 Dose Resolution

The concept of dose resolution was introduced by Baldlock as a method of evaluating the intrinsic dosimetric precision [91]. It is defined as the minimal difference between two adsorbed doses that allow them to be distinguished with specific level of confidence, p where k_p is the coverage factor.

$$D^p_{\triangle} = k_p\sqrt{2}\sigma_D \tag{2.23}$$

If the dose resolution is taken as the full width at half maximum of a Gaussian distribution then $D^p_{\Delta} = 2.35\sigma_D$. It is dependent on the dose formulation as well as the signal acquisition system and strategy. The minimal detectable dose is the dose resolution as dose approaches zero.

Chapter 3

Foil Configuration Optimization

3.1 Introduction

Dose measurements near high-Z heterogeneities have been an issue in radiation oncology, but in recent years, it has become more of a concern. Analytical transport models [92, 4, 7, 93], Monte Carlo [9, 94], methods of moments [95] and dosimetric approaches [96, 97] have all been employed to better understand and predict the dose at interfaces. The theoretical methods have been instructive in understanding the nature of secondary electrons, but they all had varying simplifying assumptions. Previous Monte Carlo simulations had significant limitations at the interface; particularly, the dose was underestimated near high-Z material [97]. Though ion chambers have been regarded as the most accurate, they have their limitations. Ion chambers can also introduce perturbations due to steep dose gradients and material differences of the detector and medium. They can only obtain point measurements which makes it difficult to get spatial dose distributions. The release of EGSnrc came with significant improvements and together with the availability of much faster computers, we were in a position to obtain more accurate spatial distributions of dose near high-Z interfaces.

The purpose of this theoretical study was twofold. The first reason for this study

was to gain a better understanding of how high energy photons interact with small high-Z materials and how various parameters can affect the distribution of dose. Much of the early work had limitations with electron transport, used low energies or used materials that were much wider than the field size. Another observation was that previous researchers often used a single layer heterogeneity. The most common type of high-Z interface in the body is the bone-marrow-bone interface, therefore two small heterogeneities are more useful than a single large plate. More recently, Alkhatib looked at the dose between a two foil arrangement by film but only two configurations were evaluated [35]. An exploration study would help identify which parameters have the greatest effect in modifying the dose in-between the two high-Z materials.

The second reason was to aid in the design of gel dosimetry experiments. Polymer gel dosimetry is a relatively time consuming process often spanning several days and I did not want to spend time on configurations that did not have any dose enhancement or too much. With such a study, good configurations can be selected and even more detailed simulations can be made for comparison with the measurement data.

I investigated the effect of geometrical configuration on dose upstream, downstream and in-between the foils. Specifically, I looked at the effects of foil thickness, size, separation, beam energy, atomic number, depth and field size. The effect of the beam angle was not investigated. Where possible, I made comparison to published data. Previous works differ in their methodology and experimental configurations so I will refer to trends rather than exact measurements for comparison.

3.2 Methods

3.2.1 Variance Reduction

Monte Carlo simulation is also a time consuming process. The length of time is dependent on the desired accuracy, what physics processes are simulated and, in this case, the number of experiments. Due to a large number of simulations, some time was spent

on optimization and variance reduction. Special attention was given to the photon and electron cut off energies, howfarless and range reduction.

3.2.1.1 Photon Splitting

Photon splitting is a common variance reduction technique and previous studies have investigated its effect on efficiency improvements [98]. Those studies were performed using phase space sources and it was not clear if the optimal splitting number would be similar with a spectrum source. In addition, it was not clear what effect the howfarless algorithm would have on the optimal splitting number. Howfarless allows larger steps to occur in homogeneous materials and is expected to affect the effectiveness of photon splitting algorithm. A sample configuration from table 3.2 was selected and all simulations were performed on the same computer. The efficiency was determined by equation 2.12 in section 2.2.4.2. In this case, s was taken to be the average error of the dose regions within 50% of the Dmax. The results are presented in Fig. 3.1.

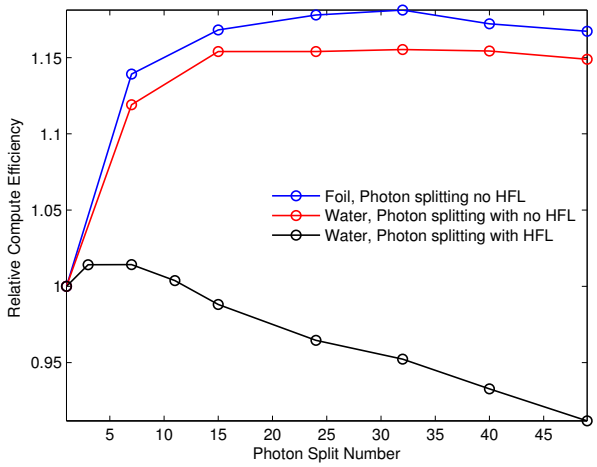

Figure 3.1 – Relative computing efficiency using photon splitting and HOWFARLESS (HFL)

In the heterogeneous case, the optimal splitting number with no howfarless is in agreement with other published studies but the improvement is significantly reduced.

Kawrakow et al. reported preliminary unpublished efficiency improvements of around 20% with monoenergetic sources, though they did not specify the splitting number. In the homogeneous case, photon splitting with the howfarless algorithm had a five-fold reduction in efficiency than when howfarless was not used. The photon splitting number was selected to be 32 and 5 for the heterogeneous and homogeneous phantoms respectively.

3.2.1.2 Other Parameters

Range Rejection was optimized by trial and error. Sample runs were performed with various cut off energies and the %DD results compared to identify when deviations began to occur. A similar approach was taken with the electron and photon cutoffs. Compiler choice and optimization options were not considered.

3.2.1.3 Parallel Computing

The use of parallel computing is one method to decrease the time for the simulation. Even though parallel computing capabilities are built into EGSnrc, some of the tools are missing from the windows implementation. A large number of simulations, however, made parallel simulation a requirement. A small computer cluster was built using Windows Server 2012 R2 HPC 2012 and Windows 8. It had 22 nodes with various speeds ranging from eight core Xeons to two core Core 2 Duos. The cluster was utilized in two ways. One approach was to send a single job to each node processor and the second approach was to send a single job to one node and distribute the simulation across each processor on that node. The third option of sending a single job to all computers was not explored because it seemed too labor intensive to warrant the effort. It would require additional coding to automatically generate new input files reflecting the modified number of histories, the generation of different random seeds, the renaming of output files to reflect weighting and running another script to combine the results. Therefore, the majority of the simulations were performed using the first approach and

the remaining used the second approach depending on machine availability.

3.2.2 Material Preparation Utility

PEGS4 is a materials data generation package that contains the cross-sectional data and stopping power information for materials used in the simulation. The default materials data had AE and AP values which did not extend to the cutoff energies desired in the project. The second issue was that the materials did not have any Raleigh scattering data. The global electron and photon cutoff energies need to be greater than or equal to the material cutoff energies AE and AP, which were defined as 512keV and 1keV respectively. Upper energy cutoffs UE and UP for secondary particle generation were also required and set to be 55.511MeV and 55MeV respectively. The PEGS4 utility was used to generate material data and a maximum number of energy points for the energy range of interest. More information on the utility can be found in the documentation [29].

3.2.3 Preliminary Foil Arrangements

DOSXYZnrc was used to perform Monte Carlo simulations of two gold foils suspended in water and a homogeneous water phantom. The gantry was not simulated because we were interested in relative measurements and not absolute dose. Instead, the Mohan spectrum was used with a vacuum surrounding the phantom [99]. The 18 MV photon spectrum was obtained by digitizing the Varian 18 MV spectrum obtained by Sheikh-Bagheri and Rogers [100]. All spectra were used as point radiation sources with 5cm x 5cm collimation at a 100cm SSD unless stated otherwise. Physics simulated include spin effects, Rayleigh scattering, atomic relaxations, electron impact ionization and bound Compton scattering. Photon cross sections were generated using the XCOM database [36] and a logarithmic energy grid using the number of energy bins from the PEGS utility .The simulation transport parameters can be found in Table 3.1. At least 32.5 million histories were obtained for each configuration in order to obtain an average error

of 1% or less for dose within 50% of Dmax.

Table 3.1 – Monte Carlo transport parameters in the heterogeneous and homogeneous phantom

Parameter	Heterogeneous	Homogeneous
HOWFARLESS	Off	On
Photon splitting	32	5
Boundary crossing algorithm (BCA)	EXACT	
Electron-step algorithm	PRESTA-II	
Global ECUT	0.521	
Global PCUT	0.01	
Range Rejection Energy	0.7	
Skin depth for BCA	3	

Due to larger step sizes with the howfarless algorithm, the number of histories for the homogeneous phantom had to be increased to obtain the necessary statistics. The size of both homogeneous and heterogeneous phantoms was 16 cm x 16 cm x 28 cm with a resolution of 1 mm in the areas of interest and 2 mm elsewhere. Two foils had the same dimensions and were placed either horizontally (i.e., orthogonal to the beam axis) or vertically (i.e, parallel the beam axis) in the center of the phantom. The foil was modeled as a single layer since I was not concerned about dose inside the heterogeneity. The effects of foil size, separation, thickness, depth, material, beam energy and field size were investigated. A summary of the various configuration is shown in Table 3.2. The calculations were performed on the cluster described in section 3.2.1 along with various custom machines.

Table 3.2 – The foil configurations for simulation. Each configuration was arranged in a horizontal and vertical manner.

Thickness (mm)	Separation (cm)	Depth (cm)	Field Size(cm)	Foil Size (cm)	Material	Energy (MV)
1, 0.75 , 0.5, 0.25, 0.125	0.5	7	5x5	1x1	Au	6, 24
0.5	0.3, 0.5, 0.7, 1, 1.3	7	5x5	1x1	Au	6, 24
0.5	0.5	7, 11, 14, 18, 22	5x5	1x1	Au	6, 24
0.5	0.5	7	2.5x2.5, 5x5, 7.5x7.5, 10x10	1x1	Au	6, 24
0.5	0.5	7	5x5	0.2x0.2, 0.6x0.6, 1x1, 2x2, 3x3, 4x4, 5x5	Au	6, 24
0.5	0.5	7	5x5	1x1	Al, Ti, Ag, Au, Pb	6, 24
0.5	0.5	7	5x5	1x1	Au	Co60,4, 6, 10, 15, 18, 24

3.2.4 Dose Analyzer

In order to process the data, a MATLAB program, Dose Analyzer, was written. It incorporated several functions from the DOSCTP project [101] resulting in some time savings. All analysis was performed using Dose Analyzer. Appendix A.1 shows a screen-shot of the program. After the reference matrix and dose matrix were loaded, they were interpolated to allow direct comparison. Next, percent depth dose (%DD) curves were determined along the central axis of the phantoms and the plots were normalized against

Dmax in the homogeneous water phantom. For this project, Dose Enhancement was defined to be the % increase in dose at that position relative to the dose in homogeneous water and given by the equation:

$$\%\ Dose\ Enhancement = \frac{Heterogeneous\ Dose - Homogeneous\ Dose}{Homogeneous\ Dose} \times 100. \quad (3.1)$$

Several parameters were of interest. First, the ranges of enhanced dose upstream and downstream were determined if any. Next, the maximum, minimum and midpoint dose between the foils were determined. Finally, the area under both curves was calculated and percentage area enhancement was determined. The maximum dose for the horizontal foils and the minimum dose for vertical foils were reviewed, but those were not included in the analysis. Dose within 0.5mm from the foil was ignored.

3.3 Results

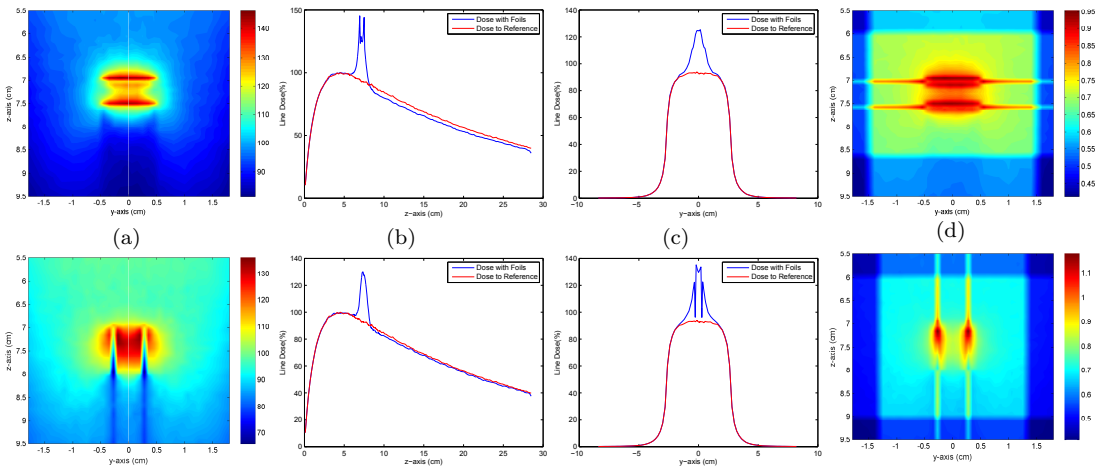

Figure 3.2 – An example of planar dose distributions for horizontal and vertical foils. The foils were irradiated with 24 MV photons and had thickness 0.5mm and separation of 5mm. For the horizontal foils, (a) shows the planar dose, (b) %DD through the center of the foils, (c) dose profile through the center and (d) Error matrix. Similarly, (e)-(h) represent the vertical configuration. All dose is in %.

The heterogeneous phantom showed significant dose modulation compared to the homogeneous phantom. Fig. 3.3 shows the dose distributions for 0.5mm foils placed horizontally (a) and vertically (e) with a 5mm separation and irradiated with 24 MV photons. For the horizontal case, the areas with the highest dose are just upstream of each foil. The forward and backscattered dose contributions between the foils resulted in a dose that was significantly higher compared to water. The vertical foil had a more distributed dose enhancement covering the majority of the region in-between the foils. The maximum dose was less than the horizontal configuration and it had a less pronounced dose reduction downstream. In this configuration, the highest dose was also directly at the side of the foils, and the dose in-between the foils was significantly higher than the dose outside. Fig. 3.3(b) and (c) show the %DD and the dose profiles for horizontal configuration respectively. The %DD curve corresponds to the white line in (a) and shows the reduction of the dose delivered downstream. Similarly, Fig. 3.2(f) and (g) show plots for the vertical foils. Both error matrices have similar ranges averaging around 1% and are representative of all the experiments. The statistical errors were larger in the high-resolution areas of the phantom.

The rest of the analysis will be restricted to the %DD slice and only the data close to the foils will be shown. Error bars were not shown for the purposes of clarity, but distributed error matrices and distributed dose for all simulations are available in appendix B.

Here, I introduce the three phantom regions. Region A is the region upstream or above the foils, Region B is the region in-between the foils and Region C is the region downstream or below the foils.

3.3.1 Energy

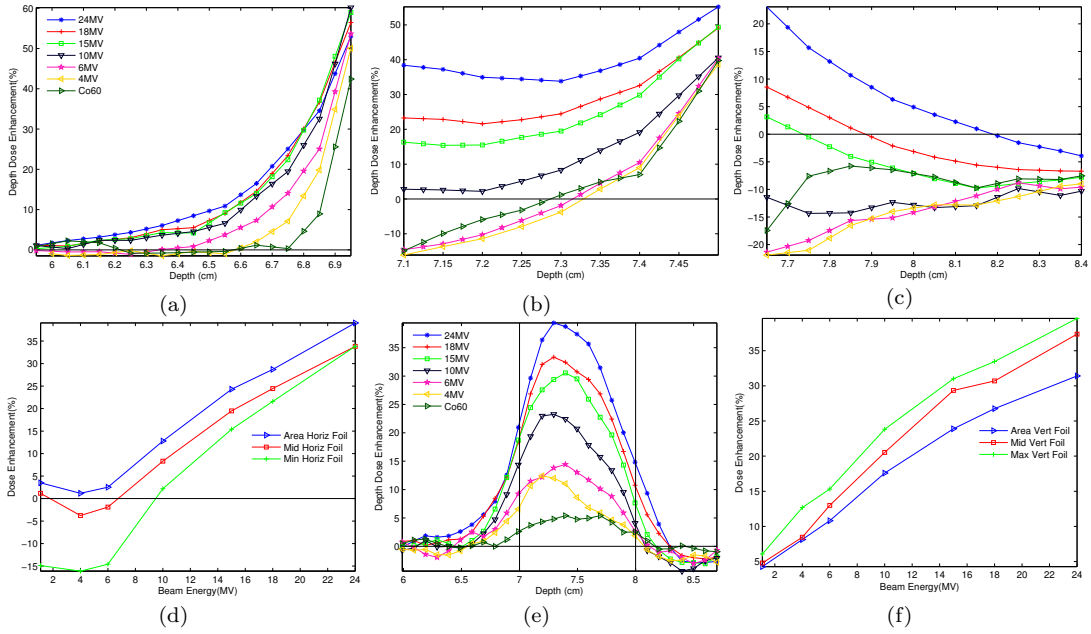

Figure 3.3 – The effect of beam energy on % dose around horizontal (a)-(d) and vertical (e)-(f) gold foils. The enhancement in dose upstream, in-between, and downstream, of the horizontal foils, are represented in (a)(b)(c) respectively. (e) Shows the dose enhancement in-between two vertical foils. (d) and (f) show the % dose enhancement at the midpoint and the minimum point or maximum point respectively. They also show the area bound by the curve in-between the foils in horizontal arrangement or the area bound by the curve and the length of the foil in a vertical arrangement, respectively. The gold foils had separation=5 mm, thickness=0.5 mm, depth=7 cm, foil size= 1 cm x 1 cm, field size=5 cm x 5 cm.

Fig. 3.3 shows the effect of energy on dose enhancement along the path of the foils. Fig. 3.3 (a) to (c) show the enhanced dose upstream of the foils (region A), in-between the two foils (region B) and in the downstream side of the foils (region C), respectively.

In region A [Fig. 3.3 (a)], the backscatter dose enhancement and range from the first foil increased with energy. The 4 MV and higher energy beams had similar maximum values between 50-60%. The highest dose immediately next to the foil did not correspond to the highest beam energy. The 24 MV beam did, however, have the largest area of increased dose. The 10 MV beam and higher also had curves more clustered together compared to the other beam energies. The maximum range of dose enhancement was

around 1.2 cm for the 24 MV beam. The 6 MV beam had a range of increased dose of around 0.6 cm and about one-half the enhancement of the 24 MV case. In region B, 15 MV and higher energy beams produced forward dose enhancement at the downstream side of the first foil. The backscatter from the second foil combined with the forward scattered component from the first foil to give significant enhancement between the foils. The forward scatter dose enhancement shown in Fig. 3.3 (b) and (c) both had a wide range in the exit dose, compared to the backscatter dose, which were much closer together. There was also around a 15% decrease in the maximum downstream of the second foil compared to the first foil. Fig. 3.3 (d) shows that the area under the curve, the midpoint dose, and the minimum dose all increase in roughly linear fashion with increasing energy above 6 MV.

The dose enhancement in-between two vertical foils was also significant for all energies as shown in Fig. 3.3 (e). The maximum dose came from the 24 MV energy and was about 40%. In general, the point of maximum dose seemed to shift closer to the upstream side of the foil with increasing energy. The upstream dose directly beside the left edge of the foil was higher than the downstream dose at the other edge by around 8%. The dose enhancement and range of enhanced dose were lower compared to the horizontal configuration, but the vertical configuration had a wider area. Fig. 3.3 (f) shows a roughly linear increase in dose enhancement with beam energy in-between the foils.

3.3.2 Foil Separation

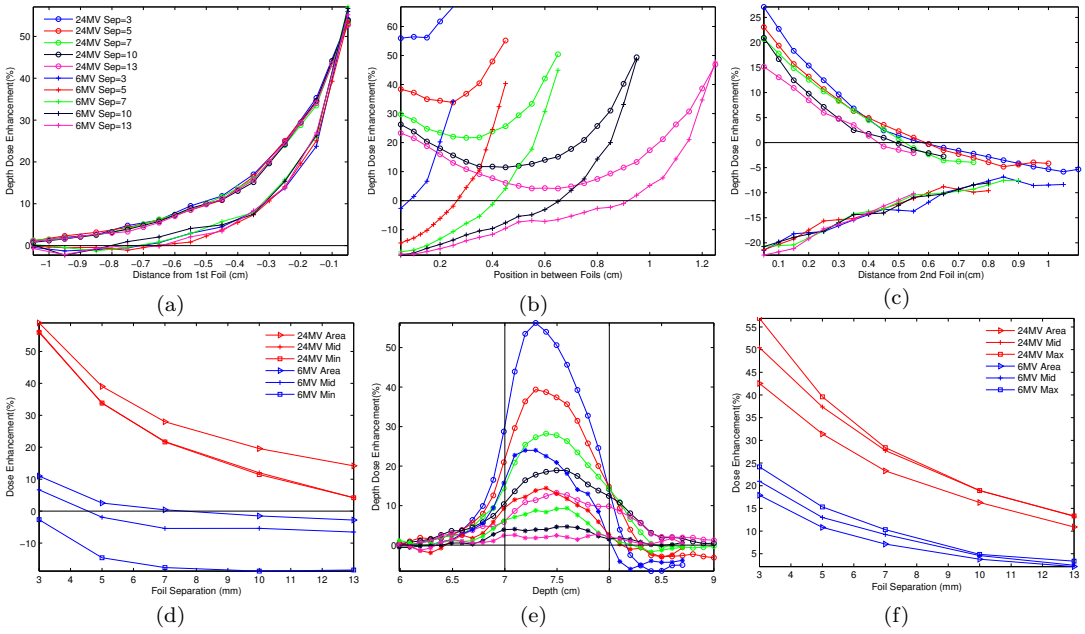

Figure 3.4 – The effect of foil separation on % dose enhancement around horizontal (a)-(d) and vertical (e) and (f) gold foils. The enhancement in dose upstream, in-between and downstream of the horizontal foils are represented in (a)-(c), respectively. (e) Shows the dose enhancement in-between two vertical foils. (d) and (f) show the % dose enhancement at the midpoint and the minimum point or maximum point respectively. They also show the area bounded by the curve in-between the foils in horizontal arrangement or the area bound by the curve and the length of the foil in vertical arrangement respectively. The energies were 24 MV and 6 MV and the foils had thickness=0.5 mm, depth=7 cm, foil size=1 cm x 1 cm, field size=5 cm x 5 cm.

Fig. 3.4 shows the effect of foil separation on depth dose enhancement. Fig. 3.4(a) indicates that the backscatter dose enhancement and range in region A are independent of separation for both the 24 MV and 6 MV case. The dose in region B, however, showed a large variation. As expected, the smallest separation had the highest peak doses with a steady decrease with increasing separation. It is observed that the larger the separation, the smaller the difference of the maximum doses at the upstream side of the second foil between 6 MV and 24 MV. By 1cm separation, the values were equal and the shape of the distribution shifts towards a minimum at the center of the two

foils. In region C, the forward scatter dose decreases with increasing separation. No enhancement was observed for the 6 MV case.

The dose enhancement occurred in-between the two vertical foils for all configurations [Fig. 3.4 (e)]. Only the 1cm and 1.3 cm foil configurations from the 6 MV case had dose maximum below 10%. The dose enhancement downstream was reversed compared to the enhancement in-between the foils. The smallest separations had the lowest dose below the foils. Figs. 3.4 (d) and (f) both show an exponential decrease in dose enhancement with increasing foil separation.

3.3.3 Foil Thickness

Fig. 3.5 shows the effect of foil thickness on dose enhancement. For the horizontal foils, the dose in region A had increased dose with increasing foil thickness in the 24 MV case. The 6 MV energy case had decreasing upstream dose with increasing foil thickness.

Between the foils, the two energies had significantly different dose distributions. While both energies had significant backscatter contributions, the low energy case had no forward contribution towards dose enhancement. The high-energy case had more spacing between each curve while the low energy cases had much less difference. In region C, the lower energy curves were more distributed.

The dose enhancement in-between two vertical foils was highest for the thickest foil with a maximum of around 48%. Similar to Fig. 3.5 (b), the low energy case had little difference between the isodose curves compared to the 24 MV which had significant gains with increasing thickness. In both the horizontal and vertical arrangement, the 6 MV beams showed a very little change with increasing thickness. The 24 MV case, however, showed that rate of increasing dose enhancement decreased with increasing thickness.

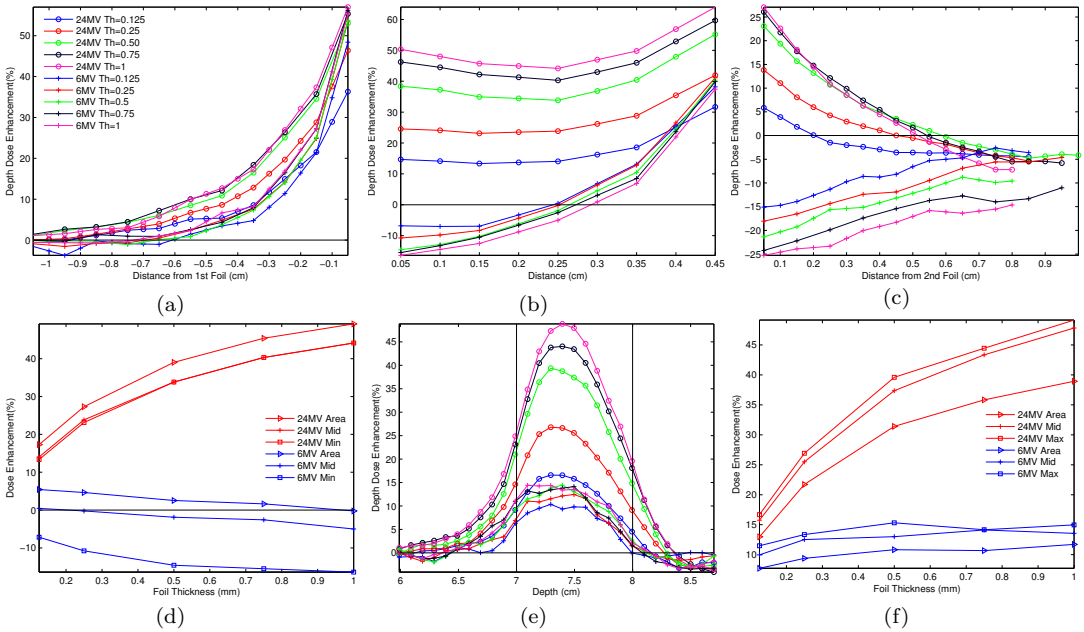

Figure 3.5 – The effect of foil thickness on % dose enhancement around horizontal and vertical gold foils. The enhancement upstream, in-between and downstream of the horizontal foils are represented in (a)-(c) respectively. (e) Shows the dose enhancement in-between two vertical foils. (d) and (f) show the % dose enhancement at midpoint and the minimum point or maximum point respectively. They also show and the area bounded by the curve in-between the foils in horizontal arrangement or the area bound by the curve and the length of the foil in vertical arrangement respectively. The energies were 24 MV and 6 MV and the foils had separation=5 mm, depth=7 cm, foil size=1 cm x 1 cm, field size=5 cm x 5 cm.

3.3.4 Atomic Number

As expected, the atomic number, Z, had a significant effect on the distributed dose. For each material, both the low and high-energy cases had comparable upstream backscatter maximums. The dose increased with increasing Z up to gold, but it declined with lead for the 24 MV case. This was observed in both the horizontal and vertical configuration [Fig. 3.6(d) and (f)]. The 6 MV case had dose backscatter maximum that increased with Z. The range of enhancement reflected the order of Z with aluminum having the least effect. In region B, the lightest materials had the least enhancement in either direction, maintaining a more even dose distribution. They also had much less difference between

the low and high-energy case. Downstream, significant differences existed between the two energies of each material.

The vertical foils had large differences between the low and high-energy configurations, but the order of enhancement for varying Z was similar to the horizontal case. As before, the lowest enhancement came from the lowest Z material.

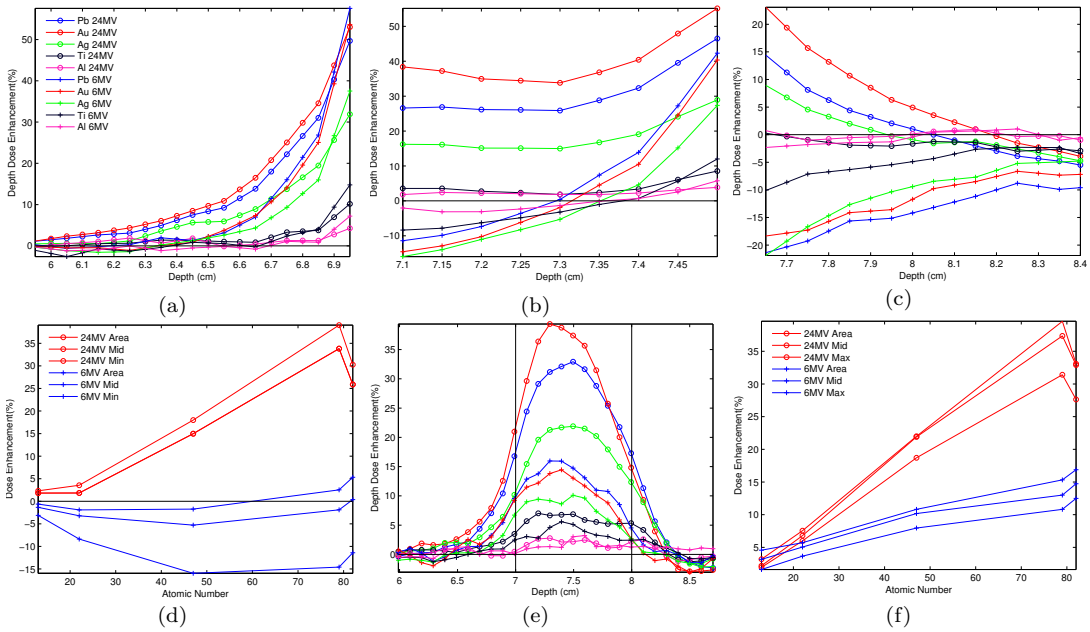

Figure 3.6 – The effect of the atomic number on % dose enhancement around horizontal and vertical gold foils. The enhancement upstream, in-between and downstream of the horizontal foils are represented in (a)-(c) respectively. (e) Shows the dose enhancement in-between two vertical foils. (d) and (f) show the % dose enhancement at the midpoint and the minimum point or maximum point respectively. They also show the area bound by the curve in-between the foils in horizontal arrangement or the area bound by the curve and the length of the foil in vertical arrangement respectively. The energies were 24 MV and 6 MV and foils had thickness=0.5 mm, separation=5 mm, depth=7 cm, foil size= 1 cm x 1 cm, field size=5 cm x 5 cm.

3.3.5 Foil Size

The effect of foil size on dose enhancement is shown in Fig. 3.7. The dose in both the horizontal and vertical configurations increased with the size of the foil. In Fig. 3.7(a), the backscatter dose enhancement was very similar for both energies and foil

sizes above 1 cm x 1 cm. The 0.2 cm x 0.2 cm, 0.6 cm x 0.6 cm and 1 cm x 1 cm foils in both energies all displayed lower dose distributions and were separate from the other foils. In-between the foils [fig. 3.7(b)], the 24 MV configurations with larger foil sizes had isodose curves clustered together as the dose approached a maximum of 60%. Downstream of the second foil, the dose distributions were similar to the distributions in-between the foils in terms of clustering. The 24 MV photons with smaller foil sizes had lower doses and the dose distribution had more difference between each other. The dose enhancement approached a maximum dose for foil sizes above 3 cm x 3 cm.

The dose enhancement in-between two vertical foils was particularly interesting. The point of maximum dose was always within 0.5 cm from the top of the foil no matter how large the foil. The region of increased dose was extended to the length of foils for foils up to 2 cm length, after which the foils had regions of dose reduction in-between the foils.

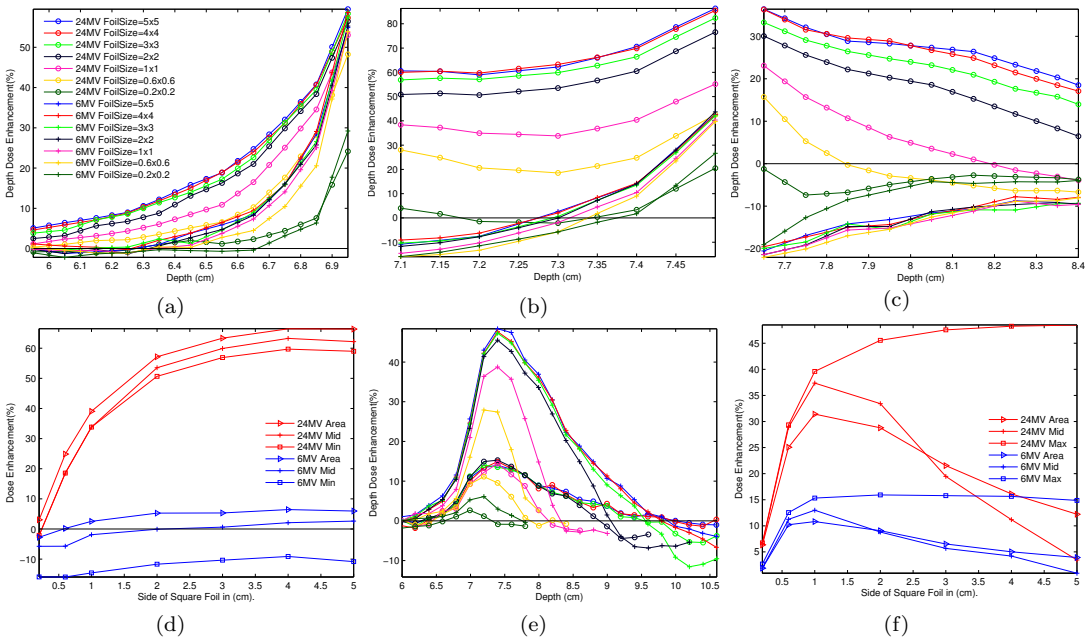

Figure 3.7 – The effect of foil size on % dose enhancement around horizontal and vertical gold foils. The enhancement upstream, in-between and downstream of the horizontal foils are represented in (a)-(c) respectively. (e) Shows the dose enhancement in-between two vertical foils. (d) and (f) show the % dose enhancement at the midpoint and the minimum point or maximum point respectively. They also show the area bound by the curve in-between the foils in horizontal arrangement or the area bound by the curve and the length of the foil in vertical arrangement respectively. The energies were 24 MV and 6 MV and had thickness=0.5mm, separation=5mm, depth=7cm, foil size= 1cmx1cm, field size=5cmx5cm.

3.3.6 Field Size

The effect of field size on dose enhancement is shown in Fig. 3.8. Figs. 3.8 (a)-(c) and (e) show that dose around the foils did not change significantly for both energies. The smallest field size had the highest dose in the high-energy case, though region A had much a smaller enhancement compared to the dose in region B and C. Figs. 3.8 (d) and (f) show that the dose enhancement in-between the vertical foils for 6 MV was roughly constant with increasing field size. For 24 MV, the dose difference was minimal for 5 cm x 5 cm field size and above.

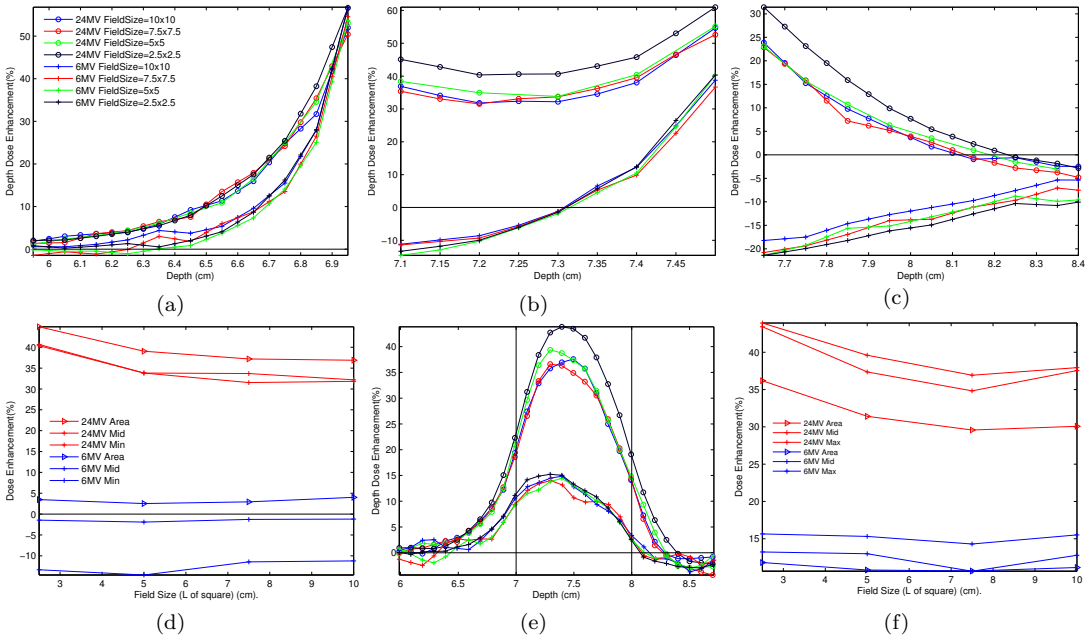

Figure 3.8 – The effect of field size on % dose enhancement around horizontal and vertical gold foils. The enhancement upstream, in-between and downstream of the horizontal foils are represented in (a)-(c) respectively. (e) Shows the dose enhancement in-between two vertical foils. (d) and (f) show the % dose enhancement at the midpoint and the minimum point or maximum respectively. They also show the area bounded by the curve in-between the foils in horizontal arrangement or the area bound by the curve and the length of the foil in vertical arrangement respectively. The energies were 24 MV and 6 MV and had thickness=0.5 mm, separation=5 mm, depth=7 cm, foil size= 1 cm x 1 cm.

3.3.7 Depth

Fig. 3.9 shows the effect of foil depth on the dose enhancement. Figs. 3.9 (a) through (c), show that dose in region A, B and C were almost the same in both energies. The dose enhancement in-between the foils was constant with depth as seen in Figs. 3.9 (d) and (f).

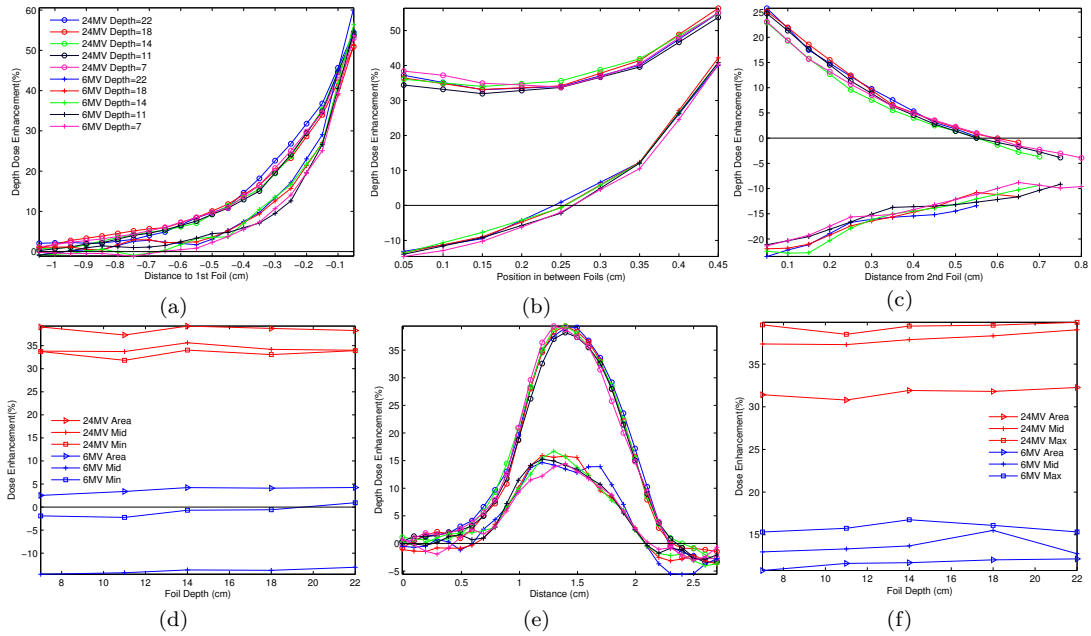

Figure 3.9 – The effect of foil depth on % dose enhancement around horizontal and vertical gold foils. The enhancement upstream, in-between and downstream of the horizontal foils are represented in (a)(b)(c) respectively. (e) Shows the dose enhancement in-between two vertical foils. (d) and (f) show the % dose enhancement at the midpoint and the minimum point or maximum point respectively. They also show the area bound by the curve in-between the foils in horizontal arrangement or the area bound by the curve and the length of the foil in vertical arrangement respectively. The energies were 24 MV and 6 MV and had thickness=0.5mm, separation=5mm, foil size= 1 cm x 1 cm, field size=5 cm x 5 cm.

3.4 Discussion

Dose at the interface can be divided into several categories. The dose from backscattered photons, secondary electrons produced in the water above or below the foil, backscattered and forward scattered electrons produced in the foil. For the photon contribution, the photoelectric effect plays a small role in high-Z materials. Even though the cross section is low for high energies, gold has a high atomic number and low energy characteristic x-rays are expected to deposit some dose close to the metal. A second source of photon dose is bremsstrahlung. As secondary electrons are slowed down, bremsstrahlung x-rays are produced having a spectrum range up to the kinetic energy of the electron.

A portion of this dose is also expected to be deposited in the vicinity of the metal. The backscattered photons are considered to be negligible and is not considered.

For this project, I am particularly interested in electrons generated by bremsstrahlung photons and pair production. The premise behind this study is that the forward and backward scatter contribution can be combined to increase the dose to the target area. It is clear from these simulations that dose enhancement is possible and that the main contributor is the backscatter contribution. Overall, the Monte Carlo simulation results were consistent with experimental data previously obtained with film [35] and single foil measurements [9]. In my simulations, the maximum dose enhancement occurs with gold foils of 0.3 mm separation, 1 mm thickness, 5 cm x 5 cm area foil and a 24 MV beam with a 2.5 cm x 2.5 cm field size.

In general, the horizontal foils have a backscatter exit dose from the second foil that is always less than the backscatter exit dose of the first foil and the forward scatter exit dose from the second foil is always less than the forward scatter exit dose of the first foil. This is due to the reduction of energy after the first foil and the associated decrease in the amount of electrons existing the foil. For the 6 MV configurations, the forward scatter from the second foil is always negative relative to the homogeneous water. In-between the foils, the lower energy often had minimum doses very close to the first foil; while the higher energy had values close to the center. This can be explained from the fact that higher energy electrons have a larger range and that more electrons from the second foil contribute dose to the region than from the first foil. One observation from the dose contours is that the dose enhancement in-between the foils is not uniform with distance from the foil. Downstream of the foils, the corner edges always seem to be areas of low dose relative to the center for higher energies (6 MV and higher). The two lowest-energy cases had a more uniform low dose profile over the length of the foil.

The vertical arrangements generally resulted in a maximum dose in-between the vertical foils. The trends observed in this orientation were very similar to the horizontal foils configurations. The exception to this is the foil size. The dose measurements for

the largest foils sizes in the 24 MV horizontal case had over a 10% larger value for minimum dose compared to the maximum dose in a vertical arrangement. In the 6 MV case, the vertical arrangement had a higher dose maximum compared to the minimum dose in the horizontal setup. Vertical foils had much more configurations that resulted in increased dose compared to the horizontal configuration. In cases where the dose reduction was observed, it often was less than 5%.

Often, older experiments made measurements at a particular distance above or below the interface. This made the comparison more difficult because close to the interface, the dose in one configuration can be higher than another but as you move further away from the foil the results can be reversed. The area under the curve gave a more realistic idea of accumulated dose in-between the foil.

3.4.1 Energy

Dose enhancement increases with energy. This should be expected since higher energy secondary electrons will have a greater range. High-energy secondary electrons tend to travel more in the forward direction as momentum has to be conserved. These electrons travel deeper in the foil and some of the electrons will contribute to dose downstream but some will get backscattered and have to traverse the foil again while losing energy. If the foil is thicker than the range of the electron, then it will get absorbed, otherwise, some electrons with sufficient energy contributes to the backscattered region. For photon energies below 15 MV, the forward electrons do not have the energy to exit the foil resulting in dose reduction. The result is a combination of electron scattering and photon attenuation.

3.4.2 Separation

Increasing the foil separation decreases the dose in-between the foils. When the foils are close then back and forward scattered electrons can easily contribute towards the dose in regions near the opposite foil. If the separation is smaller than the range of

electrons, then backscatter electrons might go on to generate more dose in the form of bremsstrahlung. As the separation gets larger, it reaches a point where the electron ranges no longer overlap.

3.4.3 Thickness

Dose enhancement increases with increasing foil thickness up to a certain thickness. When the foil thickness increases, the probability of interaction increases and more secondary electrons are generated. The range of the secondary electrons depend on energy among other factors, but increasing the foil thickness above half the range of the secondary electron do not contribute to additional backscatter enhancement. This can be seen in Fig 3.6 (d) where the 6 MV case had no increase in enhancement while the 24 MV increased towards a maximum dose. Das found that this occurred around a thickness of 3mm for 24 MV and 1 mm for 6 MV for lead in their experiment [6]. Similarly, in the forward direction, above a certain thickness, then much of the additional electrons will no longer exit as they are absorbed in the heterogeneity. The vertical foil dose distribution reveals that thinner foils had much more even distribution of increased dose along the outside length of the foils. With thicker foils, the outside portion of the foil had more enhancement towards the top.

3.4.4 Atomic Number

There is a significant increase in dose with respect to increasing atomic number. In fact, the atomic number had the largest effect on the dose. This is expected because of the larger scattering cross section of electrons in high-Z materials. More specifically, pair production and bremsstrahlung are proportional to Z^2. In the vertical configuration, almost no enhancement was seen in the aluminum case while all the others show some enhancement. With that said, the vertical configuration had less difference between the low and the high-energy cases compared to the other parameters with a significant effect on the dose.

It is interesting to note that there was a drop in downstream enhancement moving from gold to lead in the 24 MV configuration (Fig 3.6c). We note that this was not the case for Li et al. [9], who had gold with a lower maximum than lead. There are two reasons this could occur. This is perhaps because the electron density of gold is over 70% larger than that of lead (15.5g/cc vs 8.98g/cc), leading to more Compton interactions. They used the PRESTA electron crossing algorithm, which is known to underestimate lateral electron deflections in a manner that increases with Z^2 [102, 103]. Additional testing using the same energy, field size and thickness as Li revealed that lead has a higher maximum near the foil upstream. The difference in result is likely due to a combination of the reasons above, though the primary reason is probably geometrical and energy differences.

Another unexpected result was the peak dose for the 6 MV lead foil (Fig. 3.6a). The 6 MV dose maximum was higher than the 24 MV dose maximum but the curves switched after about 1.5mm from the foil. The unexpected effect on the dose distribution from 6 MV and 24 MV photons and lead and gold show the difficulty in drawing conclusions about trends involving from multiple factors.

3.4.5 Foil Size

At small foil sizes and high energy, the foil size has a significant influence on the dose. As the foil size approaches the size of the beam, then the amount of electrons that scatter towards the center of the foil reaches a maximum. The secondary electrons from 6 MV beam do not have the energy to reach the center where it can contribute to the dose. It is possible that electrons generated in water can scatter below the foil but the 2mm x 2mm case had negative enhancement indicating that this is minimal at best (Fig. 3.7b) . With increasing foil size, more electrons are generated from the foils, which contribute to dose in the center. Between larger vertical foils, electronic equilibrium was lost after traversing 1.8 cm deep into the foil, resulting in a relative dose reduction. In addition to the scattering of electrons, the vertical configuration possibly has a lot more

backscattered electrons in-between the foils compared to forward scatter electrons.

3.4.6 Field Size

Field size has a minor effect on the dose distribution depending on the energy and region of the foils. At high energies, the enhancement in-between the foils and below the last foil increase slightly with decreasing field size, while at low energies no difference is observed. In general, wider field sizes mean that more lateral electrons can get scattered in-between the foils. Above a certain field size, electrons from the field edge no longer contributes to the center of the foils. One reason for the dose increase with the smaller field sizes is that there is a reduction of dose from homogeneous case. The dose increase from the foil should be fairly constant with field size as long as the range of secondary electrons is within beam. When the dose from the 2.5 cm x 2.5 cm field size was compared to the 5 cm x 5 cm field sized this was confirmed. The dose near the foils were close but the dose further from the foil were much larger with the smaller field size having the lower dose.

Werner et al. observed similar findings downstream, but their perturbation factors increased more steadily with decreasing field size and had a strong increase after 8cm x 8cm [4]. No effect was observed for the lowest energies. Upstream from the first foil, Das reported a slight decrease in the dose from lead in the smallest field sizes [6] but we did not observe this for gold. They reported that it might be due to problems with chamber response due to the finite window thickness. Both heterogeneities were much larger than the field size.

3.4.7 Depth

There is no significant effect of depth on dose enhancement with double foil measurement. This is in agreement with the horizontal single foil measurements made by Li and Das [9, 6].

3.5 Conclusion

The degree of dose enhancement around thin lead foils was determined by Monte Carlo simulation. The most important parameters are the material, foil thickness, separation and photon energy. Enhancement increases with energy, foil thickness, atomic number and decreases with separation. For 24 MV, enhancement increases with thickness up to a certain point and for 6 MV increasing the thickness decreases the dose. Foil depth and field size did not have appreciable effect on the dose. The foils in the vertical orientation seemed to have lower doses in between the foil but they have a larger region of increased dose.

Chapter 4

The Effect of Material Shape, Material Distribution and Pair Production on Dose.

4.1 Introduction

In keeping with the theme of distributed high-Z materials, naturally the next question to ask, is what happens to the dose if more foils are used. Realistically, more than two foils will be necessary to obtain the proper dose distribution especially for larger tumors. The distribution and number of heterogeneities would vary with each patient. Each case would require simulation resulting in a significant increase in the treatment planning workload. In order to avoid this, we need a way of predicting the dose for multiple heterogeneities.

The results of the previous chapter provided information on the dose distribution between two foils but there are still some unanswered questions. I wanted to know more about the relationship between two foils and a single foil. Are there any synergistic effects from using two foils? If so, how much does it influence the dose and over what

range. Understanding this would enable the dose distribution of a single foil or shape to be used to estimate the dose around multiple distributed foils or heterogeneities.

The size and shape of the material can influence the success of a treatment. Some shapes are cheaper to produce and easier to manufacture. Cylindrical shapes in particular, already find use in the body in the form of markers and already have approvals from regulatory agencies. Markers are attractive because they are potentially easier to implant than a foils. Dosimetrically, not much work has been done for evaluating the dose around fiduciary markers irradiated by very high energy (18MV and higher) photons. A single foil will be selected and the dose around it compared to the dose around the marker. After reviewing the data from this experiment and the results from chapter 3, two configurations will be selected for dose measurement with the polymer gel.

One pattern that was observed in the results of chapter 3, particularly the horizontal foils, was dose reduction after the foils. We know that electromagnetic waves and sound waves experience reflection and transmission when moving between two dissimilar media. I wanted to know if this effect or similar phenomena occur with high energy photons. Specifically, how the dose around a single heterogeneity compares to the dose around a distributed heterogeneity of equivalent thickness. Even if the effect is minimal at high energies, do the electrons behave in a manner such that it is advantageous to distribute the high-Z material. If such interactions can influence the dose near the foils, what are its dependencies? If these effects are significant, then the distributing the heterogeneity could be used to increase or widen the distribution of dose to cancer cells and reduce the dose to healthy tissue downstream. It might even have some applications in radiation shielding, specifically, shielding with lead aprons or shielding in confined environments.

Traditionally, photon transmission through multiple media is determined by combining the attenuation coefficients and thickness for each material in an exponential

decay function. Attenuation measurements in air far downstream from the heterogeneity have confirmed this method to be accurate. Close to the high-Z material, however, the outcome is not clear. I want to verify that this is in fact the case and identify any limitations to this practice if any. I will investigate the effect of the number of foils (or foil count), foil separation and energy on dose around multiple thin lead foils. I will compare the distributed foils to a single foil of equivalent thickness and look at the difference in dose upstream, downstream and in-between the foils.

Pair production is expected to play a large role in dose enhancement when high energy beams are used in these configurations. We don't know, however, what role pair production plays in the actual distribution of dose. We will attempt to understand this by comparing the dose distributions for the above configurations with configurations where pair production is not simulated.

4.2 Methods

4.2.1 Two Foils vs Two Single Foils Combined

The phantoms in which foil separation was evaluated, were modified such that one of the two foils was removed. A second set of phantoms had the other foil removed instead. The simulations were repeated using the same setting as described in section 3.2.3. The dose from adding two single foils was compared to the dose from two foils in each case.

4.2.2 Effect of shape and geometrical arrangement

There were several factors that need to be considered in choosing a shape. These included beam energy, material weight and thickness. Even though a thicker material generates more electrons, thickness also has to be balanced by the beam energy. If the energy is too low, then the electrons will get adsorbed before they exit the material. The demise of the Varian 2300 linac placed an upper limit on the beam energy of the project to the 18 MV photon beam of Elekta Synergy accelerator (Elekta Medical Systems,

Stockholm, Sweden). A thicker material also has more weight which might increase the potential to sag especially in the horizontal configuration. Cost can also be a factor. Lead is significantly cheaper that gold and has a higher atomic number.

Though foils have the advantage of a larger surface area, I felt the need to evaluate smaller shapes. We have to consider the practicality and ease of inserting high-Z materials into the body. Fiducial markers, are already used in the body and so I thought it was necessary to evaluate the dose around a similar shape.

4.2.2.1 Single Foil

A 1cm x 1cm lead foil with a thickness of 0.5mm was selected as the optimal foil size for polymer gel dosimetry. The foil was placed in the center of the phantom with depth of 7cm and DOSXYZnrc was used to simulate horizontal and vertical single foil arrangements. The parameters were similar to those described in section 3.2.3 but several key differences exist. The photon and electron transport cutoff energies were modified to cover the entire range. The photon cutoff energy was selected to be 1kV and the electron transport cutoff energy was 512 kV. Range reduction was not employed. Similarly, a point radiation source with 5 cm x 5 cm collimation at a 100cm SSD was used with 6 MV and 18 MV photons. The phantom resolutions were modified so that the resolution in the areas of interest were 0.1mm closest to the marker and 0.5mm a bit further out. The other parts of the phantom had resolution of 2mm. Around 32.5 million histories were obtained. Another homogeneous phantom was created using the same parameters.

4.2.2.2 Gold marker

A gold Civco fiducial marker, model number, MTNW887808 was selected for simulation. DOSXYZnrc was used to simulate the dose around the marker placed at a 7cm depth and oriented parallel or perpendicular to the beam. The grooves were ignored and the marker was modeled as a rectangle prism with length 3mm and width and height

0.8mm. The same Monte Carlo parameters from the previous section was used in this study.

4.2.2.3 Configuration for Polymer Gel Measurement

After reviewing the data for the single foil and marker, the decision was made to use foils for the polymer gel dose measurement. The phantoms in section 4.2.2.1 were modified to obtain two foil phantoms. A separation of 7 mm was selected to allow more data points. Both foils were centered, had depths of 7cm and had the same dimensions as the two foils case. The simulations were repeated using the same parameters as the single foil case (section 4.2.2.1).

4.2.3 Dose Modulation with Multilayer Foils

DOSXYZnrc was used to perform Monte Carlo simulations of multilayer lead foil configurations. All foils had a combined thickness of 1 mm and a foil size of 7 cm x 7 cm. As before, lead was selected in case experiments are made in the future and the foils were larger than the beam size to better simulate shielding environments. The number of foils were 2, 4, 6, 8, and 10 with a fixed separation of 0.3 cm. For each of these, the dose distributions upstream, downstream and in-between the foils were studied and compared to the equivalent single foil. The phantom size was 16 cm x 16 cm x 28 cm with a resolution of 0.5mm in the areas of interest and 2 mm elsewhere. The foils were placed starting at a depth of 7 cm or the last foil ending at a depth of 10 cm for the evaluation of the upstream or downstream dose respectively.

The number of histories ranged from 20 to 62.5 million and the only various variance reduction techniques was photon splitting. The simulated physics were the same as section 4.2.2.1. The plots were normalized at Dmax in a homogeneous water phantom. The minimum dose enhancement and the change of integrated dose between the foils were also determined.

The effect of foil separation was evaluated by using separations of 1 mm, 3 mm,

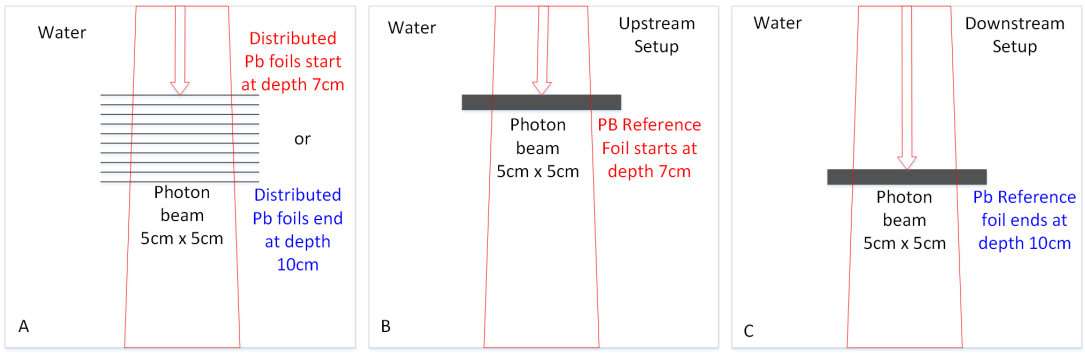

Figure 4.1 – The experimental setup showing upstream and downstream measurement. The distributed foils are depicted in A and the dose is compared to the dose from the reference foil upstream (B) or downstream (C).

5 mm, 7 mm and 9 mm and a foil count of 10. The effect of energy was evaluated using energies Co60, 4 MV, 6 MV, 10 MV, 15 MV, 18 MV and 24 MV, 10 foils, and a separation of 5mm. The effective range of increased dose was also evaluated. This was defined to be the distance from the foil for which there is a dose difference between the distributed foil and reference foil. The setup is depicted in figure 4.1

4.2.4 Effect of Pair Production

Next, the DOSXYZnrc code was modified to no longer calculate dose from pair production and compiled as a second program. The phantoms for the single foil, two foil and marker were then recalculated using the modified algorithm. For the multilayer foils, a single foil and 10 foil configuration were simulated with no pair production for 24 MV photons. The dose distribution with no pair production was subtracted from the normal distribution to obtain the pair production dose.

4.3 Results

4.3.1 Two Foils vs Two Single Foils Combined

Figure 4.2 shows the dose contours for single foils and two foil configurations with a 5mm separation. For the horizontal foils, we can see that the dose from the two foil configuration differs from the dose distribution for the combined dos e distribution. The two foil setup had an increased dose region just downstream of the first foil. The upstream peak doses from Fig. 4.2(a),(b) and (d) were 145%, 151% and 158.5% while the peak downstream doses from Fig. 4.2(a),(c) and (d) were 144%, 143%, 145.7% respectively. The vertical foils had a peak dose in between the foils of 130%, 109.2%, 110.3% and 126.5% from Fig. 4.2(e)-(h) respectively. In all regions, the overall dose around the two foils was larger than the dose from two single foils, except for region A in the horizontal orientation.

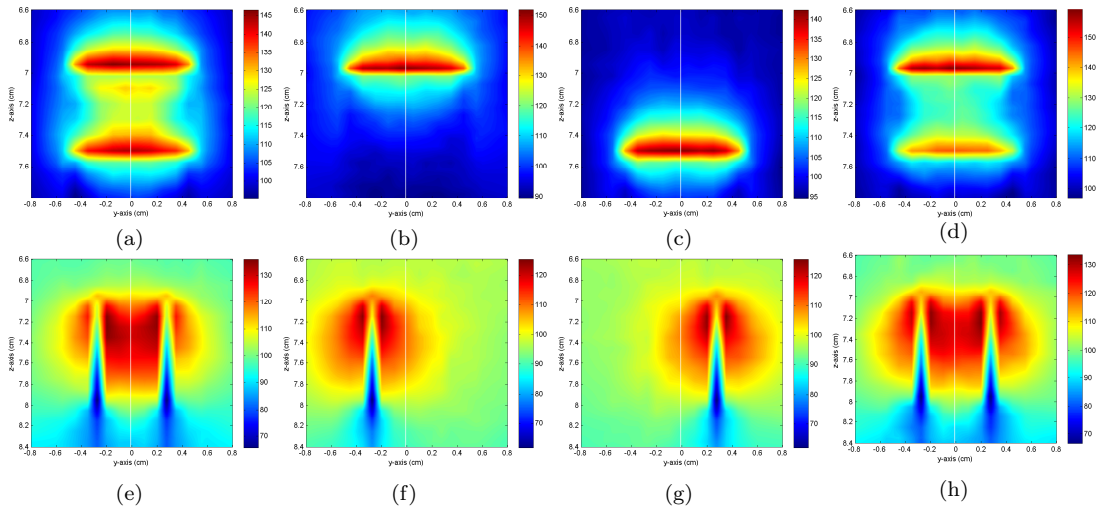

Figure 4.2 – The relative dose enhancement comparing two foils to single foils for 24 MV photons. Column one shows the dose distribution for two foils, columns two and three show the single foil dose distributions and column four shows the addition of dose from column two and three. The gold foils had separation=5 mm, thickness=0.5 mm, depth=7 cm, foil size= 1 cm x 1 cm, field size=5 cm x 5 cm.

Fig. 4.3 shows the % dose enhancement from adding dose from 2 single foils compared to the dose of two foils. In region A (3.3) of the horizontal foils, the 24 MV case had a dose difference for separations of 3 mm and 5 mm, while the other horizontal configurations had no dose difference. In region B, the closest foils displayed a dose difference for both energies. For separations larger than 5 mm, no difference was observed. The dose difference was larger near the first foil. The 6 MV configuration had a reduction in dose difference towards the second foil. In region C, the pattern reverses with the 24 MV case having a small dose difference and the 6 MV case having a dose difference.

In the vertical orientation, the dose difference was small in the buildup region but much larger after the maximum dose point for both energies. The difference was largest at the maximum dose point and decreased with depth. The combined dose from two single foils was always less than or equal to the dose from two foils. For separations of 7mm and larger, the dose difference was around 5% or less.

Overall, the dose difference in the extreme cases had maximum dose difference of around 10%. In general, increasing the separation caused the dose difference to approach zero in all configurations. The dose difference was larger for higher energies and had a larger range of dose difference in the orthogonal configuration.

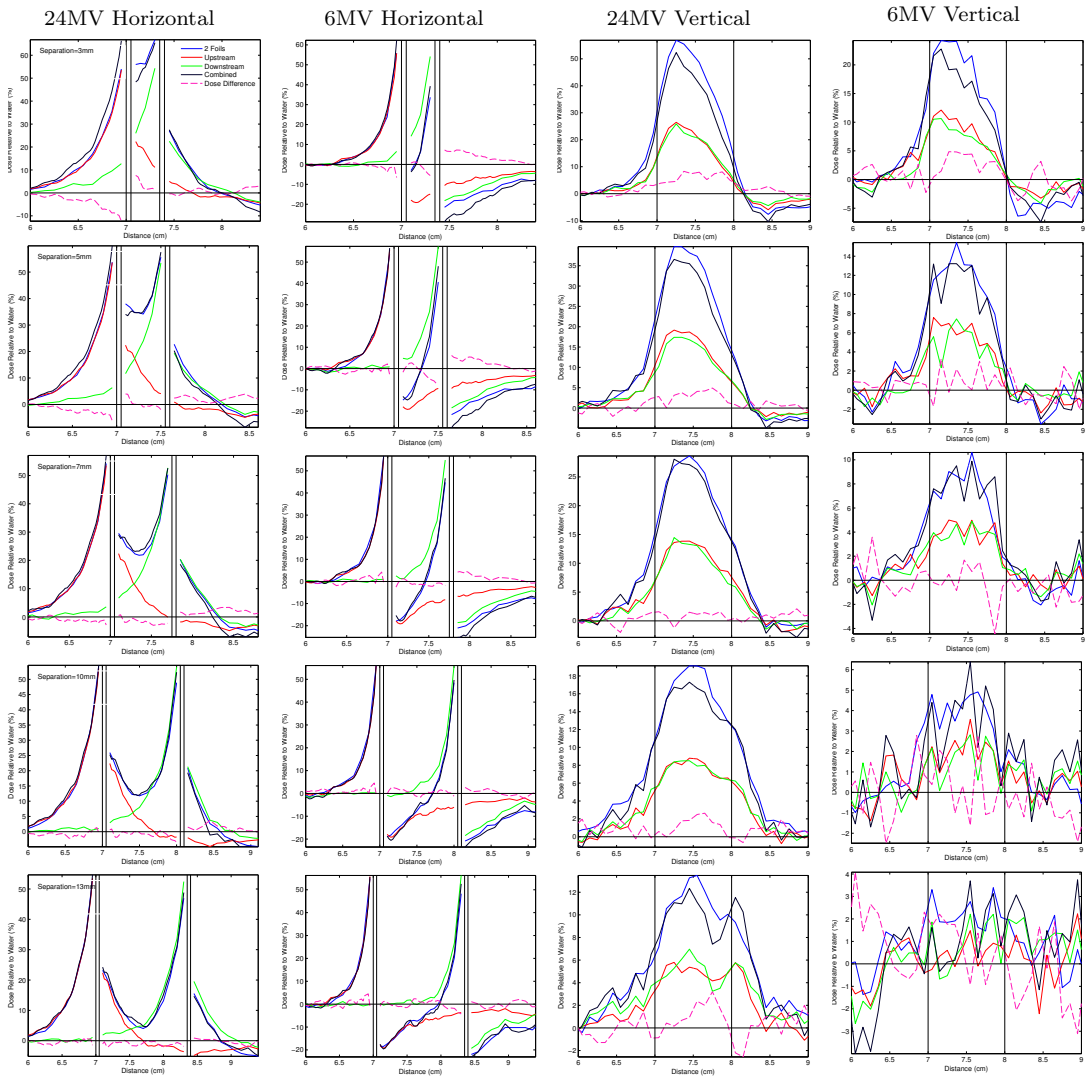

Figure 4.3 – The relative dose enhancement comparing two foils to single foils. The first and third column represent the 24 MV case and the second and fourth column represents the 6 MV case. Column one and two show the horizontal orientation while columns three and four show the vertical orientation. Rows one through five represent the separations 0.3 cm, 0.5 cm, 0.7 cm, 1 cm and 1.3 cm respectively.

4.3.2 Effect of Shape and Pair Production

4.3.2.1 Single Foil

The dose around the single foils (Fig 4.4) were similar to the dose with 24 MV foils with approximate efficiency improvement techniques. For the horizontal case, the majority of the dose was backward with some forward scatter. The effect of pair production on the dose was significant for the 18 MV irradiation. The majority of the dose from pair production was in the forward direction while the majority of the dose increase seemed to be the upstream of the foil. The 6 MV case had a small dose reduction with no pair production and significantly reduced forward dose. The vertical foils had a lot of attenuation in the foil and immediately downstream of the foils but the increased dose on the sides covered the length of the foil. When pair production was turned off in the 18MV case, the dose increase around the foil all but disappeared except for the region at the very top of the foil. In this orientation the amount of pair production matched the direction and shape of the increased dose distribution. Assuming that the range of dose enhancement is proportional to the range of pair production in the metal, the amount of pair production in water is sizable. We also note that the dose difference from pair production further away from the foils is larger before the foils compared to after.

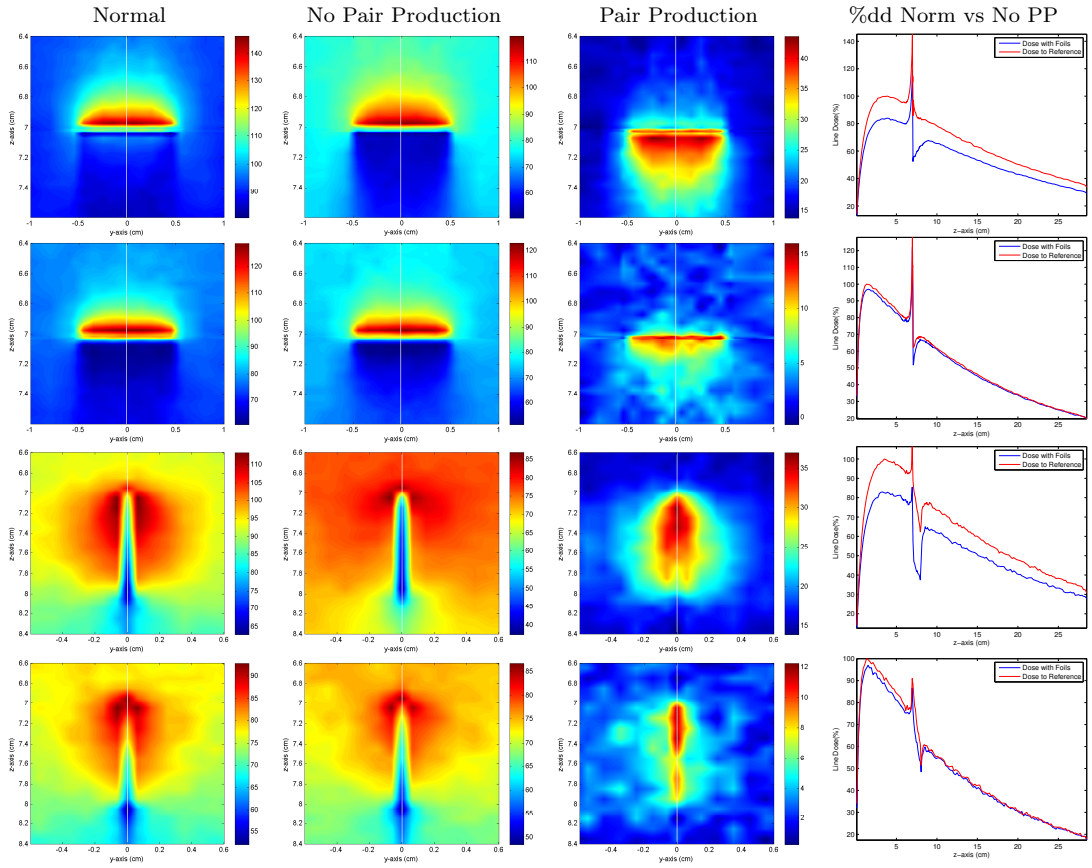

Figure 4.4 – Single horizontal and vertical foils irradiated with 18 MV or 6 MV photons. The first and third row shows dose from the 18 MV case while the second and fourth row represent the dose from 6 MV case. The first column shows the dose, the second column shows the dose with no pair production, the third column shows the dose from pair production and the last column shows the %DD for normal dose and dose with no pair production. All numbers in %.

4.3.2.2 Gold Marker

Fig. 4.5 shows the markers in horizontal and vertical orientations for 18 MV and 6 MV photons. In the horizontal case, both energies had above 60% enhancement upstream of the marker. Downstream, the 18 MV case had a small enhancement before falling below the reference while the 6 MV case had no enhancement downstream. The effect of pair production on the dose distribution also caused a dose increase in the forward

direction particularly for 18 MV case. The 6 MV and 18 MV vertical orientations had short range of increased dose upstream and dose reduction downstream. The horizontal configuration seem to have a larger amount of pair production compared to the vertical orientation.

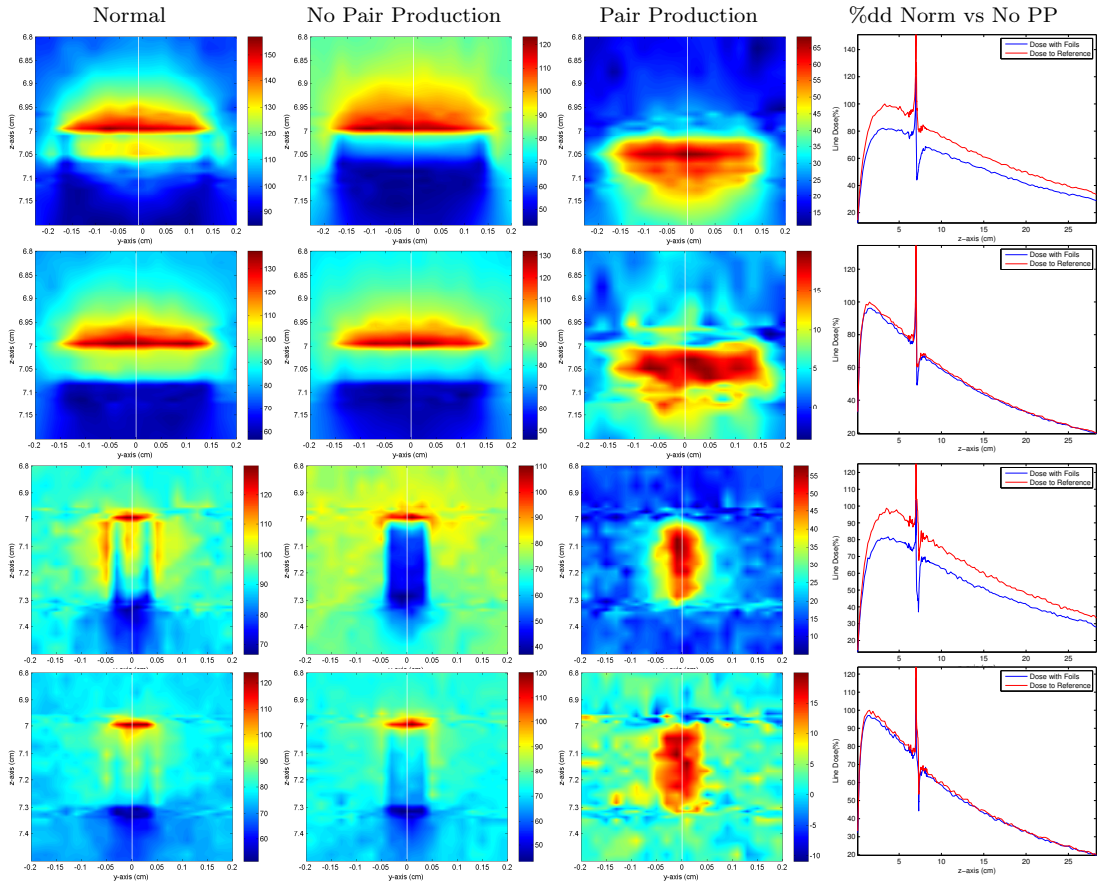

Figure 4.5 – Horizontal and vertical markers irradiated with 18 MV or 6 MV photons. The first and third row shows dose from the 18 MV case while the second and fourth row represent the dose from 6 MV case. The first column shows the dose, the second column shows the % dose enhancement, the third column shows the dose from pair production and the last column shows the %DD for normal dose and dose with no pair production. All numbers in %.

4.3.2.3 Configuration Selection

Fig. 4.6 shows the Monte Carlo dose distribution of the horizontal and vertical foil configurations and the effect of pair production for 6 MV and 18 MV photons. For the horizontal configuration, we can see that pair production results in a high dose increase that is predominantly in the forward direction [Fig. 4.6(c),(g)]. There was almost no spreading of the dose away from the foils. The %DD curves show a 16% drop in dose at Dmax and a 36% reduction at the dose minimum point between the foils. The 6 MV configuration had a 3.3% drop in dose at Dmax and a 10% reduction at the dose minimum point between the foils.

Similarly, the vertical configurations had dose distributions that were mostly in the forward direction. This orientation, however, shows some spread of dose moving away from the foil. It also had a much smaller dose difference with no pair production compared to the horizontal case. For the 18 MV setup, the dose difference in the peak dose was 23% and the dose difference at Dmax was 16%. Overall, the vertical configuration had a much larger, more useful distribution of increased dose in between the foils. Looking at both orientations, however, the range of pair production near the foils was larger in the horizontal case and the dose magnitude was larger.

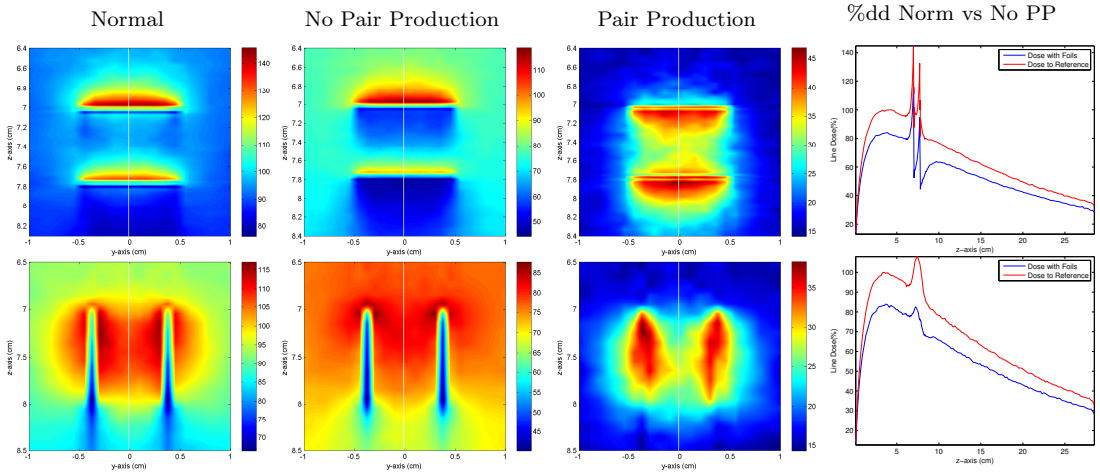

Figure 4.6 – Dual horizontal and vertical foils irradiated with 18 MV or 6 MV photons. The first and third row shows dose from the 18 MV case while the second and fourth row represent the dose from 6 MV case. The first column shows the dose, the second column shows the dose with no pair production, the third column shows the dose from pair production and the last column shows the %DD for normal dose and dose with no pair production. All numbers in %.

4.3.3 Dose Modulation with Multilayer Foils

The dose in the vicinity of the foils changed significantly for each of the parameters evaluated. Far from the foils, however, the dose distribution was exactly the same. Detailed images of the dose distributions and error matrices are displayed in Appendix C.

4.3.3.1 Effect of Foil Count

Foil count had a major effect on the dose distribution for both 24 MV and 6 MV photons as shown in Fig. 4.7. Increasing the number of foils reduced the dose upstream. At the upstream side of the first foil, the dose for the 24 MV beam had a maximum dose increase of 57% for the single foil case (or reference), while the 10 foil setup had a 32% increase (Fig. 4.7a). The 6 MV configuration (Fig. 4.7d) showed a similar trend, with the reference foil having a dose maximum of 60% and 10 foil setup with 43%. The

dose from the lower energy case was much closer together and had a shorter range of increased dose than the higher energy case. The range of increased dose did not change significantly with changes in foil count (Fig. 4.7h). The relative cumulative upstream dose also decreased steadily with increasing foil count with a dose reduction of over 2% for 24 MV beams and 0.5% at 6 MV beams (Fig. 4.7g).

At the downstream side of the last foil, the 24 MV case (Fig. 4.7c) had a dose reduction with the 10 foil case having a dose maximum 16% while the reference case had a dose maximum of 32%. The 6 MV case (Fig. 4.7f) experienced dose reduction compared to water but the trend continued with the 10 foil case having the closest dose distribution compared to water. The dose reduction compared to water increased with reducing foil count. The range of dose difference downstream of the foils for 24 MV photons increased with foil count and was much larger than the range in the upstream, extending from 3.5 cm to 7 cm (Fig. 4.7h). For 6 MV, the range was around 0.5 cm and increased slightly with foil count. For the low energy case, the relative cumulative dose increased slightly with foil count, changing around 0.5%. For 24 MV beams, the dose reduction increased with foil count with 10 foils having a 4% difference compared to the single foil reference.

In between the foils, similar trends were observed for the foils starting at 7 cm and those ending at 10 cm. Increasing the number of foils resulted in a decrease in the dose enhancement in between the foils for the 24 MV case (Fig. 4.7b). As the number of foils increased, the dose increase with depth and the high dose region shifted towards the last two foils as seen with 4 and 6 foil counts. Continued increases in foil count resulted in a shift in the maximum dose towards the center and a slight dose drop with depth for the remaining foils. The 6 MV case (Fig. 4.7e) had lower doses in between the foils compared to the 24 MV case as expected, but the dose decreased steadily with depth for increasing foil count. The relative cumulative dose between foils decreased, however, with increasing foil count (Fig. 4.7i).

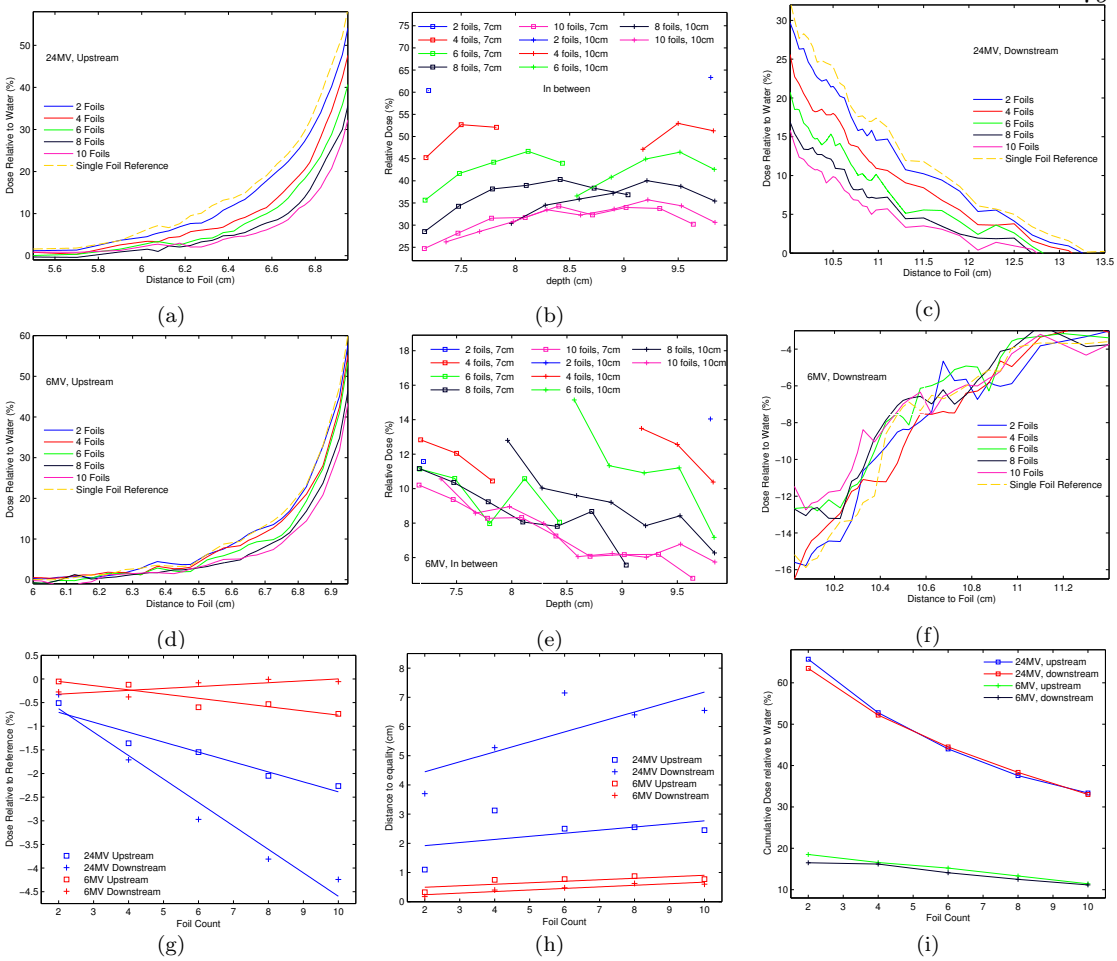

Figure 4.7 – The effect of foil count on dose around distributed foils irradiated with 24 MV or 6 MV photons. The first row shows the (a) upstream, (b) midpoint between each foil and (c) downstream dose distribution relative to water respectively for 24 MV while the second row is the 6 MV case. (g) The relative cumulative dose compared with the single foil reference. (h) The distance over which the distributed foil dose differs from the single foil reference. (i) The % enhancement in the cumulative dose for the regions between the foils.

4.3.3.2 Effect of Separation

The effect of foil separation on the dose distribution is shown in Fig. 4.8. In the 24 MV case (Fig. 4.8a), increasing the foil spacing resulted in reduced dose upstream. The 6 MV (Fig. 4.8d) configuration showed a similar trend with curves closer together and had a much shorter range of increased dose than the higher energy case. The range of

increased dose increased slightly with increasing foil separation (Fig. 4.8h). For 24 MV cases, the cumulative dose upstream decreased steadily with increasing foil separation, but separation did not have much effect on the 6 MV case (Fig. 4.8g).

In the downstream region of the last foil, the 24 MV (Fig. 4.8c) case had a dose reduction with increasing separation. The 1 mm foil separation had a dose maximum of 23% while the 9 mm separation resulted in a dose maximum of 7%. The 6 MV case (Fig. 4.8f) experienced dose reduction downstream compared to water, with the largest separations having dose values closest to water. The range of dose difference for the 24 MV case was much larger than for 6 MV (Fig. 4.8h). For the low energy case, the relative cumulative dose increased slightly with foil separation, while for 24 MV beam, the dose reduction increased 3.5% over the range of separation (Fig. 4.8g).

In between the foils, increasing the separation resulted in a shift from a distribution with a clear maximum just right of the center for the 24 MV beam to a mostly even and decreased dose distribution (Fig. 4.8b). The 6 MV case (Fig. 4.8c), had lower doses in between the foils compared to the 24 MV case and the dose decreased steadily with depth for increasing separation. As before, the relative cumulative dose for both energies decreased with increasing separation (Fig. 4.8i).

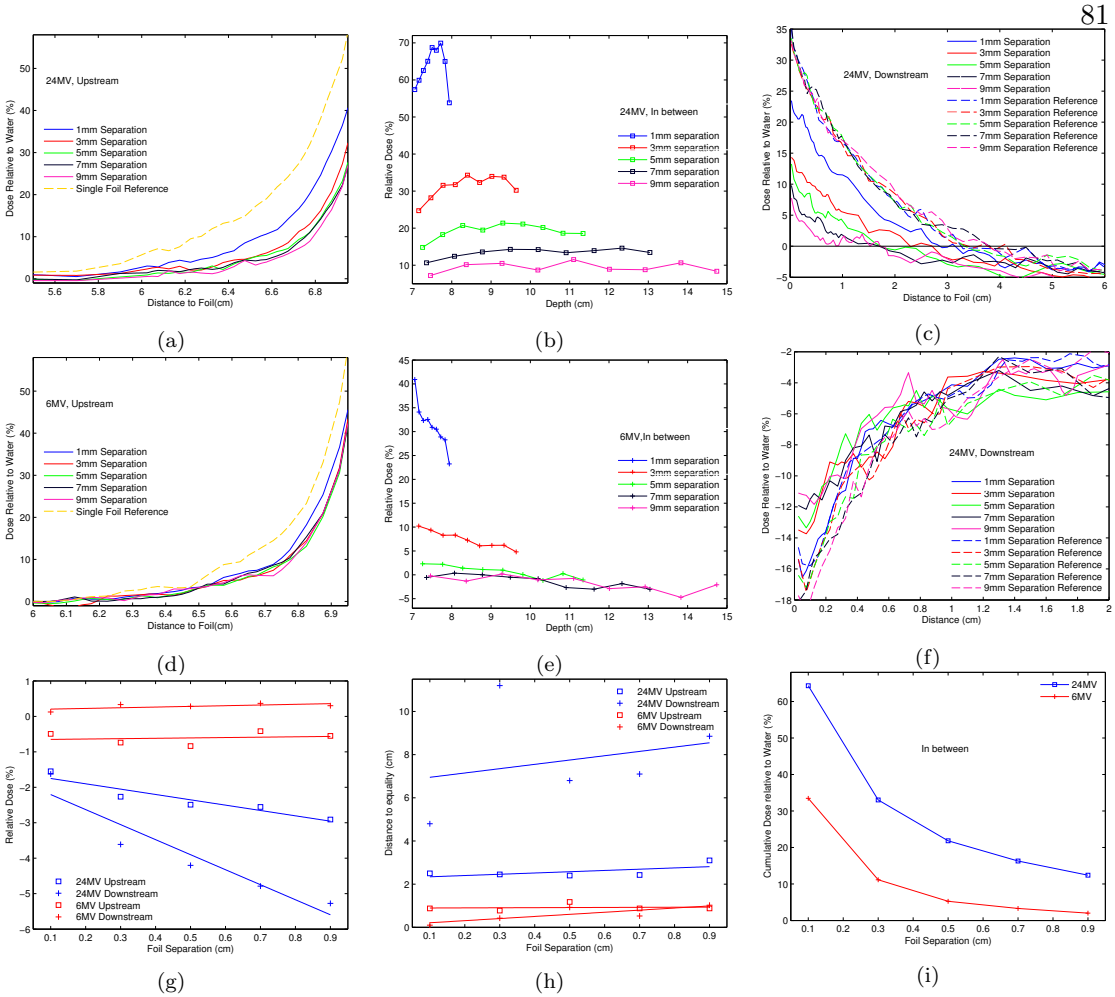

Figure 4.8 – The effect of foil separation on dose around distributed foils irradiated with 24 MV or 6 MV photons. The first row shows the (a) upstream, (b) midpoint between each foil and (c) downstream dose distribution relative to water respectively for 24 MV while the second row is the 6 MV case. (g) The relative cumulative percentage dose difference compared with the single foil reference. (h) The distance over which the distributed foil dose differs from the single foil reference. (i) The % enhancement in the cumulative area under the curves for the regions between the foils.

4.3.3.3 Effect of Energy

Increasing the photon energy increased the upstream dose for the distributed foils and increased the dose difference between the distributed foils and the single foil reference (Fig. 4.9a). The upstream range of dose difference increased steadily with the energy

(Fig. 4.9e). The relative cumulative upstream dose also decreased steadily with increasing energy (Fig. 4.9d). Downstream of the foils, the higher energies (Fig. 4.9c) had the largest dose reduction and the largest range in dose difference. Particularly, energies of 15 MV and above had sizable dose range difference while lower energies had minor changes.

Decreasing the photon energy resulted in a decline in the dose distribution in between the foils. At high energies, the dose peaked in the center, then at medium energies the dose was more even then at lower energies the highest dose moved towards the initial foils. The cumulative area in between the foils increased however with increasing beam energy (Fig. 4.9f).

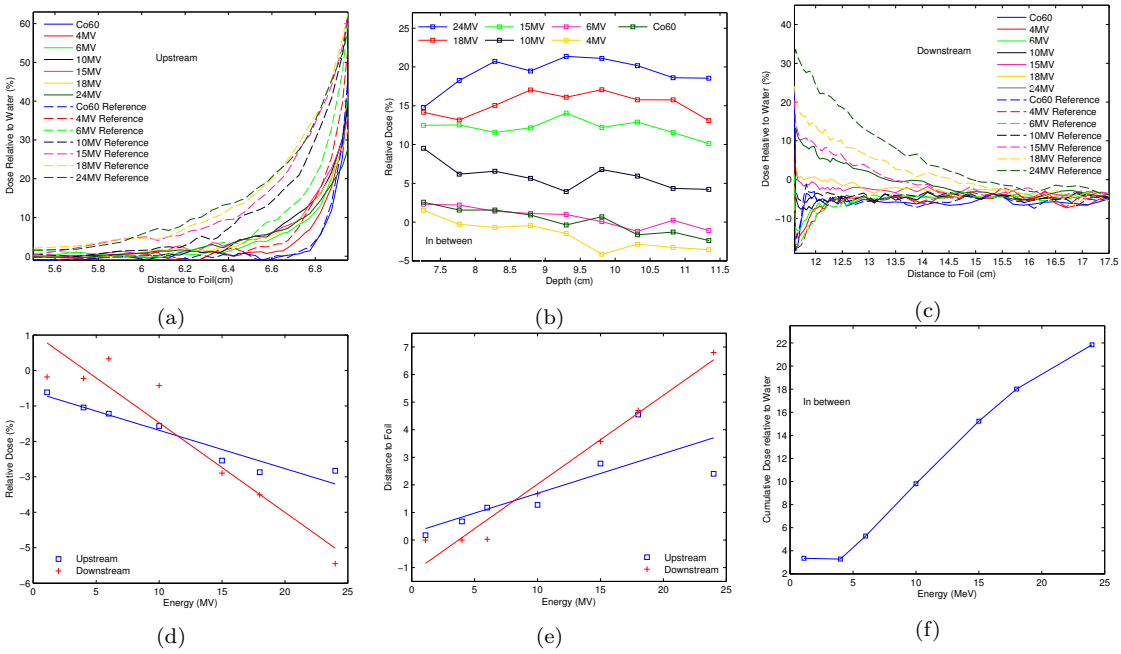

Figure 4.9 – The effect of beam energy on dose around distributed foils irradiated with various photon energies. The first row shows the (a) upstream, (b) midpoint between each foil and (c) downstream dose distribution relative to water respectively. (d) The relative cumulative percentage dose difference compared with the single foil reference. (e) The distance over which the distributed foil dose differs from the single foil reference. (f) The cumulative dose in between the foils. The energies used were 24 MV, 18 MV, 15 MV, 10 MV, 6 MV, 4 MV and Co60.

4.3.3.4 No Pair Production

When pair production was disabled, the %DD curves showed that there was very little forward scatter from each of the foils (Fig. 4.10b). The minimum doses in-between the foils had a slight curvature with a relative dose maximum in the center, while the pair production free curve had a slight curvature with a relative minimum dose. The dose reduction after the distributed foils was less than the single foil (Fig. 4.10b). In the single foil case, the effect of no pair production is even more pronounced. Figure 4.10f shows the range for which there is a dose difference downstream between the reference foil and distributed foils with no pair production. Under normal simulation conditions, the pattern is similar where the doses in both the reference foil and distributed foils have the same dose after some distance from the foils.

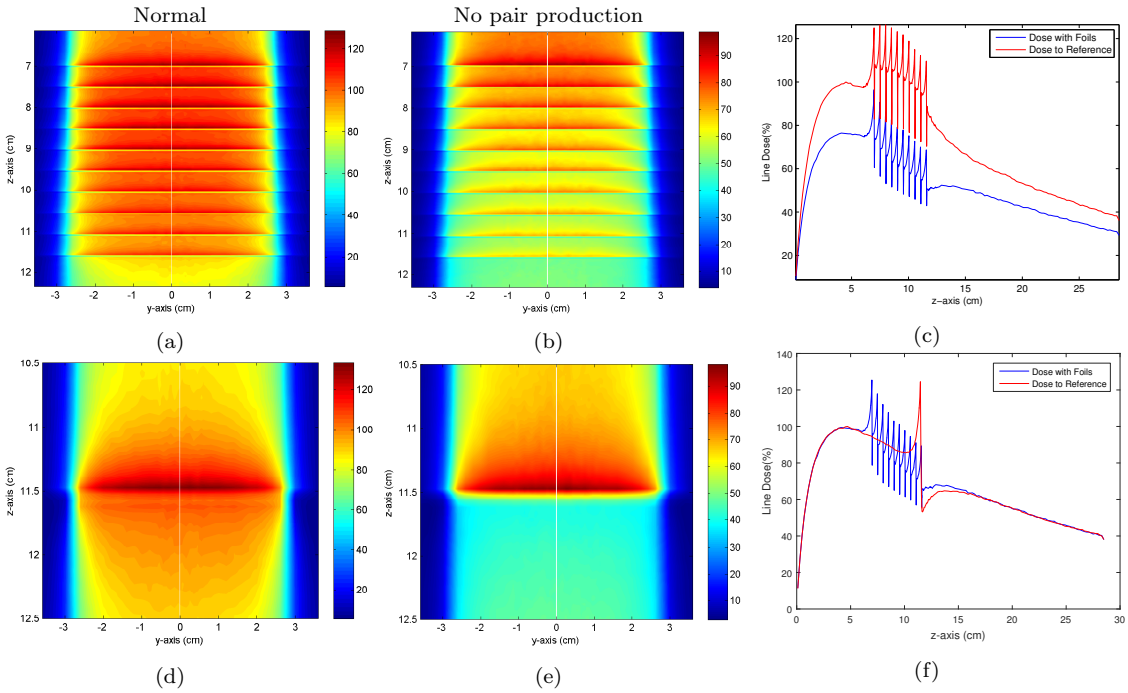

Figure 4.10 – The effect of pair production on distributed foils. (a) Shows contours for distributed foils and (b) pair production turned off. Similarly, (d) and (e) represents the single foil case. (c) Shows the %dd of the 10-foil configuration and that of the same configuration with the pair-production turned-off. (f) shows %dd for the single foil and distributed foils with pair production turned off. The beam energy was 24 MV and all numbers are in %.

4.4 Discussion

4.4.1 Two Foils vs Two Single Foils Combined

For the foil arrangements with close separation, the combined single foil dose was sometimes different from the two foil in a particular region. The dose difference between the foils indicate that backscatter from the second foil reaches the first foil in the two foil configuration. This can also lead to increased bremsstrahlung and thus increased dose. High-energy bremsstrahung x-rays tend to go in the direction of the electrons but the dose deposit has a range because it has a spectrum.

Another reason for the dose difference is more attenuation occurring in the two foil configuration than the single foil configuration. In region A, when the two foil configuration is compared to the upstream single foil, the dose is basically the same. Similarly, when the two foil configuration is compared to the two combined single foils for region C, the dose is comparable. When the dose enhancement range in the forward and backward direction is larger than the foil separation, then a dose difference is observed between both configurations. Despite having a difference in maximum dose, the dose distributions were very similar. In this experiment, foil separations of 7mm and large had an acceptable average dose difference of less than 2%.

Using the dose around a single heterogeneity to generate the dose around distributed heterogeneities can result in significant time savings since each patient configuration would not need to be simulated. We should be careful when trying to add single heterogeneities together but at the end of the day this might not matter. If the delivered dose is higher than the dose to water and less than the normal tissue complication limit, then it is advantageous to use this approach. Even if the dose is not exactly correct, the patient is not at risk of receiving too much dose. If clinicians are not comfortable with this approach, then the materials could be arranged in a body-centered cubic manner such that there is less overlap. Worst case, the attenuation could be factored in to get a more correct dose distribution. For perspective, exact dose values from nanoparticle based enhancement is not realistic and is also subject to errors.

4.4.2 Effect of shape of high-Z material on dose

Both the foils and markers produced significant dose increases near the heterogeneity. As expected, the dose and the amount of pair production from the foils were larger than from the marker. For both the markers and foils, pair production always seem to increase dose in the forward direction. This was also instructive in understanding the difference in dose distribution for low and high energies.

I think that both foils and markers could be candidates for dose enhancement based

therapy. Multiple foils can be arranged in various ways to provide the desired dose between the foils. Overall, the vertical orientation is recommended for general dose enhancement. Inserting the foils vertically into the tumor bed is easier and gives a more even dose. One would need to account for the direction of the foils during treatment, but this is easier with real-time imaging. Even if there are imaging artifacts, the foil direction should still be attainable. Arc treatments could also be used to take advantage of backscatter dose in either direction.

The foils might also have applications in shielding critical organ downstream. As we saw earlier, in horizontal configuration, the dose increase is mostly from backscattered electrons. At the appropriate energy, the downstream dose is reduced significantly. The foils are also flexible so they could be bent to fit surfaces. One issue that still needs to be addressed is how to keep the foils from moving. This could also be a significant challenge that some people may not want to deal with but the possibilities cannot be ignored.

The main advantage of markers is that they are already approved for use in the body. Markers can also have grooves that should prevent migration and should be cheaper than foils. The markers could be manufactured to have various lengths depending on the application. The suggested dimension would be around 0.8-1mm long with a 0.8mm diameter. This would reduce the cost, reduce directional effects but still be large enough to handle. Technologies and techniques from brachytheraphy could easily be adapted to facilitate implantation.

Long term study of patients with shrapnel and markers should be evaluated to better understand material migration. Depending on where the metal is, migration might not be a factor and the body's reaction to the presence of foreign materials include encapsulation which can allow long term inertness of the metal [104].

4.4.2.1 Polymer Gel Selection

Based on these results, I decided to use the foils for the polymer gel measurement. There were several reasons for this. The main reason was that the dose from the foils was much larger than the dose around the markers. The others were logistical reasons connected with the experiment. One of these was the resolution on the MRI. A smaller object is harder to see and requires a higher resolution which means more noise. A marker is much more difficult to control and suspend than a foil.

4.4.3 Dose Modulation with Multilayer Foils

The Monte Carlo simulation results showed it is possible to modulate the dose distribution by distributing the foil. This was accomplished while limiting the range of downstream and upstream dose deposition. When compared to the single foil, the majority of configurations resulted in lower or comparable doses upstream and downstream. In situations where you need to ensure no dose increase occurs downstream, then using a low energy configuration where electron equilibrium is lost might be useful. The backscatter electrons will give increased dose upstream and reduced dose after the last foil.

The results confirmed that the dose is the same for both the reference and distributed foils far downstream. Even if the dose is the same far from the foils, we need to be careful if the region of interest (ROI) is near the foils. The lower dose increase near the foils for distributed foils compared to a single foil means that it might have applications in shielding in confined spaces. We note that the slope of both curves are the same, indicating that both curves have the same energy.

Some of the patterns observed are the same as in chapter 3. Increasing energy and decreasing separation increased the dose in between the foils. The midpoint measurement for upstream and downstream measurements followed the same pattern indicating again that depth does not affect the dose. It is clear that backscatter or reflection is

the main contributor in reducing dose downstream. Generally, the 6 MV case showed much less difference between the distributed foils and the reference foil. Downstream, however, both distributed and reference foils consistently had less dose when compared to homogeneous water.

4.4.3.1 Foil count

By increasing the number of foils, it is possible to create a wider region of increased dose with a more even distribution than simply using two foils of equivalent thickness. One consequence of this is that the average dose between the foils decreases. This is not necessarily negative since any change in dose above 10% is considered to be clinically significant. It was observed that the dose between the foils increased with the depth up to a certain point, then started to decrease after that. The shift in maximum dose is perhaps caused by differences in depth required to reach the equivalent foil thickness at which equilibrium begins to be lost.

Multiple foils decreased interactions between particles traveling in the forward and backward directions in comparison to the single foil case. The upstream dose is primarily from back scattered electrons and so a thicker foil would allow more electrons to be generated. In the downstream region, significant dose reductions were observed compared to the single foil. We note at this point that the same amount of water and lead have been traversed by the photons. In between the foils, the cumulative dose decreased relative to water. Even though the cumulative dose in-between the foil increased with foil count, the cumulative dose from the corresponding homogeneous region increased at a faster rate.

Distributing the foils mean that there is a higher chance for proper increased dose coverage. Thinner foils might even be desirable in some situations. Thinner foils are also useful if higher photon energies are not available or desired. Higher photon energies can leave a larger range of increased dose that might extend to unintended regions downstream. Thinner foils are more malleable and can be curved to suit the intended

target. This might complicate the treatment but L-shaped configurations would minimize migrations and take advantage of the horizontal and vertical dose distribution.

4.4.3.2 Separation

Increasing the separation also resulted in a more even distribution of dose between the foils. The smallest separation had the most dose in the 24 MV case. The high dose region was shifted slightly off center and resulted from the combined dose influence of foils above and below the center.

For the smallest separation, dose distribution above and below the foils were most like the reference configuration. Increasing the separation had little effect on the upstream dose. Generally, backscatter from the deeper foils did not influence the upstream dose except for the 1 mm separation setup. The dose from the 3 mm separation in the 24MV case was also slightly elevated compared to the higher separation cases. In region C, there was a clear reduction of dose for the larger separations. Since the the difference in energy has to go somewhere, it must have been redistributed over a wider range upstream of the last foil. This is very important for reducing the dose downstream.

4.4.3.3 Energy

All configurations except Co60 beam had some difference in the dose upstream and downstream. The majority of the energies also had the midpoint dose that decreased with depth. This resulted in less forward scatter for lower energies.

4.4.4 Effect of Pair Production

The effect of pair production was evident in the dose distribution of all the configurations evaluated. At first it was surprising to see the vast majority of the pair production dose in the forward direction but this makes sense. If the photon has a lot of energy then the electron and position that is generated will go in a similar direction as the initial photon and they both deposit energy near the point of creation. The two photons created from

annihilation, however, are isotropic will generally deposit the energy further away from the point of creation. With that said, the low energy configurations did not seem to have more spread in pair production dose compared to the higher energy configurations.

If the majority of the pair production dose is in the forward direction, then the backscatter electrons must be from some other interaction. When Compton effect was disabled the dose difference was too large to make conclude anything about the distribution of dose. Disabling photoelectric effect was not pursued.

4.5 Conclusion

The dose from combining two single foils was compared to two foil simulations and found to be very close. When the foils were close together, dose differences occurred because of attenuation and additional dose enhancement. Foils arranged vertically had a larger dose difference than horizontal foils and high energy configurations had a larger difference than low energy configurations. These are differences that can be accounted for and corrected. This showed it was possible to determine the dose from multiple heterogeneities by using the dose distribution of one heterogeneity.

We looked at how the shape of the heterogeneity can influence dose by comparing the dose between a foil and a marker. The foils generated more dose than the marker but the marker has multiple advantages over foils. More research is necessary to obtain the ideal dimension for the marker. After reviewing the data, a foil configuration was selected for polymer gel dosimetry.

We also looked at the degree of dose enhancement around multiple thin lead foils. We conclude that it is possible to modulate the distribution of increased radiation dose by using multi-layer foils. Increasing the number of foils reduced the minimum dose between the foils but distributed the dose over a larger area. It also decreases the range of increased dose relative to the single foil. Increasing separation decreases the upstream and downstream dose. Energy had the largest effect on the distribution, with higher

energies having more reduced dose compared to the reference configuration. The exponential decay approach to determining the dose downstream of multiple heterogeneities can be affected by the distribution of the heterogeneities. The equation is does not account for electrons and is thus only valid at distances larger than the range of the electrons generated in the heterogeneities.

Chapter 5

Phantom Material Evaluation

5.1 Introduction

The second phase of this project was to investigate the feasibility of measuring dose in the vicinity of a high-Z material with a polymer gel. This section is divided into two parts. The first part was where I investigated different polymer gels, various embedded materials and tried to optimize the configuration. The second part is where I did a chemical compatibility study to make sure there weren't any adverse chemical reactions. Much of the work in this chapter was done in conjunction with the work in chapter 6.

There are many factors that can affect the performance of a polymer gel dosimeter (PGD). Ultimately, these factors depend on the gel components, composition, and the manufacturing process. All polymer gels have the same basic components. They need water, a source of monomers, a binder material, oxygen scavenger and sometimes a cross-linker. The use and amount of additional chemical modifiers can be adjusted to obtain the desired characteristics. From a clinical perceptive, the polymer gel is expected to behave reliability over different energies, dose rates, among other factors. Much of these have to do with general purpose applications and convenience; however, they need to be addressed before polymer gel dosimeters can enter routine clinical use. The

objective was to identify a suitable gel for the application based on available materials and sensitivity among other factors.

5.2 Gel Requirements

For this project, much of the gel evaluation criteria for clinical situations were not critical. I limited the evaluation to sensitivity, stability and tissue equivalence. Other factors such as dose rate and energy dependence were not critical since it was easy to keep those factors within an acceptable limit for my application. If an energy dependence exists for instance, we simply need to have different calibration measurements for each energy. Chemical hazards, ease of manufacture and clarity, for instance, were considered but were not deciding factors.

5.2.1 Sensitivity

Sensitivity is very important, but it is also the most variable since it is likely coupled to other parameters. It is known for instance that making a gel more solid can also translate into lower radiation sensitivity and in some cases increasing the amount of monomers decreases the solidity [105]. The expected dose enhancement from irradiation of high-Z materials at high energies is significantly less than compared to low energies and the spatial range of enhancement is on the order of millimeters. The ability to resolve dose gradients is paramount to the evaluation of the dose. However, the gel should not be too sensitive. If it's too sensitive, then polymerization may be initiated prematurely by light or heat.

5.2.2 Solidity

Since the edges of the container would not receive radiation, it was vital for the edges of the gel to be mechanically strong enough to support the increased density of the gel center. When the gel is placed horizontally and undergoes a high-resolution MRI scan,

the scan time along with MR heating might cause portions of the gel to melt, affecting the spatial and dosimetric integrity of the gel. The gel would need to be solid and not just rely on hydrogen bonds to maintain solidity. This requirement would also address the issue of polymer gel storage.

One of the lingering problems of polymer gel dosimeters is the variation of dose response due to variations in temperature history [84]. A typical polymer gel is stored in the refrigerator to maintain the gel state and it is brought to room temperature before irradiation and imaging. The difference in cooling rate for the smaller calibration vials and the larger phantom results in differences in dose response. The deviations are not reproducible, making it difficult to model and introduce a systematic error. Various attempts have been made to provide a reliable method of correction, but it is still a source of error [106]. If the gel is solid at room temperature, then refrigeration is not needed and variations introduced by cooling and warming can be minimized. Some amount of effort was spent on this aspect.

5.2.3 Tissue Equivalence

One of the advantages of polymer gels is that they consist of mostly water. This makes it very likely to be within the norms of tissue equivalency, however, it needs to be confirmed. Significant deviations from tissue equivalency will result in significant differences in the measured and predicted dose.

5.3 Gels Evaluated for the Study

The most likely source of dose response variation in polymer gels is the gelatin. The other components are well characterized and are used in industrial processes reliably. Gelatin, however, is less standard, being very dependent on the collagen source and the process used to create it. Gelatin is a mix of peptides and proteins. This explains why temperature history is important. Even though gelation is thermoreversible, it does

not mean that the gel moves between two exact states of liquid and gel[85]. Gelatin is susceptible to thermal and enzymatic hydrolysis depending on the environment[107].

Gelatin has many of the desirable characteristics for this dosimetry and we would be hard-pressed to find a better alternative. Depending on the dosimeter type, gelatin or some other matrix is actually required for polymerization. When de Deene evaluated nMAG without gelatin, no dose response was observed[87]. This indicates that gelatin not only holds the precipitated polymethacrylic acid in place but also plays a role in the initiation of polymerization. This might be from cross-linking with the methacrylic acid (MAA) or from chemical changes in the solution introduced by the presence of gelatin. PAG based gels using bis, however, don't need gelatin to respond to radiation [108].

In contrast to polymer gels, film, which also contains gelatin, is much less susceptible to reproducibility issues. With film, a single calibration curve is required for a particular type of film. Two observations from film manufacturing are that film does not require low-temperature storage and that high temperature cross-linking is used to get a permanent gel. Therefore, I hypothesized that the difference in dose response between calibration vials and the phantom can be reduced significantly by removing the need for low-temperature storage.

It is known that gel strength is dependent on gel concentration, the intrinsic gel strength, environment pH, temperature, cooling rate and the presence of additives[85]. Slow cooling, for instance, results in higher melting points because more time is allowed for better orientation of the gelatin molecules resulting in stronger junction zones[109].

Various groups have noted increased polymerization with THPC. This is in agreement with early gelatin researchers who regarded THPC to be foremost a cross-linker [85]. Jirasek et al. proposed several reaction schemes for THPC[110]. The most likely reason for increased polymerization is the release of the small amount of formaldehyde remaining from manufacturing.

In the next section, we explored different gels and incorporated some of the above principles into the procedure. The goal was to have a gel that was solid enough so

that it did not require refrigeration to maintain the solidity. We kept in mind that the container would be filled, minimizing any risk of movement. We began by focusing on the core components, then, if necessary, looked at additional cross-linkers. I did not discuss the other characteristics because it was more clear how to achieve those.

5.3.1 Evaluation

Four kinds of polymer gels were evaluated: PAGAT, MAGIC, nMAG and MAGAT. Various compositions of each gel were fabricated, irradiated, and imaged, and the general suitability was evaluated. The volume of the test samples ranged from 100ml to 500ml to evaluate the effect of small variations in the composition and overall repeatability. The final compositions evaluated are detailed in Table 5.1

Table 5.1 – Final composition of various polymer gels tested. In percentage by weight unless stated otherwise.

Component	PAGAT	MAGIC	nMAG (THPS)	MAGAT (THPC)	Formula
Gelatin (300 bloom)	6	8	10	10	$C_6H_{12}O_6$
Water (Deionized, Millipore filtered)	88	82.8	83.37	86.98	H_2O
Ascorbic Acid	-	0.352	-	-	$C_6H_8O_6$
Hydroquinone	-	0.2	-	-	$C_6H_6O_2$
Methacrylic Acid	-	8	6	3	$C_4H_6O_2$
Copper Sulphate	-	0.02	-	-	$CuSO_4.5H_2O$
Acrylamide	3	-	-	-	C_3H_5NO
N,N'-Methylenebisacrylamide (Bis)	3	-	-	-	$C_7H_{10}NO$
THPC	5mM	-	-	1mM*	$C_4H_{12}ClO_4$
THPS	-	-	2.5mM	-	$C_8H_{24}O_{12}P_2S$

*Recommend 2.5mM

5.3.2 Acrylamide Type

A PAGAT gel was evaluated due to its popularity and desirable clinical characteristics. Overall, the gel did not perform very well for the compositions we used. It seemed

to have significant issues with the oxygen effect, requiring large doses to react. When it did respond, the edges were sharp indicating a threshold below which no response was seen. One good characteristic was that it did not experience polymerization pre-irradiation. It took much longer to fully dissolve the bis and acrylamide than expected. The gel was clear, which made it easy to see inside, but the manufacturing difficulties and weak dose-response left much to be desired. Perhaps it required more THPC, but after several attempts, the decision was made to abandon that gel. Not much time was spent evaluating the gel since theoretically it was way less sensitive than methacrylic acid-based gels. The chemicals were also more toxic compared to methacrylic based gel, hence, there was the issue of disposal.

5.3.3 Methacrylic Acid Type

The first methacrylic acid gel evaluated was the MAGIC polymer gel. This gel was particularly difficult to make due to significant variations in the sensitivity. Sometimes high doses were required to respond, but more often polymerization began before irradiation. Though some fogging was expected, the amount of polymerization varied with each experiment. Fogging, in this case, was not ideal because it made a visual inspection of the contents of the jar more difficult. A major part of the inconsistency was the low amount of copper sulfate, particularly in small batches. Small variations of copper sulfate and ascorbic acid produced wide variations in gel sensitivity, which in turn caused variations in the effectiveness of the oxygen scavenging. The need for a catalyst was another source of unnecessary variation and the decision was made to move to a single component oxygen scavenger.

Both THPS and THPC were investigated as oxygen scavengers and immediate improvements were observed with regard to oxygen effects. They both worked reasonably well, so we did a test to see which scavenger resulted in a stronger gel. The test was straight forward. The amount of chemicals was similar, 1 day after manufacturing at room temperature, the gels were rotated to see which type had less movement. In this

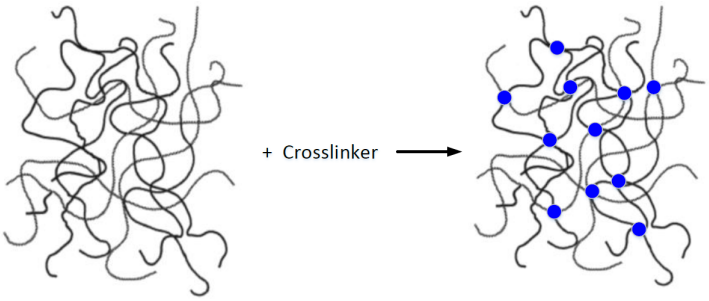

Figure 5.1 – Gelatin cross-linking to maintain structure

test, the THPS produced a more solid gel so the decision was made to use nMAG. Note that the THPC based gel is called MAGAT.

5.3.4 Improvements

The following improvements were made to the manufacturing procedure. Decreases in pH significantly affect the gel strength as confirmed by the reduction of melting temperature after the addition of MAA. The amount of gelatin was increased to 10% weight to address this issue. The increase in gelatin also translates into an increase of gel sensitivity and a reduction of the effect on pH. I decided to split the THPS in half and apply half to the gelatin to cross-link it before it came into contact with the MAA. The pH of the MAA was also increased by dissolving it in 50% of the water to make it closer to the pH of the gelatin After 30 seconds the MAA was added. After two minutes, the remaining second half of THPS was added for oxygen scavenging. Adding the THPS in two parts led to a much stronger gel compared to not splitting the THPS. Fig. 5.1 demonstrates the strategy for cross-linking.

The optimal time gap between the addition of the first half of THPS and the addition of MAA needs more investigation to better characterize the response. It was observed that taking too long to add the MAA resulted in immediate solidification when it was eventually added. This formed an irreversible gel that was unusable and occurred if we waited for more than around 50 seconds. The gel was not polymerized in the sense that

no visible change in opacity or density was seen, but the gel was no longer liquid. It formed a clear, strong, rubbery, solid gel that did not liquefy when the temperature was raised. By varying the time gap before the addition of MAA, it is possible to get various gel strengths without the need and complications of additional cross-linkers. The proper division of THPS should also be investigated to determine how much cross-linking is necessary for the application while ensuring that enough oxygen scavenging occurs. The exact temperature for cross-linking needs evaluation as well. The set temperature for 10% wt gelatin solution is 35C so there is a lower limit at which this can be done. Cross-linking at a lower temperature might be better[107] but additional chemicals needed to be added. Hence, I did not want to be too close to the set temperature.

Due to the rapid chemical changes in the gel after THPS, time rather than temperature was chosen as the metric. Temperature changes vary based on the volume of gel, container shape and even equipment being used. We used a custom water bath with a motorized overhead stirrer for large batches but traditional water bath and stir plate for smaller volumes.

There are a number of possibilities as to why waiting too long to add MAA results in solidification. After THPS is added, the gelatin begins cross-linking and consuming any dissolved oxygen. This continues until the addition of MAA where the processes are interrupted. One possibility is that the addition of monomers to the low oxygen gel mixture in the presence of light, heat or free radicals from gelatin increases the likelihood of self-polymerization. The fact that it does not occur until the monomers are present indicates that it is due to polymerization, but visibly it is inconsistent with ionizing irradiation. The difference in energy between visible light and ionizing radiation might be a factor, but polymerization from light and heat also resulted in fogging, which makes it less likely. Another reason is that the gelatin is just heavily cross-linked and a small amount of MAA is necessary to solidify the gel. We should note that the solidification was so quick that much of the MAA did not mix with the gelatin-THPS mixture. Microscopy and Fourier Transform Raman spectroscopy should

be able to shed light on what it is going on, but this is left for future research.

Some time after the discovery that separating the THPS in two resulted in increased strength, I decided to re-evaluate THPC (or MAGAT) with this procedure. The sensitivity with 6% MAA was significantly higher than with THPS. To compensate for this, the amount of MAA was reduced to 3%. One consequence of this was that the gel was significantly clearer than the nMAG gel.

An oxygen diffusion test was also done with THPS and THPC to compare the effectiveness of the oxygen scavenging abilities, to look at the overall sensitivity, and to fine-tune the compositions. For this experiment, various gel compositions were poured into calibration vials leaving a 1-inch gap and no gap. They were left for 24 hours then the gels were irradiated. In general, the nMAG with the air gap had regions of no response closest to the air cavity followed by a transition area of higher polymerization and a region of the normal response. The dosimeter responded normally when air gap was minimized. It was observed that increasing the amount of THPS resulted in decreased sensitivity in the gel. For MAGAT, no transition zone buildup was observed, but there was a longer zone of no response followed by a normal response. Reducing the THPC resulted in a reduction of sensitivity. The response zone of the THPC was higher compared to THPS. The no response zone with THPC was also longer than with THPS but roughly the same when the buildup region of the gel using THPS was included. The decision was made to reduce the amount of THPC since the gel responded well with the lower amount.

5.4 Foil Support Selection

To measure the dose around the foils, the foils need to be properly suspended. There are several requirements for the support fixtures. Perhaps one of the more important requirements is the ability to customize the position of the foils. This would allow last minute fine adjustments to be made to the fixtures. Similar to the gel, the material

should be as close to tissue equivalent as possible. It should be relatively cheap. The solid nature of the gel would make it more difficult to clean the material completely so all parts except the foils are single use. The ideal solution would be to machine the parts from solid water or another water equivalent solid material, but that would be very expensive. The clearance for the cantilevers would also be a significant challenge. This limited the use of custom machining. The strategy was to identify materials that could work and moved on if they performed satisfactorily. If the material failed in some area, then the search continued. The goal was not to find the ideal material for the job.

Recently, there has been increased interest in using Acrylonitrile Butadiene Styrene (ABS) and 3D printing in radiation oncology [111, 112]. Previous applications have been limited to mostly making phantoms, but the decision was made to use this approach. More specifically, ABSplus™ is a proprietary material from Stratasys (Eden Praire, Minnesota) that is stronger and more stable than ABS. It is a production grade thermoplastic that gives the ability to print thin layers of material while being strong enough to work with. Not only did 3D printing minimize waste, but it facilitated rapid prototyping and reduced the time to reach a satisfactory design. Rather than print all the parts, a high-density polyethylene (HDPE) rod was chosen as the central support pole. Using this would reduce the cost and time to print the fixture while allowing smoother adjustments when coupled with the ABSplus™ cantilever parts.

The gel container needed to have three important characteristics. It needed to be a wide mouth jar that was wide enough to allow the passing of the entire fixture. The second requirement was that the base of the container needed to be flat. This would allow proper attachment of the fixture to the base of the container and provide a flat base for depth dose measurements. The third requirement was that it would be large enough to facilitate depth dose measurement inside the container and have enough room around the edges to avoid any issues with oxygen from the walls. Ideally, a Barex®, PET or glass container would be used. Barex as mentioned before, is oxygen impermeable and is ideal for gel phantoms. PET and glass are generally chemical resistant and

less susceptible to oxygen diffusion. Multiple searches, however, did not reveal any containers that met the requirements and was within budget. The decision was made to use a large polystyrene container with the condition that the container was wide enough to avoid oxygen diffusion near the walls.

Lead is very similar to gold. So, the decision was made to use lead. This would significantly reduce the cost and give us the freedom to dispose of the foils if necessary. In our initial experiments, foils were suspended by a tape only at the edge of the square foil putting the lead in direct contact with the polymer gel. No reaction was expected since MAA is a weak acid. This was also supported when no visible changes were observed after adding the gel and at inspection before irradiation. After irradiation and imaging, the region of increased R2 was much larger than expected. The results were not inconsistent with the predicted result and it was repeatable. During one manufacturing session, the room light was on as the gel was added and a cloudy mist was seen moving away from the region of interest. Testing revealed that the foils were the source of the cloud, which was the material in the thin protective oxide layer around the metal. The reaction looked similar to what would be considered normal fogging as expected from light polymerization. Hence, this would have been undetected. Figure 5.2 shows sample images from testing. Figure 5.2b shows a foil that was submerged in 6% MAA solution for 60 seconds then with a drop of acid place at the top. In Fig. 5.2c, the foils were submerged for 3 days resulting in a lighter, shiny surface.

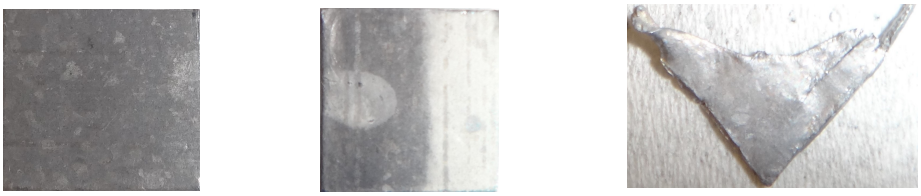

(a) (b) (c)

Figure 5.2 – A lead foil that was (a) not expose to MAA, (b) dipped for 60 seconds and had a drop on the top and (c) left for 3 days.

One solution to preventing the reactions from the foil was to use some acid to pickle the metal. Placing the foils in 6% MAA solution removed the oxide layer as

demonstrated above. The disadvantage of this approach was that it was not clear what acid concentration was required and how long it must be submerged in the acid solution to remove all the coating. If the metal was exposed to the acid for too long, then the metal surface ion integrity could be affected. If the residual oxide layer was not fully removed, then it could influence the measured dose. More extensive testing would be required to determine the optimal procedure. To solve this problem, in later experiments we completely enclosed the lead foil with 3M™ Polyester Tape 8991. The polyester tape was chosen because of its suitability for high-temperature applications, its thin thickness (0.06mm) and chemical resistance. Other tapes being considered were much thicker and had a stronger glue making it less flexible and more difficult to work with.

Every effort was made to exclude unnecessary material from the region of interest. The tape and ABSplus™ were closest to the foil and were exposed to the direct path of the radiation beam. Simulations looking at the effect of ABSplus™ indicated that the effect on dose was minimal relative to water. In either case, enough spacing around the foil was provided to ensure that ABSplus did not interfere with the measurement. The tape could not be avoided and is not expected to interfere significantly with dose.

5.5 Effective Z and Density

One of the main advantages of PGD is the water equivalence of the dosimeter. The closer the PGD is to water, fewer perturbations exist and the dose response is more likely to reflect the dose response in water. Two ways to evaluate this is to determine the effective Z and the density. The effective Z depends on energy. The Auto Zeff software (version 1.7) [113]was used to generate the effective Z of water, nMAG, MAGAT, MAGIC and PAGAT dosimeters. Fig. 5.3 shows the relative effective Z for the dosimeters up to 24MeV. We can see that PAGAT is the most water equivalent with a relative effective Z of 1.013 at 18MeV. The MAGAT, nMAG, and MAGIC had relative values of 1.015,

1.018, 1.01775 respectively. Therefore, all of these materials can be considered tissue equivalent.

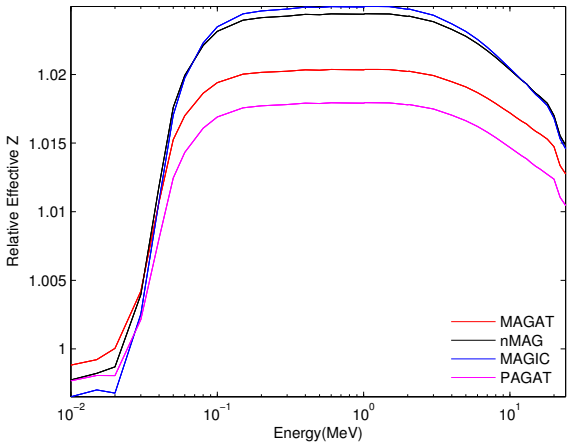

Figure 5.3 – Effective Z relative to water for various polymer gels.

Another way to evaluate equivalence is to look at the density of the material. This can also help when exact compositions for a material are not available. In my case, neither density nor a chemical formulation was available for the polyester tape and no density data was available for the custom polymer gels. The most straightforward method of finding density was to use a CT imaging approach. There is, however, no direct relationship between CT number and density. When tissue equivalent material is imaged with diagnostic energies, the primary interactions are by photoelectric, Compton, and Raleigh scattering. The photoelectric interaction depends on Z while the other two are independent of Z. This makes it difficult to assign the attenuation coefficient μ. This can be overcome by generating an HU calibration curve. By imaging objects of known density, it is possible to generate a piece-wise linear curve. The resulting curve is unique, however, to the scanner and tube voltage [114]. CT images of the gel and embedded materials were obtained using the Phillips Big Bore at the University of Minnesota, Fairview and the calibration curve was derived from its commissioning data. The CT scans were only performed for nMAG and MAGAT. Fig. 5.4 shows the

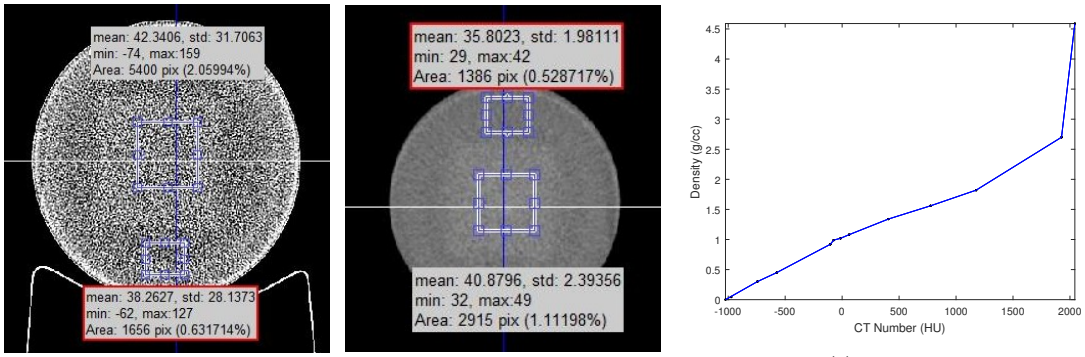

(a) (b) (c)

Figure 5.4 – CT Image of (a) nMAG , (b) MAGAT and (c) the ramp used to convert CT values to density.

CT images of a nMAG and MAGAT phantom in the ATOM-PG program (see section 6.2.4). The average CT numbers were 38.26 and 35.8 which reveals an average density of around 1.062 and 1.05984 for nMAG and MAGAT respectively. This is well within the range of accepted tissue equivalent media. The polyester tape was also evaluated by a similar process, but it was not possible to distinguish the tape from the surrounding material. The combined thickness of the tape was 0.12mm which was much smaller than the thickness of the CT slice. The fact that the material is very thin and it does not show up on the image is a good indication that it does not have a significant influence on the dose measurement. This might also be an indication that the tape density is very close to that of the gel. For the purposes of comparison, the HDPE rod was evaluated and found to have a density of 0.929, which is in agreement with published data.

Table 5.2 summarizes the material densities involved in the PGD experiments. All the materials that are in the area of interest have a density within 5% of water.

Table 5.2 – Density of Materials

Material	Mass Density	CT Density
Polystyrene	1.05	-
ABSPlus™	1.04	-
HDPE	0.93-0.97	0.929
Polyester Tape	NA	NA
MAGAT	NA	1.06
nMAG	NA	1.062

5.6 Chemical Compatibility

The reaction of the lead foils with methacrylic acid necessitates the need of chemical compatibility testing. Compatibility studies are useful because they can aid in the elimination process when multiple choice are available. The polymer gel would need to be compatible with any material which it comes into contact with for at least the duration of the experiment.

There are many factors that determine compatibility between materials. There are also just as many tests that can be performed to determine the effect if any by each factor. The scope of this study was limited to factors that can be easily evaluated and was limited primarily to visual inspection of the materials. Two primary purposes of the test are to make sure the supports are strong enough to hold the load within the environment and that the flow of particles from the support to the gel is limited if any. The primary criteria were color changes in the material or solution, changes in material strength and changes to the surface. Changes caused by support material diffusing towards the solution were especially important. We were less concerned if the gel chemicals diffused into the support or if it developed micro cracks as long as it did not weaken the structure during the experiment time frame. There was some flexibility with the materials, but that was also limited by other factors such as the density.

5.6.1 Methods

The test began by making representative solutions of individual chemicals and placing them in glass vials. The materials investigated were HDPE, ABSplus™, polystyrene, and tape. Gelatin was not evaluated and the result for lead foils was presented in section 5.4 . These materials were chosen because of their density and their use in earlier experiments. Samples of each material were weighed, and pictures of both the material and solution were taken. The materials were inserted into the solutions and covered. The samples were left at room temperature in the dark for 8 days except for about 3 hrs of room light exposure. The time frame was limited to the maximum possible processing time. Afterward, the samples were removed and compared to the pictures. The material combinations were deemed compatible if the following requirements were met. There were no visible signs of change (eg, precipitation, discoloration), the change in mass is no more than 10%, as well as several discretionary factors. The test of material strength was determined by pulling on the material and bending. If significant damage was observed in the experiment or in literature, then further experiment might be pursued or a specific test might be carried to out to observe the severity of the effect. This was also supplemented by a review of chemical compatibility charts from various online resources.

5.6.2 Results

Based on the existing literature, the several material combinations were deemed compatible. The results of the experiment are summarized in Table 5.3. Hydroquinone had a significant effect on ABS according to the two compatibility databases [115, 116] but this was not observed in our specific formulation. The hydroquinone and tape combination also resulted in a reduction in mass of the tape. Hydroquinone is also incompatible with polystyrene according to the several online compatibility databases but visible damage was not seen on the material. MAA and tape combination had a

higher than desired mass change of 10.29% and some color fading. The THPS and tape combination also had some color fading. The PAGAT gel components had no issues.

Table 5.3 – Compatibility Study of Gel Chemicals and Support Materials

Material Combination	Mass			Inspection		Conclusion
	Before (g)	After (g)	Change (%)	Material	Solution	
Hydroquinone / HDPE	1.102	1.097	-0.4537	nvc	ctlp	pass
Hydroquinone / PS	0.359	0.357	-0.5571	nvc	ctlp	D [115], pass
Hydroquinone / ABSplus	0.180	0.181	0.5555	nvc	ctlp	pass
Hydroquinone / Tape	0.054	0.052	-3.7037	nvc	ctlp	pass
MAA/HPDE	1.091	1.096	0.4582	nvc	nvc	pass
MAA/PS	0.804	0.803	-0.1243	nvc	nvc	pass
MAA/ABSplus	0.172	0.175	1.7442	nvc	nvc	pass
MAA/Tape	0.068	0.075	10.2941	sf	nvc	unclear
Copper Sulfate / HPDE	0.924	0.924	0	nvc	nvc	A[117], pass A-B[118], pass
Copper Sulfate / PS	0.404	0.401	-0.7425	nvc	nvc	A[117], pass
Copper Sulfate / ABSplus	0.168	0.172	2.3809	nvc	nvc	pass
Copper Sulfate / Tape	0.060	0.063	5	nvc	nvc	pass
THPC/HDPE	1.233	1.236	0.2433	nvc	nvc	pass
THPC/PS	0.375	0.374	-0.2666	nvc	nvc	pass
THPC/ABSplus	0.172	0.177	2.9069	nvc	nvc	pass
THPC/Tape	0.062	0.061	-1.6129	nvc	nvc	pass
THPS/HDPE	1.213	1.21	-0.2473	nvc	nvc	pass
THPS/PS	0.54	0.538	-1.1111	nvc	nvc	pass

THPS/ABSplus	0.172	0.174	1.1628	nvc	nvc	pass
THPS/Tape	0.068	0.068	0	sf	nvc	pass
Ascorbic Acid /HDPE	1.034	1.036	0.1934	nvc	nvc	pass
Ascorbic Acid/PS	0.604	0.604	0	nvc	nvc	pass
Ascorbic Acid/ABSplus	0.172	0.175	1.7441	nvc	nvc	pass
Ascorbic Acid/Tape	0.039	0.040	2.5641	nvc	nvc	pass
Acrylamide /PS	0.436	0.438	0.4587	nvc	nvc	pass
Acrylamide/ABSplus	0.141	0.142	0.704	nvc	nvc	pass
Acrylamide/Tape	0.064	0.064	0	nvc	nvc	pass
Acrylamide/HDPE	0.546	0.545	-0.1832	nvc	nvc	pass
Bis/PS	0.649	0.648	-0.1541	nvc	nvc	pass
Bis/ABSplus	0.172	0.173	0.5814	nvc	nvc	pass
Bis/Tape	0.082	0.082	0	nvc	nvc	pass
Bis/HDPE	0.589	0.589	0	nvc	nvc	pass
MAA (6%)/Tape (4 d)	0.099	0.109	10.1	sf	nvc	pass
MAA (3%)/Tape (4 d)	0.078	0.085	8.97	rf	nvc	pass
THPS/Tape (4 d)	0.09	0.089	-1.11	slf	nvc	pass

A - Excellent
B - Good
C - Poor, probably not suitable
D - Not recommended

nvc - No Visible Change
nda - Information not available

sf - some fading
rf - reduced fading
slf - slight fading
ctlp - clear to light pink

5.6.3 Discussion

The majority of combinations were compatible based on the definition outlined. According to the reference, hydroquinone has adverse effects on both ABS and Polystyrene. It might not be possible however to eliminate it fully. Hydroquinone is a stabilizer for MAA and prevents polymerization of the monomers while in storage. MAA includes a few parts per million of hydroquinone for this purpose. The decision to use ABSplus prevented the use of any gel that required high amounts of hydroquinone. It is possible to use the MAGIC gels without hydroquinone, but the ascorbic acid is not an adequate oxygen scavenger. The hydroquinone in MAA, however, did not have any visible effect on the polystyrene or ABS though this might depend on the amount proportion of MAA. One experiment using an 8.5%w/w MAA resulted in significant bleaching of the ABSplus™ in the gel. Lower percentages of around 6% did not display these features. The color change in the hydroquinone solutions occurred in all combinations and is likely from the destabilization of the hydroquinone solution with time[119].

The MAA seemed to have an impact on the tape, showing a sizable increase in weight after the study. This was slightly higher than the $\mp 10\%$ but in this case, the increase in mass was on the tape indicating that particles flowed from the chemicals. There was also a slight fading in the color of the tape, but no changes were observed in the MAA solution. The THPS-tape combination also resulted in some slight color fading but did not result in a change in weight. In all cases, the integrity of the tape remained intact and no sign of damage was seen.

Acrylamide is a suspected carcinogen, a severe neurotoxin, a reproductive hazard and teratogen that is easily absorbed through the skin (MSDS 2013) [120]. This makes it difficult to work with and dispose of, especially when there is a significant amount of unirradiated gel. Acrylamide-based gels have improved performance with regard to spatial integrity, temperature sensitivity, and dose-rate dependence compared to MAA type gels. For this project, we gave a fixed dose rate and a gel that does not use

refrigeration makes these advantages inconsequential.

Consequently, it was decided to use both nMAG and MAGAT gels to evaluate dose around the foil. An MAA type gel was chosen due to its significantly improved sensitivity compared to the Acrylamide-based gels. The MAGAT gel was found to have better material compatibility, better tissue equivalency and much better clarity than the nMAG. It should be noted that the compatibility study was done over 8 days where in reality, the average experiment duration was 4 days from manufacturing to scanning. The THPS/tape and MAA tape combination were repeated with a shorter time span and or lower concentration and the results were a bit lower. Inspection of the tape and materials after experiment did not reveal any issues. The color fade was less than observed in the previous testing. It is expected that any interaction while the materials are in contact with chemicals in solution will be significantly reduced in a solid gel.

5.7 Conclusion

Various polymer gels and compositions were evaluated. As the results, nMAG and MAGAT were selected for the dose comparison. The foil support materials were also selected and a chemical compatibility study performed between them. The results showed that the gel and fixture component are compatible for the time period of our experiments.

Chapter 6

Polymer Gel and Monte Carlo Dose Comparison

6.1 Introduction

Alkhatib et.al. postulated that the high energy photons should be able to enhance dose by means of increased electron-positron-pair production if the high-Z material is placed in water medium [35]. The idea was confirmed experimentally for two foils arranged in parallel where the foils are parallel or orthogonal to the beam axis. They used radiographic films to quantify the dose and the shape of the enhance dose area in solid acrylic phantom. Their study, however, did not provide the detailed spatial variation of dose around the foils. I wanted to get a more detailed dose distribution around metal foils and assess the feasibility of doing this with a polymer gel. This chapter was an attempt to answer this question.

Earlier, we identified some of the more important factors that contribute to dose enhancement in the vicinity of the foils and selected a configuration for comparison. Before we could do this, we needed to do some checks in our Monte Carlo source models. Earlier, we were mostly looking at dose ratios so it was independent of the

specific dose characteristics of the linear accelerator. Though PGD is an inherently relative measurement technique, I wanted to make sure that the simulation was a close as possible to the setup since there were other factors that I cannot control. This began by checking if the beam characteristics such as the depth dose and beam profile matched the simulation source output. If not, I need to take the appropriate steps. Following that, we go into detail about the manufacturing procedures, then discuss the tools and methods for evaluating the gel. We then discuss the results, limitation of this approach, my conclusion and suggest improvements for the future.

6.2 MAGAT Phantom

6.2.1 Foil Support

In order to support the foils in the polymer gel, two fixtures had to be created. Rhino 5 AutoCAD software was used to design the base support as well as horizontal and vertical cantilever bars. The file was exported as a stl file and printed with ABSplus™ plastic using a Stratasys Dimension 1200es 3D Printer. The fixture was placed in an P400SC™ Waterworks™ (alkaline solution) bath for 8 hours to dissolve any support material used in the printing process. Dark or bright colors were used to increase visibility of the support in the gel.

The lead foils were obtained from Alfa Aesar and had a 0.25mm thickness and 99.998% (Puratronic®) purity. The foils were cut in to 1cm squares and stacked in groups of two. The foils set were encapsulated with 3M™ Polyester Tape 8991 to prevent chemical reactions. Care was taken to remove any bubbles near the foil and surrounding area. The tape had a thickness of 0.06mm which ensured minimal disturbance to the measurement. The edges of the square were removed to allow a path for bubbles to rise to the surface. The encapsulated foil was placed in the ABS fixture and a HDPE square rod attached to the arms and base. The same tape was used to fill the gaps between the rod and the support. We used two types of foil arrangements. In one

PGD container, two foils were placed so that the foil plane was orthogonal to the beam axis. For the second, two foils were placed in parallel to the beam axis. The separation between the two foils was typically 7 mm. The fixture was then centered and secured to the bottom of the 960ml polystyrene container. Fig. 6.1 shows samples of the printed support with foils attached. The foils were positioned 3.5 mm from the base and had a 7mm separation.

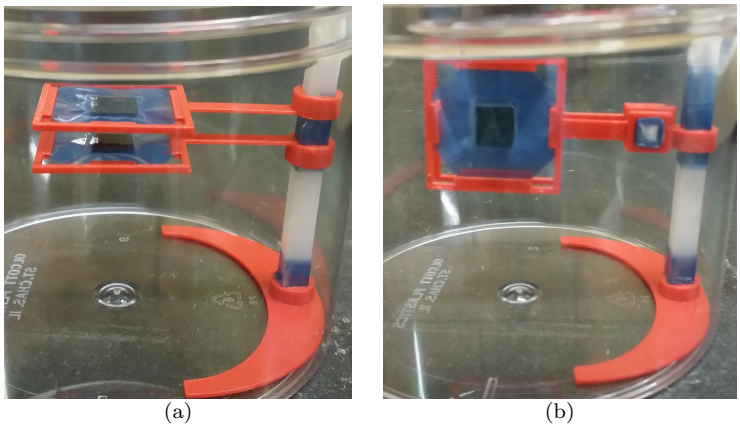

(a) (b)

Figure 6.1 – The foils show the double foil case in the horizontal arrangement (a) and the vertical arrangement (b) respectively.

6.2.2 Gel Manufacture

nMAG and MAGAT gel were manufactured in-house using compositions described in section 5.3.1. All components were from Sigma Aldrich except the water which was Millipore filtered deionized (resistivity>18.2MΩ). A custom water bath and overhead stirrer were used for the manufacturing process [Fig. 6.2(a)]. The water bath was set to a temperature of 45°C and 50% of the water poured in a beaker and placed in the bath. As the water was heated, the gelatin was weighed then added to the water progressively while mixing with the overhead stirrer. The heating continued until all of the gelatin was dissolved and a clear solution obtained. At this point the heat was turned off and temperature allowed to drop. The remaining 50% water was added to the MAA in order

to reduce the pH of the acid. At 40°C, 50% of the THP was added to the gelatin to crosslink the gelatin before it came into contact with the MAA. After 30 seconds, the MAA solution was added to the gelatin mixture. Care was taken to ensure that large clumps were broken up. When the temperature reached 32°C the remaining 50% THP was added to the mixture and mixed for 2 minutes. The gelatin was then poured in the 960ml container until it was filled, ensuring not to disturb the foil and reduce the amount of bubbles introduced.

The caps were sealed and the containers turned on their sides to allow any bubbles trapped under the foils to rise to the surface. The containers were tapped to remove any remaining bubbles. The remaining gelatin was poured into the 20ml glass calibration vials and loosely sealed to allow bubbles to float to the top. The containers were returned to vertical setup and the cover loosened slightly. The gels were then covered with aluminum foil to reduce exposure to light and next placed into vacuum bags. A vacuum pump used to remove any air from the bag and place it in another vacuum. This was repeated twice to reduce the likelihood of air leakage. Everything was placed in an opaque container and left at room temperature until the time of irradiation. Fig. 6.2(b) and (c) shows the gel after manufacture.

(a) (b) (c)

Figure 6.2 – The custom water bath used for manufacturing the gel (a). A nMAG (b) and MAGAT (c) phantom containing horizontal foils and vertical foils after fabrication.

6.2.3 Dose quantification and Analysis

The PGD were irradiated approximately 36 hours after manufacture. One hour before irradiation the gels were brought to the room to acclimate. The calibration vials were placed horizontally in the center of a water tank with a depth of 8 cm to the top of the vials. An Elekta Synergy linear accelerator (Elekta AB, Stockholm, Sweden) was used to deliver an 18 MV 20 cm x 20 cm beam with various magnitudes of dose. In all cases, the large heterogeneous gel phantoms had a depth of 3 cm and had a 100cm SSD. It was irradiated with an 18 MV photon beam with a 5cm x 5cm field size. Fig. 6.3 (a) illustrates the geometrical arrangement of the foils inside the PGD container relative to the isocenter of the linear accelerator. In this case, 4Gy was delivered to Dmax. The depth of the first foil was 7 cm for both the horizontal foil arrangement and vertical foil arrangement. Following irradiation, the gels were left at room temperature.

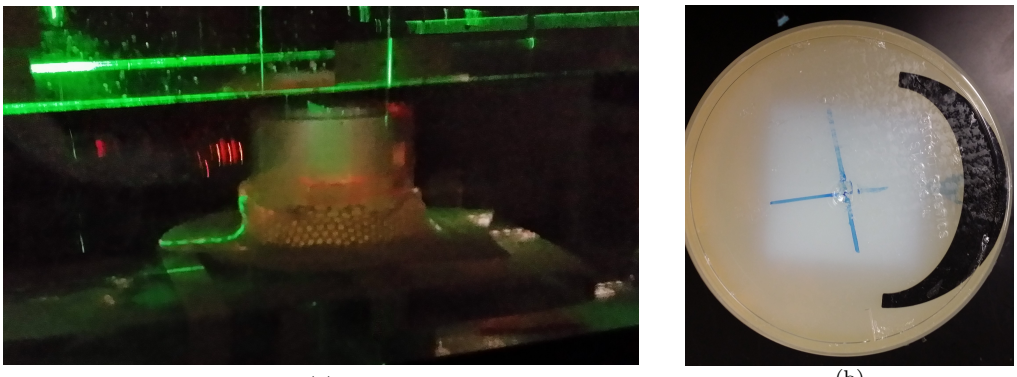

(a) (b)

Figure 6.3 – Picture showing (a) the heterogeneous phantom setup before irradiation and (b) shows the polymerized region after irradiation

The presence of high-Z material excluded the use of x-ray and optical tomographic techniques; therefore, I have chosen to use an MRI scanner. MRI scanning was preformed two days after irradiation. The gels were brought to the MRI room at the Center for Magnetic Resonance Research (CMRR) 1 hour before to acclimate to the room. The

Figure 6.4 – Siemens 3T imager showing Phantom and calibration vials in the head coil.

phantom and calibration vials were placed in a Styrofoam holder and placed in a 12-channel head matrix coil. The gels were centrally positioned in the head coil and aligned with the in-room lasers as seen in Fig. 6.4. Next, a 3T MRI scanner, Magnetom Trio A Tim (Siemens Medical Solutions, Erlangen, Germany) was used to acquire images. We measured the spin-spin relaxation rate (R_2) distribution by applying the multi-spin echo pulse sequence available on the Siemens MRI scanners (designated as "cp_mc" on the machine), which is a variation of the standard Car-Purcell-Meiboom-Gill (CPMG) pulse sequence. The imaging parameters were specifically selected for the polymer gel as follows: the field-of-view = 256 mm x 256 mm, 256x256 pixels, 1 or 2-mm slice thickness without gap, TR=7560 ms (approximately 7 x the spin-lattice relaxation time T1), echo spacing = 15.2 ms, and the number of echoes = 16. The main phantoms were scanned in both transverse and sagittal directions for better dose quantification around the foils.

6.2.4 Analysis Methods

In order to efficiently analyze the dosimetric data, analysis was performed using an in-house MATLAB (The MathWorks, Inc., Natick, MA) program, ATOM-PG. A screen-shot of the ATOM-PG program is shown in Appendix A.2. The previous versions of

Table 6.1 – Estimated uncertainties in the experiment

Error Source	Uncertainty (%)
Foil and phantom positioning	3
Dose rate	0.5
Volume contraction after irradiation	0.5
Spatial stability	0.5
Temperature variation during scanning and irradiation	2
MRI artifacts	2

in-house programs, ATOM and PG3DCMP [121], were completely revised for a much more improved interface with more functions including instant comparison of the MC and PGD data. The MRI data was processed by using a module from the ATOM program. This program calculated the R_2 values of all pixels from 16 images taken at 16 different echo times for all the slices. It was assumed that the echo signal decayed exponentially in time. The maximum likelihood estimation method was used to estimate the decay constant, i.e., R_2, in the exponential decay equation. To improve the accuracy of the R_2 estimation, the VAREC algorithm [122], which automatically selects the number of echo signals useful for the estimation, was used. Note that the first echo signal was omitted from the R_2 estimation. The calibration vials were used to determine the relationship between the dose and R_2 and the R_2-to-dose data were approximated by a linear or quadratic fit equation. For the dose quantification recorded in the phantom, R_2 values were converted to absorbed dose by applying the R_2-to-dose calibration data.

Doses between the PDG measurements and Monte Carlo simulation data were compared mainly by plotting line profiles along a line crossing the foils and in parallel to the foils. Gamma Analysis was not performed because the current data were too noisy to justify such analyses.

The errors from the experiment were separated into two categories. The first was estimated based on prior experiments and observation. The second was calculated from the calibration curve and R_2 background data. Table 6.1 shows a summary of the estimated errors and their source.

Every effort was made to minimize uncertainty and incorporate good manufacturing principles. Configurations that could introduce unnecessary error were avoided. Doses above 10Gy for example, were not used since that would require multiple fractions. The above errors were combined with the calculated errors to obtain an error matrix.

6.3 Monte Carlo

6.3.1 Output Specifications and Comparison Methods

First, we needed to determine the accuracy of the beam model and determine if it was sufficient. Earlier simulations used a generic source that is not an exact match of the linear accelerator

Simulation of the gantry is an extensive process requiring multiple iterations to obtain a matched dose distribution. As a result, the decision was made not to simulate the gantry head unless it was deemed necessary. There were several considerations that were made in determining the verification requirements. The first was that we were not concerned about the buildup region of the curve. The second was that the both %DD curves had to be parallel for the region below Dmax. The third is that small differences in alignment were considered insignificant as they can be corrected. Finally, evaluation was considered for data in the area of interest. The statistical variations arising from having small voxel sizes make it possible for a few data points have dose differences higher than the criteria. This was fine since no smoothing or averaging was done to the data.

The flow chart in Fig. 6.5 summarizes the procedure for dose verification. The main deciding factor in determining the need for gantry simulation was the having a dose difference of more than 3%. Depth Dose along the central axis and profiles at depth of 7cm were taken for 18 MV photons. The golden data were obtained from the commissioning data for the Elekta Synergy at University of Minnesota - Fairview hospital.

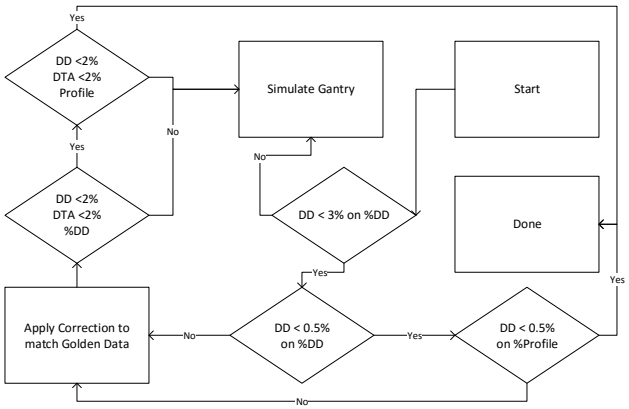

Figure 6.5 – Flow chart showing gantry output verification process. DTA is distance to agreement and DD is the dose difference.

This cutoff stems from the well-established fact that total dose deviations above 5% are detrimental to the patient [123]. The more conservative criterion allows for variations in the dose and provide a buffer. If the % depth dose was less than 3% then it was compared to see if the % depth dose and profile dose differences were below 0.5%. If that was the case, then no further work was necessary. If one of them failed the criteria, then a correction is made to the Monte Carlo data to match it to the golden data. At this point, a new criterion is used to determine how good the correction is. The matched data is required to agree within 2% of the dose and be within 2 mm of the desired dose. If this was not possible then the gantry head would be simulated. All analysis was performed with Dose Analyzer software. See section 3.2.4.

6.3.2 Beam Comparison and Correction

The %DD shown in Fig. 6.6a indicates that the Monte Carlo result is more penetrating than the commissioning data. The Monte Carlo data had a Dmax of around 4 cm but both curves had a similar slope. The entire Monte Carlo data fell within 3% commissioning data along the central axis. The profile data fell within the 3% criteria

for the central 3.5 cm of the beam which is well within the region of interest. Towards the edge of the beam, the percent deviation approaches 8% though the distance to agreement is around 2.5 mm. As far the criteria are concerned, both charts show that the Monte Carlo results are acceptable.

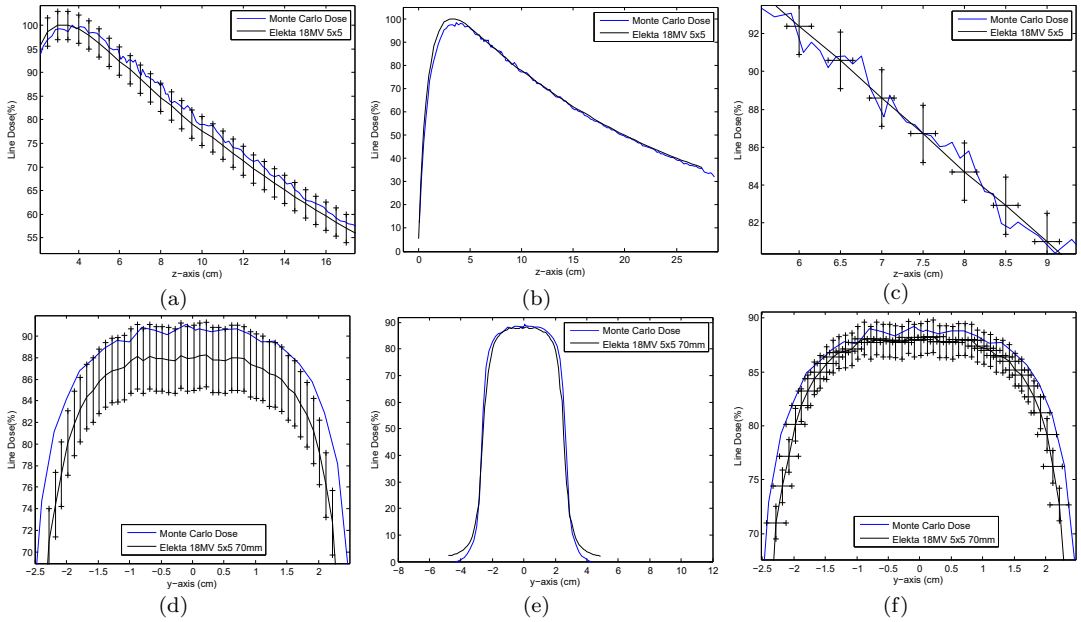

Figure 6.6 – Percent depth dose (a) and Profile dose (d) curve comparing Monte Carlo data vs Elekta golden data for a 18 MV beam with 5 cm x 5 cm field size at 100 cm SSD. Comparison of corrected Monte Carlo and gantry data for percent depth dose (b) and profile dose (e). (c) and (f) show the 2% and 2 mm boundaries for the region of interest in the %DD and profile dose respectively.

The entire Monte Carlo data set was manually adjusted by shifting and scaling until the data came in closer proximity to the commission data. Fig. 6.6 (b) and (e) show the results after the adjustment for the %DD and profile dose respectively, while Fig. 6.6 (c) and (f) show the comparison at 7 cm depth with the 2%-2mm criteria. The images show the vast majority of the points are within the 2% -2mm requirement in the area of interest. The corrected %DD matched exactly indicating that both beams have the exact energy. The corrected profile dose was a significant improvement compared to the original. The regions toward the beam edge still did not meet the criteria but we are

not interested in the dose there. Gel dosimetry is a relative technique and so scales and shifts are permitted.

6.3.3 Monte Carlo Simulation of Experiments

Even though I simulated the intended arrangement earlier, I could not simply use the data. Due to the high probability of foil movement after tapping the phantom, I could no longer be sure if the initial arrangement was still the same. Initially, the phantoms were scanned by CT in order to get DICOM data. As expected, the high-Z material had significant artifacts near the foils. I attempted to reassign the material density near the foils based on known density values from the gel. Ideally, if I could remove the artifacts then I could pass the image to the CTcreate module, which would allow me to generate an exact phantom based on the actual dimensions. This was eventually abandoned since it was labor intensive and in some areas unclear what was actual dose and what was from artifacts from the metal. In order to deal with this, I was forced to verify the foil configuration my evaluating the MRI. If the foils had shifted, then the Monte Carlo model was adjusted as best I could to match the new arrangement. The Monte Carlo dose was then compared with the gel.

6.4 Results

6.4.1 Characterization of nMAG and MAGAT PGD

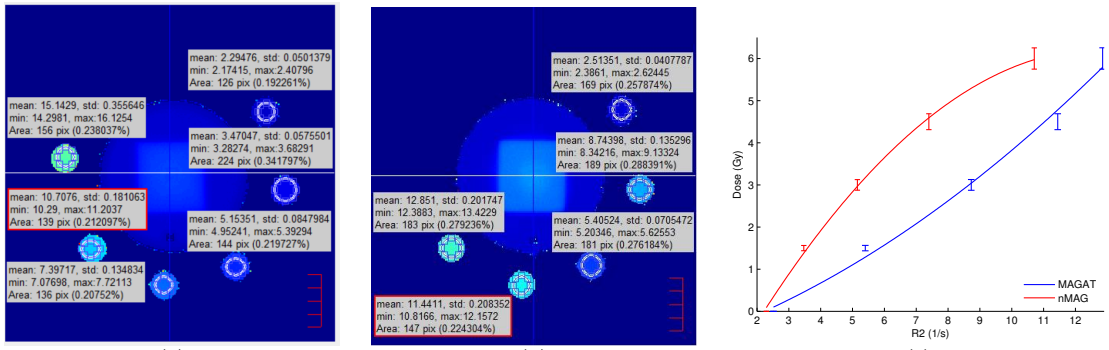

(a) (b) (c)

Figure 6.7 – Picture showing R2 Images of the (a) nMAG phantom, the (b) MAGAT phantom and (c) the resulting calibration curve for both phantoms. The nMAG calibration curve is governed by the equation, $Dose = -0.055321R_2^2 + 1.4187R_2 - 2.876$ with a coefficient of determination 0.99857, while for the MAGAT, $Dose = 0.018718R_2^2 + 0.2631R_2 - 0.6814$ and the coefficient of determination is 0.99202. For MAGAT, the 8Gy vial was not included for a better fit in the region of interest.

Both MAGAT and nMAG were manufactured based on the results from the oxygen test, then they were irradiated and scanned. The radiation response characteristics of both polymer gels can be seen in the R_2-to-dose response curves presented in Fig. 6.7. The background R_2 is about 2 s^{-1} and the R_2 value increases steadily with increasing dose up to 6 Gy. The dose response characteristics suggest that the the maximum dose should be limited to 5 Gy for nMAG and 6 Gy for MAGAT. One clear difference between the graphs is the direction of curvature. The THPS type gels have a negative curvature so R_2 gets more pronounced with increasing dose. This is in contrast to most reports studying THPC and THPS [87] but it is in agreement with Maryanksi et al [124]. His study on the effect of cross-linking revealed an increased saturation R_2 with more cross-linked gels. The response must be biphasic since at some point increasing dose will no longer have an effect on R_2. I conclude that this is a result of the difference in the extent and or nature of cross-linking in the gels. I did not attempt to look at

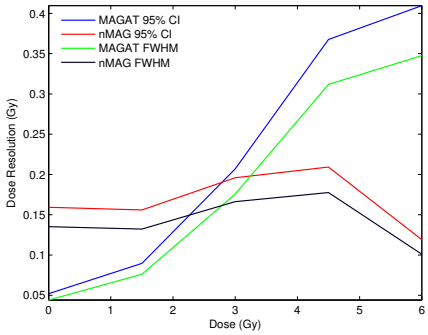

Figure 6.8 – The dose resolution of nMAG and MAGAT polymer gels using the CPMG pulse sequence with a 95% confidence.

saturation R_2 since it was well above my dosage of interest. The MAGAT gel had a slightly higher R_2 for zero dose indicating it is a stiffer gel. This makes sense due to a reduced amount of MAA.

The dose resolution for nMAG and MAGAT are shown in Fig. 6.8. The dose resolution (95%) at Dmax was around 0.2Gy and 0.3Gy for nMAG and MAGAT respectively. The minimal detectable dose is lower with MAGAT but, nMAG had a more consistent dose resolution over the experiment dose range. Using this information, I decided to give 4 Gy to Dmax point for both polymer gel types.

6.4.2 nMAG

6.4.2.1 Two Horizontal Foil Arrangement

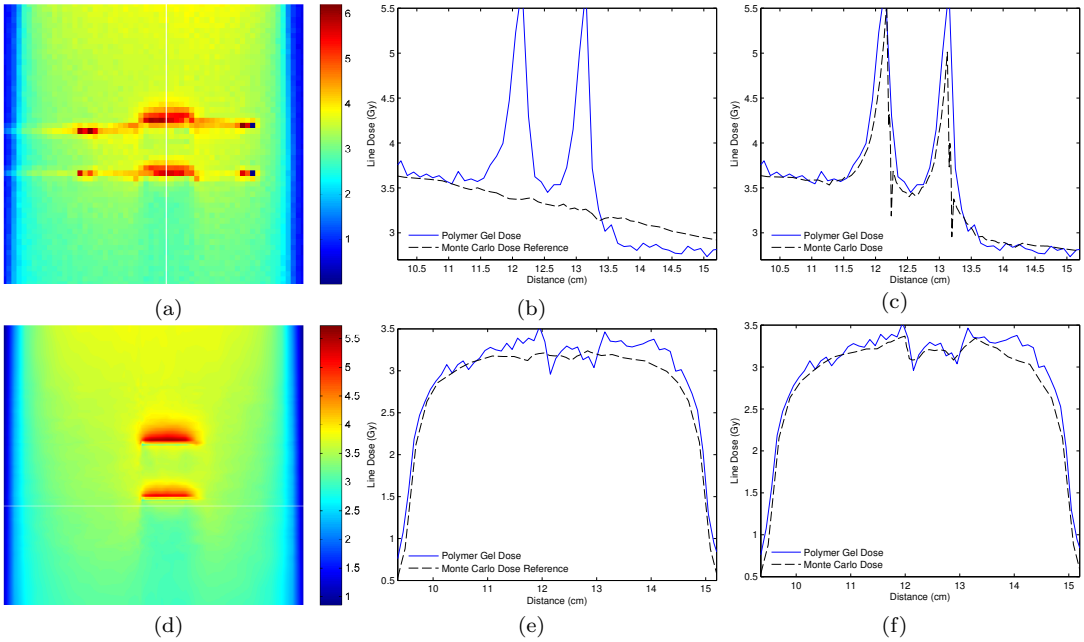

Figure 6.9 – Dual foils orthogonal to beam axis irradiated with 18 MV photons. Dose images from Polymer Gel and Monte Carlo are shown in (a) and (d) respectively. The depth dose curves of the polymer gel compared to Monte Carlo dose with plain water (b) and with foils (c). The profile dose curves 2mm downstream of the second foil where the polymer gel is compared to the Monte Carlo with plain water (e) and with foils (f).

Fig. 6.9 presents the dose distributions for two horizontal foils placed orthogonal to the photon beam axis. Figures 6.9 (a) and (d) show the color wash on the sagittal plane for polymer gel dose and Monte Carlo simulation respectively. Fig. 6.9 (c) is the vertical slice through the foil center comparing the polymer gel and simulation. The blue lines indicate PGD measured doses; whereas the black dashed lines indicate the MC simulation results.

The measured depth dose along the central axis showed increased dose upstream and between the foils, but had a decreased dose downstream. The minimum dose occurred at a point closer to the first foil. The range of increased dose was 1.1 cm above and

0.18cm below the foils. The minimum dose point between the foils had an enhancement of 1.8%. The dose reduction downstream averaged around 10.1%. There was very good agreement between the Monte Carlo data and the measured doses. The measurements and Monte Carlo results were within 1% in between the foils. The profile dose also showed good agreement between simulation and measurement. Directly below the foil, the midpoint dose difference was around 1.9% but the low dose regions at the edge had a dose difference of up to 4.1%.

6.4.2.2 Two Vertical Foil Arrangement

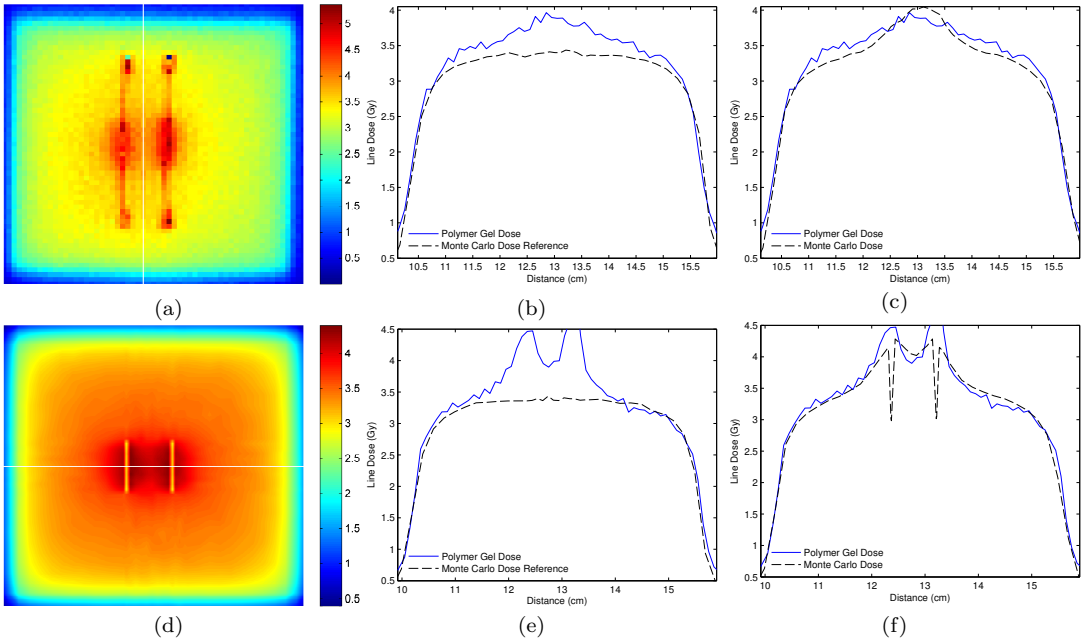

Figure 6.10 – Dual foils parallel to beam axis irradiated with 18 MV photons. Dose images from Polymer Gel and Monte Carlo are shown in (a) and (d) respectively. The depth dose curves of the polymer gel compared to Monte Carlo dose with plain water (b) and with foils (c). The profile dose curves for the polymer gel compared to the Monte Carlo with plain water (e) and with foils (f).

Fig. 6.10 shows the dose distribution for the two foil arrangement where the foils are parallel to the beam. Parallel to the beam, the dose increase has a maximum enhancement of around 16.5%. The dose difference between experiment simulation was

about 3.7% at the maximum point. The range of increased dose was around 4.3 cm. Perpendicular to the foils, we can see a dose increase through the center of the foil of around 13.7% and the difference between the polymer gel dose and simulation dose was 0.9%.

6.4.3 MAGAT

6.4.3.1 Two Horizontal Foil Arrangement

The MAGAT PG had limited response in the larger size heterogeneous phantom. The reduction of THPC in the final configuration resulted in ineffective oxygen scavenging in the larger phantom though it was sufficient in the smaller volume. The decision was made not to repeat it since the THPS configuration worked reasonably well. Fig. 6.11 shows the response of the two foil horizontal configuration. The measured dose was lower than delivered and so no comparison was made with the Monte Carlo dose. We can still see that the upstream dose was enhanced by around 38% while the dose downstream was reduced by around 7% compared with the surrounding dose. The other configuration will not be shown since the gel doses are incorrect.

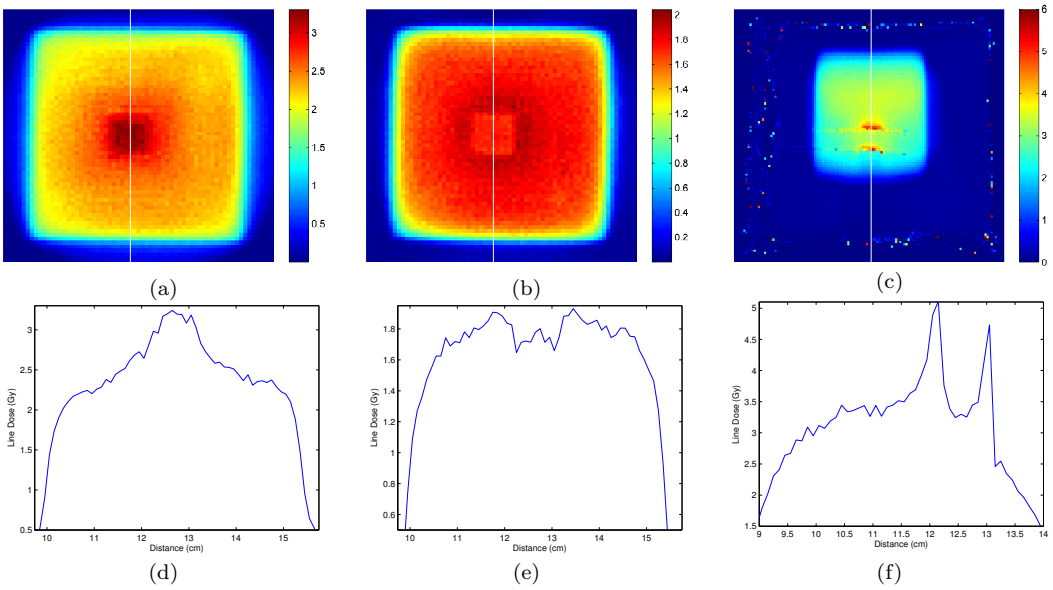

Figure 6.11 – Dual foils parallel to beam axis irradiated with 18 MV photons. The images show the axial dose from (a) 2mm above the first foil, (b) 2mm below the second foil and (d) and (e) are the corresponding profiles. The sagittal dose image (c) shows regions of no response and (f) is the corresponding depth dose curve.

6.5 Discussion

6.5.1 nMAG Detectors

For the horizontal two foil arrangement, both the Monte Carlo simulation and the PGD measurements showed that the dose between the foils was a well-like distribution. The current foil separation results in a dose distribution that is approximately the sum of two single foils. The dose in the backward direction of the lead foil fell off rapidly with distance away from the foil surface, but the dose in the forward direction fell off even faster. My measurements confirmed this dose characteristic and agreed with the Monte Carlo simulation results.

In the vertical orientation, the drop in dose from the Monte Carlo is a result of significant attenuation trough the foil and partial volume effect have blurred the image from the MR. The note that the increased dose difference for the profile dose are also

influenced by the difference between the Monte Carlo source and the linac beam. This configuration looked like the beam was at a slight angle, but the decision was made not to spend significant time trying to match the exact configuration.

6.5.2 MAGAT Detectors

The MAGAT phantoms did not respond as expected. Oxygen testing in the smaller calibration vials indicated good response but this was not sufficient in the larger container. In retrospect, this is not surprising since the glass calibration vials have better oxygen impermeability than the larger polystyrene containers. The vacuum storage seemed to work visibly but it was very possible that air diffused into the container. This could also be explained by dissolved oxygen in the water but was never bound by the scavenger.

The amount of THPC was reduced because I was trying to reduce the sensitivity and increase the tissue equivalence. At this point, the decision was made to not spend any more time on it since we already had the results from THPS. The improvements from using THPC was not critical to the task of determining the feasibility of measuring dose with gel dosimeter. This combined with restraints on time and resources made the decision necessary. Simply increasing the amount of THPC to around 2.5mM should solve the issue of oxygen impaired dose response.

6.5.3 Other Detectors

There is extensive literature in which the dose variation along the beam axis was measured in both backward and forward direction of thin metal foils such as lead, gold and titanium. These studies were done to quantify backscatter and forward scatter correction factors. The measurements used parallel-plate ionization chambers, radiographic films, or small TLD chips. Among these measurement devices, the parallel-plate ionization chamber is considered the most accurate with the smallest uncertainty. This tool also could provide the dose data with a high spatial resolution along the beam

axis because of the thin layer of the active measurement volume. However, the ionization chamber introduced additional material heterogeneity due to its structure material; hence, it is somewhat suspicious if the measured dose accurately reflects the real dose at the points near a metal foil. Radiographic films can be easily placed at a short distance from a foil. In particular, the EBT2 and EBT3 films, which are less light sensitive than the radiographic XV films, can be used without enclosing in an envelope. However, the radiochromic films must be placed in water-like solid phantom to create varying distances from the foil. Hence, the technique also suffers from introducing additional material heterogeneity in the measurement setup. The micro - TLD is water-equivalent, but it also requires a solid phantom with adequate holes to accommodate the chips. Hence, a potential air gap between TLD chips and the solid water-like material is unavoidable. A polymer gel dosimeter removes the problems of introducing additional undesirable material heterogeneity associated with other common radiation detectors; hence, it is an ideal tool for dose measurement in the vicinity of metal foils.

6.5.4 Limitations of the current approach and future research

Technically, suspending the foils in the gel was fairly challenging. To minimize the dose perturbation, we decided to suspend the lead foils in a 3D printed ABSplus apparatus. While ABSplus is considered tissue equivalent, the fixture was designed with sufficient clearance to keep the plastic out of the region of interest. One of the issues that we ran into was the movement of the foils. After the gel was poured, bubbles had the tendency to get trapped under the tape despite having openings in the corners of the fixture. The act of rotating the container and tapping the sides of the container to dislodge the bubbles also potentially caused movement of the foils. In addition to this, the weight of the foils sometimes caused the tape to sag. To deal with this issue, we decided to measure the foil spacing on the MR image and adjust the simulation to match the actual setup as much as possible.

In our initial experiments, lead foils were suspended by a tape holding the foil only

at the edge. This configuration placed the lead in direct contact with the polymer gel. Because of its acidity, there were noticeable chemical reactions between the thin protective lead oxide coating and polymer gel, causing an erroneous high dose cloud around the foil. One solution was to use an acid to pickle the metal. Placing the foils in 6% MAA solution for 5 minutes removed the vast majority of the oxide layer, however, it was not clear how strong the solution should be or how long the metal should be submerged to remove all of the coatings. If the metal remained too long, then the metal surface integrity could be affected and if a residual oxide layer was present, then it could influence the measured dose. More extensive testing would be required to determine the optimal procedure. To solve this problem, we completely enclosed the lead foil with polyester tape. Consequently, the experimental configuration resulted in the small material heterogeneity of about 0.06mm thick on each side. We consider, however, this heterogeneity is insignificant compared with the unavoidable heterogeneity needed with other dose measurement tools.

One of the shortcomings of the current measurement method was the inherent low SNR of MRI. Because of this, it was not feasible to obtain high spatial resolution R2 data and a noiseless image at the same time.

There was also some question about potential image artifacts caused by the metal. Though lead is diamagnetic, deviations in the magnetic field could have a fatal impact on the dose measurement accuracy. Attempts to reduce susceptibility artifacts by the reducing the voxel size, increase signal averaging, and increasing receiver bandwidth were limited by the significant decrease in SNR and or the corresponding increase in scan time. Shorter echo times was another option but this was not explored much since the current settings provided acceptable images for the region around the metal. Partial volume effects were observed but no visible image distortion was observed. With that said, we consider the 1mm region around the foils to be unusable.

Some oxygen contamination caused the outer layer of the polymer gel near the container walls to erroneously respond to the radiation. This was a minor issue, however,

since we were interested in the dose near the foils which was located in the center of a large container. If one needs to obtain the effects of the metals on the 3D dose distribution in a larger volume, this problem becomes important.

The ultimate goal of this study was to obtain detailed 3D dose distributions around the small high-Z material. Due to many technical difficulties, we were not able to fully accomplish this goal. These issues could be solved in the future. The spatial resolution could be enhanced by using an MRI scanner with the even higher magnetic field than the 3T machine. Fortunately, 9T or higher field scanners are readily available in our institution as well as at many other academic institutions. Artifacts from the metal can be addressed by quantifying the image artifacts computationally and applying the corrections to the original data. There are two potential solutions for dealing with oxygen contamination. One is to do all the gel manufacturing and storage in an anoxic environment. Another is to use a phantom material which is oxygen impermeable. For example, we could fabricate gel containers from Barex® or thick glass in exchange for a higher cost.

6.6 Conclusion

An nMAG polymer gel was used to measure the fine structures around small metallic objects. The measurement accuracy was investigated by comparing the measured data with Monte Carlo simulations. The results confirmed the previous publication which showed that the dose of an 18MV photon beam can be increased in between thin high-Z foils. Furthermore, the current studies provided more detailed data on the spatial distribution around metal foils than the previous study. With further improvement, our measurement technique can be applied to obtain a true 3D dose distribution around small high-Z material immersed in the tissue-like medium.

Chapter 7

Summary and Future Directions

7.1 Summary

The degree of dose enhancement around two thin high-Z metal foils of various configurations was determined by Monte Carlo simulation. The most important parameters are the atomic number, foil thickness, separation and photon energy. Generally, enhancement increases with energy, foil thickness, atomic number and decreases with separation. Foil depth and field size did not have appreciable effect on the dose. The foils in the vertical orientation seemed to have lower doses in between the foil but they have a larger region of increased dose.

We next compared to two foils to the combined dose of two single foil distributions. The results matched over wider separations but at closer distances, there were discrepancies in different regions due to attenuation and or additional dose enhancement. The dose around a gold marker was also obtained and compared to a single lead foil. For the specific dimension, the horizontal configuration had the largest dose. Surprisingly, the 6 MV horizontal case had a larger dose enhancement than the 18 MV vertical orientation. We then went on to look at the dose around multiple distributed foils and compare it to a single foil of equivalent thickness. The effect of the number of foils, separation and

energy were evaluated. It was shown that the degree of dose enhancement could be modulated by using multilayer high-Z foils. Increasing the number of foils reduced the maximum dose between the foils but resulted in a decrease of the cumulative dose between foils. Increasing the number of foils decreased the range of increased dose relative to the single foil. Increasing separation decreases the upstream and downstream dose. The maximum dose downstream of the last foil was less when using a higher number of foils and increasing the foil separation. We also looked at the effect of pair production in the high-Z materials.

After this we shifted into the experimental portion of the project. Various polymer gels and compositions were evaluated and both nMAG and MAGAT were selected for the dose comparison. A manufacturing procedure was developed that met our goals. The foil support materials were also selected and a chemical compatibility study performed between them. The results showed that the gel and fixture component are compatible for the time period of our experiments.

Next, we attempted to measure the dose distributions in the neighborhood of the metal foils which were directly placed in the polymer gel. Using the information from the Monte Carlo above, we tested two geometrical configurations. The first configuration had two foils horizontal to the beam and the second had the foils parallel to the beam. The measurement accuracy was investigated by comparing the measured data with Monte Carlo simulations. The results confirmed the previous publication which showed that the dose of an 18 MV photon beam can be increased in between thin high-Z foils. Furthermore, the current studies provided more detailed data on the spatial distribution around metal foils than the previous study. With further improvement, our measurement technique can be applied to obtain a true 3D dose distribution around small high-Z material immersed in the tissue-like medium.

7.2 Future work

7.2.1 Polymer Gel

The MAGAT polymer gel shows significant promise compared to the nMAG polymer gel. THPC proved to be a much better oxygen scavenger and due to its clarity resulted in a much clearer gel. This would allow much better visualization of objects inside the gel and allow much more exact positioning of the gel with respect to the beam.

The issue of oxygen contamination would also have to be addressed. Using Barex® or other custom containers is one option. The use of a glove box is also possible but it might be impractical for working with objects inside the gel. Using a vacuum system to storage all the gels under a vacuum has a lot of potential but more research into the proper equipment is needed. The bags in particular were not as effective for our experiment. Perhaps the oxygen on the containers played a role in this.

The optimal time gap between the addition of the first half of THP and the addition of MAA needs more investigation to better characterize the response. The proper division of THP should also be investigated to determine how much cross-linking is necessary for the application while ensuring that enough oxygen scavenging occurs. The exact temperature for cross-linking needs evaluation as well.

In terms of quantification, the use of higher magnetic fields would provide stronger signals. Higher Magnetic fields, however, bring a whole new set of problems. The biggest of which is nonlinearity of the magnetic field. We expect that these effects are negligible within our scale and that overall, the advantages outweigh the issues. The dose resolution equation could also be an instrument of improvement. More extensive studies on how the graph changes with echo time could be used to find a lower curve and identify the dose that gives the highest resolution.

7.2.2 Monte Carlo

The first thing that should be done is to simulate the configurations that were not done during this work. These include the effect of beam angle in the two foil configuration and the effect of multiple small foils on dose in the horizontal and vertical orientation. The effect of multiple-layer high-Z foils on dose near the foils should also be investigated experimentally.

We still need to know more about the distribution of dose within each simulation. Fortunately, computers are getting faster and access to larger computer clusters are coming within reach of many institutions. The availability of the entire 3D data for each simulation presents several possibilities. The first priority would be modeling the effect of each parameter (i.e. foil separation, thickness, etc.) on dose then finding out how the shape of the foil affects dose. From this, each plot could be modeled to allow the prediction of dose elsewhere in the phantom or for new configurations. Various machine learning algorithms could also be applied to the data to better understand the relationship between the parameters. After this, we have most of the tools for estimating dose at small scale. I would then apply these techniques to generate the optimal positioning of foils or markers to maximize the dose to the intended target.

The advantage of this approach is that the dose from the high-Z materials is separate from prescription dose to tissue. It does not complicate the treatment plan for the patient. The data could be provided in relative terms and simply added to the patient dose calculation. At some point, this could lead to a reduced dose from the external beam while still maintaining the minimum dose to treat the cancer. Not everyone would be comfortable with such a modification however. A better approach is to allow the high-Z material to increase the dose to the tumor provide it is within the maximum dose limits.

In the future, if things go well, the model could be expanded to look at even smaller particles. A similar approach of using the dose distribution around a single particle to

estimate the dose around many nanoparticles could also be used.

References

[1] Alex F Bielajew. Fundamentals of radiation dosimetry and radiological physics.

[2] Faiz M. Khan. *The Physics of Radiation Therapy*. Lippincott Williams & Wilkins, 4th edition edition, 2010.

[3] B. L. Werner, I. J. Das, and F. M. Khan. The production of secondary electrons in an electron beam. *Med Phys*, 14(6):992–5, 1987. Werner, B L Das, I J Khan, F M CA-38180/CA/NCI NIH HHS/United States CA-44173/CA/NCI NIH HHS/United States Research Support, U.S. Gov't, P.H.S. United states Med Phys. 1987 Nov-Dec;14(6):992-5.

[4] B. L. Werner, I. J. Das, F. M. Khan, and A. S. Meigooni. Dose perturbations at interfaces in photon beams. *Med Phys*, 14(4):585–95, 1987. Werner, B L Das, I J Khan, F M Meigooni, A S P01 CA-15548/CA/NCI NIH HHS/United States R01 CA-38180/CA/NCI NIH HHS/United States R01 CA-43748/CA/NCI NIH HHS/United States Comparative Study Research Support, U.S. Gov't, P.H.S. United states Med Phys. 1987 Jul-Aug;14(4):585-95.

[5] B. Ciesielski, L. E. Reinstein, L. Wielopolski, and A. Meek. Dose enhancement in buildup region by lead, aluminum, and lucite absorbers for 15 MVp photon beam. *Med Phys*, 16(4):609–13, 1989. Ciesielski, B Reinstein, L E Wielopolski, L Meek, A Research Support, Non-U.S. Gov't United states Med Phys. 1989 Jul-Aug;16(4):609-13.

[6] I. J. Das and F. M. Kahn. Backscatter dose perturbation at high atomic number interfaces in megavoltage photon beams. *Med Phys*, 16(3):367–75, 1989. Das, I J Kahn, F M CA-38180/CA/NCI NIH HHS/United States CA-43748/CA/NCI NIH HHS/United States Research Support, U.S. Gov't, P.H.S. United states Med Phys. 1989 May-Jun;16(3):367-75.

[7] B. L. Werner, I. J. Das, and W. N. Salk. Dose perturbations at interfaces in photon beams: secondary electron transport. *Med Phys*, 17(2):212–26, 1990. Werner, B L Das, I J Salk, W N R01CA38180/CA/NCI NIH HHS/United States Research Support, U.S. Gov't, P.H.S. United states Med Phys. 1990 Mar-Apr;17(2):212-26.

[8] I. J. Das. Forward dose perturbation at high atomic number interfaces in kilovoltage x-ray beams. *Med Phys*, 24(11):1781–7, 1997. Das, I J United states Med Phys. 1997 Nov;24(11):1781-7.

[9] X. A. Li, J. C. Chu, W. Chen, and T. Zusag. Dose enhancement by a thin foil of high-z material: a Monte Carlo study. *Med Phys*, 26(7):1245–51, 1999. Li, X A Chu, J C Chen, W Zusag, T Med Phys. 1999 Jul;26(7):1245-51.

[10] C. Baldock, Y. De Deene, S. Doran, G. Ibbott, A. Jirasek, M. Lepage, K. B. McAuley, M. Oldham, and L. J. Schreiner. Polymer gel dosimetry. *Phys Med Biol*, 55(5):R1–63, 2010. Baldock, C De Deene, Y Doran, S Ibbott, G Jirasek, A Lepage, M McAuley, K B Oldham, M Schreiner, L J R01 CA100835-07/CA/NCI NIH HHS/ England Phys Med Biol. 2010 Mar 7;55(5):R1-63. Epub 2010 Feb 11.

[11] M. J. Maryanski, R. J. Schulz, G. S. Ibbott, J. C. Gatenby, J. Xie, D. Horton, and J. C. Gore. Magnetic resonance imaging of radiation dose distributions using a polymer-gel dosimeter. *Phys Med Biol*, 39(9):1437–55, 1994. 0031-9155 (Print) Comparative Study Evaluation Studies Journal Article Research Support, Non-U.S. Gov't Research Support, U.S. Gov't, P.H.S. Validation Studies.

[12] Y. De Deene, N. Reynaert, and C. De Wagter. On the accuracy of monomer/polymer gel dosimetry in the proximity of a high-dose-rate 192ir source. *Phys Med Biol*, 46(11):2801–25, 2001. 0031-9155 (Print) Journal Article.

[13] P. Papagiannis, E. Pappas, P. Kipouros, A. Angelopoulos, L. Sakelliou, P. Baras, P. Karaiskos, I. Seimenis, P. Sandilos, and D. Baltas. Dosimetry close to an 192ir HDr source using n-vinylpyrrolidone based polymer gels and magnetic resonance imaging. *Med Phys*, 28(7):1416–26, 2001. 0094-2405 (Print) Journal Article Research Support, Non-U.S. Gov't.

[14] M. Fragoso, P. A. Love, F. Verhaegen, C. Nalder, A. M. Bidmead, M. Leach, and S. Webb. The dose distribution of low dose rate cs-137 in intracavitary brachytherapy: comparison of Monte Carlo simulation, treatment planning calculation and polymer gel measurement. *Phys Med Biol*, 49(24):5459–74, 2004. 0031-9155 Evaluation Studies Journal Article Validation Studies.

[15] G. Lymperopoulou, P. Papagiannis, A. Angelopoulos, P. Karaiskos, E. Georgiou, and D. Baltas. A dosimetric comparison of 169yb and 192ir for HDr brachytherapy of the breast, accounting for the effect of finite patient dimensions and tissue inhomogeneities. *Med Phys*, 33(12):4583–9, 2006. Lymperopoulou, G Papagiannis, P Angelopoulos, A Karaiskos, P Georgiou, E Baltas, D Comparative Study Research Support, Non-U.S. Gov't United States Med Phys. 2006 Dec;33(12):4583-9.

[16] M. H. Lin, T. C. Huang, M. J. Kao, J. Wu, C. L. Chen, and T. H. Wu. Three-dimensional dosimetry in brachytherapy: A magat study. *Appl Radiat Isot*, 67(7-8):1432–7, 2009. Lin, Min-Hsing Huang, Tzung-Chi Kao, Ming-Jen Wu, Jay Chen, Chia-Lin Wu, Tung-Hsin England Appl Radiat Isot. 2009 Jul-Aug;67(7-8):1432-7. Epub 2009 Feb 26.

[17] O. Senkesen, E. Tezcanli, B. Buyuksarac, and I. Ozbay. Comparison of 3D dose distributions for HDr 192ir brachytherapy sources with normoxic polymer gel dosimetry and treatment planning system. *Med Dosim*, 39(3):266–71, 2014. Senkesen, Oznur Tezcanli, Evrim Buyuksarac, Bora Ozbay, Ismail Comparative Study United States Med Dosim. 2014 Autumn;39(3):266-71. doi: 10.1016/j.meddos.2014.04.003. Epub 2014 Jun 3.

[18] Y. Watanabe, R. Mooij, G. M. Perera, and M. J. Maryanski. Heterogeneity phantoms for visualization of 3D dose distributions by MRI-based polymer gel dosimetry. *Med Phys*, 31(5):975–84, 2004. 0094-2405 Journal Article.

[19] G. M. Perera Y. Watanabe and R. B. Mooij. presented at the first international meeting on applied physics. *Badajoz, Spain, (unpublished)*, 2003.

[20] T. Shimozato, K. Yasui, R. Kawanami, K. Habara, Y. Aoyama, K. Tabushi, and Y. Obata. Dose distribution near thin titanium plate for skull fixation irradiated by a 4-MV photon beam. *J Med Phys*, 35(2):81–7, 2010. Shimozato, Tomohiro Yasui, Keisuke Kawanami, Ryota Habara, Kousaku Aoyama, Yuichi Tabushi, Katsuyoshi Obata, Yasunori India J Med Phys. 2010 Apr;35(2):81-7. doi: 10.4103/0971-6203.62199.

[21] T. Nagahata, H. Yamaguchi, H. Monzen, and Y. Nishimura. [the use of polymer gel dosimetry to measure dose distribution around metallic implants]. *Nihon Hoshasen Gijutsu Gakkai Zasshi*, 70(10):1160–5, 2014. Using Smart Source Parsing Oct.

[22] H Matsumura Y FAU Maeda and Maeda H. A new concept for macromolecular therapeutics in cancer chemotherapy: mechanism of tumoritropic accumulation of proteins and the antitumor agent smancs.

[23] Patra CR, Debabrata Bhattacharya R FAU Mukhopadhyay, Priyabrata Mukhopadhyay D FAU Mukherjee, and Mukherjee P. Fabrication of gold nanoparticles for targeted therapy in pancreatic cancer. *Adv Drug Deliv Rev*, 62(3):346–61, 2010.

[24] Issels RD, Jaap Lindner LH FAU Verweij, Peter Verweij J FAU Wust, Peter Wust P FAU Reichardt, Baard-Christian Reichardt P FAU Schem, Sultan Schem BC FAU Abdel-Rahman, Soeren Abdel-Rahman S FAU Daugaard, Christoph Daugaard S FAU Salat, Clemens-Martin Salat C FAU Wendtner, Zeljko Wendtner CM FAU Vujaskovic, Rudiger Vujaskovic Z FAU Wessalowski, Karl-Walter Wessalowski R FAU Jauch, Hans Roland Jauch KW FAU Durr, Ferdinand Durr HR FAU Ploner, Andrea Ploner F FAU Baur-Melnyk, Ulrich Baur-Melnyk A FAU Mansmann, Wolfgang Mansmann U FAU Hiddemann, Jean-Yves Hiddemann W FAU Blay, Peter Blay JY FAU Hohenberger, and Hohenberger P. Neoadjuvant chemotherapy alone or with regional hyperthermia for localised high-risk soft-tissue sarcoma: a randomised phase 3 multicentre study.

[25] F. Dughiero and S. Corazza. Numerical simulation of thermal disposition with induction heating used for oncological hyperthermic treatment. *Medical and Biological Engineering and Computing*, 43(1):40–46, 2005.

[26] Cherukuri P and Curley SA. Use of nanoparticles for targeted, noninvasive thermal destruction of malignant cells.

[27] J. F. Hainfeld, F. A. Dilmanian, D. N. Slatkin, and H. M. Smilowitz. Radiotherapy enhancement with gold nanoparticles. *J Pharm Pharmacol*, 60(8):977–85, 2008. Hainfeld, James F Dilmanian, F Avraham Slatkin, Daniel N Smilowitz, Henry M England J Pharm Pharmacol. 2008 Aug;60(8):977-85.

[28] I. Kawrakow. Accurate condensed history Monte Carlo simulation of electron transport. i. egsnrc, the new egs4 version. *Medical Physics*, 27(3):485–498, 2000.

[29] I Kawrakow and D Rogers. The egsnrc code system: Monte Carlo simulation of electron and photon transport. 2000.

[30] Jean-Philippe Pignol and Eli Lechtman. Reply to comment on "implications on clinical scenario of gold nanoparticle radiosensitization in regards to photon energy, nanoparticle size, concentration and location". *Physics in Medicine and Biology*, 57(1):291, 2012.

[31] D. W. Rogers. Comment on 'monte Carlo simulation on a gold nanoparticle irradiated by electron beams'. *Phys Med Biol*, 58(6):1999–2001; discussion2003–5, 2013. Rogers, D W O Comment England Phys Med Biol. 2013 Mar 21;58(6):1999-2001; discussion 2003-5. doi: 10.1088/0031-9155/58/6/1999. Epub 2013 Mar 4.

[32] W. N. Rahman, C. J. Wong, T. Ackerly, N. Yagi, and M. Geso. Polymer gels impregnated with gold nanoparticles implemented for measurements of radiation dose enhancement in synchrotron and conventional radiotherapy type beams. *Australas Phys Eng Sci Med*, 35(3):301–9, 2012. Rahman, Wan Nordiana Wong, Christopher James Ackerly, Trevor Yagi, Naoto Geso, Moshi Evaluation Studies Research Support, Non-U.S. Gov't Australia Australas Phys Eng Sci Med. 2012 Sep;35(3):301-9. doi: 10.1007/s13246-012-0157-x. Epub 2012 Aug 15.

[33] T. Marques, M. Schwarcke, C. Garrido, V. Zucolot, O. Baffa, and P. Nicolucci. Gel dosimetry analysis of gold nanoparticle application in kilovoltage radiation therapy. *Journal of Physics: Conference Series*, 250(1):012084, 2010.

[34] S Jain, D G Hirst, and J M O'Sullivan. Gold nanoparticles as novel agents for cancer therapy. *The British Journal of Radiology*, 85(1010):101–113, January 2011.

[35] Ahmad Alkhatib, Yoichi Watanabe, and John H. Broadhurst. The local enhancement of radiation dose from photons of mev energies obtained by introducing

materials of high atomic number into the treatment region. *Medical Physics*, 36(8):3543, 2009.

[36] M. J. Berger, J. H. Hubbell, S. M. Seltzer, J. Chang, J. S. Coursey, R. Sukumar, D. S. Zucker, and K. Olsen. XCOM: Photon Cross Section Database (version 1.5), 2010.

[37] William R. Hendee and E. Russell Ritenour. *Medical Imaging Physics*. John Wiley & Sons, Inc., 2003.

[38] Frank Herbert Attix. *Introduction to Radiological Physics and Radiation Dosimetry*, pages i–xxi. Wiley-VCH Verlag GmbH, 2007.

[39] J. T Bushberg. *The Essential Physics of Medical Imaging*. Lippincott Williams & Wilkins, Philadelphia, 2002.

[40] Nicholas Metropolis. The beginning of the Monte Carlo method. *Los Alamos Science*, 15(584):125–130, 1987.

[41] Paula A. Whitlock Malvin H. Kalos. *Monte Carlo Methods*. Wiley, 2nd edition, 2008.

[42] D.W.O. Rogers Bielajew and A.F. *Monte Carlo Techniques of Electron and Photon Transport for Radiation Dosimetry*. The Dosimetry of Ionizing Radiation. New York: Academic, 1990.

[43] D. W. Rogers. Fifty years of Monte Carlo simulations for medical physics. *Phys Med Biol*, 51(13):R287–301, 2006. Rogers, D W O Review England Phys Med Biol. 2006 Jul 7;51(13):R287-301. Epub 2006 Jun 20.

[44] V. A. Semenenko, J. E. Turner, and T. B. Borak. NORec, a Monte Carlo code for simulating electron tracks in liquid water. *Radiat Environ Biophys*, 42(3):213–7, 2003. Semenenko, V A Turner, J E Borak, T B Comparative Study Evaluation

Studies Validation Studies Germany Radiat Environ Biophys. 2003 Oct;42(3):213-7. Epub 2003 Aug 15.

[45] J. Spiga, E. A. Siegbahn, E. Brauer-Krisch, P. Randaccio, and A. Bravin. The geant4 toolkit for microdosimetry calculations: application to microbeam radiation therapy (mrt). *Med Phys*, 34(11):4322–30, 2007. Spiga, J Siegbahn, E A Brauer-Krisch, E Randaccio, P Bravin, A United States Med Phys. 2007 Nov;34(11):4322-30.

[46] Michael K. K. Leung, James C. L. Chow, B. Devika Chithrani, Martin J. G. Lee, Barbara Oms, and David A. Jaffray. Irradiation of gold nanoparticles by x-rays: Monte Carlo simulation of dose enhancements and the spatial properties of the secondary electrons production. *Medical Physics*, 38(2):624, 2011.

[47] A F Bielajew, D W O Rogers, and A E Nahum. The Monte Carlo simulation of ion chamber response to 60 co-resolution of anomalies associated with interfaces. *Physics in Medicine and Biology*, 30(5):419, 1985.

[48] M. J. Berger. Monte Carlo calculation of the penetration and diffusion of fast charged particles. *Methods in Comput. Phys.*, 1:135–215, 1963.

[49] Edward W. Larsen. A theoretical derivation of the condensed history algorithm. *Annals of Nuclear Energy*, 19(10-12):701–714, 1992. In Honour of Jacques Devooght.

[50] Alex F. Bielajew and D.W.O. Rogers. Presta: The parameter reduced electron-step transport algorithm for electron monte carlo transport. *Nuclear Instruments and Methods in Physics Research Section B: Beam Interactions with Materials and Atoms*, 18(1-6):165–181, 1986.

[51] Hirayama H Nelson W R and Rogers D W O. The egs4 code system slac report 265. Technical Report SLAC report 265, Stanford Linear Accelerator Institute, 1985.

[52] F. B Brown. MCnp - a general Monte Carlo n-particle transport code, version 5. Technical Report LA-UR-03 1987, Los Alamos National Laboratory, 2003.

[53] J. M. FernÃ¡ndez-Varea F. Salvat and J. Sempau. Penelope 2011: A code system for Monte Carlo simulation of electron and photon transport. Technical report, OECD Nuclear Energy Agency, 2011.

[54] J. Sempau, J.M. FernÃ¡ndez-Varea, E. Acosta, and F. Salvat. Experimental benchmarks of the Monte Carlo code penelope. *Nuclear Instruments and Methods in Physics Research Section B: Beam Interactions with Materials and Atoms*, 207(2):107–123, June 2003.

[55] M. Rodriguez, J. Sempau, and L. Brualla. Primo: a graphical environment for the Monte Carlo simulation of varian and elekta linacs. *Strahlenther Onkol*, 189(10):881–6, 2013. Rodriguez, M Sempau, J Brualla, L Research Support, Non-U.S. Gov't Germany Strahlenther Onkol. 2013 Oct;189(10):881-6. doi: 10.1007/s00066-013-0415-1. Epub 2013 Sep 6.

[56] S. Agostinelli, J. Allison, K. Amako, J. Apostolakis, H. Araujo, P. Arce, M. Asai, D. Axen, S. Banerjee, G. Barrand, F. Behner, L. Bellagamba, J. Boudreau, L. Broglia, A. Brunengo, H. Burkhardt, S. Chauvie, J. Chuma, R. Chytracek, G. Cooperman, G. Cosmo, P. Degtyarenko, A. Dell'Acqua, G. Depaola, D. Dietrich, R. Enami, A. Feliciello, C. Ferguson, H. Fesefeldt, G. Folger, F. Foppiano, A. Forti, S. Garelli, S. Giani, R. Giannitrapani, D. Gibin, Cadenas, G. Gracia Abril, G. Greeniaus, W. Greiner, V. Grichine, A. Grossheim, S. Guatelli, P. Gumplinger, R. Hamatsu, K. Hashimoto, H. Hasui, A. Heikkinen, A. Howard,

V. Ivanchenko, A. Johnson, F.W. Jones, J. Kallenbach, N. Kanaya, M. Kawabata, Y. Kawabata, M. Kawaguti, S. Kelner, P. Kent, A. Kimura, T. Kodama, R. Kokoulin, M. Kossov, H. Kurashige, E. Lamanna, T. LampÃ©n, V. Lara, V. Lefebure, F. Lei, M. Liendl, W. Lockman, F. Longo, S. Magni, M. Maire, E. Medernach, K. Minamimoto, P. Mora de Freitas, Y. Morita, K. Murakami, M. Nagamatu, R. Nartallo, P. Nieminen, T. Nishimura, K. Ohtsubo, M. Okamura, S. O'Neale, Y. Oohata, K. Paech, J. Perl, A. Pfeiffer, M.G. Pia, F. Ranjard, A. Rybin, S. Sadilov, E. Di Salvo, G. Santin, T. Sasaki, N. Savvas, Y. Sawada, S. Scherer, S. Sei, V. Sirotenko, D. Smith, N. Starkov, H. Stoecker, J. Sulkimo, M. Takahata, S. Tanaka, E. Tcherniaev, E. Safai Tehrani, M. Tropeano, P. Truscott, H. Uno, L. Urban, P. Urban, M. Verderi, A. Walkden, W. Wander, H. Weber, J.P. Wellisch, T. Wenaus, D.C. Williams, D. Wright, T. Yamada, H. Yoshida, and D. Zschiesche. Geant4 - a simulation toolkit. *Nuclear Instruments and Methods in Physics Research Section A: Accelerators, Spectrometers, Detectors and Associated Equipment*, 506(3):250–303, 2003.

[57] J. Allison, K. Amako, J. Apostolakis, H. Araujo, P. A. Dubois, M. Asai, G. Barrand, R. Capra, S. Chauvie, R. Chytracek, G. A. P. Cirrone, G. Cooperman, G. Cosmo, G. Cuttone, G. G. Daquino, M. Donszelmann, M. Dressel, G. Folger, F. Foppiano, J. Generowicz, V. Grichine, S. Guatelli, P. Gumplinger, A. Heikkinen, I. Hrivnacova, A. Howard, S. Incerti, V. Ivanchenko, T. Johnson, F. Jones, T. Koi, R. Kokoulin, M. Kossov, H. Kurashige, V. Lara, S. Larsson, F. Lei, O. Link, F. Longo, M. Maire, A. Mantero, B. Mascialino, I. McLaren, P. M. Lorenzo, K. Minamimoto, K. Murakami, P. Nieminen, L. Pandola, S. Parlati, L. Peralta, J. Perl, A. Pfeiffer, M. G. Pia, A. Ribon, P. Rodrigues, G. Russo, S. Sadilov, G. Santin, T. Sasaki, D. Smith, N. Starkov, S. Tanaka, E. Tcherniaev, B. Tome, A. Trindade, P. Truscott, L. Urban, M. Verderi, A. Walkden, J. P. Wellisch, D. C. Williams, D. Wright, and H. Yoshida. Geant4 developments and

applications. *Nuclear Science, IEEE Transactions on*, 53(1):270–278, 2006.

[58] J. F. Carrier, L. Archambault, L. Beaulieu, and R. Roy. Validation of geant4, an object-oriented Monte Carlo toolkit, for simulations in medical physics. *Med Phys*, 31(3):484–92, 2004. Carrier, J F Archambault, L Beaulieu, L Roy, R Research Support, Non-U.S. Gov't United States Med Phys. 2004 Mar;31(3):484-92.

[59] Emily Poon, Jan Seuntjens, and Frank Verhaegen. Consistency test of the electron transport algorithm in the geant4 Monte Carlo code. *Physics in Medicine and Biology*, 50(4):681, 2005.

[60] Indrin J. Chetty, Bruce Curran, Joanna E. Cygler, John J. DeMarco, Gary Ezzell, Bruce A. Faddegon, Iwan Kawrakow, Paul J. Keall, Helen Liu, C.-M. Charlie Ma, D. W. O. Rogers, Jan Seuntjens, Daryoush Sheikh-Bagheri, and Jeffrey V. Siebers. Report of the aapm task group no. 105: Issues associated with clinical implementation of Monte Carlo-based photon and electron external beam treatment planning. *Medical Physics*, 34(12):4818–4853, 2007.

[61] B Walters, I Kawrakow, DWO Rogers, et al. Dosxyznrc users manual. *NRC Report PIRS*, 794, 2013.

[62] Alex F Bielajew. *Fundamentals of the Monte Carlo method for neutral and charged particle transport*. University of Michigan (Unpublished), 2009.

[63] Iwan Kawrakow and Alex F. Bielajew. On the representation of electron multiple elastic-scattering distributions for Monte Carlo calculations. *Nuclear Instruments and Methods in Physics Research Section B: Beam Interactions with Materials and Atoms*, 134(3-4):325–336, 1998.

[64] D.W.O. Rogers and J.E. Cygler, editors. *Clinical Dosimetry Measurements in Radiotherapy*. Medical Physics Publishing, 2009.

[65] B. R. B. Walters and I. Kawrakow. Technical note: Overprediction of dose with default presta-i boundary crossing in dosxyznrc and beamnrc. *Medical Physics*, 34(2):647–650, 2007.

[66] D. W. O. Rogers and Radhe Mohan. *The Use of Computers in Radiation Therapy: XIIIth International Conference Heidelberg, Germany May 22–25, 2000*, chapter Questions for comparison of clinical Monte Carlo codes, pages 120–122. Springer Berlin Heidelberg, Berlin, Heidelberg, 2000.

[67] P. Guo, J. Adamovics, and M. Oldham. A practical three-dimensional dosimetry system for radiation therapy. *Med Phys*, 33(10):3962–72, 2006. 0094-2405 (Print) Journal Article Research Support, N.I.H., Extramural.

[68] M. J. Day and Gabriel Stein. Chemical effects of ionizing radiation in some gels. *Nature*, 166(4212):146–147, 1950.

[69] J C Gore and Y S Kang. Measurement of radiation dose distributions by nuclear magnetic resonance (nmr) imaging. *Physics in Medicine and Biology*, 29(10):1189, 1984.

[70] L E Olsson, B A Westrin, A Fransson, and B Nordell. Diffusion of ferric ions in agarose dosimeter gels. *Physics in Medicine and Biology*, 37(12):2243, 1992.

[71] W. I. Rae, C. A. Willemse, M. G. Lotter, J. S. Engelbrecht, and J. C. Swarts. Chelator effect on ion diffusion in ferrous-sulfate-doped gelatin gel dosimeters as analyzed by MRI. *Med Phys*, 23(1):15–23, 1996.

[72] Charlesby A Alexander P and Ross M. The degradation of solid polymethyl-methacrylate by ionizing radiations. *Proc. R. Soc. A 223 392*, 1954.

[73] A. L. Boni. A polyacrylamide gamma dosimeter. *Radiation Research*, 14(4):374–380, 1961.

[74] Zhong J Kennan R P, Maryanski M J and Gore J C. Hydrodynamic effects and cross relaxation in cross linked polymer gels. *Proc. Int. Soc. for Magnetic Resonance in Medicine (New York)*, 1992.

[75] Gore J C Maryanski MJ and Schulz R J. Radiation dosimetry by MRI: solvent proton relaxation enhancement by radiation-controlled polymerisation and cross-linking in gels. *Proc. Int. Soc. for Magnetic Resonance in Medicine (New York)*, 1992.

[76] M.J. Maryanskl, J.C. Gore, and R. Schulz. Three-dimensional detection, dosimetry and imaging of an energy field by formation of a polymer in a gel, May 27 1997. US Patent 5,633,584.

[77] P. M. Fong, D. C. Keil, M. D. Does, and J. C. Gore. Polymer gels for magnetic resonance imaging of radiation dose distributions at normal room atmosphere. *Phys Med Biol*, 46(12):3105–13, 2001. 21619007 0031-9155 Journal Article.

[78] H. Y. Carr and E. M. Purcell. Effects of diffusion on free precession in nuclear magnetic resonance experiments. *Phys. Rev.*, 94:630–638, May 1954.

[79] S. Meiboom and D. Gill. Modified spin echo method for measuring nuclear relaxation times. *Review of Scientific Instruments*, 29(8):688–691, 1958.

[80] J. V. Trapp, S. A. Back, M. Lepage, G. Michael, and C. Baldock. An experimental study of the dose response of polymer gel dosimeters imaged with x-ray computed tomography. *Phys Med Biol*, 46(11):2939–51, 2001. 0031-9155 (Print) Journal Article Research Support, Non-U.S. Gov't.

[81] J. C. Gore, M. Ranade, M. J. Maryanski, and R. J. Schulz. Radiation dose distributions in three dimensions from tomographic optical density scanning of polymer gels: I. development of an optical scanner. *Phys Med Biol*, 41(12):2695–704, 1996. 0031-9155 (Print) Journal Article.

[82] O. Lopatiuk-Tirpak, K. M. Langen, S. L. Meeks, P. A. Kupelian, O. A. Zeidan, and M. J. Maryanski. Performance evaluation of an improved optical computed tomography polymer gel dosimeter system for 3D dose verification of static and dynamic phantom deliveries. *Med Phys*, 35(9):3847–59, 2008. 0094-2405 (Print) Journal Article.

[83] M. L. Mather, P. H. Charles, and C. Baldock. Measurement of ultrasonic attenuation coefficient in polymer gel dosimeters. *Phys Med Biol*, 48(20):N269–75, 2003. 0031-9155 (Print) Journal Article.

[84] Y. De Deene, G. Pittomvils, and S. Visalatchi. The influence of cooling rate on the accuracy of normoxic polymer gel dosimeters. *Phys Med Biol*, 52(10):2719–28, 2007. De Deene, Y Pittomvils, G Visalatchi, S N02-CO-41101/CO/NCI NIH HHS/ England Phys Med Biol. 2007 May 21;52(10):2719-28. Epub 2007 Apr 25.

[85] A.G. Ward and A. Courts. *The Science and Technology of Gelatin*. Food Science and Technology Series. Academic Press, 1977.

[86] De Deene Y, C Venning A FAU Hurley, B J Hurley C FAU Healy, C Healy BJ FAU Baldock, and Baldock C. Dose-response stability and integrity of the dose distribution of various polymer gel dosimeters.

[87] Y. De Deene, K. Vergote, C. Claeys, and C. De Wagter. The fundamental radiation properties of normoxic polymer gel dosimeters: a comparison between a methacrylic acid based gel and acrylamide based gels. *Phys Med Biol*, 51(3):653–73, 2006. 0031-9155 (Print) Journal Article.

[88] A. Karlsson, H. Gustavsson, S. Mansson, K. B. McAuley, and S. A. Back. Dose integration characteristics in normoxic polymer gel dosimetry investigated using sequential beam irradiation. *Phys Med Biol*, 52(15):4697–706, 2007. Karlsson, A Gustavsson, H Mansson, S McAuley, K B Back, S A J England Phys Med Biol. 2007 Aug 7;52(15):4697-706. Epub 2007 Jul 18.

[89] Y. De Deene. Fundamentals of MRI measurements for gel dosimetry. *Journal of Physics: Conference Series*, 3:87–114, 2004.

[90] John R. Taylor. *An Introduction to Error Analysis: The Study of Uncertainties in Physical Measurements*. University Science Books, 2nd edition, 1997.

[91] C Baldock, M Lepage, SA. Back J Baldlock, P J Murry, P M Jayasekera, D Porter, and T Kron. Dose resolution in radiotherapy polymer gel dosimetry: effect of echo spacing in mri pulse sequence. *Physics in Medicine and Biology*, 46(2):449, 2001.

[92] Arthur L. Boyer and Edward C. Mok. Calculation of photon dose distributions in an inhomogeneous medium using convolutions. *Medical Physics*, 13(4):503–509, 1986.

[93] B. L. Werner. Dose perturbations at interfaces in photon beams: annihilation radiation. *Med Phys*, 18(4):713–8, 1991. Werner, B L R01 CA38180/CA/NCI NIH HHS/United States Research Support, U.S. Gov't, P.H.S. United states Med Phys. 1991 Jul-Aug;18(4):713-8.

[94] F. Verhaegen. Evaluation of the egsnrc Monte Carlo code for interface dosimetry near high-z media exposed to kilovolt and 60co photons. *Phys Med Biol*, 47(10):1691–705, 2002. Verhaegen, Frank England Phys Med Biol. 2002 May 21;47(10):1691-705.

[95] V Kulkarni RN FAU Sundararaman, M A Sundararaman V FAU Prasad, and Prasad MA. The dose across a plane bone-tissue interface. *Radiation Research*, 51(0033-7587 (Linking)):1–9, January 1972.

[96] M. Ravikumar, R. Ravichandran, and S. S. Supe. Forward scatter dose effect at metallic interfaces irradiated by x and gamma ray therapy beams. *Strahlenther Onkol*, 177(11):611–5, 2001. Ravikumar, M Ravichandran, R Supe, S S Comparative Study Germany Strahlenther Onkol. 2001 Nov;177(11):611-5.

[97] Nilsson B, P Montelius A FAU Andreo, and Andreo P. A study of interface effects in 60co beams using a thin-walled parallel plate ionization chamber. *Med Phys*, 19(6):1413–21, 1992.

[98] I. Kawrakow and B. R. Walters. Efficient photon beam dose calculations using dosxyznrc with beamnrc. *Med Phys*, 33(8):3046–56, 2006. Kawrakow, I Walters, B R B Comparative Study Evaluation Studies United States Med Phys. 2006 Aug;33(8):3046-56.

[99] R. Mohan, C. Chui, and L. Lidofsky. Energy and angular distributions of photons from medical linear accelerators. *Med Phys*, 12(5):592–7, 1985. Mohan, R Chui, C Lidofsky, L Med Phys. 1985 Sep-Oct;12(5):592-7.

[100] D. Sheikh-Bagheri and D. W. Rogers. Monte Carlo calculation of nine megavoltage photon beam spectra using the beam code. *Med Phys*, 29(3):391–402, 2002. Sheikh-Bagheri, Daryoush Rogers, D W O R01 CA52692/CA/NCI NIH HHS/United States Research Support, Non-U.S. Gov't Research Support, U.S. Gov't, P.H.S. United States Med Phys. 2002 Mar;29(3):391-402.

[101] J C L Chow and M K K Leung. A graphical user interface for calculation of 3D dose distribution using Monte Carlo simulations. *Journal of Physics: Conference Series*, 102(1):012003, 2008.

[102] Iwan Kawrakow. Electron transport: lateral and longitudinal correlation algorithm. *Nuclear Instruments and Methods in Physics Research Section B: Beam Interactions with Materials and Atoms*, 114(3-4):307–326, July 1996.

[103] I. Kawrakow and Alex F. Bielajew. On the condensed history technique for electron transport. *Nuclear Instruments and Methods in Physics Research Section B: Beam Interactions with Materials and Atoms*, 142(3):253–280, July 1998.

[104] James M Anderson, Analiz Rodriguez, and David T Chang. Foreign body reaction to biomaterials. *Seminars in immunology*, 20(2):86–100, December 2007.

[105] M. Lepage, P. M. Jayasakera, S. A. Back, and C. Baldock. Dose resolution optimization of polymer gel dosimeters using different monomers. *Phys Med Biol*, 46(10):2665–80, 2001. 21542472 0031-9155 Journal Article.

[106] M. L. Taylor, R. D. Franich, P. N. Johnston, R. M. Millar, and J. V. Trapp. Systematic variations in polymer gel dosimeter calibration due to container influence and deviations from water equivalence. *Phys Med Biol*, 52(13):3991–4005, 2007. Taylor, M L Franich, R D Johnston, P N Millar, R M Trapp, J V England Phys Med Biol. 2007 Jul 7;52(13):3991-4005. Epub 2007 Jun 6.

[107] Helene Babin and Eric Dickinson. Influence of transglutaminase treatment on the thermoreversible gelation of gelatin. *Food Hydrocolloids*, 15(3):271–276, 2001.

[108] Kim B McAuley. Fundamentals of polymer gel dosimeters. *Journal of Physics: Conference Series*, 56(1):35, 2006.

[109] Djagny VB, S Wang Z FAU Xu, and Xu S. Gelatin: a valuable protein for food and pharmaceutical industries: review.

[110] A. Jirasek, M. Hilts, C. Shaw, and P. Baxter. Investigation of tetrakis hydroxymethyl phosphonium chloride as an antioxidant for use in x-ray computed tomography polyacrylamide gel dosimetry. *Phys Med Biol*, 51(7):1891–906, 2006. 0031-9155 (Print) Journal Article Research Support, Non-U.S. Gov't.

[111] E. D. Ehler, B. M. Barney, P. D. Higgins, and K. E. Dusenbery. Patient specific 3D printed phantom for imrt quality assurance. *Phys Med Biol*, 59(19):5763–73, 2014. Ehler, Eric D Barney, Brett M Higgins, Patrick D Dusenbery, Kathryn E England Phys Med Biol. 2014 Oct 7;59(19):5763-73. doi: 10.1088/0031-9155/59/19/5763. Epub 2014 Sep 10.

[112] B. D. Harris, S. Nilsson, and C. M. Poole. A feasibility study for using abs plastic and a low-cost 3D printer for patient-specific brachytherapy mould design. *Australas Phys Eng Sci Med*, 38(3):399–412, 2015. Using Smart Source Parsing Sep; doi: 10.1007/s13246-015-0356-3. Epub 2015 Jun 25.

[113] M. L. Taylor, R. L. Smith, F. Dossing, and R. D. Franich. Robust calculation of effective atomic numbers: The auto-zeff software. *Medical Physics*, 39(4):1769–1778, 2012.

[114] O. Morin, J. Chen, M. Aubin, A. Gillis, J. F. Aubry, S. Bose, H. Chen, M. Descovich, P. Xia, and J. Pouliot. Dose calculation using megavoltage cone-beam CT. *Int J Radiat Oncol Biol Phys*, 67(4):1201–10, 2007. Morin, Olivier Chen, Josephine Aubin, Michele Gillis, Amy Aubry, Jean-Francois Bose, Supratik Chen, Hong Descovich, Martina Xia, Ping Pouliot, Jean Research Support, Non-U.S. Gov't United States Int J Radiat Oncol Biol Phys. 2007 Mar 15;67(4):1201-10.

[115] Cole-palmer chemical compatibility database.

[116] http://legacy.shurflo.com/pdf/industry/ccchart.pdf.

[117] http://sevierlab.vet.cornell.edu/resources/chemical-resistance-chart-detail.pdf.

[118] http://www.apumpstore.com/documents/gracochemcompatibility.pdf.

[119] A. Weris. Stabilization of hydroquinone solutions with citric acid, December 17 1974. US Patent 3,855,150.

[120] Y. Xu, B. Cui, R. Ran, Y. Liu, H. Chen, G. Kai, and J. Shi. Risk assessment, formation, and mitigation of dietary acrylamide: current status and future prospects. Food Chem Toxicol Dietary acrylamide Epidemiology Maillard reaction Omics Risk analysis Toxicology EDAT- 2014/04/10 06:00 MHDA- 2014/04/10 06:00 CRDT- 2014/04/10 06:00 PHST- 2013/12/11 [received] PHST- 2014/03/23

[revised] PHST- 2014/03/28 [accepted] PHST- 2014/04/05 [aheadofprint] AID - S0278-6915(14)00174-4 [pii] AID - 10.1016/j.fct.2014.03.037 [doi] PST - ppublish.

[121] Y. Watanabe and Y. Nakaguchi. 3D evaluation of 3Dvh program using bang3 polymer gel dosimeter. *Med Phys*, 40(8):082101, 2013. Watanabe, Yoichi Nakaguchi, Yuji United States Med Phys. 2013 Aug;40(8):082101. doi: 10.1118/1.4813301.

[122] Yoichi Watanabe and Hitoshi Kubo. A variable echo-number method for estimating r2 in MRI-based polymer gel dosimetry. *Medical Physics*, 38(2):975, 2011.

[123] Brahme A. Dosimetric precision requirements in radiation therapy.

[124] M. J. Maryanski, C. Audet, and J. C. Gore. Effects of crosslinking and temperature on the dose response of a bang polymer gel dosimeter. *Phys Med Biol*, 42(2):303–11, 1997. 0031-9155 (Print) Journal Article Research Support, U.S. Gov't, P.H.S.

Appendix A

Software

A.1 Dose Analyzer

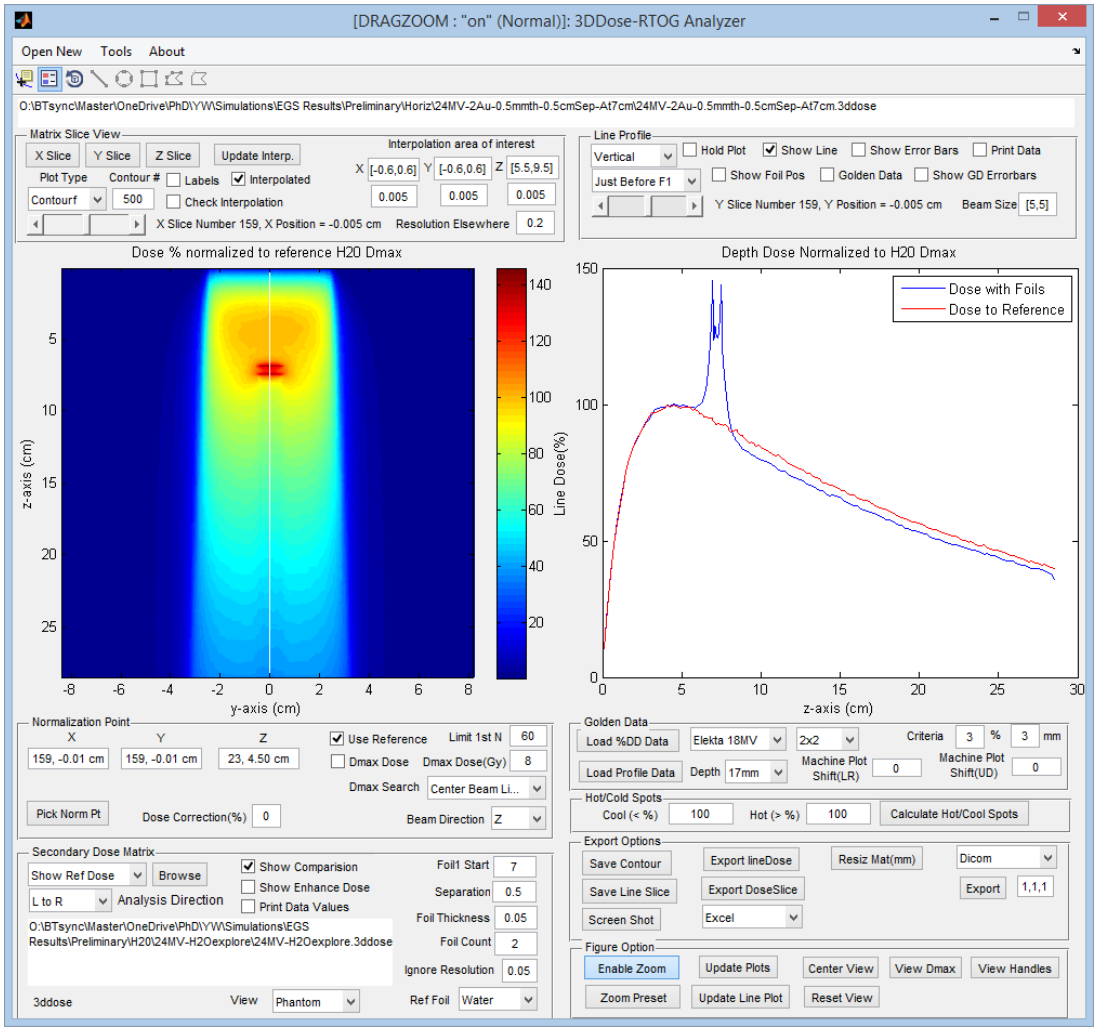

Figure A.1 – Layout of Dose Analyzer Software

A.2 ATOM PG

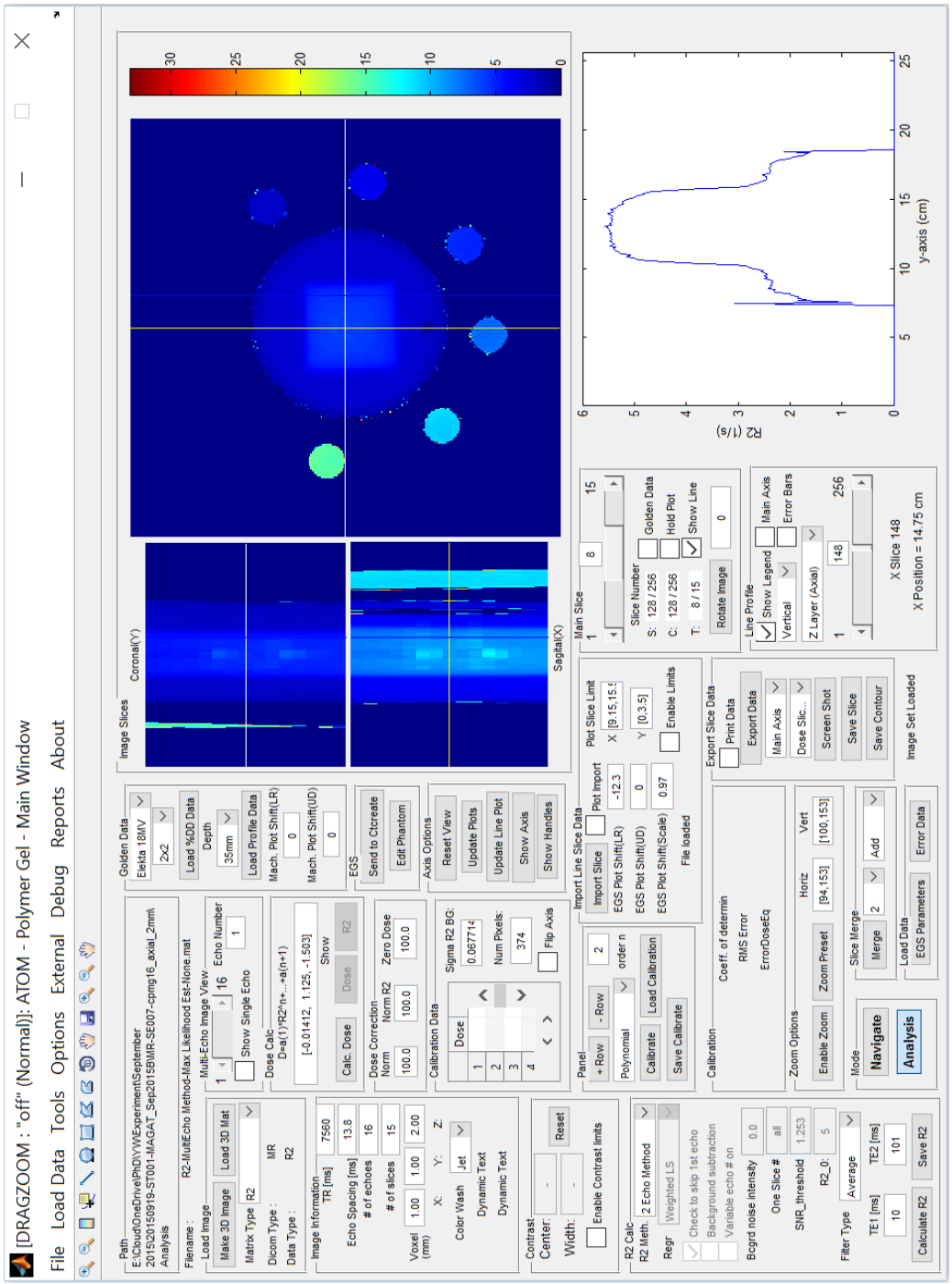

Figure A.2 – Layout of ATOM-PG Software.

Appendix B

Foil Configuration

B.1 Effect of Energy - Horizontal

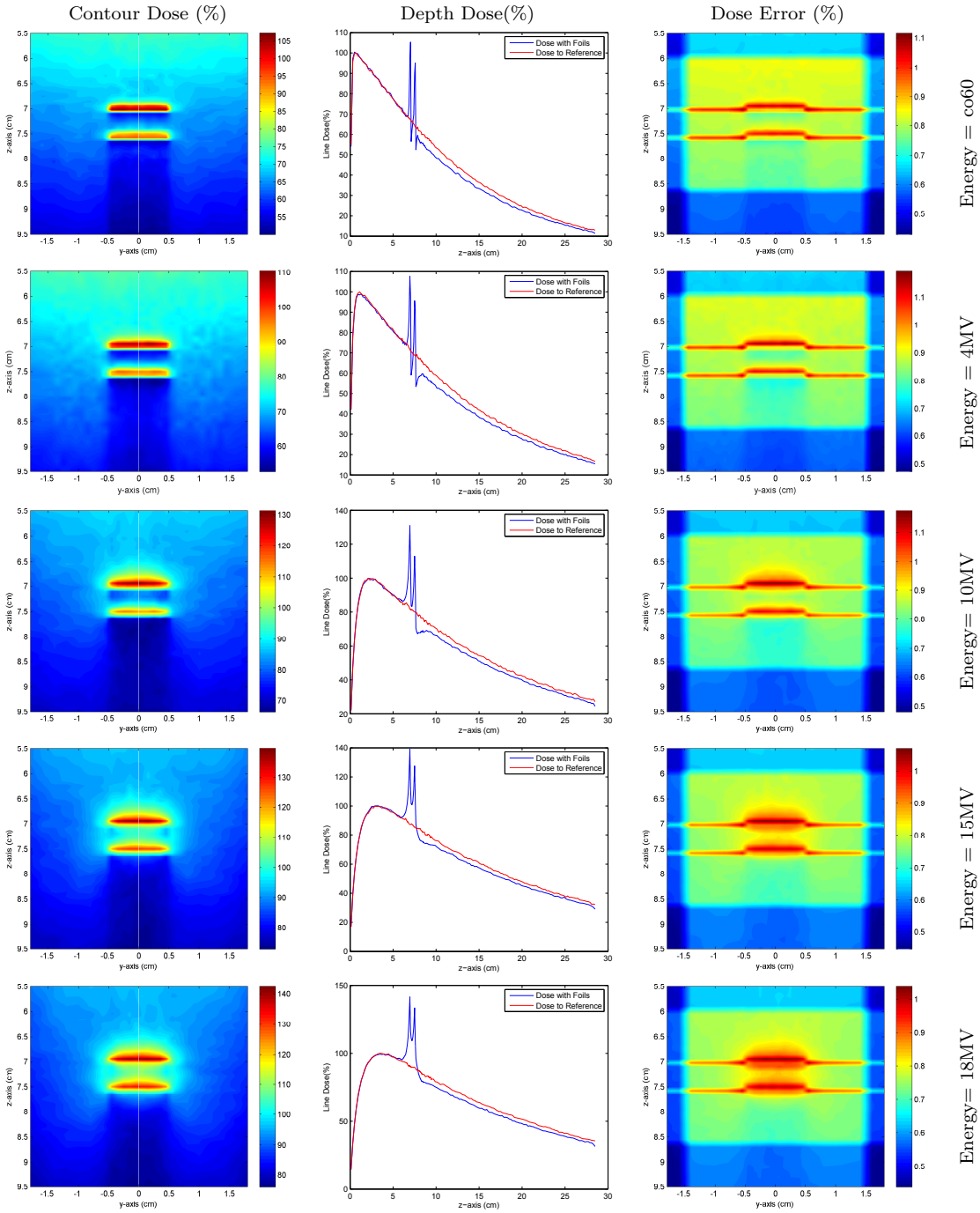

Thickness=0.5mm, Separation=7mm, Depth=7cm, Material=Gold, Field Size=5x5cm, Foil Size=1x1cm

B.2 Effect of Energy - Vertical

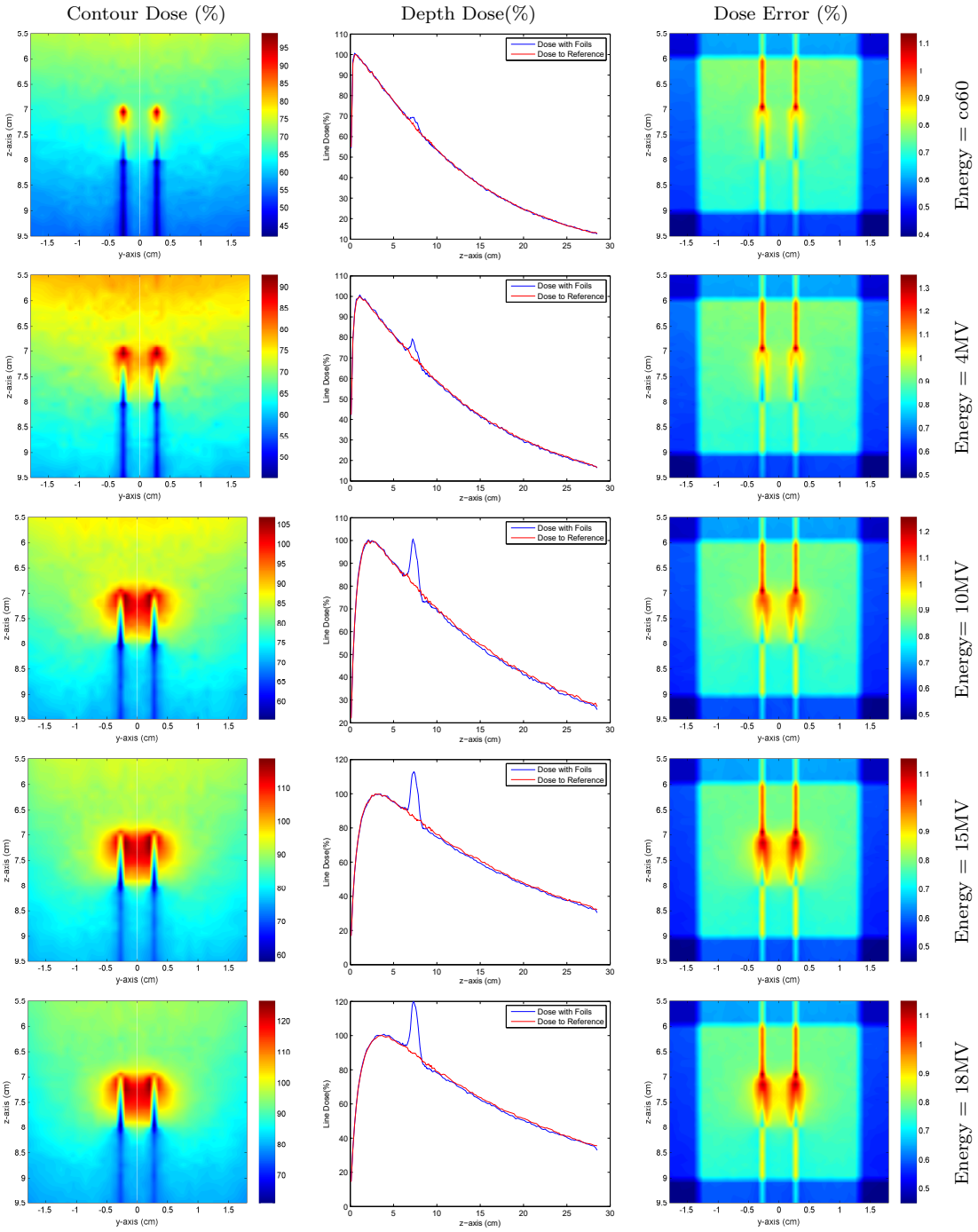

Thickness=0.5mm, Separation=7mm, Depth=7cm, Material=Gold, Field Size=5x5cm, Foil Size=1x1cm

B.3 Effect of Foil Separation - 24MV Horizontal

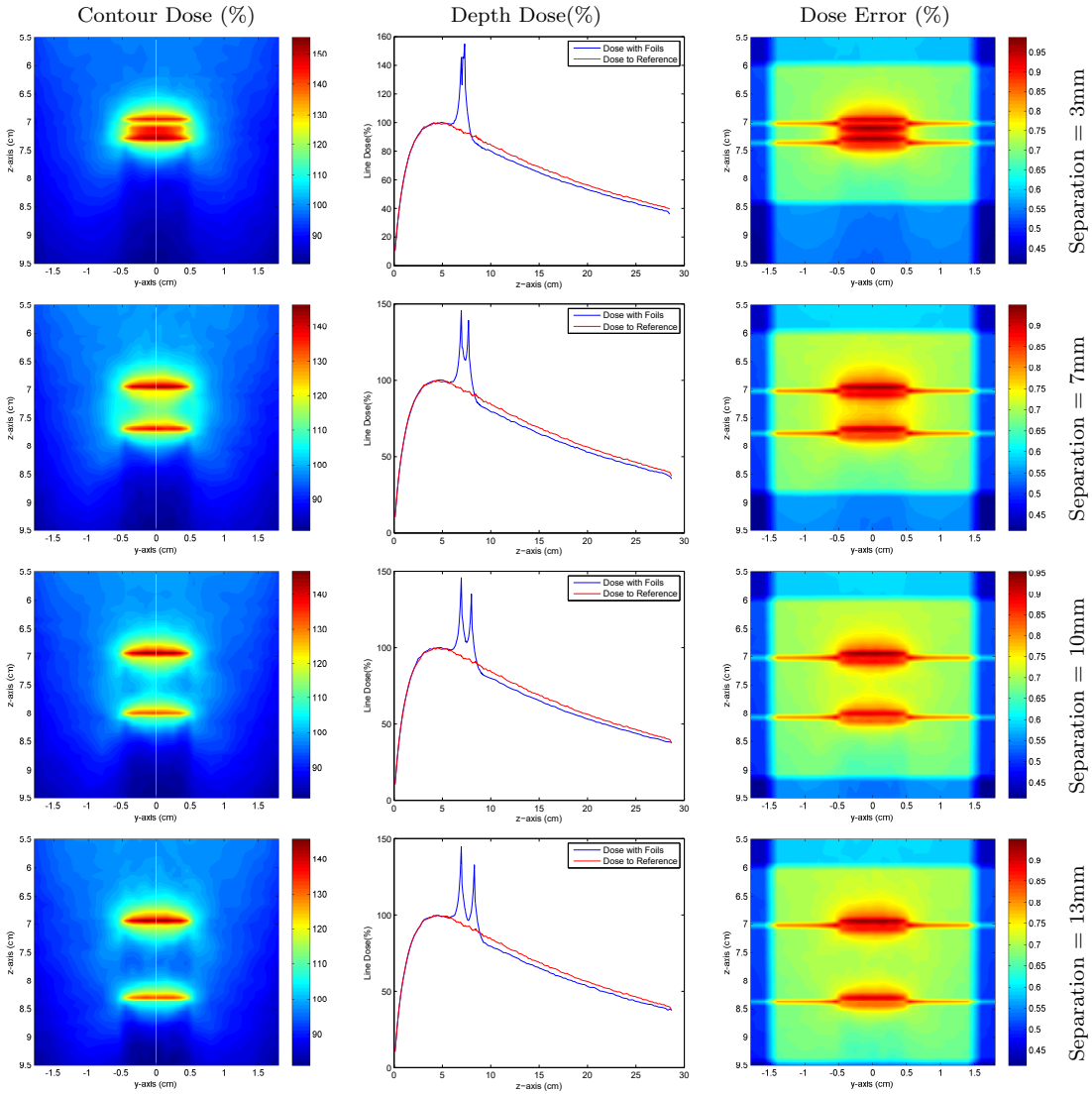

Thickness=0.5mm, Depth=7cm, Material=Gold, Field Size=5cm x 5cm, Foil Size=1cm x 1cm

B.4 Effect of Foil Separation - 6MV Horizontal

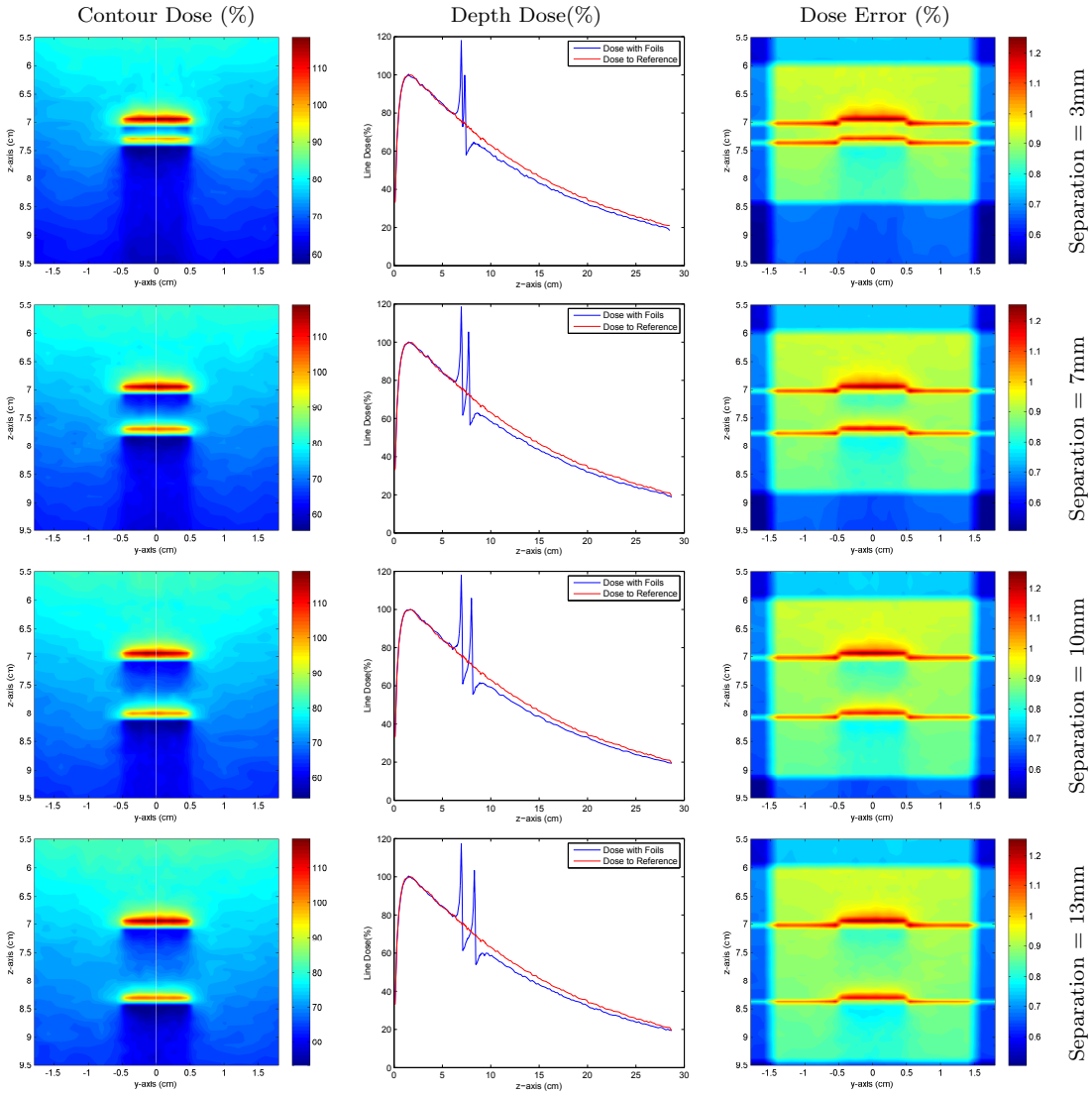

Thickness=0.5mm, Depth=7cm, Material=Gold, Field Size=5cm x 5cm, Foil Size=1cm x 1cm

B.5 Effect of Foil Separation - 24MV Vertical

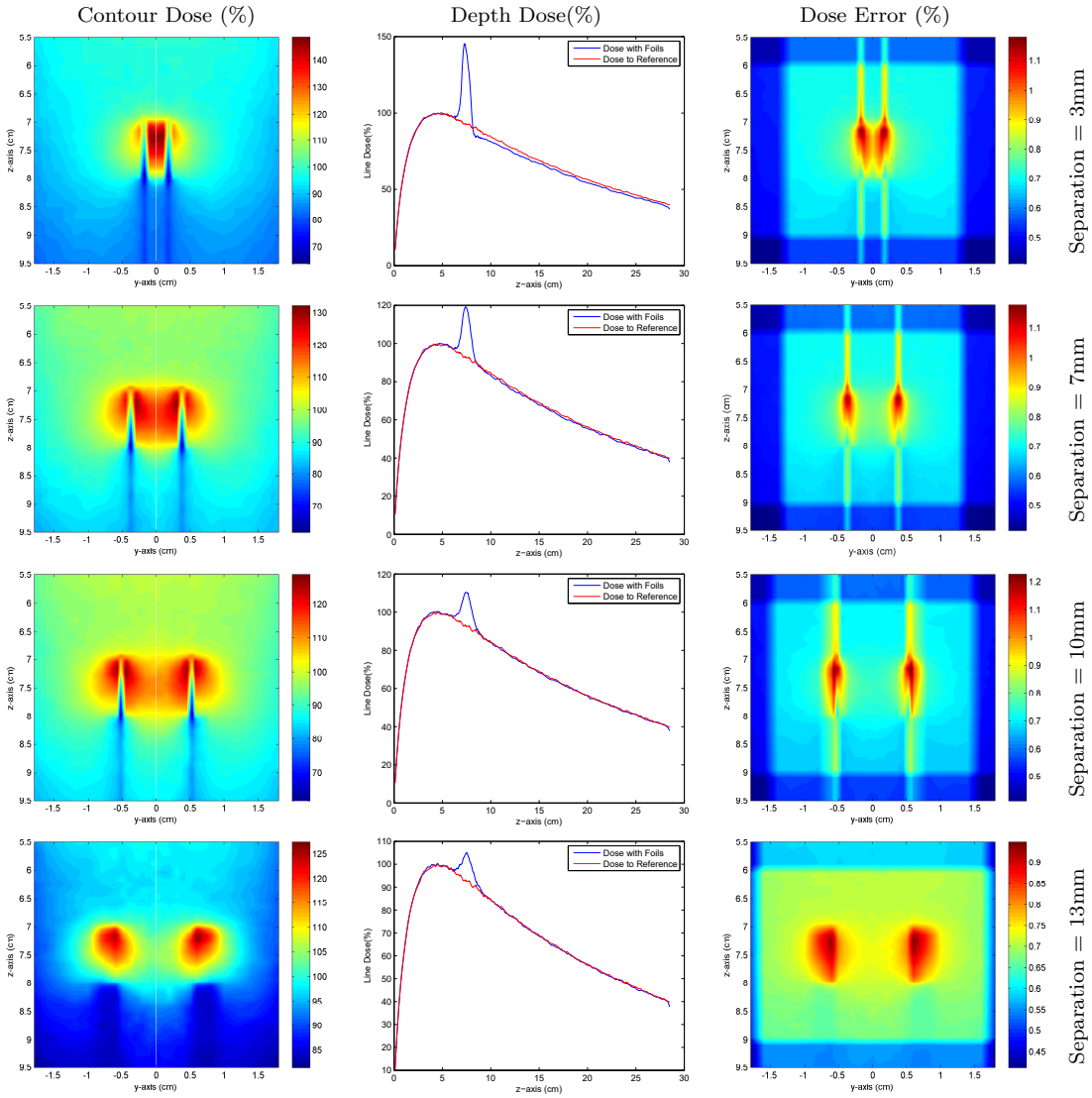

Thickness=0.5mm, Depth=7cm, Material=Gold, Field Size=5cm x5 cm, Foil Size=1cm x 1cm

B.6 Effect of Foil Separation - 6MV Vertical

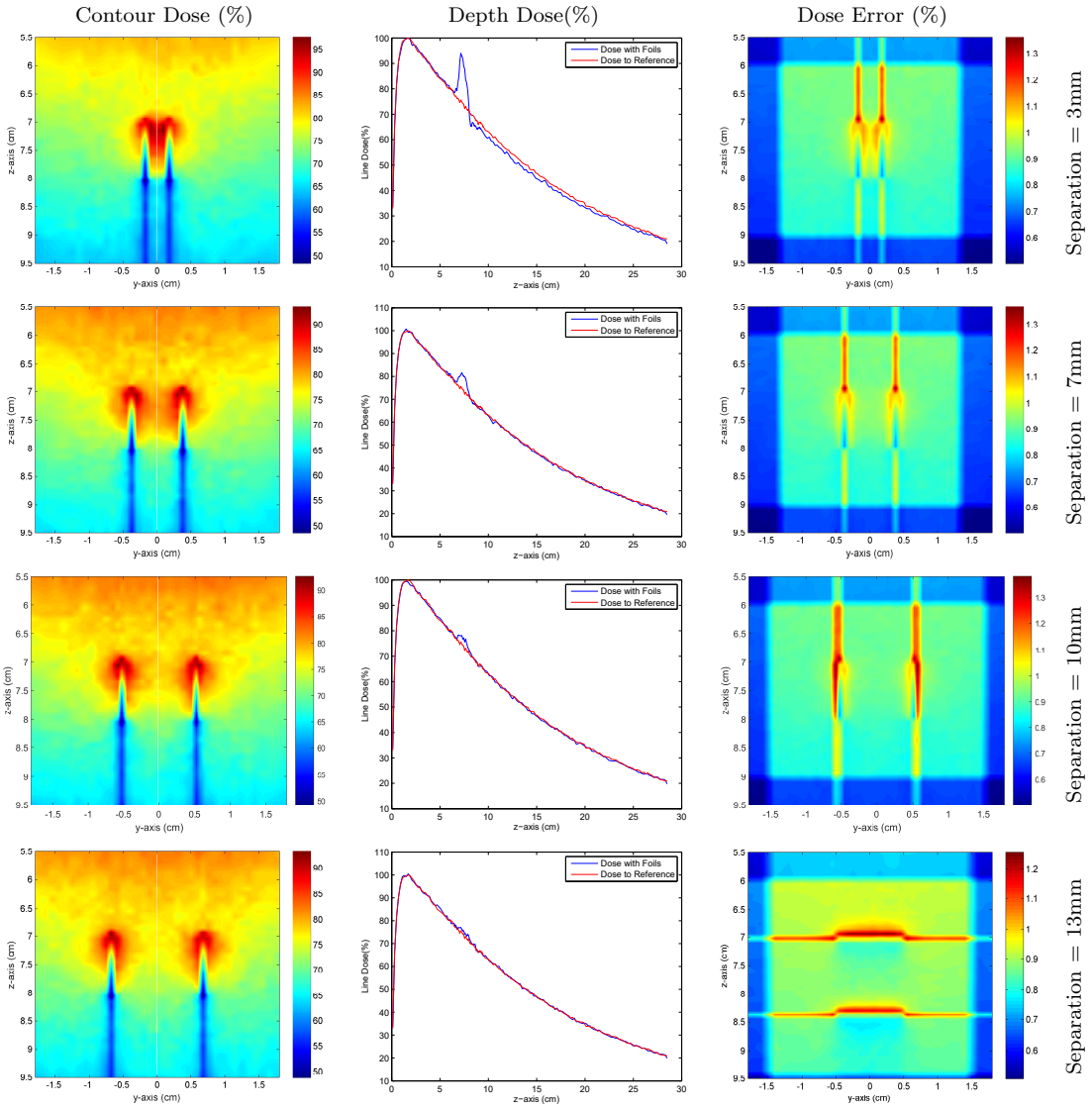

Thickness=0.5mm, Depth=7cm, Material=Gold, Field Size=5cm x 5cm,Foil Size=1cm x 1cm

B.7 Effect of Foil Thickness - 24MV Horizontal

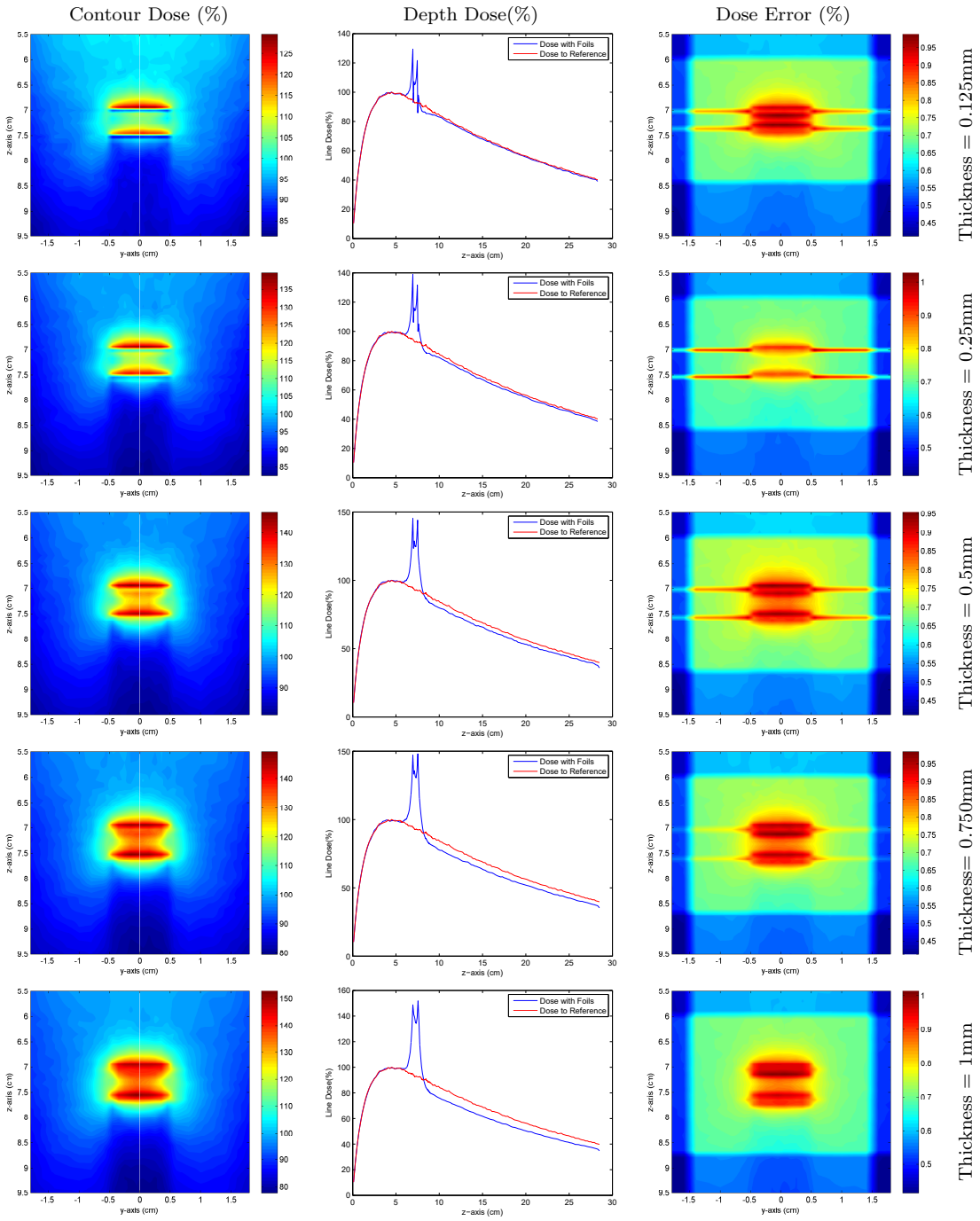

Depth=7cm, Separation=7mm, Material=Gold, Field Size=5cm x 5cm, Foil Size=1cm x 1cm

B.8 Effect of Foil Thickness - 6MV Horizontal

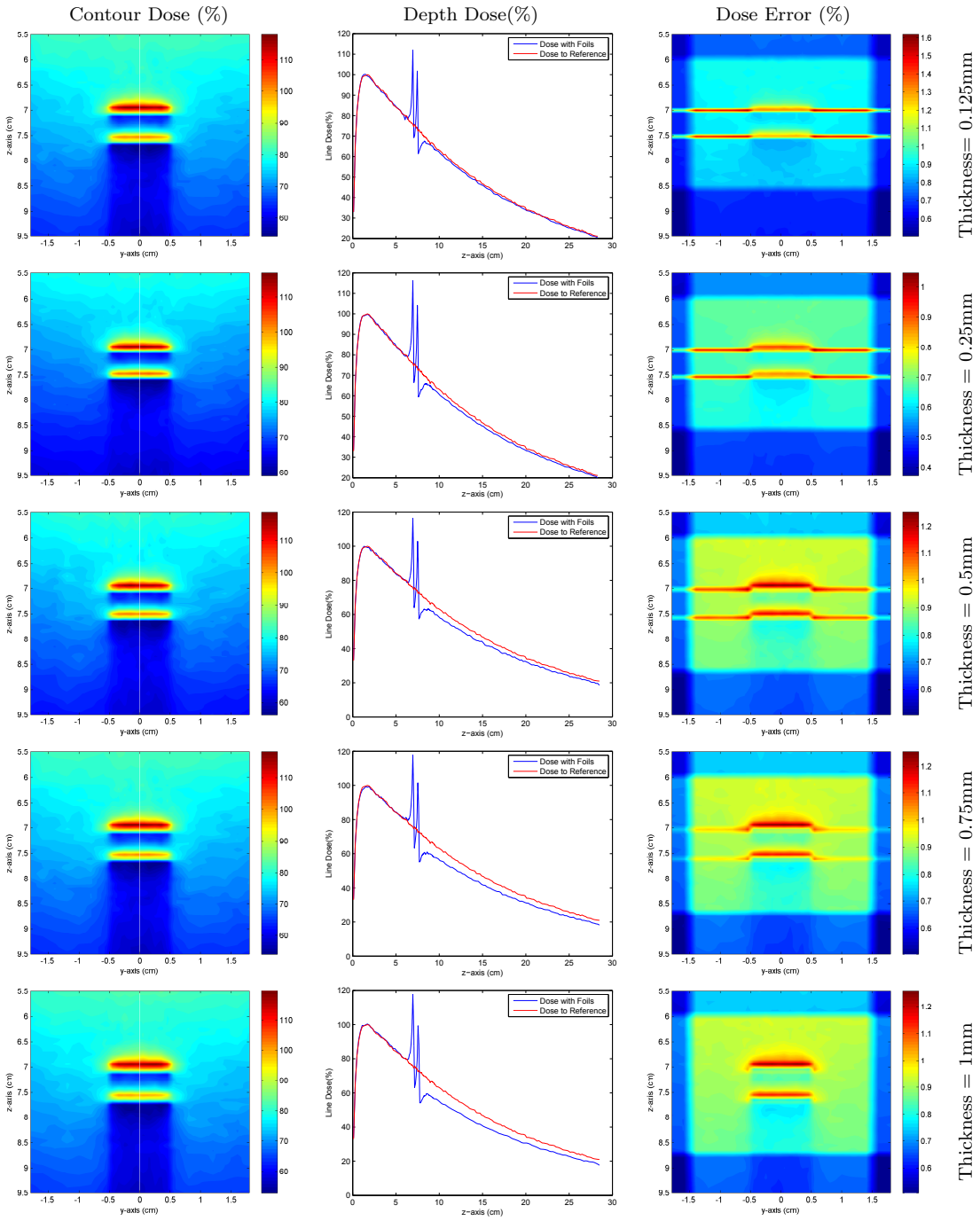

Depth=7cm, Separation=7mm, Material=Gold, Field Size=5cm x 5cm, Foil Size=1cm x 1cm

B.9 Effect of Foil Thickness - 24MV Vertical

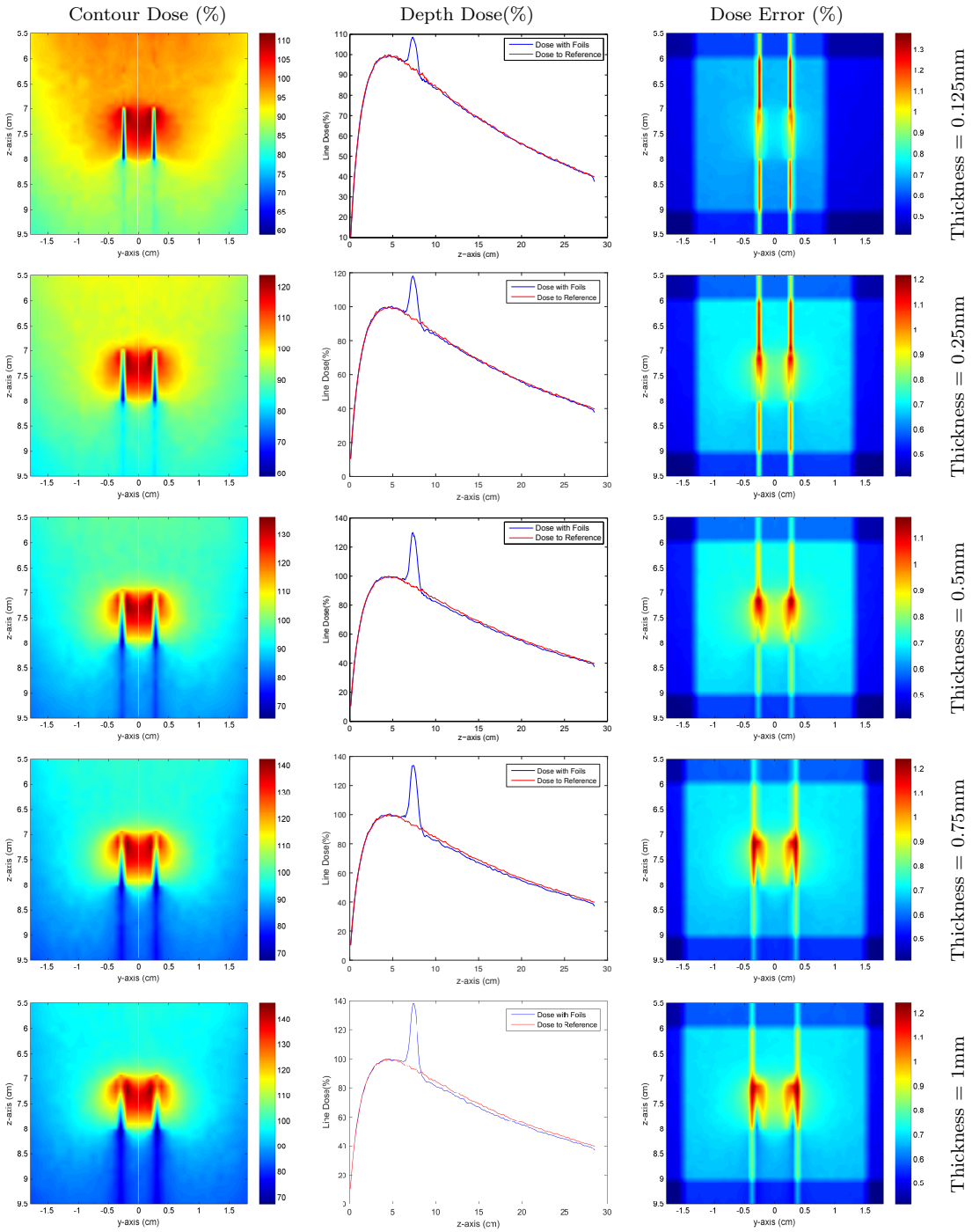

Depth=7cm, Separation=7mm, Material=Gold, Field Size=5cm x 5cm, Foil Size=1cm x 1cm

B.10 Effect of Foil Thickness - 6MV Vertical

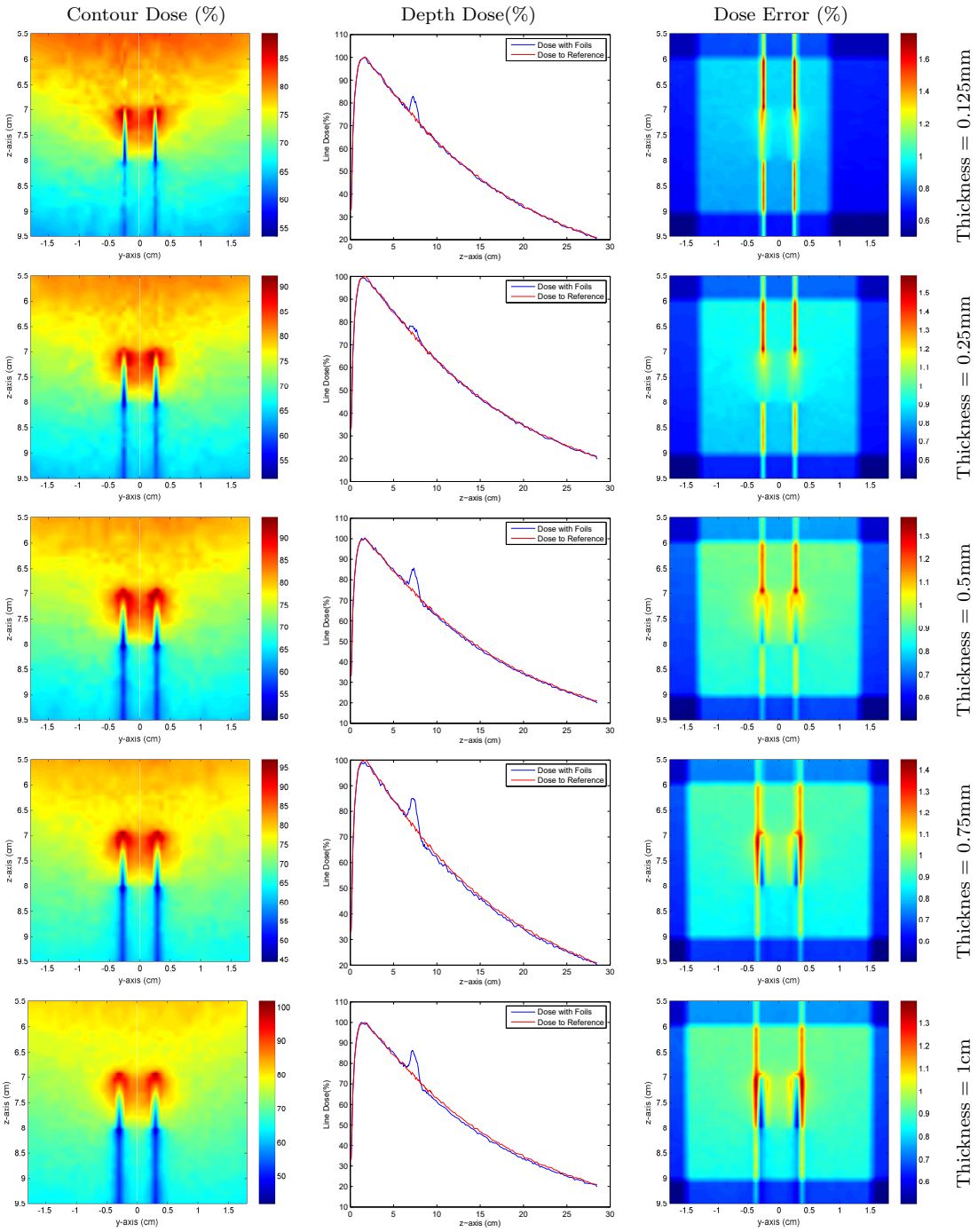

Depth=7cm, Separation=7mm, Material=Gold, Field Size=5cm x 5cm, Foil Size=1cm x 1cm

B.11 Effect of Foil Material - 24MV Horizontal

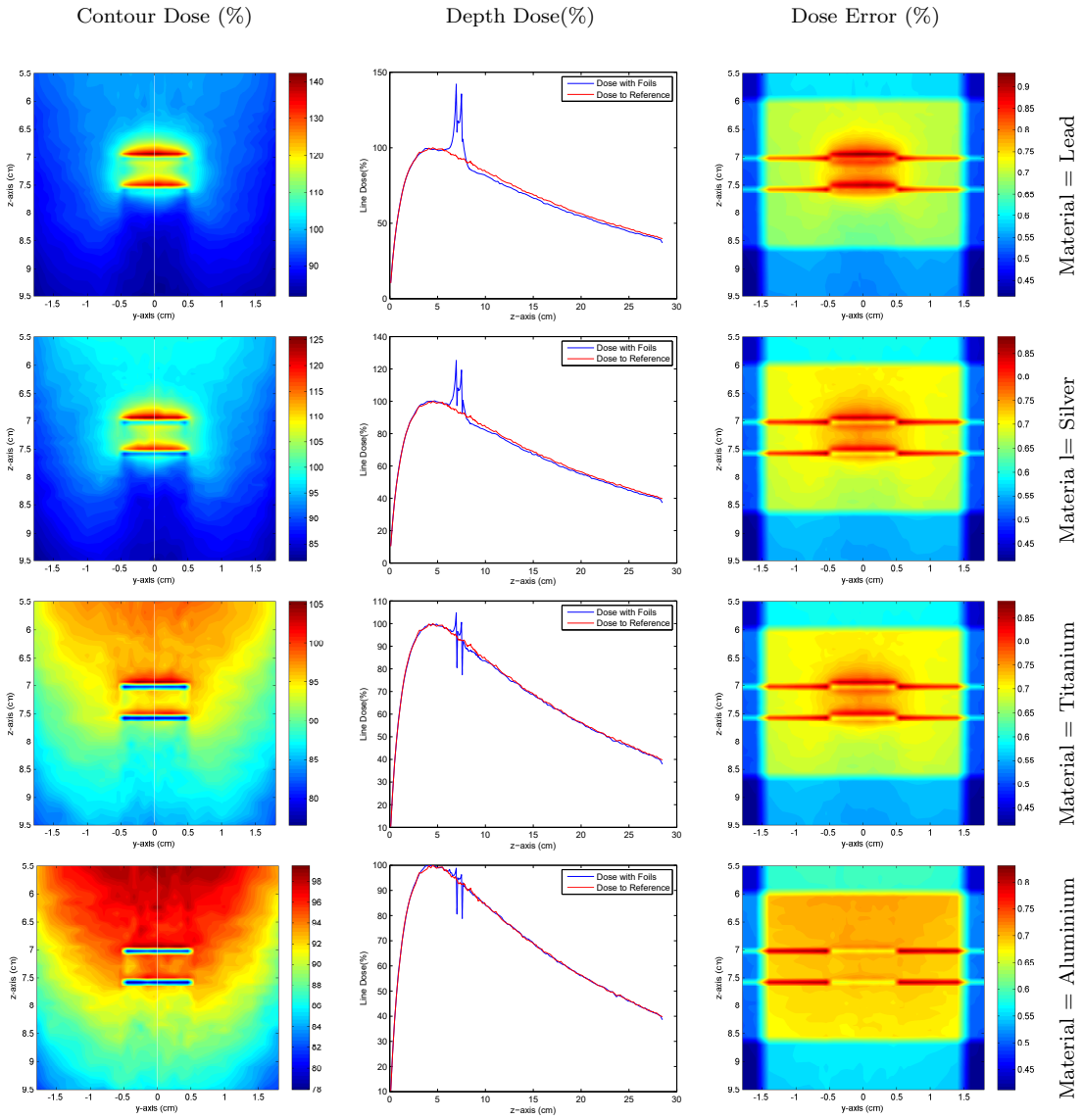

Thickness=0.5mm, Separation=7mm, Depth=7cm, Field Size=5cm x 5cm, Foil Size=1cm x 1cm

B.12 Effect of Foil Material - 6MV Horizontal

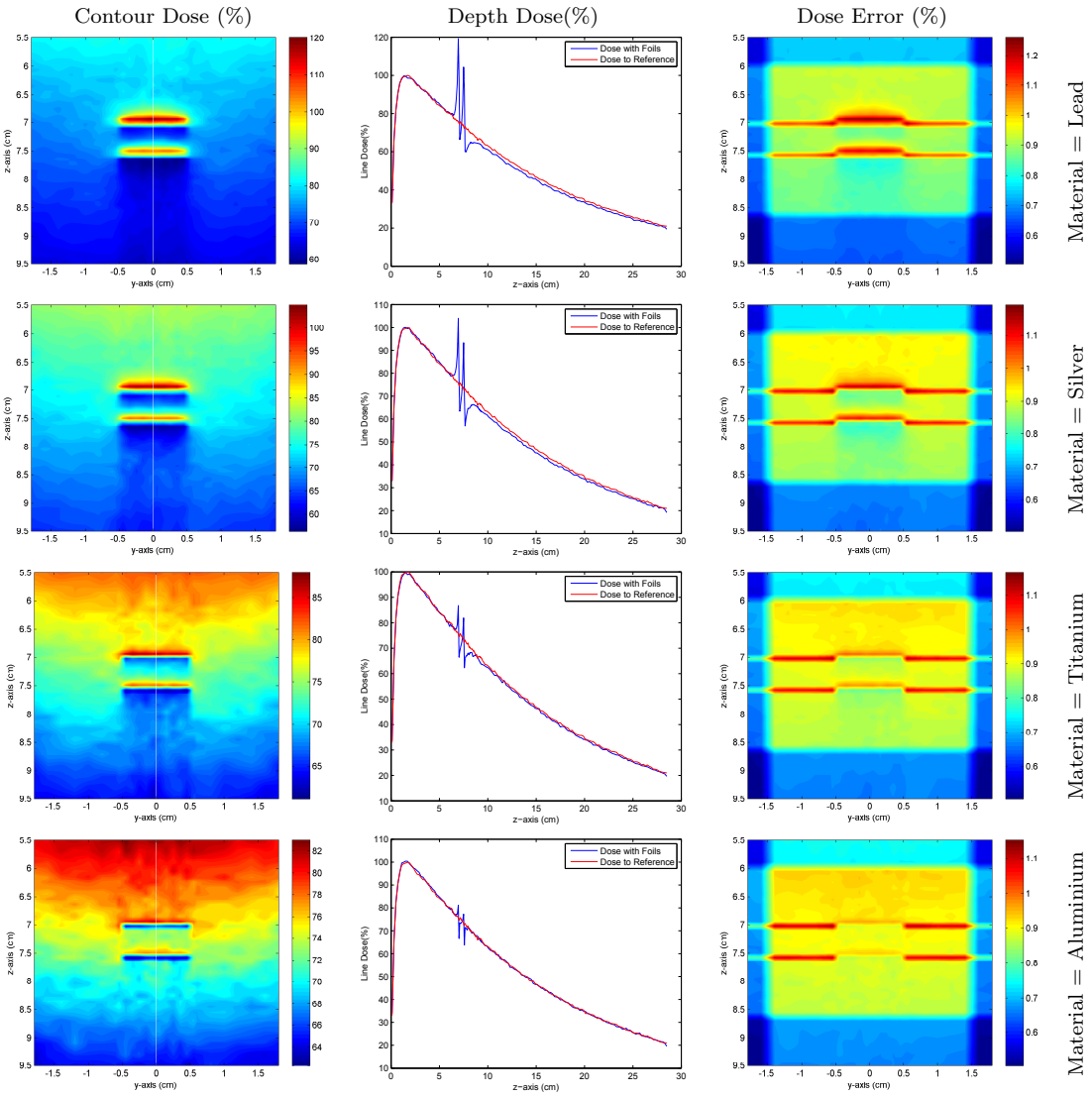

Thickness=0.5mm, Separation=7mm, Depth=7cm, Field Size=5cm x 5cm, Foil Size=1cm x 1cm

B.13 Effect of Foil Material - 24MV Vertical

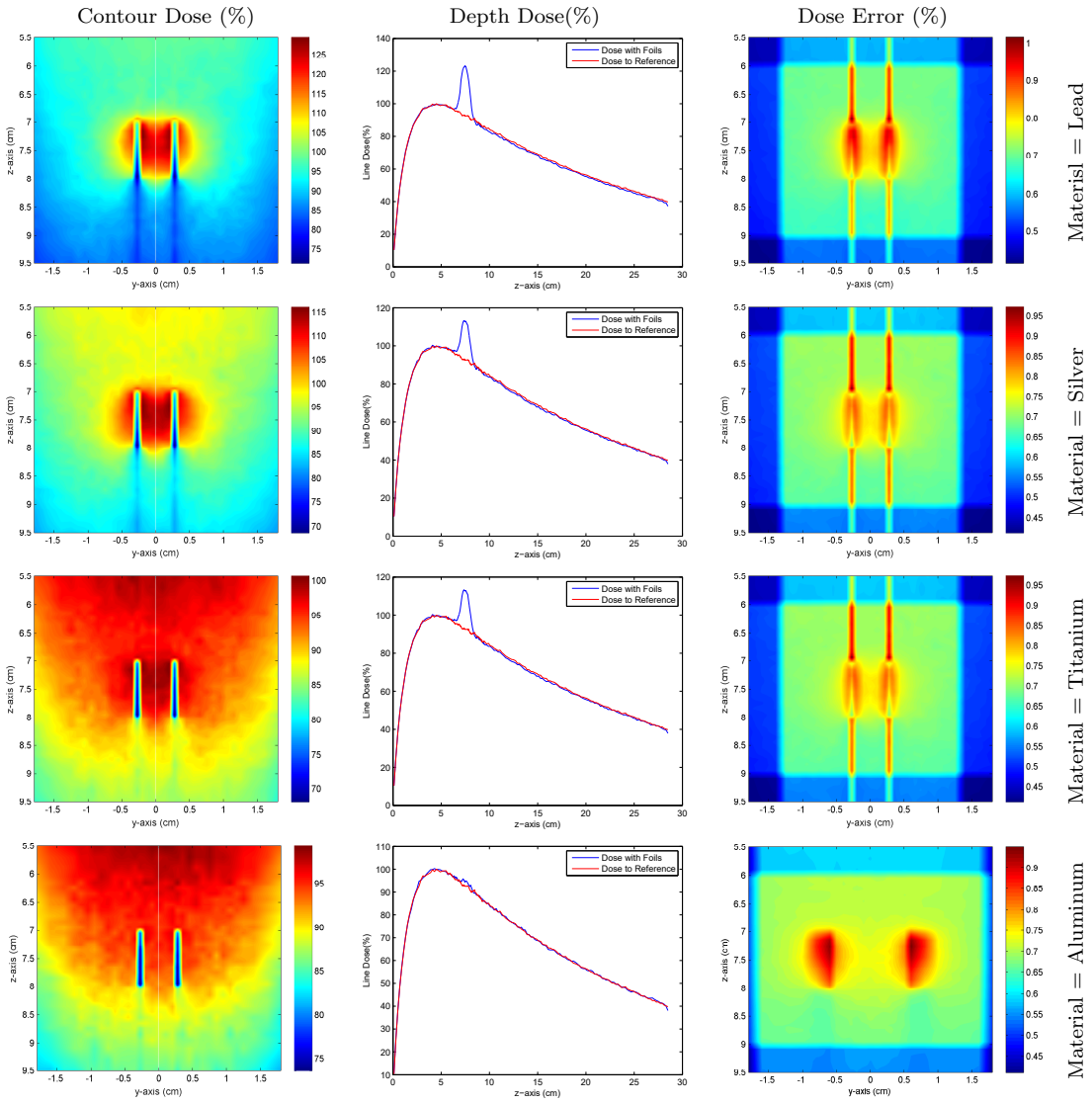

Thickness=0.5mm, Separation=7mm, Depth=7cm, Field Size=5cm x 5cm, Foil Size=1cm x 1cm

B.14 Effect of Foil Material - 6MV Vertical

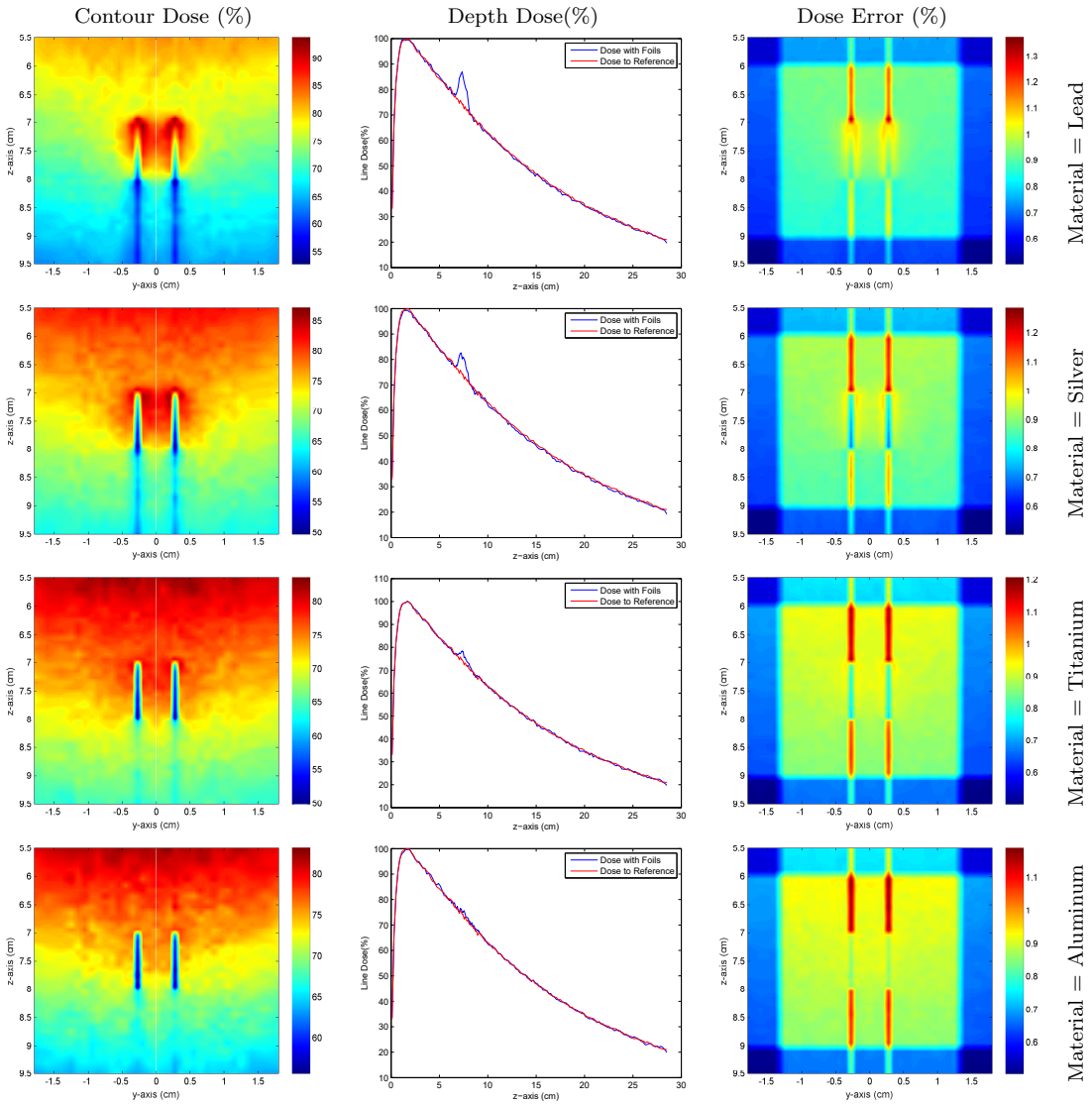

Thickness=0.5mm, Separation=7mm, Depth=7cm, Field Size=5cm x 5cm, Foil Size=1cm x 1cm

B.15 Effect of Foil Size - 24MV Horizontal

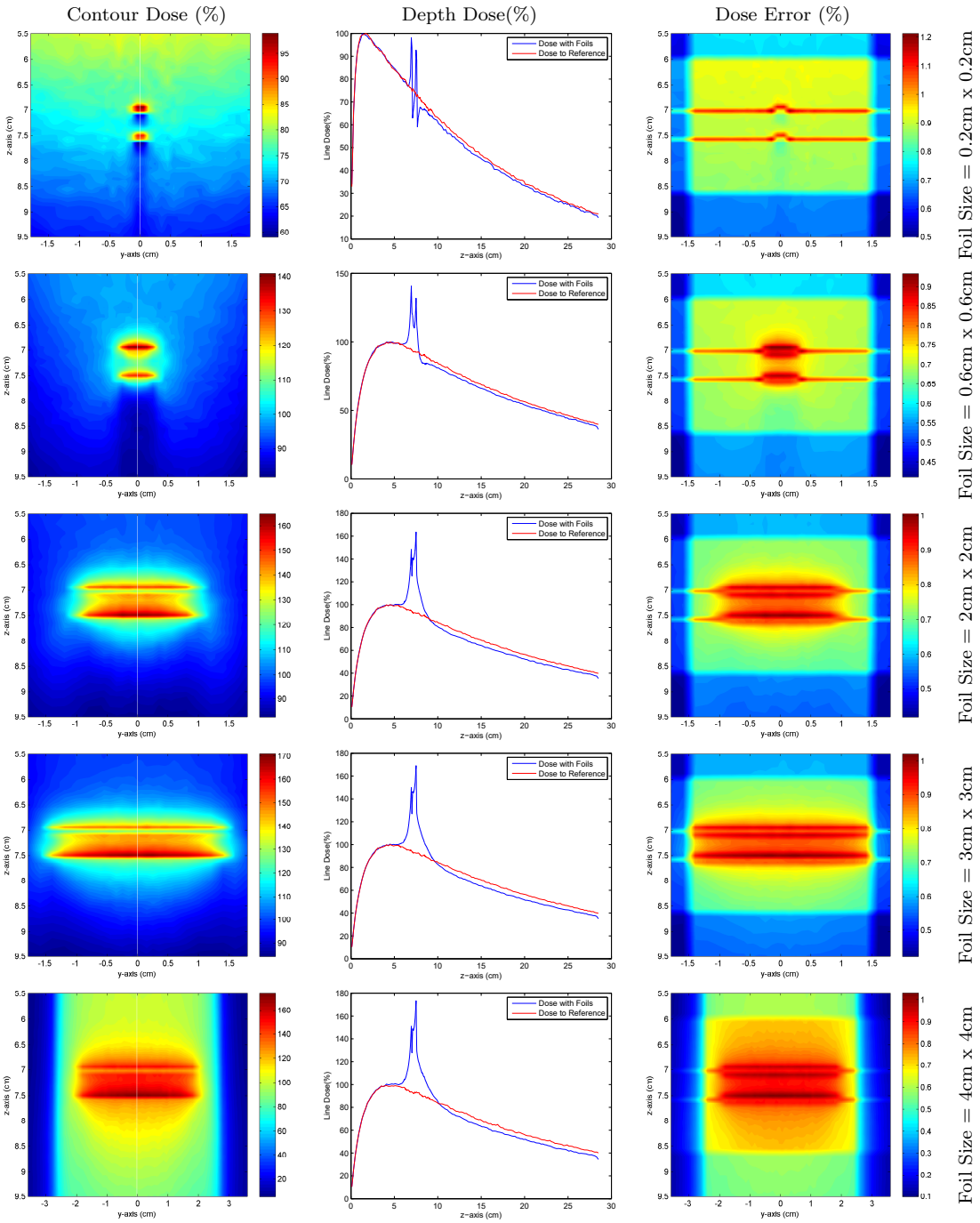

Effect of Foil Size - 24MV Horizontal (Continued)

Contour Dose (%) | Depth Dose(%) | Dose Error (%)

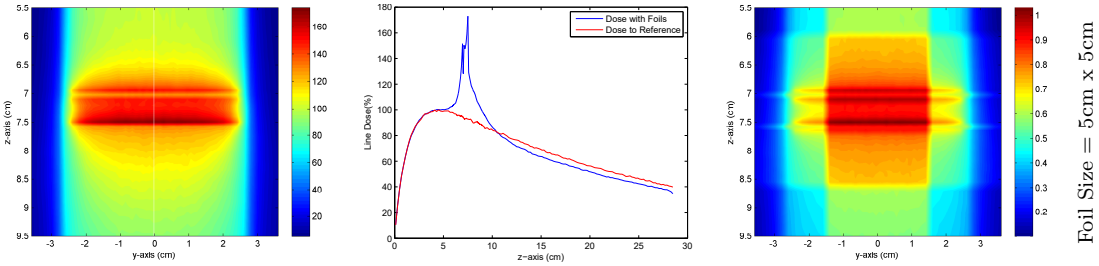

Foil Size = 5cm x 5cm

Thickness=0.5mm, Separation=7mm, Depth=7cm, Material=Lead, Field Size=5cm x 5cm,

B.16 Effect of Foil Size - 6MV Horizontal

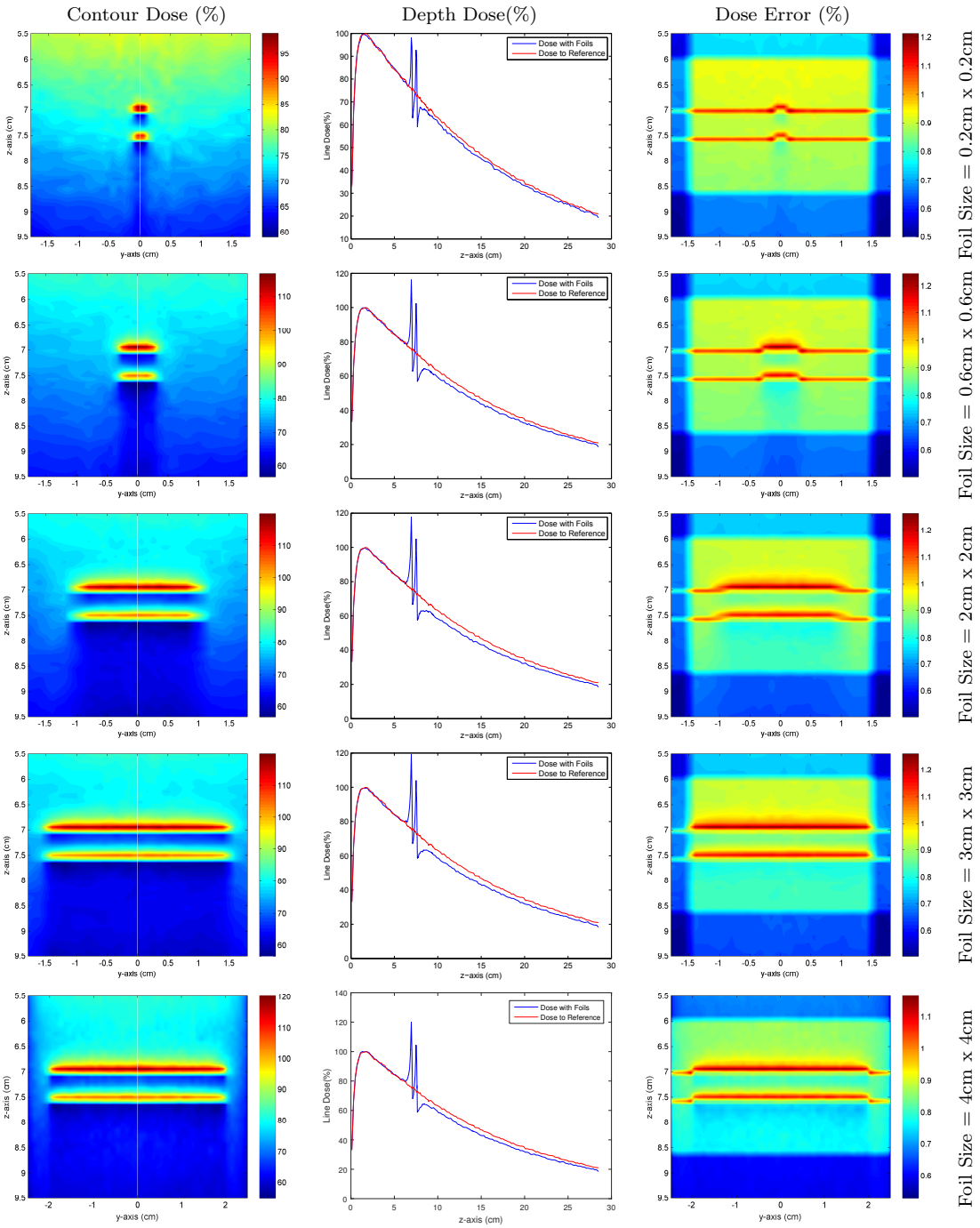

Effect of Foil Size - 6MV Horizontal (Continued)

Contour Dose (%) | Depth Dose(%) | Dose Error (%)

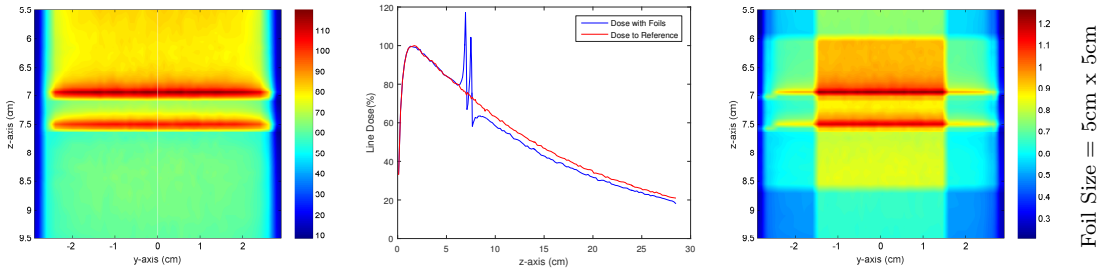

Foil Size = 5cm x 5cm

Thickness=0.5mm, Separation=7mm, Depth=7cm, Material=Lead, Field Size=5cm x 5cm

B.17 Effect of Foil Size - 24MV Vertical

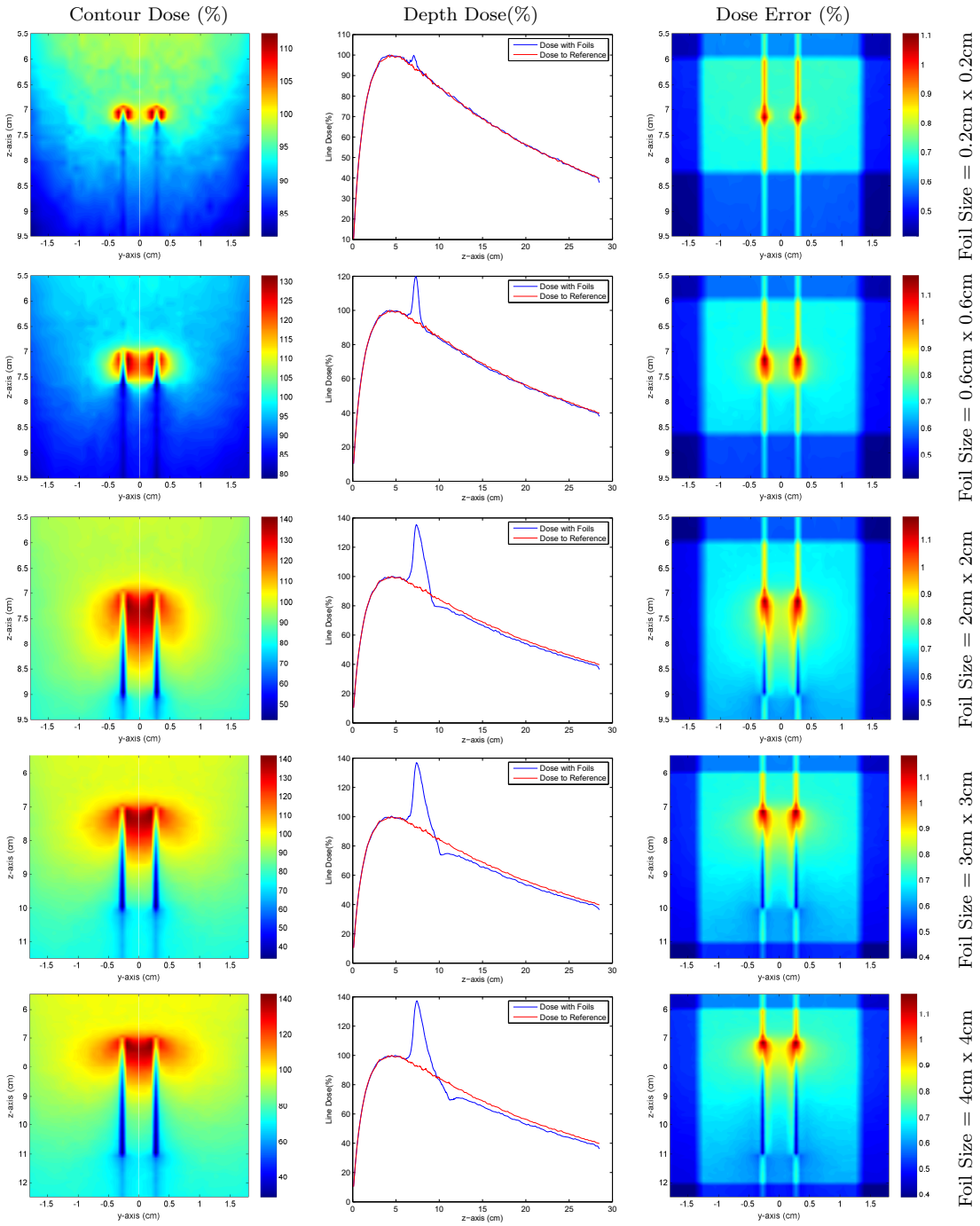

Effect of Foil Size - 24MV Vertical (Continued)

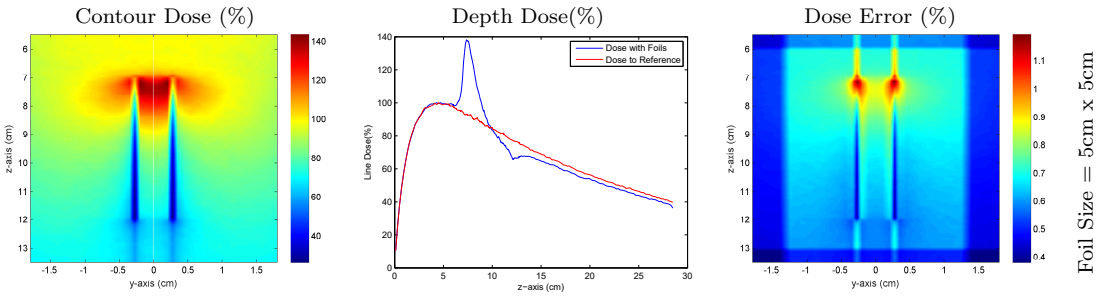

Thickness=0.5mm, Separation=7mm, Depth=7cm, Material=Lead, Field Size=5cm x 5cm

B.18 Effect of Foil Size - 6MV Vertical

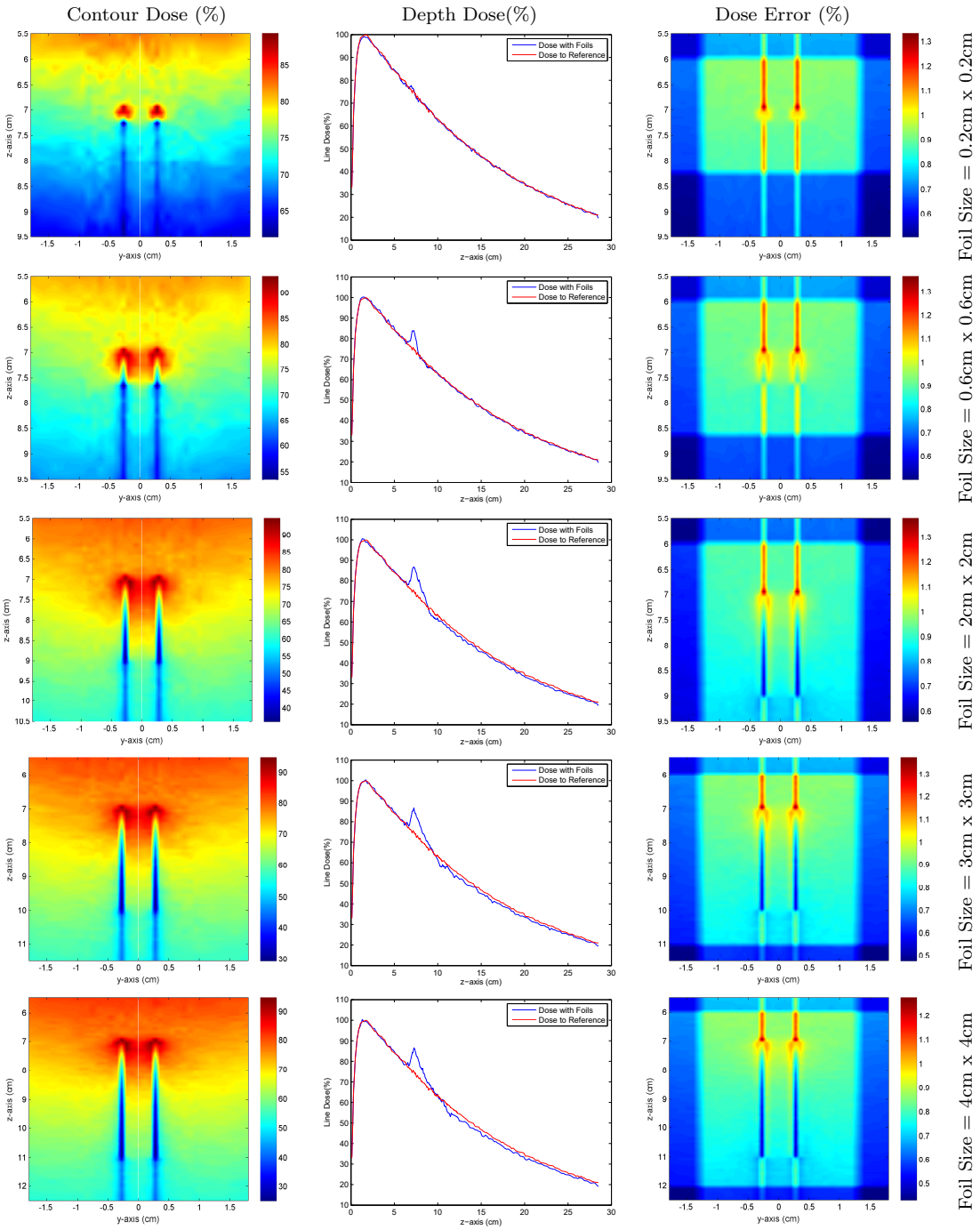

Effect of Foil Size - 6MV Vertical (Continued)

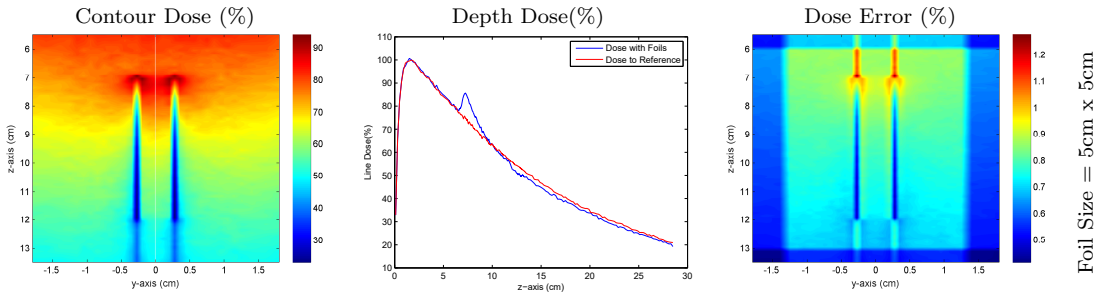

Thickness=0.5mm, Separation=7mm, Depth=7cm, Material=Lead, Field Size=5cm x 5cm

B.19 Effect of Field Size - 24MV Horizontal

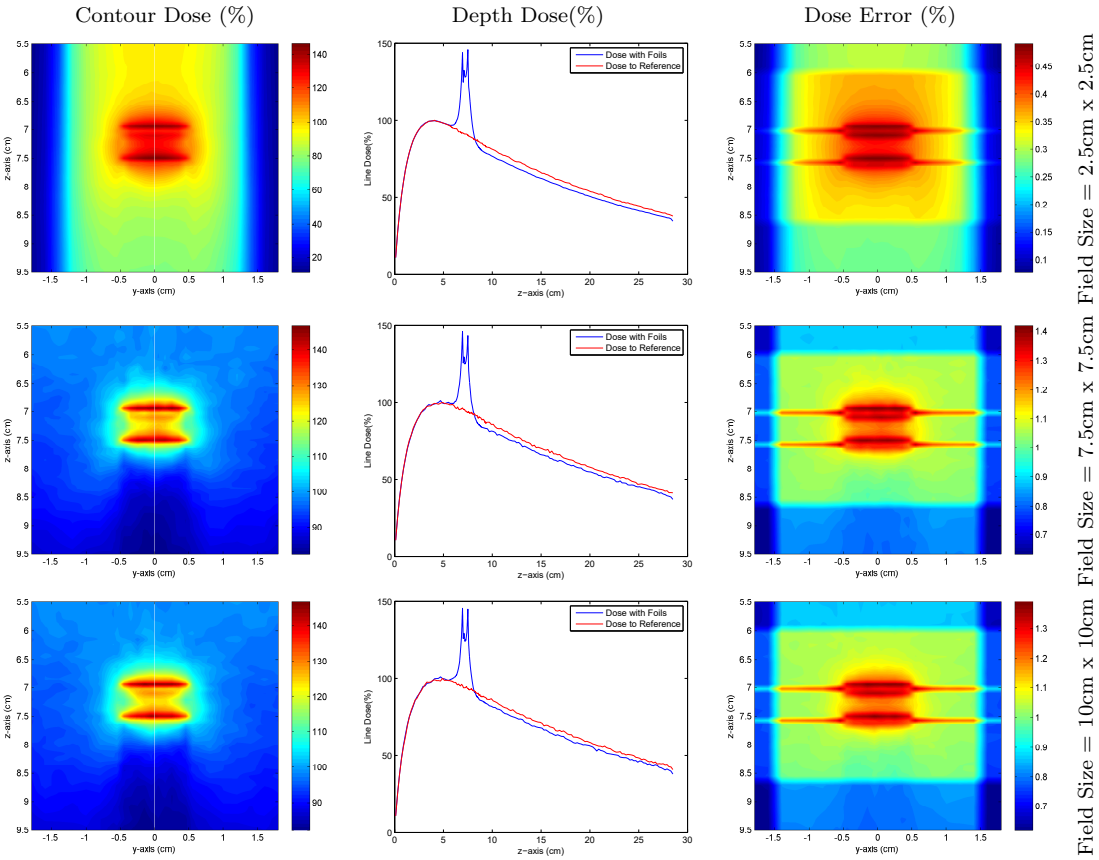

Thickness=0.5mm, Separation=7mm, Depth=7cm, Material=Lead, Foil Size=1cm x 1cm

B.20 Effect of Field Size - 6MV Horizontal

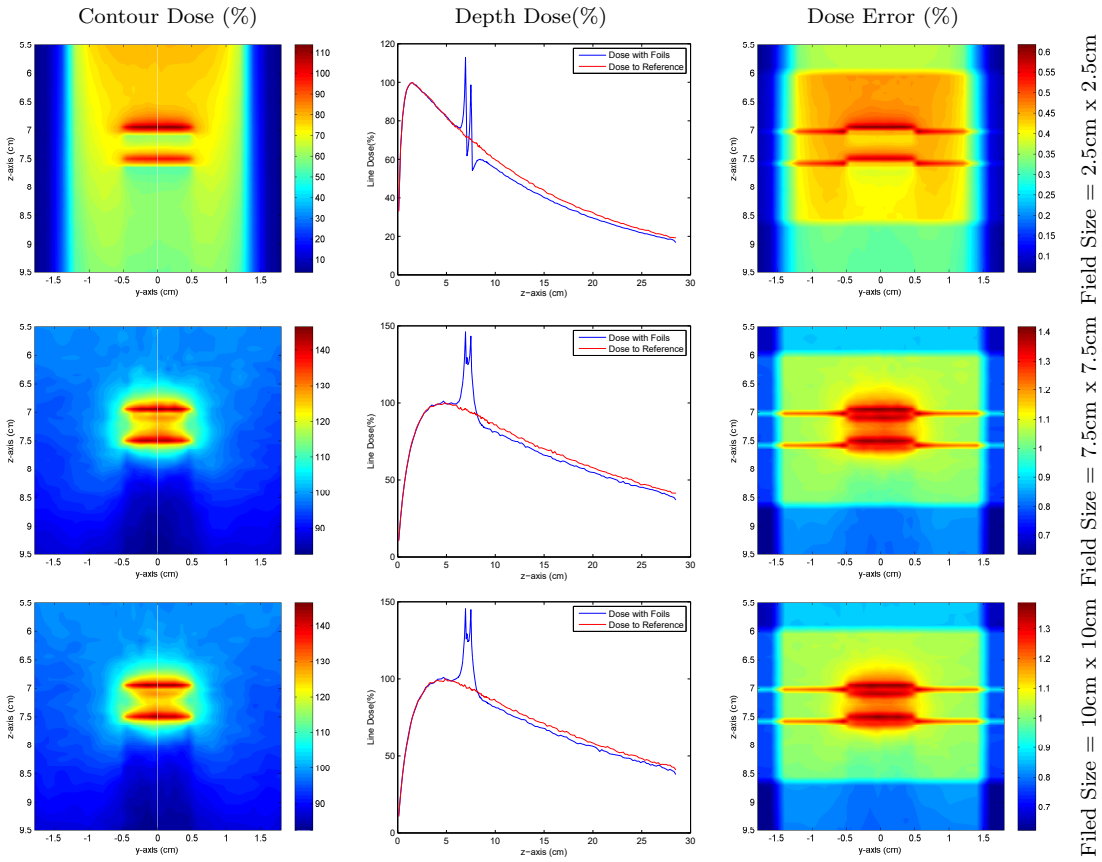

Thickness=0.5mm, Separation=7mm, Depth=7cm, Material=Lead, Foil Size=1cm x 1cm

B.21 Effect of Field Size - 24MV Vertical

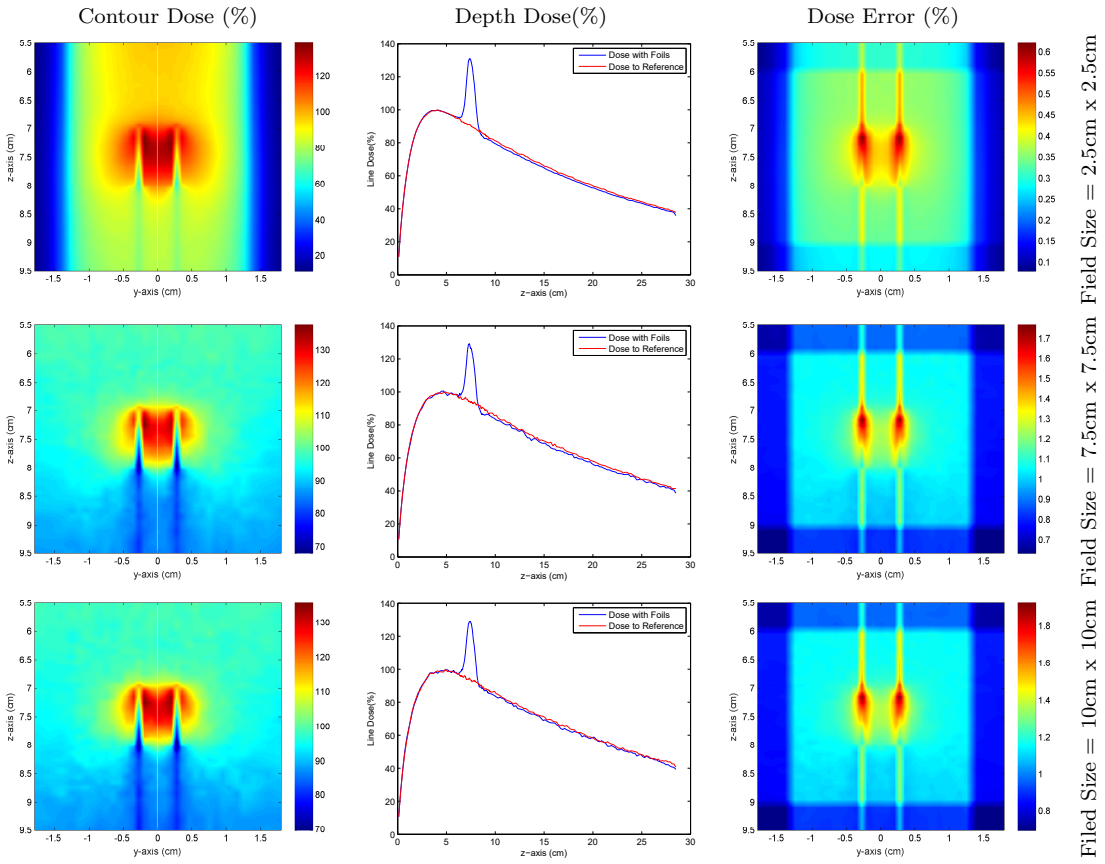

Thickness=0.5mm, Separation=7mm, Depth=7cm, Material=Lead, Foil Size=1cm x 5cm

B.22 Effect of Field Size - 6MV Vertical

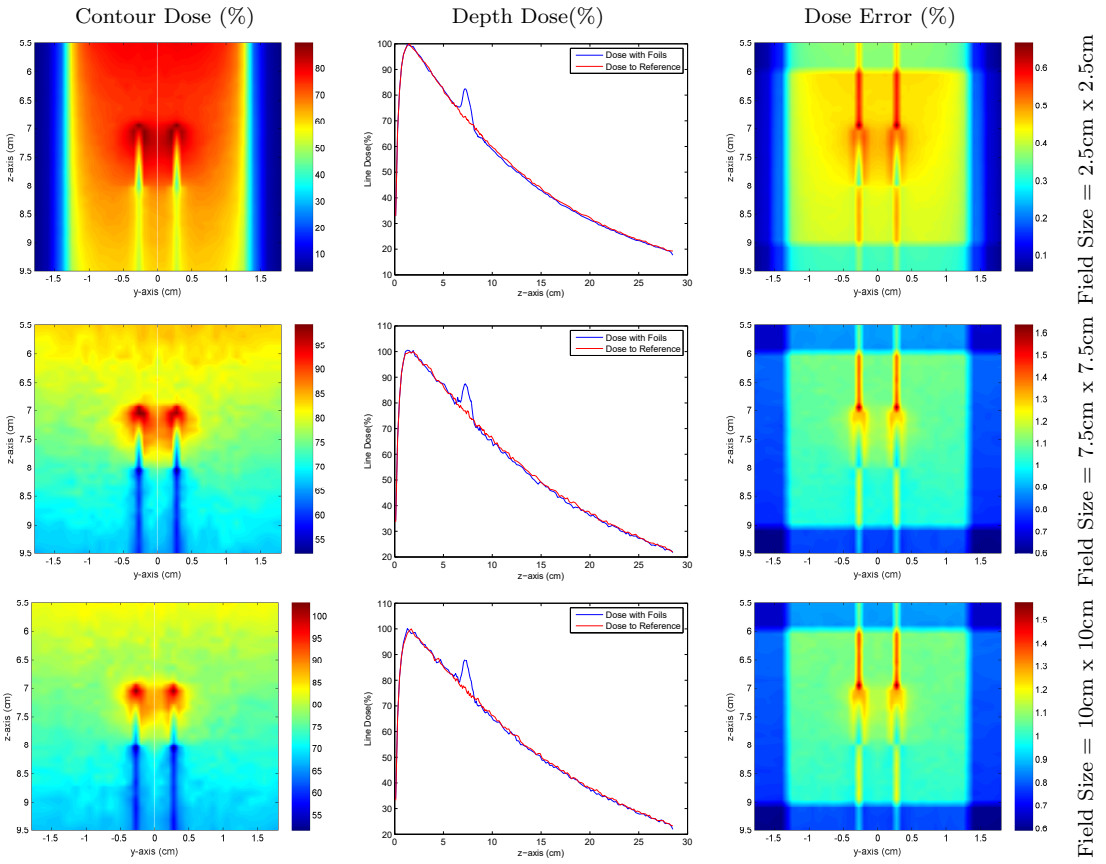

Thickness=0.5mm, Separation=7mm, Depth=7cm, Material=Lead, Foil Size=1cm x 1cm

B.23 Effect of Foil Depth - 24MV Horizontal

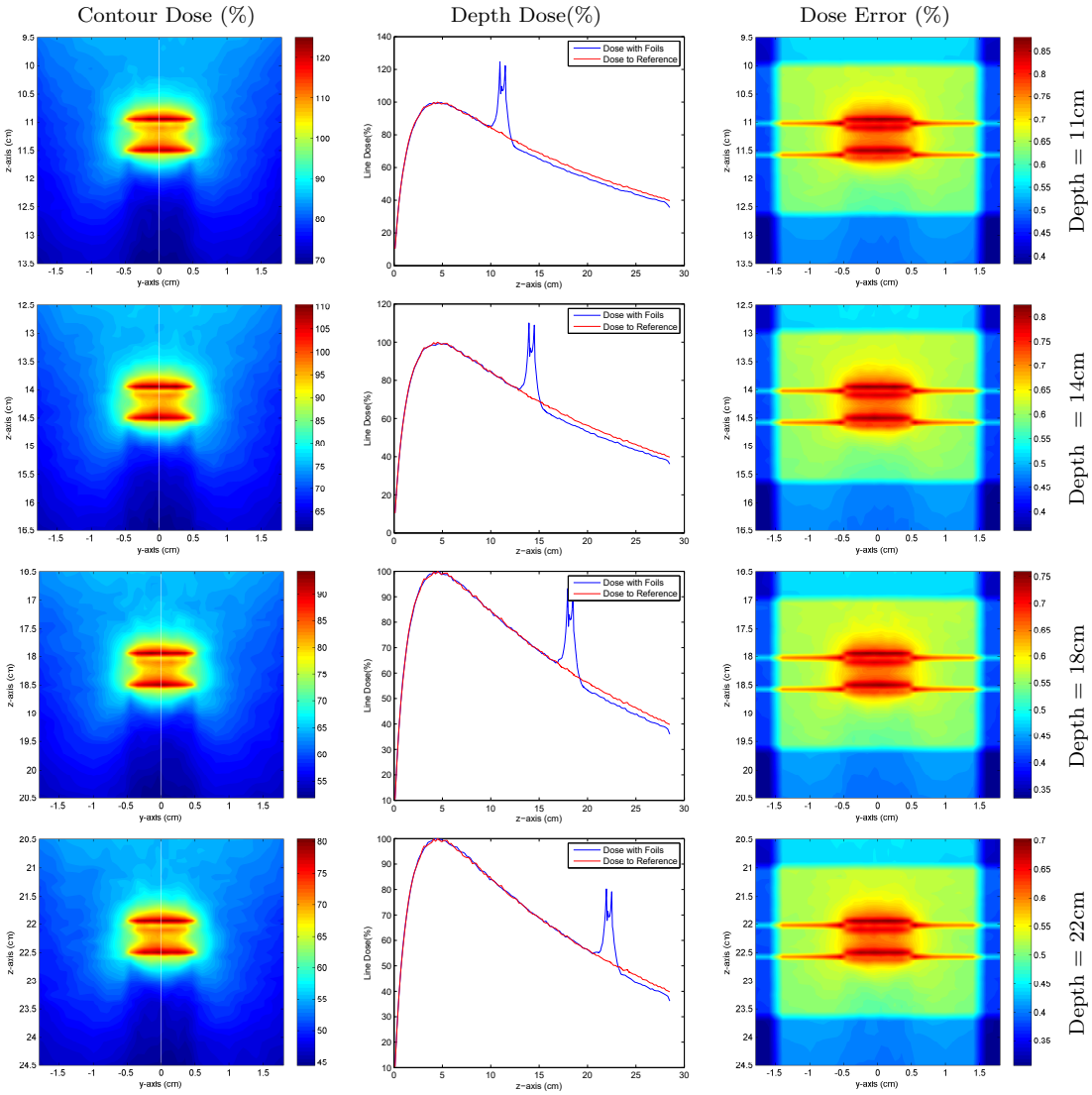

Thickness=0.5mm, Separation=7mm, Material=Gold, Field Size=5cm x 5cm, Foil Size=1cm x 1cm

B.24 Effect of Foil Depth - 6MV Horizontal

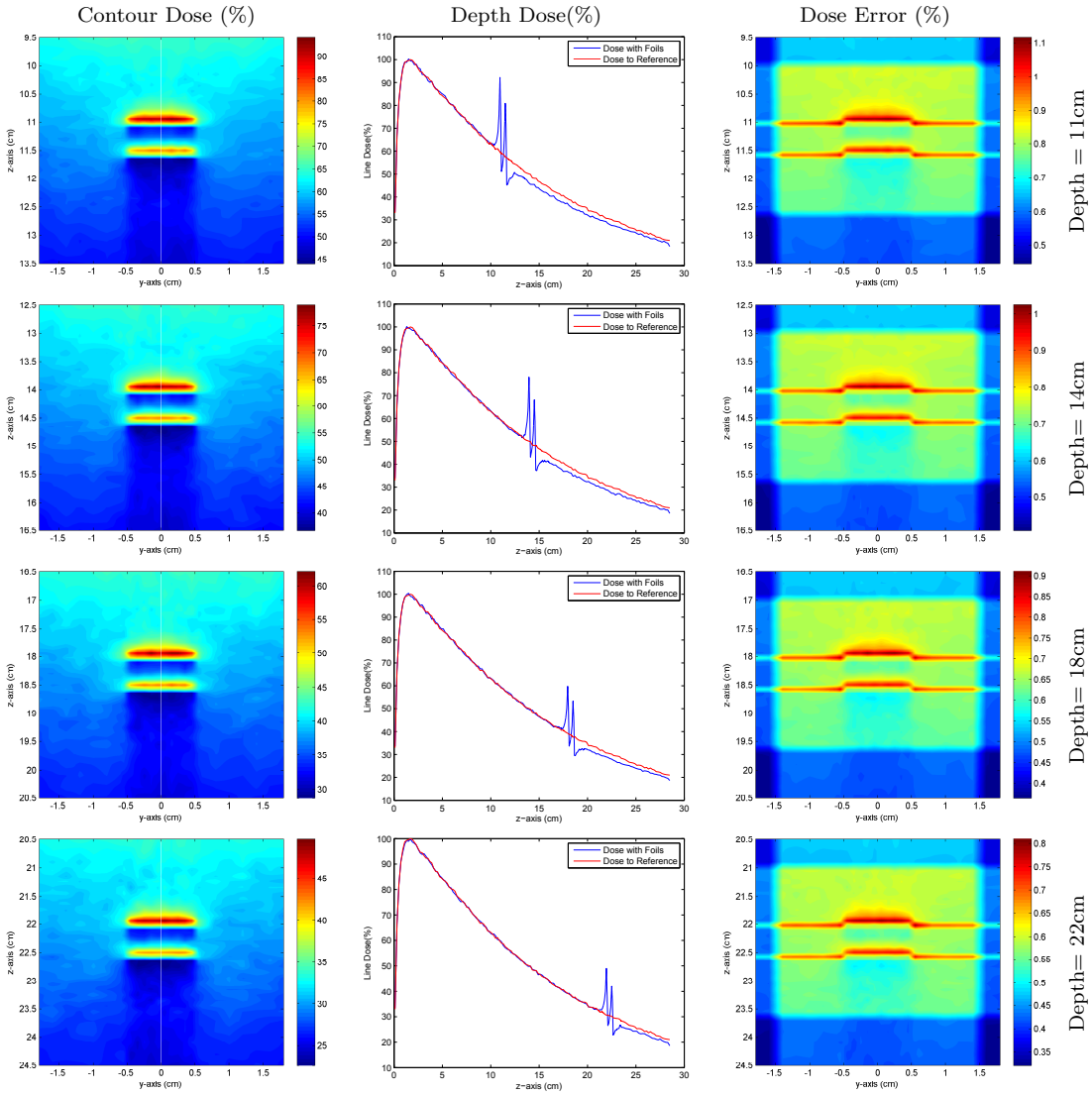

Thickness=0.5mm, Separation=7mm, Material=Lead, Field Size=5cm x 5cm, Foil Size=1cm x 1cm

B.25 Effect of Foil Depth - 24MV Vertical

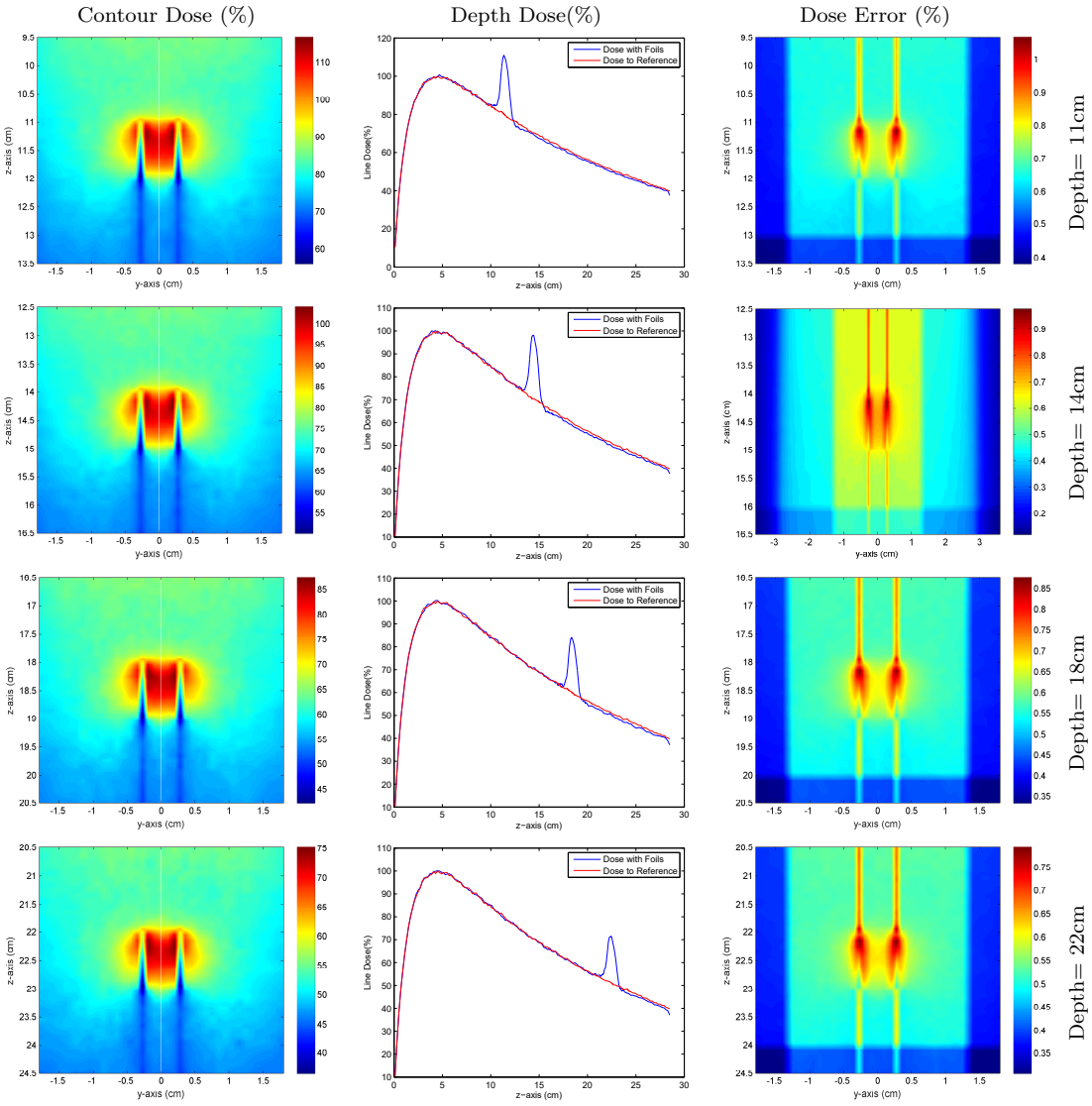

Thickness=0.5mm, Separation=7mm, Material=Lead, Field Size=5cm x 5cm

B.26 Effect of Foil Depth - 6MV Vertical

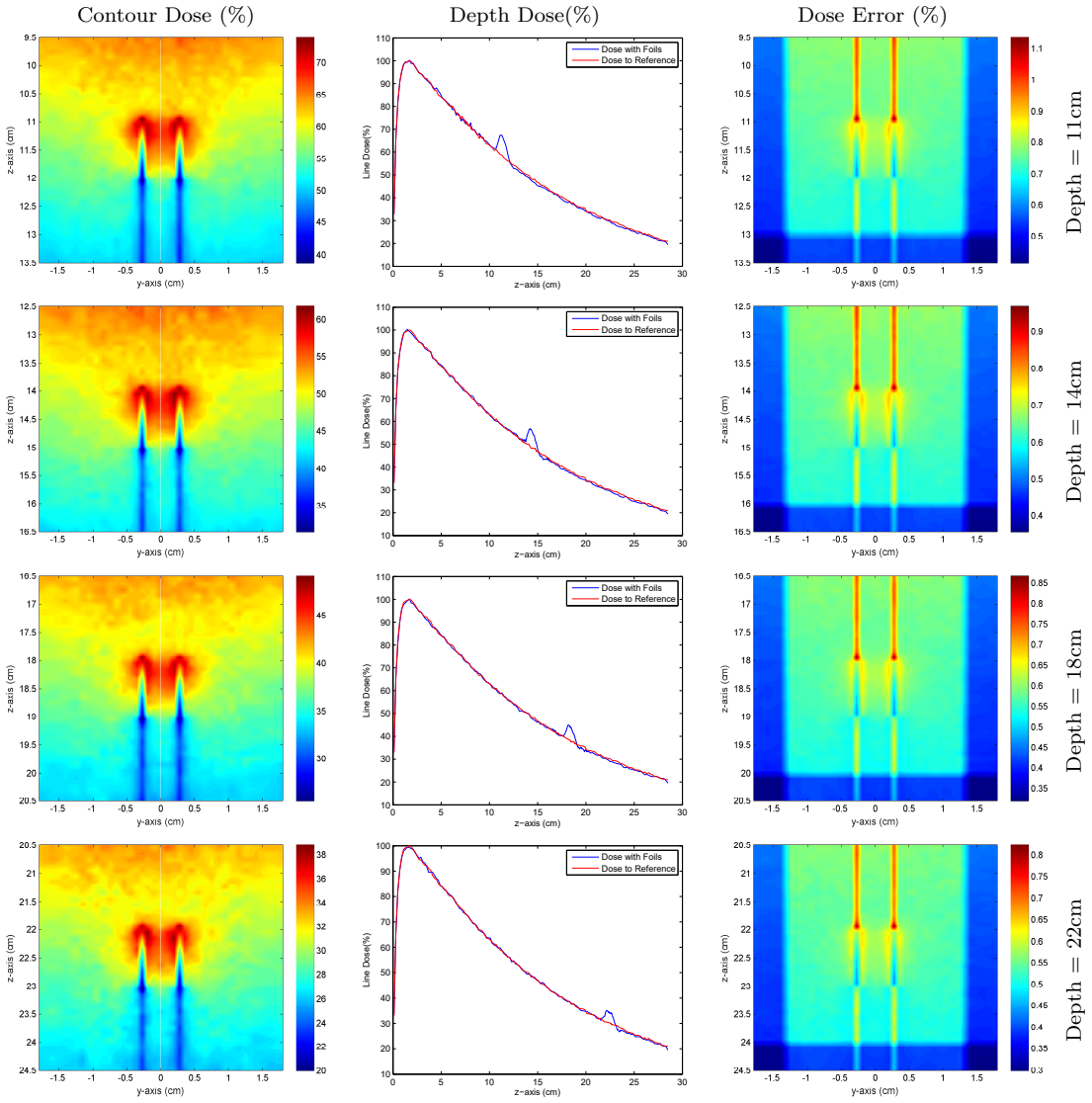

Thickness=0.5mm, Separation=7mm, Material=Lead, Field Size=5x5cm, Foil Size=1cm x 1cm

Appendix C

Multiple Foils

C.1 Effect of Foil Count - 24MV Upstream

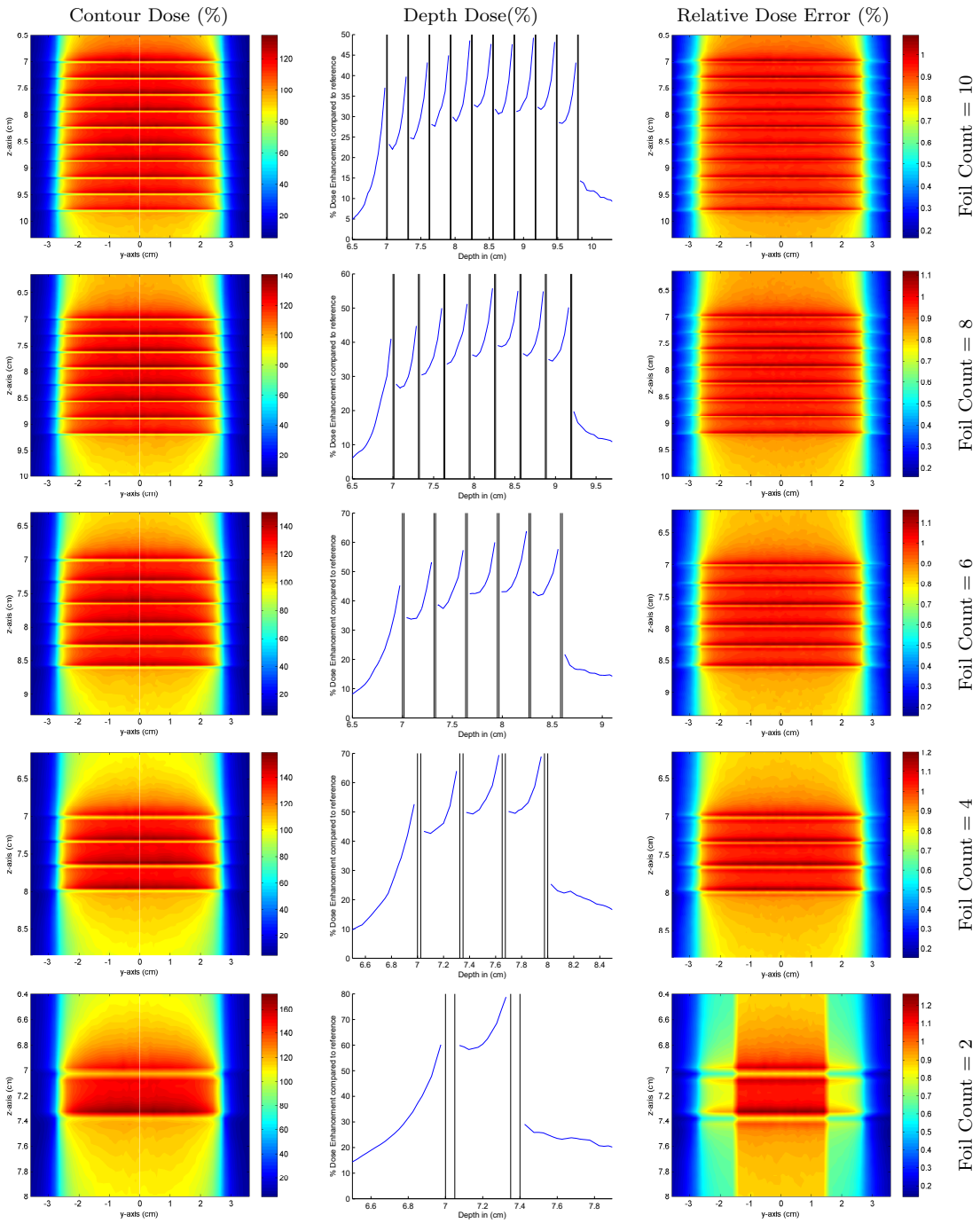

Effect of Foil Count - 24MV Upstream (Continued)

Contour Dose (%) | Depth Dose(%) | Relative Dose Error (%)

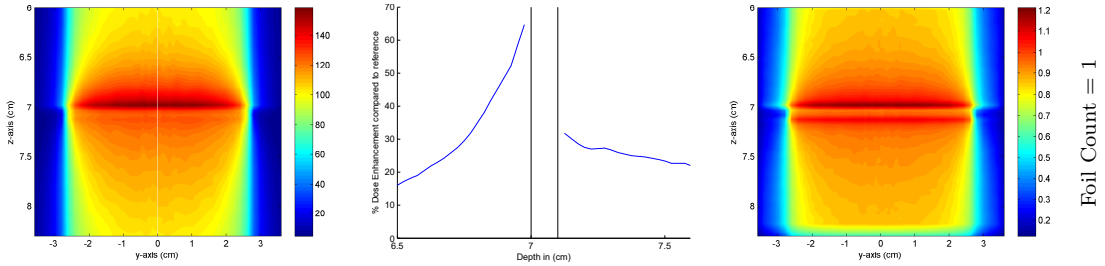

Foil Count = 1

Material=Lead, Separation=3mm, Field Size=5cm x 5cm, Foil Size=7cm x 7cm

C.2 Effect of Foil Count - 6MV Upstream

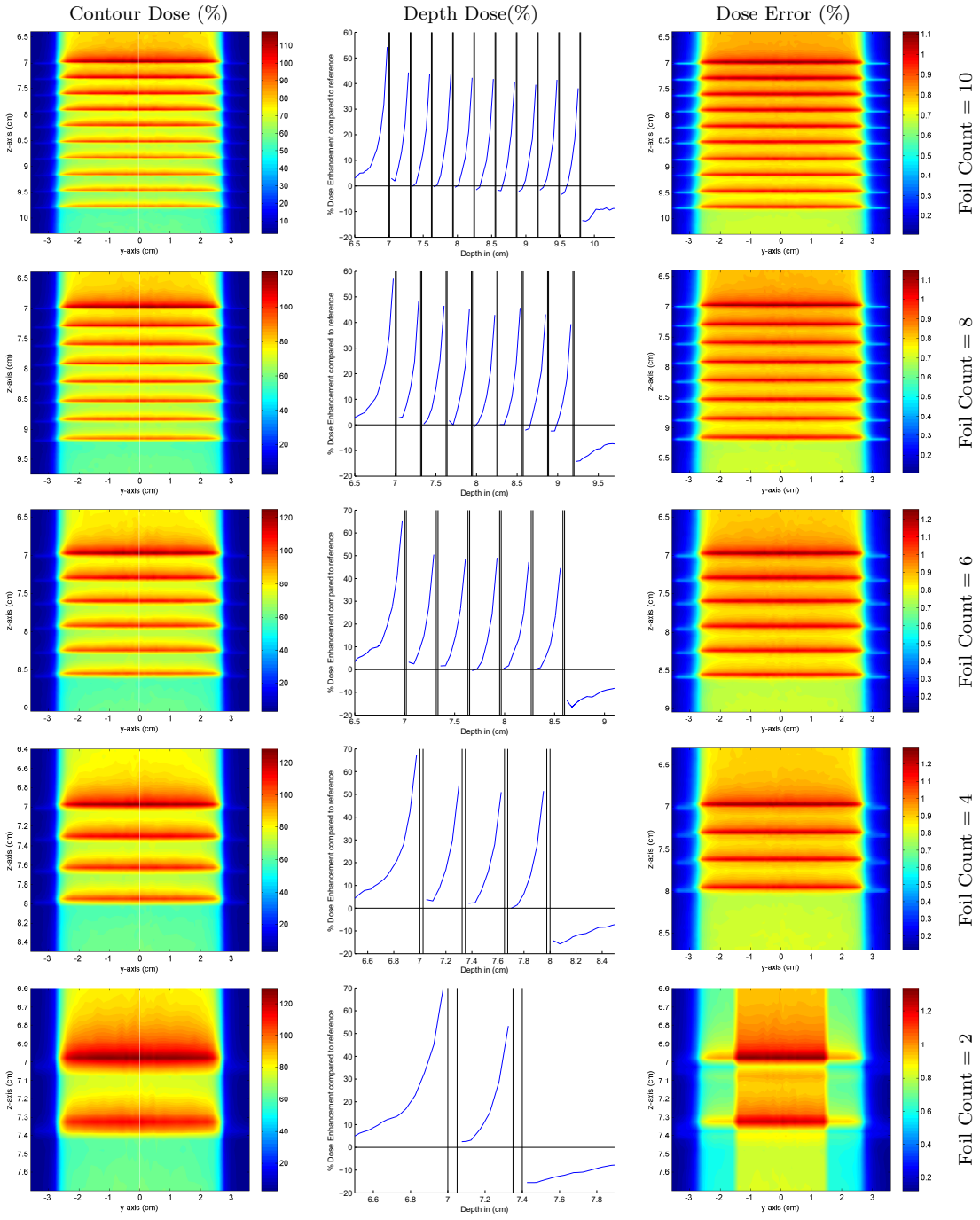

Effect of Foil Count - 6MV Upstream (Continued)

Contour Dose (%) | Depth Dose(%) | Dose Error (%)

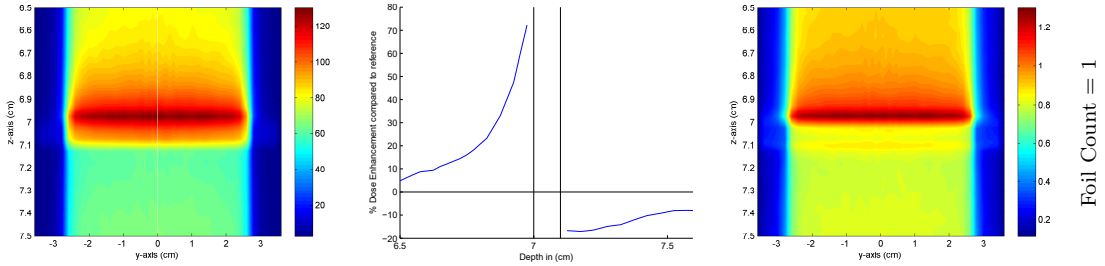

Foil Count = 1

Separation=3mm, Depth=7cm, Material=Lead, Field Size=5x5cm, Foil Size=7cm x7cm

C.3 Effect of Foil Count - 24MV Downstream

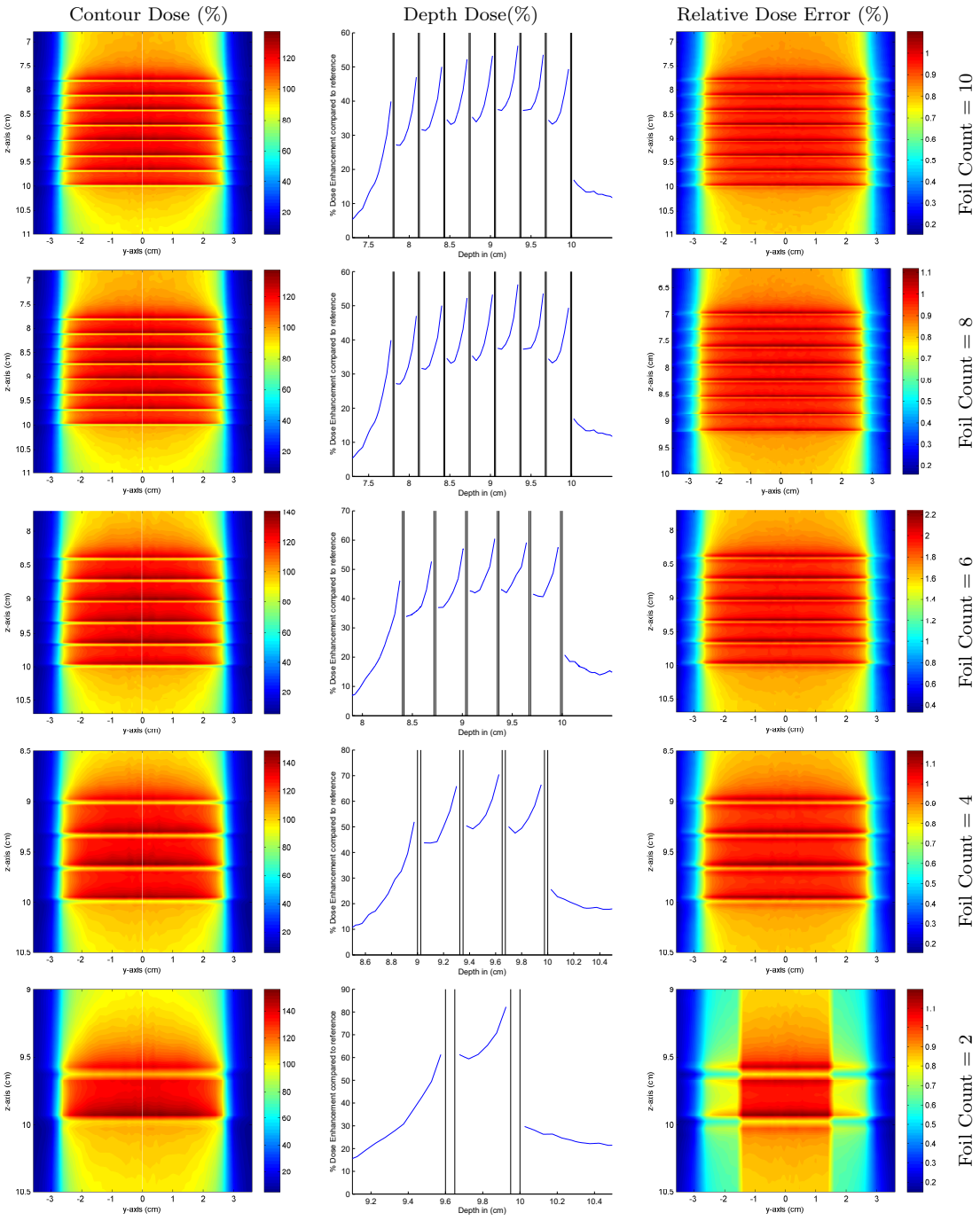

Effect of Foil Count - 24MV Downstream (Continued)

Contour Dose (%) | Depth Dose(%) | Relative Dose Error (%)

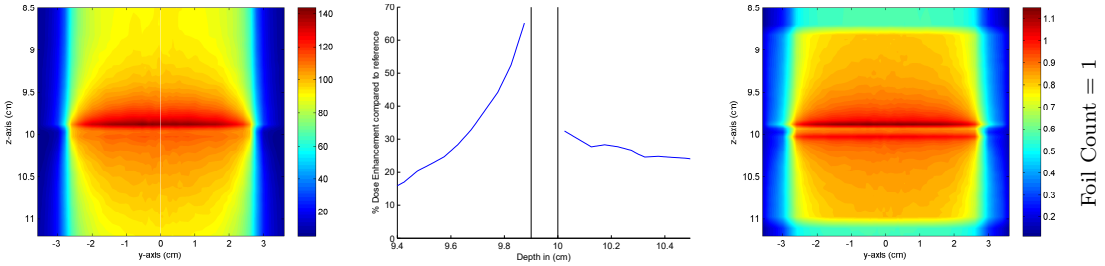

Foil Count = 1

Separation=3mm, Material=Lead, Field Size=5cm x 5cm, Foil Size=7cm x 7cm

C.4 Effect of Foil Count - 6MV Downstream

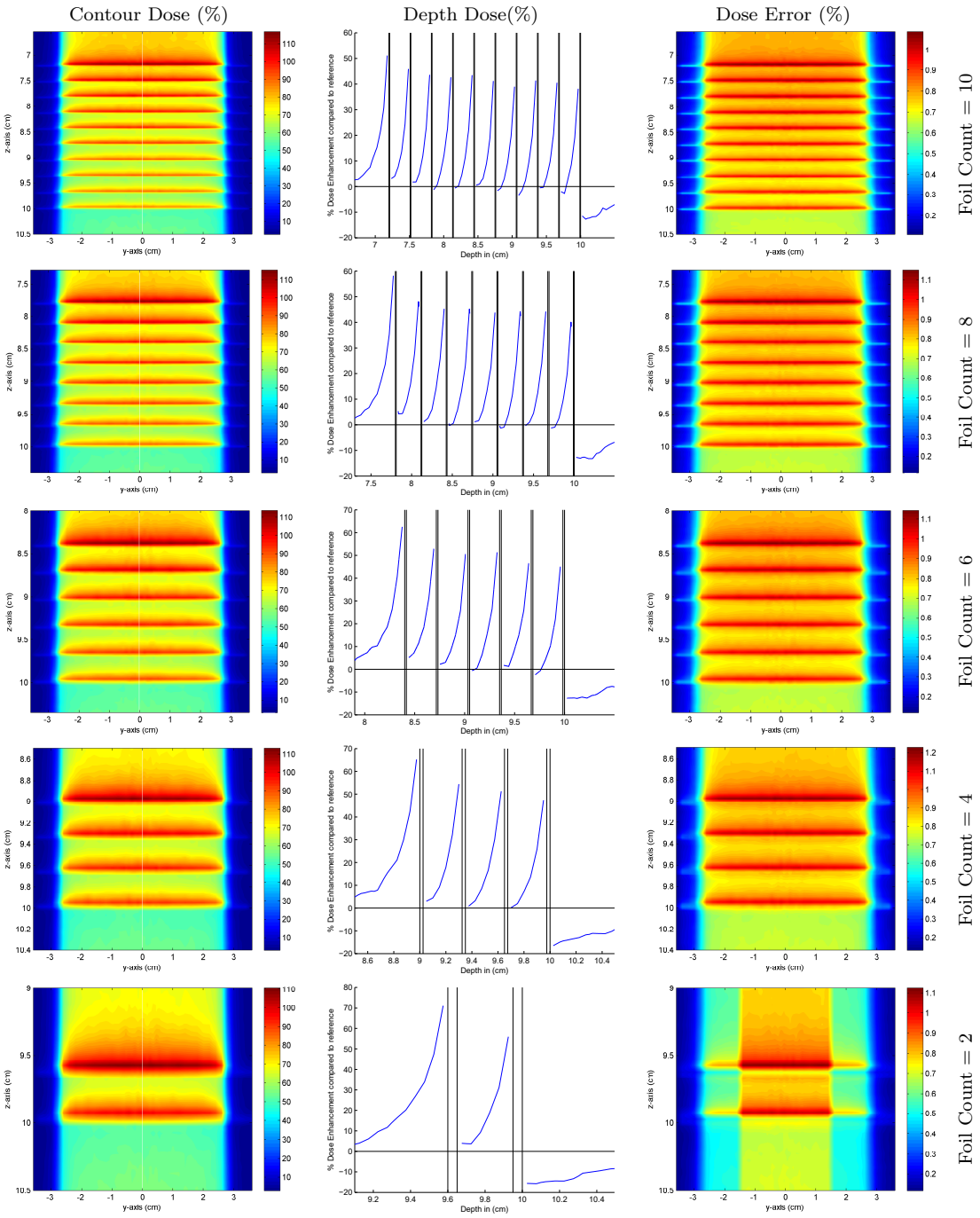

Effect of Foil Count - 6MV Downstream (Continued)

Contour Dose (%) | Depth Dose(%) | Dose Error (%)

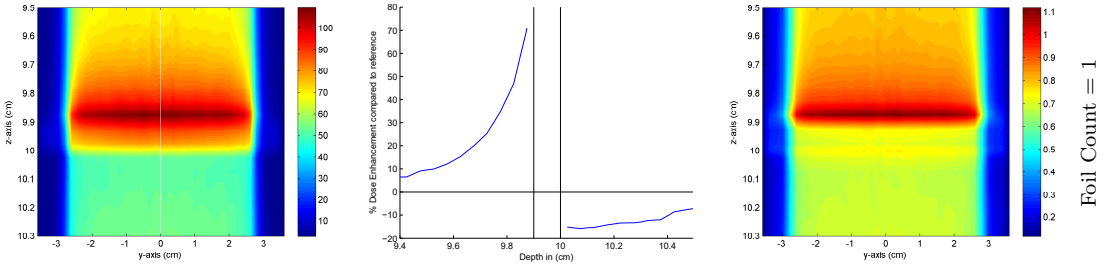

Foil Count = 1

Separation=3mm, Thickness=0.5mm, Material=Lead, Field Size=5cm x 5cm, Foil Size=1cm x 1cm

C.5 Effect of Separation - 24MV

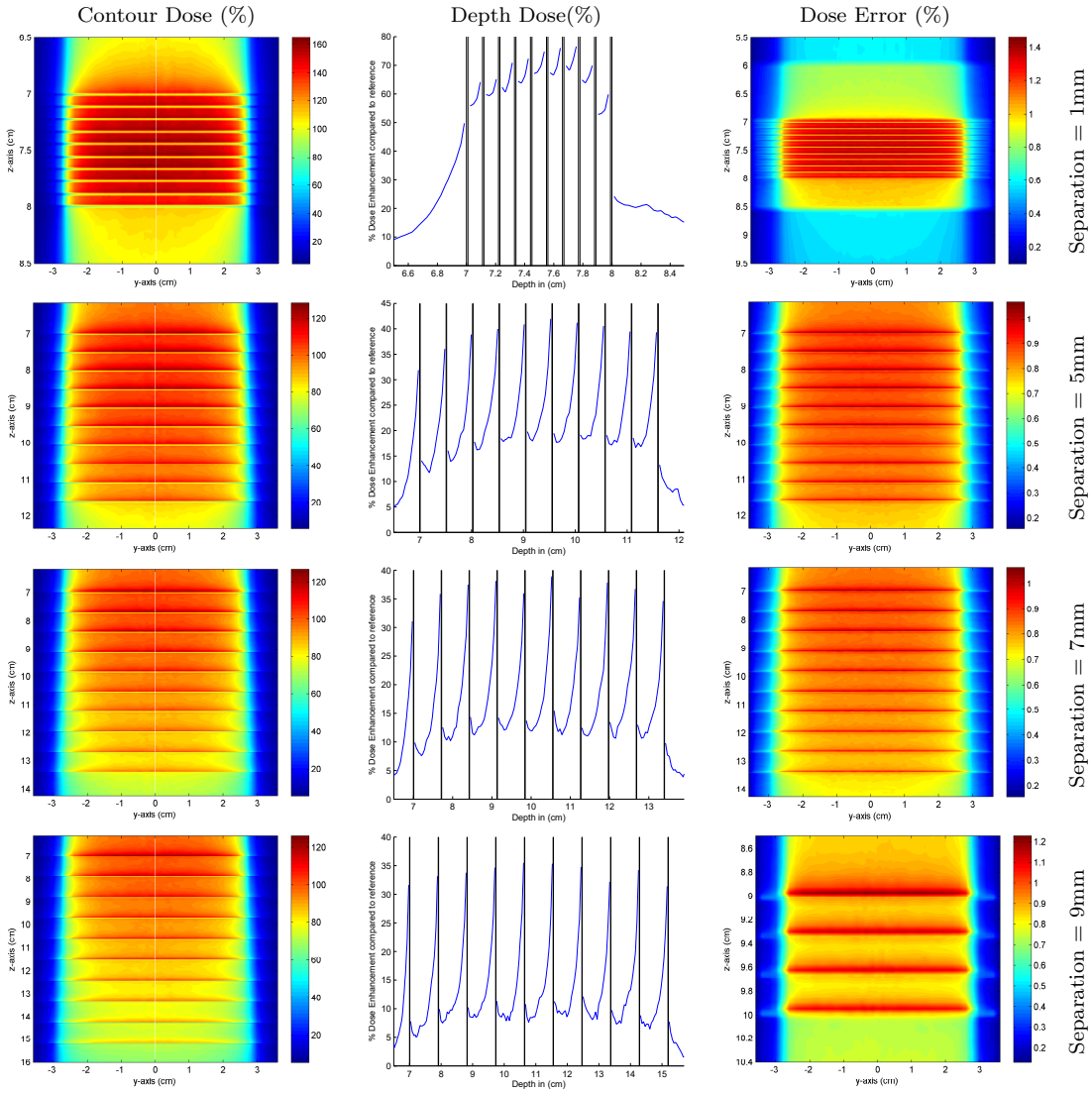

Separation=3mm, Thickness=0.1mm, Material=Lead, Field Size=5cm x 5cm, Foil Size=7cm x 7cm

C.6 Effect of Separation - 24MV Single Foil Downstream

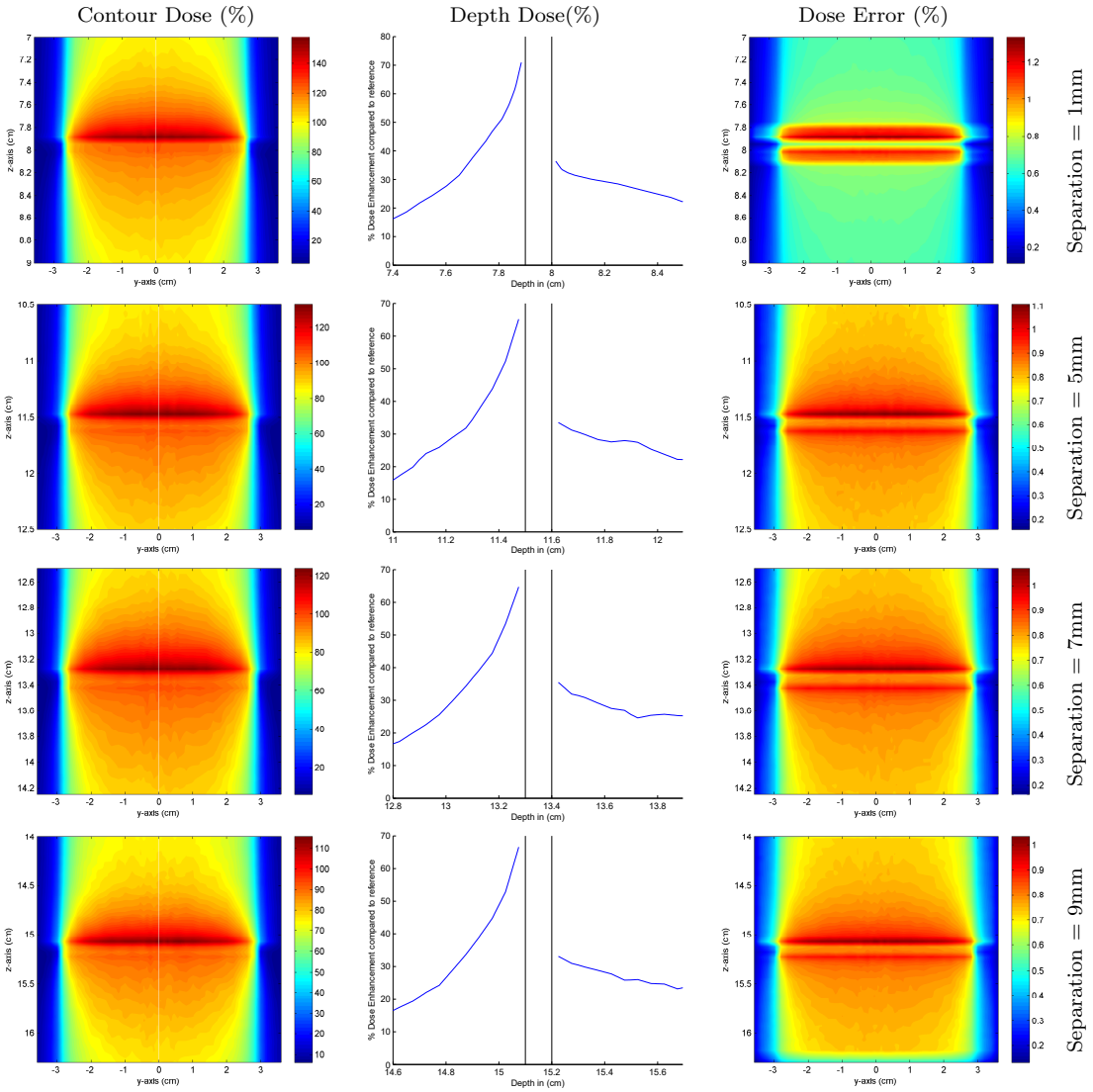

Separation=3mm, Thickness=0.1mm, Material=Lead, Field Size=5cm x 5cm, Foil Size=7cm x 7cm

C.7 Effect of Separation - 6MV

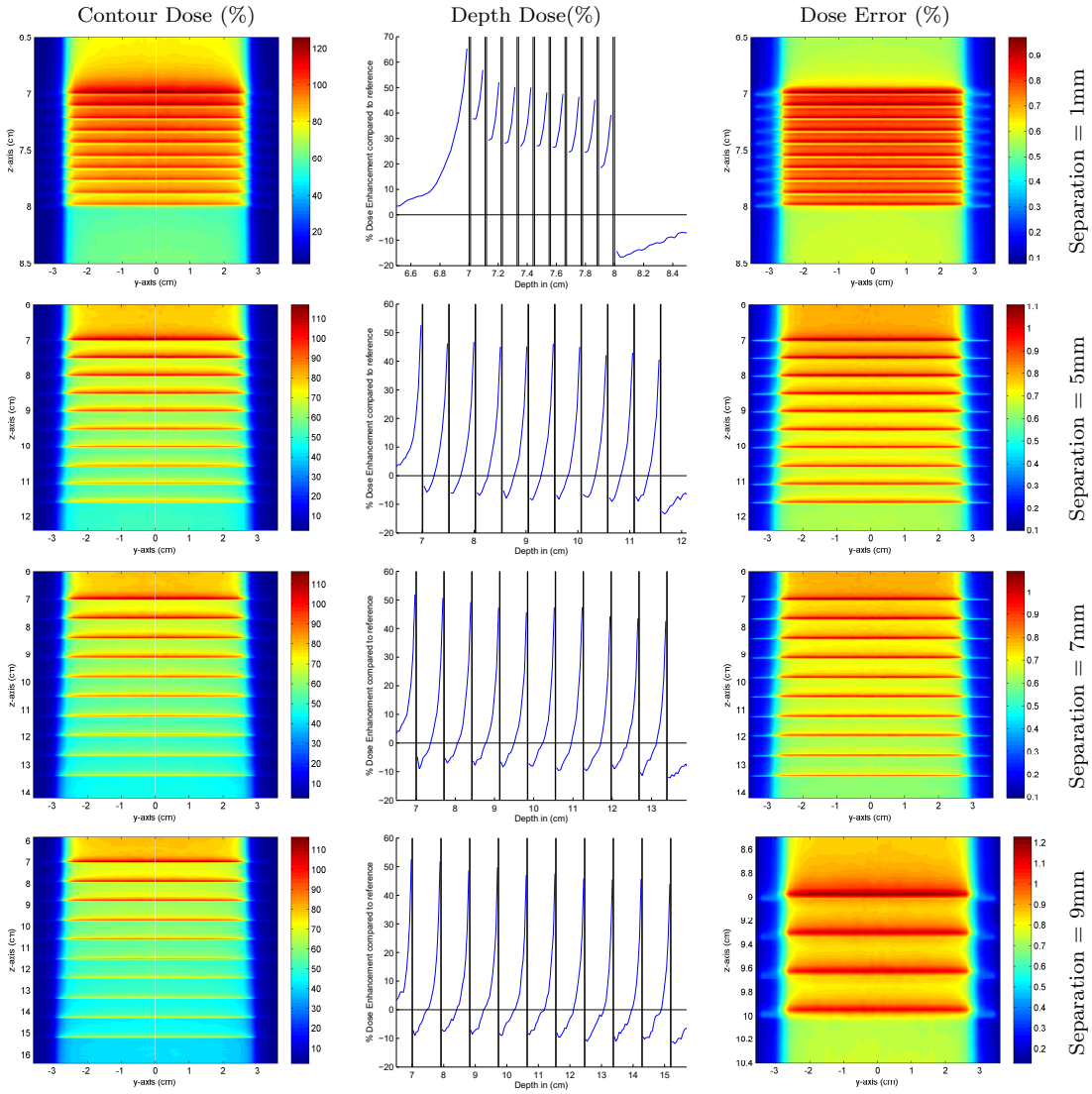

Thickness=0.1mm, Material=Lead, Field Size=5cm x 5cm, Foil Size=7cm x 7cm

C.8 Effect of Separation - 6MV Single Foil Downstream

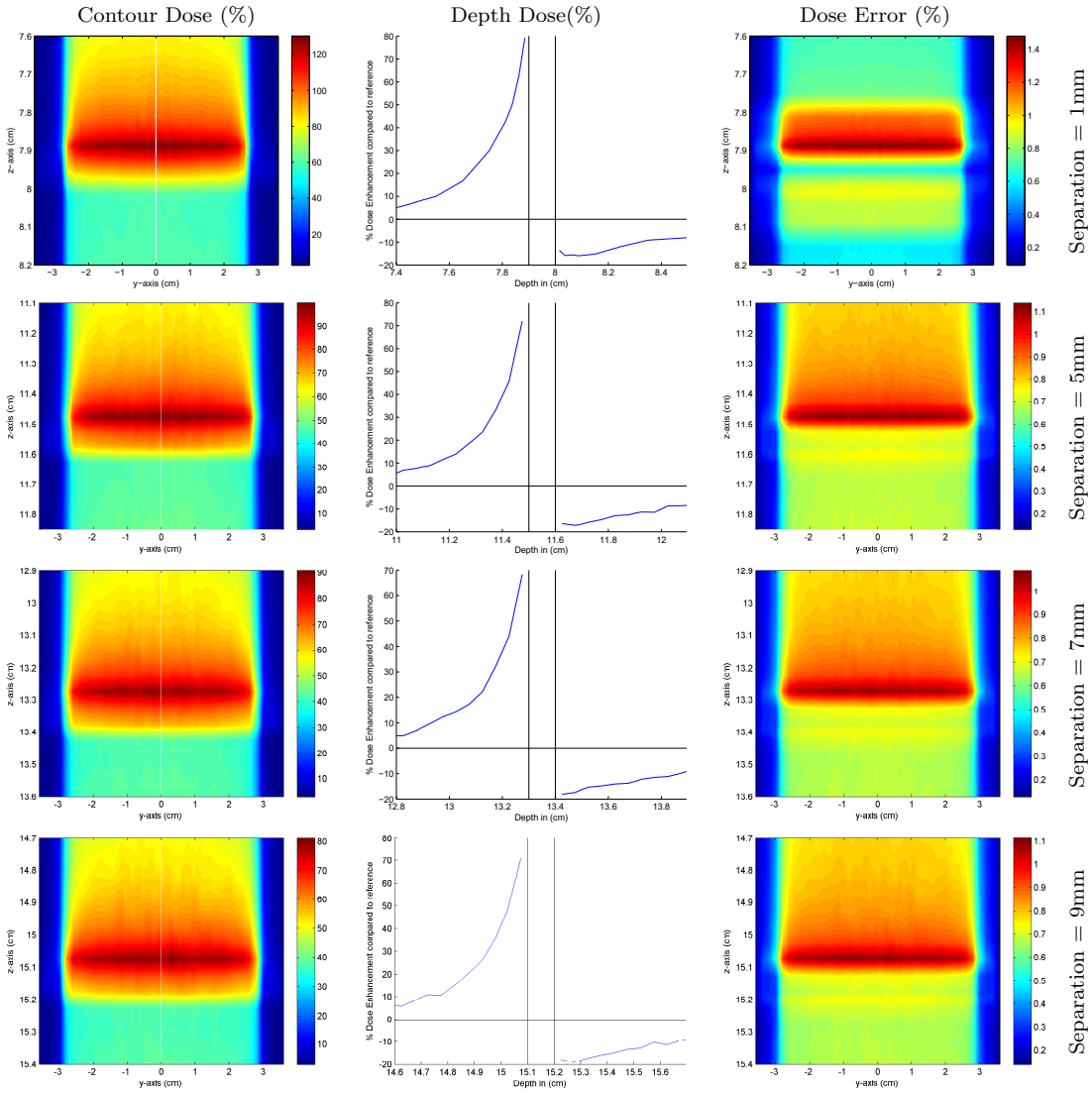

Thickness=1mm, Material=Lead, Field Size=5cm x 5cm, Foil Size=7cm x 7cm

C.9 Effect of Energy - Single Foil Upstream

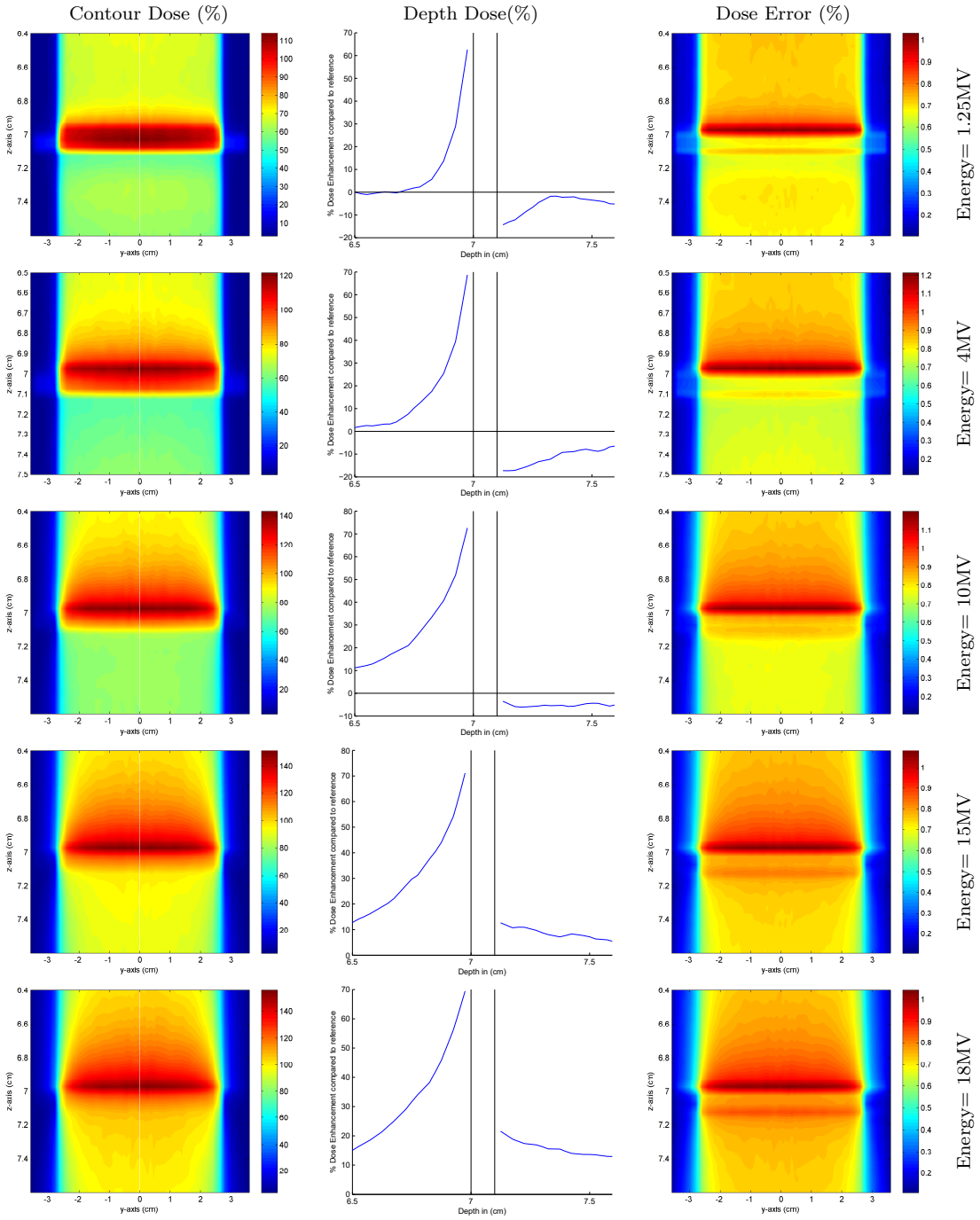

Thickness=1mm, Depth=7cm, Material=Lead, Field Size=5cm x 5cm, Foil Size=7cm x 7cm

C.10 Effect of Energy - Distributed Foils

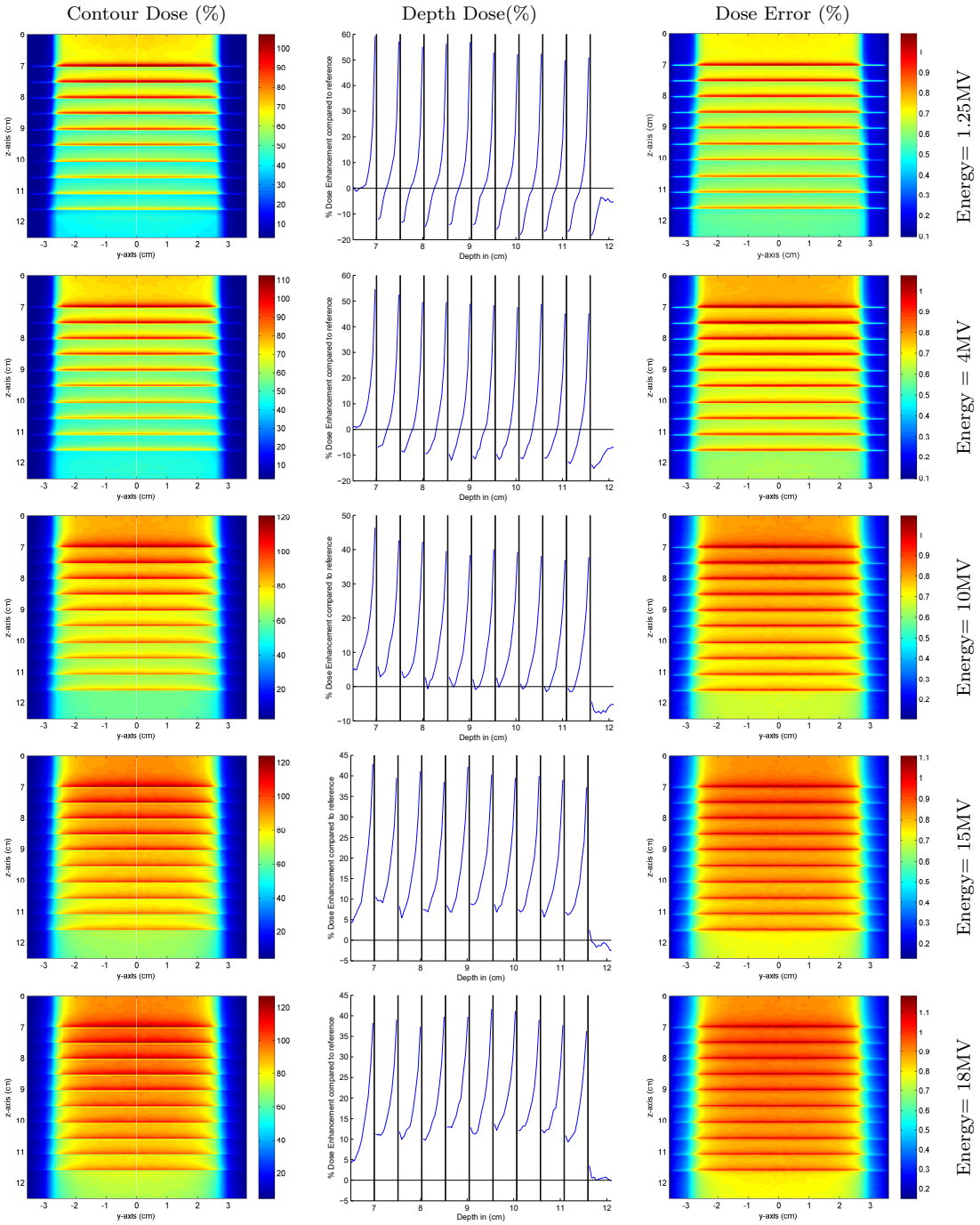

Thickness=0.1mm, Depth=7cm, Material=Lead, Field Size=5cm x 5cm, Foil Size=7cm x 7cm

C.11 Effect of Energy - Single Foil Downstream

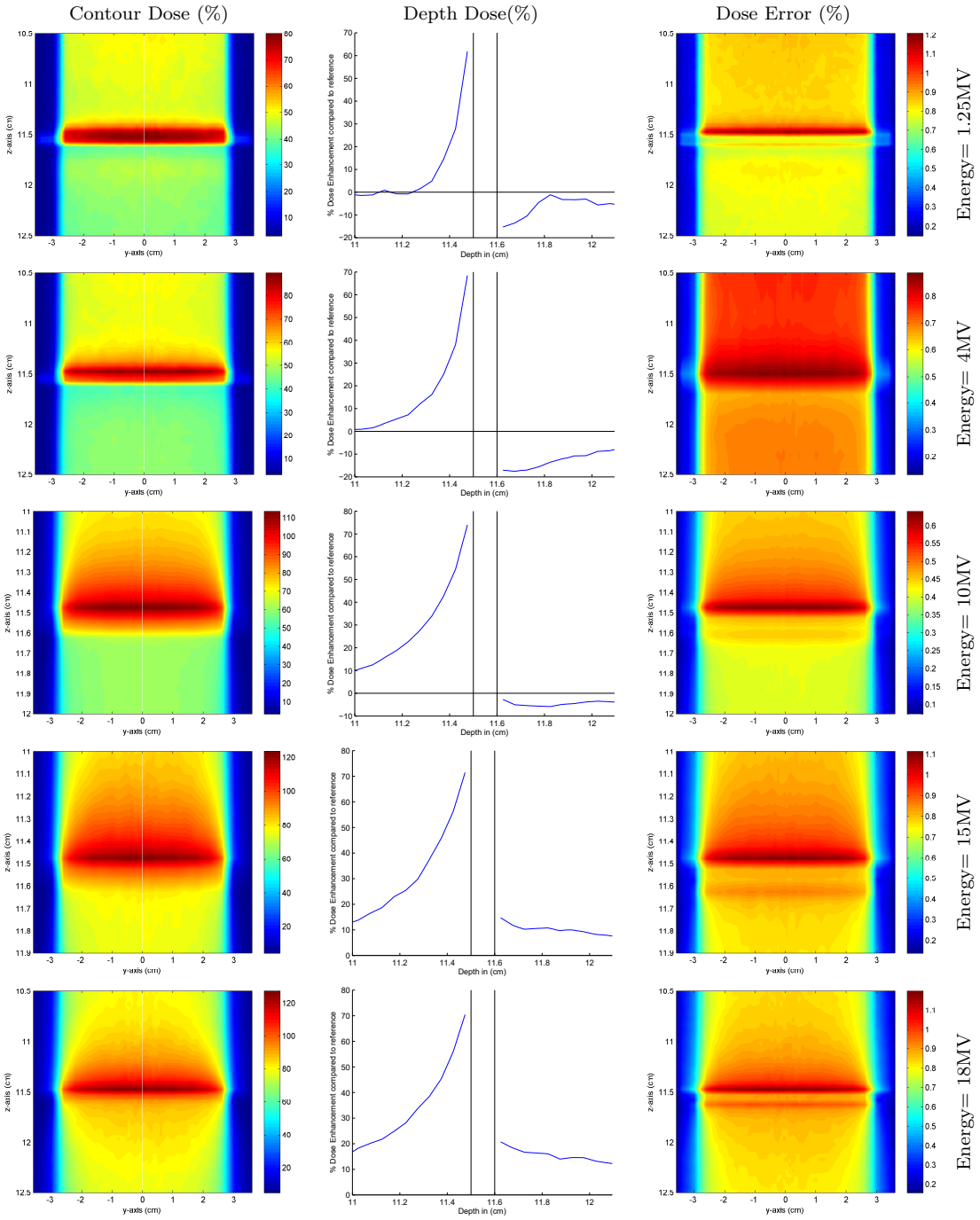

Thickness=1mm, Material=Lead, Field Size=5cm x 5cm, Foil Size=7x7cm